Doctoral Thesis in
Nanoscience and Nanotechnology

VNIVERSITAT DE VALÈNCIA

Vacuum Processed Narrow and Wide Bandgap Perovskites for Photovoltaic Applications

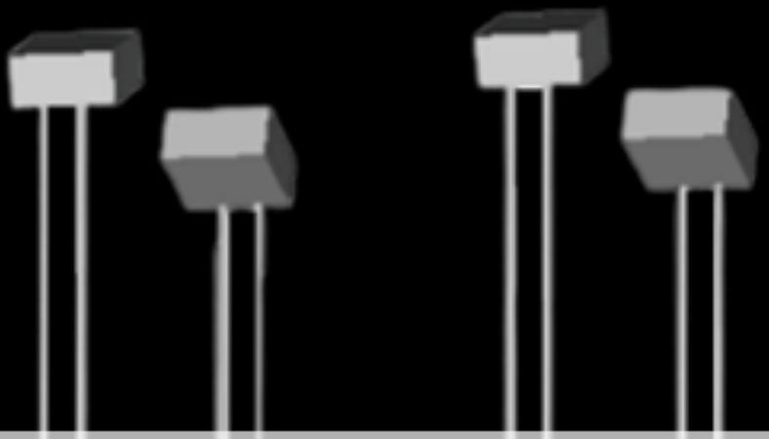

Ana María Igual Muñoz

Supervisors:
Prof. Dr. Hendrik Jan Bolink
Dr. Pablo Pérez Boix

July 2021

VNIVERSITAT DE VALÈNCIA

Doctorado en

Nanociencia y Nanotecnología

Instituto de Ciencia Molecular, Universitat de València

Ph. D. thesis:

Vacuum Processed Narrow and Wide Bandgap Perovskites for Photovoltaic Applications

Ph. D. candidate:

Ana María Igual Muñoz

Supervisors: Dr. Pablo Pérez Boix

Prof. Dr. Hendrik Jan Bolink

Tutor: Dr. Hendrik Jan Bolink

July 2021

Prof. Dr. Hendrik Jan Bolink, profesor titular de la Universidad de Valencia en el Instituto de Ciencia Molecular (ICMol) y el Dr. Pablo P. Boix, investigador de la Universidad de Valencia en el Instituto de Ciencia de Materiales (ICMUV) certifican que la memoria presentada por la doctoranda Ana Mª Igual Muñoz con el título "Vacuum Processed Narrow and Wide Bandgap Perovskites for Photovoltaic Applications" corresponde a su Tesis Doctoral y ha sido realizada bajo su dirección, autorizando mediante este escrito la presentación de la misma.

En Valencia, a 06 de Julio de 2021

BOLINK HENDRIK JAN - X5015834V
Digitally signed by BOLINK HENDRIK JAN - X5015834V
Date: 2021.07.07 10:24:34 +02'00'

Prof. Dr. Hendrik Jan Bolink

PABLO| PEREZ| BOIX
Digitally signed by PABLO| PEREZ|BOIX
Date: 2021.07.06 17:11:14 +02'00'

Dr. Pablo P. Boix

"We have the tools; technology is on our side. The climate emergency is a race we are losing, but it is a race we can win."

António Guterres

Dedicado a mi familia

Agradecimientos

La primera persona a la que me gustaría agradecer es a mi director de tesis, Henk. Gracias por haber confiado en mí para realizar la tesis en una de las líneas de investigación más interesantes, de alta calidad científica y actuales de hoy en día. Por tu apoyo y guía durante estos años, por haberme valorado y ayudado a enfocar mi carrera profesional hacia dónde deseaba. También me gustaría agradecer a mi supervisor de tesis Pablo, por haberme ayudado tanto, siempre con un toque de humor, haciendo un largo camino más ameno. Y por continuar ayudándome cuando ya había salido del camino.

A todos los miembros de mi grupo de investigación, el llamado MOED, pasados y presentes. Gracias Cristina, por haberme acompañado el corto tiempo que estuviste, por inspirarme y hacerme querer ser un mejor científico. También por haber seguido a mi lado todo este tiempo, no como compañera, si no como amiga. Lidón, otra inspiración en mi doctorado, y para toda mi carrera investigadora. Has sido otra de las personas de las que me llevo una verdadera amistad. Gracias por haberme escuchado durante horas y horas en la Sala Limpia, por haber sido siempre mi comodín y por todo lo que me has enseñado, que no es poco. Siempre me tendrás cuando me necesites. A quién hizo posible que esté escribiendo esto, Dani. Desde un año antes que los demás, compartí contigo un par de meses de mi vida, que hubieran sido mucho menos divertidos si no hubieras estado ahí. Gracias a ti, entre otros, me animé a venir a este grupo y siempre lo recordaré. Tú también me tendrás aquí siempre cuando me necesites. A otra verdadera amiga, Aroa. Recuerdo cuando me dijeron que te ibas a unir a la síntesis de perovskitas de banda prohibida estrecha, nunca me imaginé que a lo que realmente te unirías sería a mi vida. Me has aportado tantos buenos momentos y tantas risas que no caben en estas páginas. También quiero agradecer a Michele, por su constante implicación en mi investigación, su sabiduría y habilidades que me ha transmitido de la mejor de las maneras. A Maria Grazia y Azin, aunque ya no estéis aquí os sigo teniendo a mi lado, siempre recordaré aquel viaje, espero poder seguir acompañándoos siempre. Por otro lado, tenemos a todos los que hacéis posible que el grupo funcione: Jorge, María, Alejandra, Ángel... Todo lo que

habéis hecho por mí, os lo agradezco. Al resto de miembros que están y que estuvieron, Laura, Jorge Á., Paco, Wiria, Vaheed, Chris, Sang, Bas…Sabéis que sigo estando aquí si me necesitáis, gracias por haberme acompañado también.

A mis amigos de la Universidad, por escucharme y acompañarme desde hace casi una década. Por haber compartido conmigo tantos momentos y haberme apoyado cuando lo necesitaba. Y a Jesús, que también me ha acompañado casi diez años, y me seguirá acompañando muchos más, aunque ya no lo hará desde la escalera de incendios, aquí estoy. A los que me acompañaron en un tiempo previo a mi tesis y no quiero olvidar, José, Katia, Alejandro… Y al resto de los que me han rodeado siempre, como verdaderos amigos que fueron y serán.

El mayor de todos los agradecimientos es para mi familia. Porque sé que soy como soy gracias a ellos. Porque siempre han estado ahí y siempre lo estarán. A mis abuelos, que me han cuidado y me han querido como solo un número de personas que puedo contar con los dedos de mi mano. A mi hermana, Lucía. La persona para la que me esforzaré siempre en ser una inspiración. A mi madre. No tengo palabras para ti mamá. Todo lo que he hecho y haré, te lo dedico. Todo esto es gracias a ti, porque nunca te rendiste.

Por último, a la familia que se escoge. A Jose, por escogerme y por ser el compañero que he escogido. Por haberme dado la fuerza que necesitaba para seguir adelante siempre. Por haberlo compartido todo conmigo y porque lo sigamos compartiendo, para siempre. Y a las alegrías de mi vida, a los que me dan su calor y su tranquilidad cuando llego a casa cansada.

Contents

Chapter 1

Introduction and Aim of the Thesis

1. Introduction and Aim of the Thesis

1.1. The Energy Challenge

The global energy demand has increased from 10.000 TWh in 1990 to more than 20.000 TWh in 2019 (Figure 1).[1] The need to produce energy has depleted conventional energy sources based on fossil fuels, resulting in an increase in the annual mean temperature of Earth due to the production of greenhouse gases. For this reason, the need to produce clean and renewable energy instead of traditional fossil fuels is imminent.

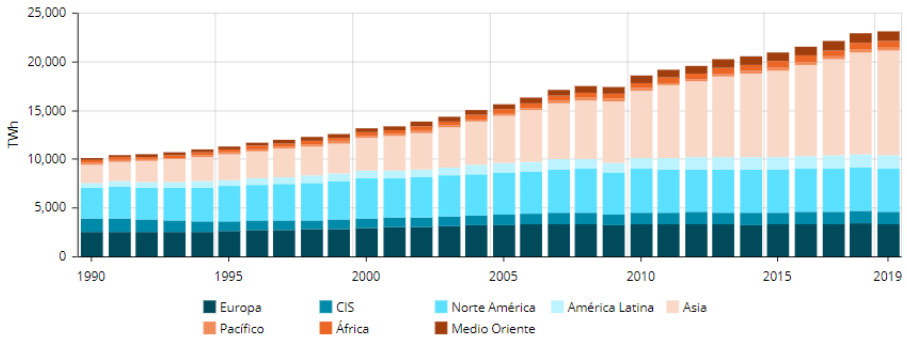

Figure 1. Global energy consumption from 1990 to 2019. [1]

Among the different candidates, solar energy is a promising alternative. This is due to the large amount of energy that reaches the Earth in the form of solar irradiation, which could provide the whole world with the energy needed to continue with its industrial and domestic development. Photovoltaic technologies (PV) directly transform solar light into energy. In 2050, PV is expected to increase its energy supply to 16% of the total energy demand, which corresponds to 4.5 TW. However, more ambitious roadmaps expect between 9 and 23 TW of energy supplied by solar cells.[2,3]

Photovoltaic devices were developed in 1883, when Charles Fritts employed selenium and a thin layer of gold obtaining an efficiency of less than a 1%, in

order to harvest all the energy the sun irradiates to the Earth.[4] Generally, crystalline semiconductors have been employed to generate current from solar energy, such as Gallium arsenide (GaAs), silicon (Si), Cadmium telluride (CdTe) or Copper indium gallium selenide/sulfide (CIGS). However, recently, a new generation of solar cells has emerged.

1.2. Metal Halide Perovskites

Solar cells based on metal halide perovskites were first reported in 2006 by Kojima A. *et al*, when their efficiency was a modest 2.2%.[5] During the last years, these devices increased their efficiency up to a certified 25.5% and uncertified 25.6%.[6,7] The evolution of the best research photovoltaic technologies can be observed in Figure 2, where the unprecedented increase in efficiency of perovskite solar cells can be observed. Perovskite-based photovoltaic devices present several advantages over other technologies: their earth-abundant compounds, low-cost and easy tunability of the bandgap among others, make them one of the most promising technologies to increase photovoltaic efficiency and reach the goal of generating renewable competitive energy.

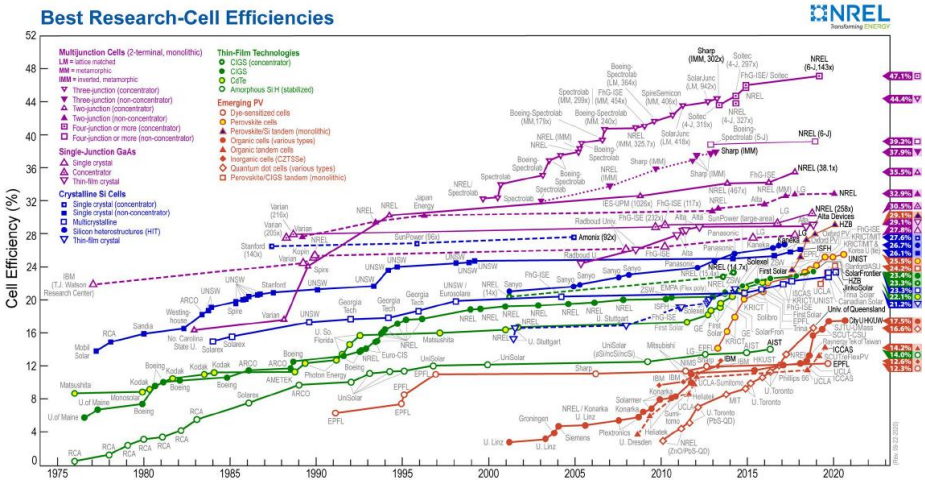

Figure 2. Best research photovoltaic cell efficiencies. [7]

These devices are specifically based on metal halide perovskites, a type of perovskite which has a three-dimensional structure known as ABX_3. Where A

represents a monovalent cation, which can be organic or inorganic (such as cesium, methylammonium (MA) or formamidinium (FA)), B represents a divalent metal as Pb^{+2}, Sn^{+2} or Ge^{+2} and X represents a halide anion such as I^-, Br^- or Cl^-. An example of the structure can be observed in Figure 3, where the simplest ABX_3 can be seen in the inset and in the center of the graph a more complex perovskite is displayed, in which different A and B cations are employed.

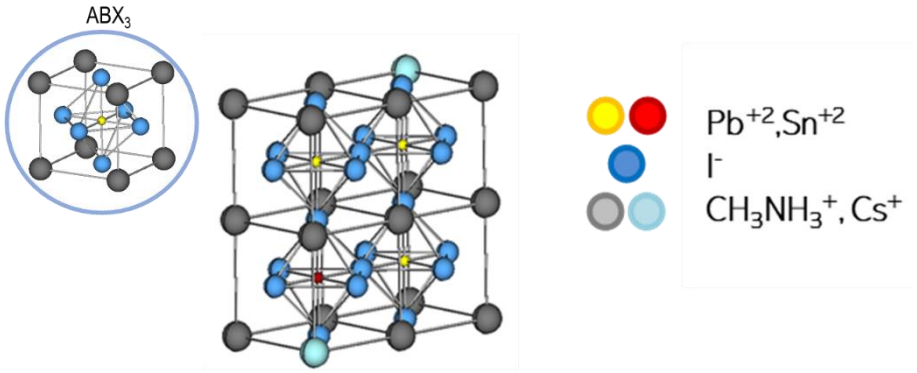

Figure 3. Structure of a perovskite composed of methylammonium cesium lead tin iodide and the typical ABX_3 (inset).

A parameter commonly employed to estimate how stable this structure is, is the Goldschmidt tolerance factor.[8] This tolerance factor is phenomenologically estimated to be more than 0.8 and less than 1 for a stable compound.[9]

The formula that determines the tolerance factor of a compound is shown in Equation 1.

$$t = \frac{r_A + r_X}{\sqrt[2]{2}(r_B + r_X)} \quad (1)$$

Where t attains for tolerance factor and r for the radius of the respective components. The effect of tuning the tolerance factor through the introduction of different cations in the perovskite structure has already been shown to be an excellent technique to enhance the properties of perovskites.[10] As an example, Figure 4 shows how the introduction of cesium in a formamidinium lead iodide ($FAPbI_3$) structure promotes a more stable perovskite through the introduction of a smaller cation in the A site of the perovskite.

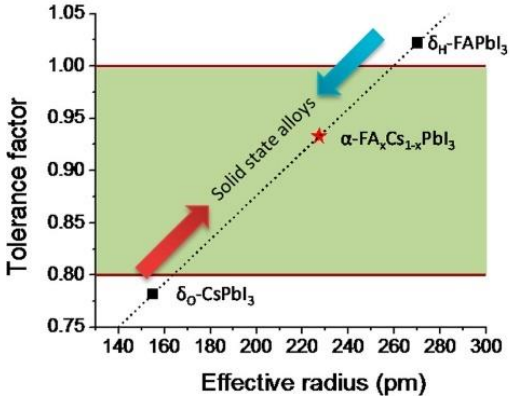

Figure 4. Dependence of the tolerance factor on the A-Site cation. [10]

On the other hand, apart from their structure, composition and stability, perovskites present some exciting properties that make them suitable for photovoltaic applications. One of the main ones is their high charge carrier mobility. This property is related to how much the charge carriers, electrons and holes, can move inside a semiconductor.[11–13] Carrier diffusion lengths between 0.1 μm and 10 μm have been reported, which allow the charge carriers to move inside the material from highly populated areas to low populated areas.[11,14,15] They also present high carrier lifetimes of more than 1μs. This property describes the time that carriers take to recombine. Higher carrier lifetimes are needed to ensure higher open circuit voltages (V_{OC}), as it enables a higher concentration of charge carriers.[16] Furthermore, from an optical description, they also show significant absorption coefficients, in the range of 10^5 cm^{-1}.[15,17] This allows for more efficient conversion of the sunlight into electricity and contributes to achieve larger open circuit voltages, as it allows to prepare thinner films reducing the total recombination rate.[18] They also show a sharp absorption onset demonstrating small amounts of defects and imperfections.[19]

Finally, one of the most critical properties would be the bandgap tunability, as it opens a wide range of applications for this kind of compounds, including solar cells with higher efficiencies through the development of multijunction devices.[20–22] Multijunction devices consist of a stack of several layers. The combination of absorbers with different bandgaps (E_gs) reduces the thermalization losses and ensures to exploit a larger part of the solar spectrum, with potential efficiencies higher than the conventional single junction limit.[23–25] Such an approach can

combine perovskites with other PV technologies such as silicon or thin film solar cells to fabricate multijunction tandems. Developing the capability of multi-junction devices by the combination of perovskite materials as top cell with silicon-based materials as bottom cell is actually one of the main research and innovation goals suggested by the Energy Materials Industrial Research Initiative (EMIRI) technology roadmap, (SP3- Annex I).[26] Similarly, the combination of two perovskite absorbers with complementary bandgaps can have the same effect. Therefore, adjusting the perovskite E_g becomes a key step. The importance of bandgap engineering is displayed in Figure 5. This figure shows the combination of bandgaps and efficiencies that can be obtained through their use in multijunction devices with two absorbers.

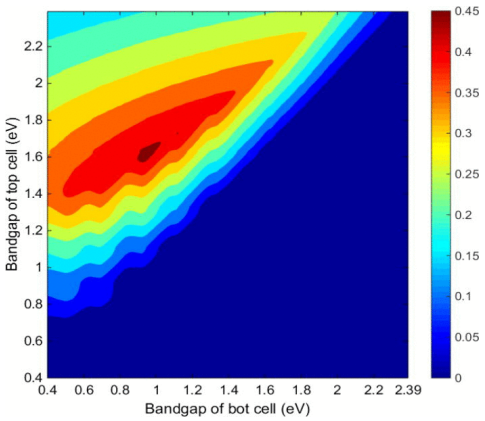

Figure 5. Calculations of the efficiency for multijunction devices depending on the bandgap of their absorbers.[27]

1.3. Bandgap Tunability

Perovskites present the capability of tuning their bandgap by the total or partial substitution of their components. As an example, the most studied hybrid perovskite methylammonium lead iodide ($MAPbI_3$), presents a E_g of 1.5-1.6 eV.[28] However, when larger FA^+ is introduced in its structure, the E_g is narrowed down to 1.48 for pure $FAPbI_3$.[29] On the other hand, if smaller Cs^+ is introduced, the E_g can be widened up to 1.73 eV for pure cesium lead iodide ($CsPbI_3$).[30] E_g can also be tuned by the substitution of the divalent cation, for example, in the perovskite

with structure formamidinium cesium lead iodide ($FA_{0.75}Cs_{0.25}PbI_3$) G.Eperon *et.al.* introduced Sn^{+2} to narrow the E_g down to 1.2-1.3 eV.[20] This tunability of the bandgap can be seen in Figure 6.

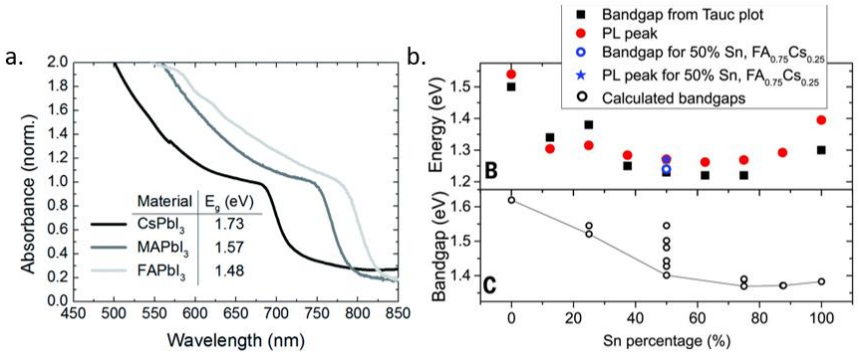

Figure 6. Tunability of the bandgap through a) Introduction of a monovalent cation in position A. [30] *b) Introduction of a divalent cation in position B.*[20]

In this sense, this thesis focuses on the development of narrow bandgap (narrow-E_g) and wide bandgap (wide-E_g) perovskites with the aim to fabricate efficient, lower cost tandems in the future.

1.3.1. Narrow-Bandgap Perovskites

One of the main concerns surrounding perovskites has been to enhance their efficiency to develop low-cost devices. $MAPbI_3$ perovskite shows a E_g of 1.5-1.6 eV, far from the theoretically determined to be the "optimum E_g", of ~1.3 eV, for single-junction devices, as estimated by the Shockley Queisser Limit.[31] On the other hand, for the pure tin perovskite, methylammonium tin iodide ($MASnI_3$), we find a bandgap of 1.2-1.3 eV. [32] In contrast, tin-lead perovskites present an unconventional behavior called bandgap-bowing. This effect describes a non-monotonic behavior in the E_g where the constant b in Equation 2 causes a deviation on the linear interpolation in the bandgap.

$$E_g(A_{1-x}B_x) = (1-x)E_g(A) + xE_g(B) - bx(1-x) \qquad (2)$$

In Equation 2, A and B stand for the divalent metals and x for the stoichiometry of the compound. Due to this effect, tin-lead perovskites show narrower bandgaps in the alloyed compounds than their pure counterparts. For example, in the case of methylammonium tin lead iodide ($MASn_{1-x}Pb_xI_3$) with different amounts of tin and lead, the pure lead perovskite presents a E_g of 1.5-1.6 eV, the pure tin compound has a E_g of 1.2-1.3 eV, and the alloys can vary between 1.3eV and 1.1 eV, as can be observed in Figure 7.

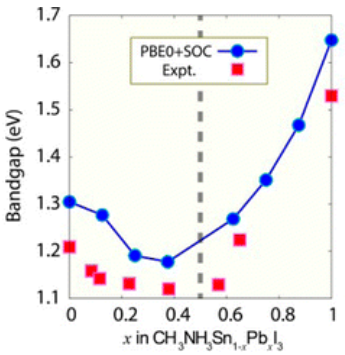

Figure 7. Bandgap evolution by composition variation for $MASn_{1-x}Pb_xI_3$. [32]

Some researchers have been trying to achieve the optimum E_g of 1.34 eV by means of this effect.[31,33–36] In 2017, Yang Z. and co-workers achieved this value using a combination of tin and lead as the divalent cation and a combination of bromide and iodide as the halide in the perovskite obtaining efficiencies as high as 17.63%.[37]

On the other hand, this bowing of the E_g also allows to prepare even narrower perovskites with E_gs of around 1.2 eV, suitable for the preparation of multijunction devices with wider-bandgap perovskites to achieve efficiencies over 30%.[38,39] These narrower bandgaps were already obtained by Ogomi Y. and co-workers through the use of $MASn_{0.5}Pb_{0.5}I_3$ perovskite.[40]

The combination of tin and lead inside the perovskite structure opens a wide range of opportunities for the development of narrow-E_g perovskites. These perovskites can be used as the single-junction optimum E_g perovskite or as low-E_g absorbers in multijunction devices. However, they present several difficulties in their preparation, such as the oxidation of Sn^{+2} to Sn^{+4}.

1.3.2. Wide-Bandgap Perovskites

Perovskites showing a E_g between 1.7 eV and 1.9 eV are commonly considered "Wide-E_g". This feature enables their use as a wide bandgap absorber in multijunction devices in combination with Si or narrow-E_g perovskites. Normally, this widening of the bandgap is achieved by combining different halides.[41] For example, through the introduction of bromide inside the $MAPbI_3$ structure, bandgaps up to 2.23 eV for pure methylammonium lead bromide ($MAPbBr_3$) can be obtained.[42] On the other hand, the use of inorganic cations instead of the commonly used MA and FA increases the E_g and the thermal stability of these perovskites.[43–45] Furthermore, the introduction of smaller amounts of bromide enhances the stability of its black-phase, the one employed for solar cell applications.[46–49] However, perovskites combining different halides present a major detrimental effect which is called halide segregation.[50] This occurs when, after illumination, regions of lower E_g perovskite and others of higher E_g perovskite are formed within the same film. This phenomenon is attributed to the presence of mobile halogen vacancies in the structure. When these regions are formed, the photogenerated carriers travel to the low-E_g regions that act as recombination centers leading to V_{OC} losses.[51,52]

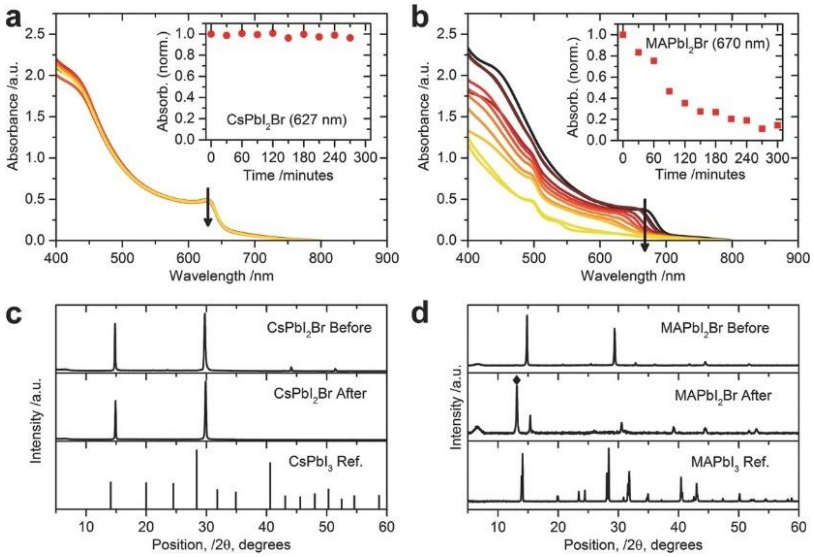

Figure 8. Comparison of the stability of $CsPbI_2Br$ and $MAPbI_3$ perovskite layers.[48]

The perovskite employing cesium lead iodide bromide ($CsPbI_2Br$) has been widely studied, which has resulted in current efficiencies of up to 16.79%.[53] In 2016, R. Sutton *et al.* showed how the introduction of bromide in this perovskite enhanced its ambient stability and proved better thermal stability than with conventional $MAPbI_3$. A comparison between them is shown in Figure 8. These perovskites were synthesized through a two-step method depositing lead bromide ($PbBr_2$) and dipping this layer into a solution with the amounts required of cesium iodide (CsI) and cesium bromide (CsBr) to form the desired perovskite. The layers of $CsPbI_2Br$ were employed in devices, achieving efficiencies up to 9.8%.[48] In 2017, C. Chen *et al.* synthesized both $CsPbI_3$ and $CsPbI_2Br$ films, achieving efficiencies as high as 9.4% and 11.8% for sublimed and solution-processed $CsPbI_2Br$, respectively.[54] In 2018, studies on the optimization of the contacts were performed. L. Yan *et al.* demonstrated how they could achieve efficiencies as high as 14.6% with improved stability, employing a novel electron transporting material (ETM) based on the combination of tin oxide (SnO_2) and zinc oxide (ZnO).[55] 2019 was an exceptional year for the development of this kind of perovskite. During this year, different approaches were employed to manufacture impressively well-performing solar cells. The work done by Y. Zhang *et al.* was key, as they achieved the highest power conversion efficiency (PCE) up to date for this perovskite: 16.37%. In these studies, they synthesized the perovskite through spin coating and annealed it at 280ºC. Afterwards, they evaporated a thin layer of CsBr on top to fill the grain boundaries in the perovskite surface, also passivating the hole transporting material (HTM). Furthermore, to stabilize the black phase of the perovskite they introduced lead acetate ($Pb(Ac)_2$) in the precursor solution, improving the crystallization of the film.[56] In 2020, Y. Han and co-workers synthesized the $CsPbI_2Br$ perovskite solar cells (PSC) with the highest efficiency (16.79%) up to date. This work was based on the addition of the additive calcium chloride ($CaCl_2$) in very small quantities being 0.5% the optimal one, which improved the crystallinity and hence the morphology. Furthermore, it passivated the trap states in the perovskite leading to higher efficiency devices.[53] However, the synthesis of these perovskites through sublimation methods yielded lower efficiencies than solution-processed counterparts, being the highest the one obtained by H. Lin *et al.* [57] In their studies, they developed a method where they separated two sides of the evaporator and constantly evaporated CsBr and lead iodide (PbI_2). As the sample holder was constantly rotating, they were able to achieve perovskites formed by 1560 layers of each precursor. Their best

performing solar cells achieved PCE as high as 13% for 660 pairs of precursors. This is a modest efficiency compared to the ones obtained through solution processing methods, indicating that further studies on the formation of these perovskites through sublimation must be done to develop a low-cost method to synthesize them.

1.4. Processing Techniques

Different techniques have been developed to synthesize metal halide perovskites. However, several properties may change in the resulting films depending on the used technique. Two main branches are found among the different techniques in the literature: solution-based methods and vacuum-based deposition techniques (Figure 9).[58]

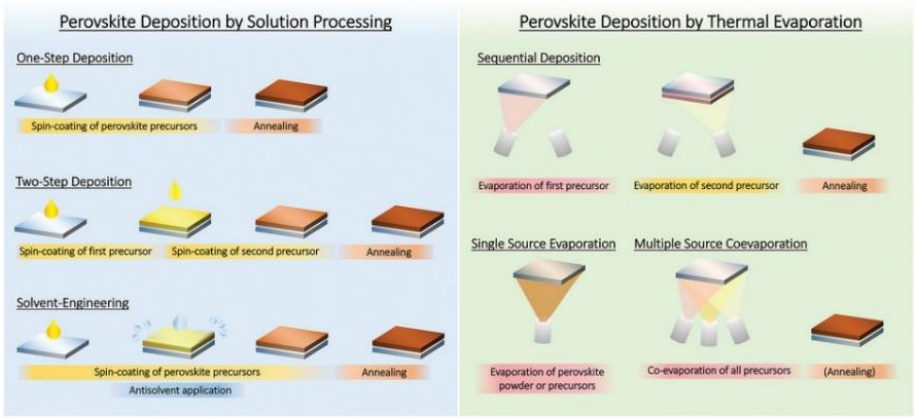

Figure 9. Processing methods to develop perovskite films divided into solution-based and thermal sublimation.[58]

The former can be divided into three main methods:

- One-step deposition:

This method is based on the preparation of a single solution where all the precursors of the perovskite are mixed. After this preparation, the solution is deposited through spin-coating or similar methods onto the substrate and requires a post-annealing treatment to eliminate the remaining solvent in the film. This is a

commonly used method to develop perovskites, and several advances have been introduced to obtain better quality films, such as the introduction of different additives or the use of different solvents. McMeekin D.P. and coworkers employed this method to synthesize formamidinium cesium lead bromide iodide $FA_{0.83}Cs_{0.17}Pb(Br_{0.7}I_{0.3})_3$.[23] In previous studies, they demonstrated how the employment of hydrohalic acids promotes the formation of nucleation sites allowing to obtain morphologies with grains exceeding the micron size.[59] Furthermore, they employed a K^+ additive, which has been already used to improve the photovoltaic performance through modification of the crystal lattice and reduction of the grain boundaries.[60] Other additives have been employed on perovskites synthesized by one-step solution methods, such as barium or acetate.[61,62] Furthermore, research on different solvents has been done, obtaining a wide variety of options even with green solvents as Polar Clean.[63]

- Two-step deposition:

This technique is based on the initial deposition of part of the perovskite precursors and a second deposition of the rest. It has several advantages as it allows for better morphology control, determined by the first precursor deposited, which are typically the lead-based compounds. The second deposition may be done through spin-coating, dipping or vapor-assisted.[64–66] Different techniques to enhance the properties of the films have been introduced. The incorporation of additives such as rubidium, cesium and different alkali metals has been studied.[67,68]

- Solvent engineering:

This method is based on the addition of a solvent where perovskites are poorly miscible during the spin-coating of the precursors. This fact changes the deposition kinetics of the perovskite triggering a fast film formation. For this reason, better morphologies may be achieved.[69,70] This technique leads to better results. However, the vast number of parameters needed in this method makes solvent-engineering a poorly reproducible and non-scalable method.

As for the vapor deposition techniques, there are three main methods to deposit perovskites:

- Flash evaporation:

This technique is based on the initial formation of the perovskite through different methods, as for example ball-milling and then a sublimation of the already mixed precursors.[71] It has shown to be an excellent technique to synthesize films, including those combining tin and lead as the divalent cations.[72] Decent efficiencies were achieved employing this technique for lead-based perovskites.[73] However, this technique shows inferior control on the composition of the films, due to the need of subliming all the components at the same time.

- Sequential deposition:

This method is similar to the sequential solution-based one previously described, named as two-step deposition. The procedure consists of individually subliming the precursors by consecutive steps. However, the technique requires a thermal post-treatment to form the desired perovskite. This technique resulted in very good efficiencies on photovoltaic devices employing the wide-bandgap $CsPbI_2Br$ perovskite. As mentioned before, Lin H. and co-workers, employed this method to prepare highly efficient sublimed cesium-based perovskites.[57]

- Multiple source co-evaporation:

This technique uses the simultaneous sublimation of all the different precursors of the perovskite to form the perovskite in situ onto the substrates. It requires control of the stoichiometry which is normally done by monitoring the mass deposited on Quartz Crystal Microbalances (QCM). This will be the main technique employed in this thesis because of the advantages it presents, especially its high control on the composition of the films.

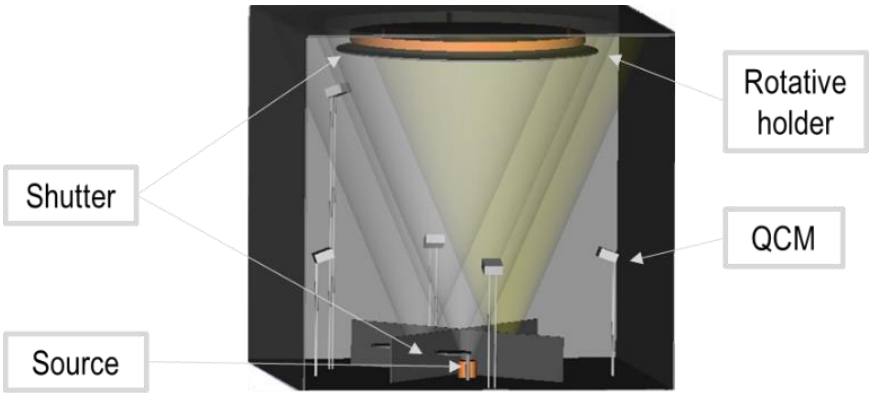

Figure 10. 3D design of an evaporator employing 4 sources and 5 QCMs.

In Figure 10 a scheme of one of the evaporators employed in this thesis is displayed. This illustration shows an evaporator chamber where four sources are being employed to evaporate four different precursors. On the other hand, five sensors employing QCMs can be observed. These sensors were calibrated to detect the specific amounts of each precursor through the mass deposited on them, and a fifth one to determine the quantity of perovskite formed on the substrates. In the upper part of the evaporator a rotating holder holds the substrates. The rotative holder is key to achieve a homogeneous formation of the perovskite. Furthermore, five shutters may be observed on the design. These shutters are employed to control, with high precision, the composition of the perovskite, acting as barriers to not deposit the different precursors both in the substrates and in the QCMs.

The first devices fabricated employing this method in 2013 showed efficiencies up to 15%.[74,75] However, these devices where employing $MAPbI_3$ as the absorber, which is simpler to synthesize as it only requires controlling two precursors at the same time. Afterwards, the technique has evolved, obtaining efficiencies beyond 20%.[76,77] The technique has also proven to be successful both for wide-E_g and narrow-E_g perovskites, allowing them to obtain working devices.[78,79] All of these studies, combined with the advantages that it offers, encourage the scientific community to employ it as the method to synthesize low-cost scalable perovskites.

Some of the advantages that this technique presents are:

- High purity of sublimed materials: sublimation is a purification method so the materials that end up in the substrate present higher purity than the ones used employing solution-based methods.
- Large area compatibility: the area depends basically on the size of the substrates, as can be seen in Figure 10.
- Precise control of the thickness, stoichiometry, and morphology of the films.
- Low substrate temperature, no need of thermal post-treatments.
- Intrinsically additive technique: this technique allows to prepare different layers without the use of solvents that affect the layers previously deposited.
- No need to use toxic solvents.
- Consolidated technique that has already been used in industry.

1.5. Solar Cells Operation

PSCs can be arranged in several configurations. The sandwiched configurations, where the perovskite absorber is between both electron and hole conductive layers, can be summarized as p-i-n and in n-i-p structures (depending on which contact is the light incidence side).

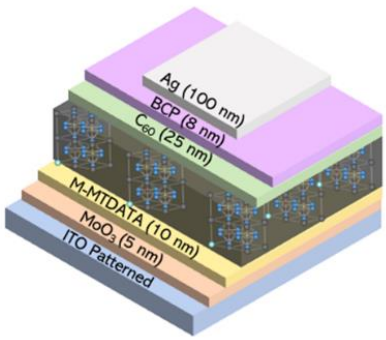

Figure 11. 3D design of a p-i-n architecture.

In the p-i-n structure, sunlight is incident from the hole (positive (p) charge carrier) extraction electrode. The n-i-p structure is the reversed architecture, where the sunlight is incident from the electron (negative (n) charge carrier) extraction contact, ETM is firstly reached then the absorber and finally the HTM. As an example of the p-i-n architecture Figure 11 can be observed.

When illuminated, perovskites generate electron-hole pairs that become free electrons and holes due to their generally low exciton binding energies. These charge carriers are extracted by the HTM and ETM and collected at the electrodes. As discussed in chapter 1.2, perovskites present some intrinsic properties, such as high mobility of the charge carriers, that lead to low non-radiative recombination. These properties minimize the energetic losses and are key to make efficient solar cells.

Two main methods can be employed to determine how efficient solar cells are:

- External Quantum Efficiency (EQE) or Incident Photon-to-electron Conversion Efficiency (IPCE): this technique consists of measuring the number of photons that are successfully converted to electrical current depending on the wavelength of the incident photons.

- Current density under illumination versus voltage scan (J-V curves): the measurement of this feature allows to obtain different values required to determine the PCE. PCE is an important parameter of the devices, as it represents their capability to convert sunlight into electricity and it is calculated as represented in Equation 3.

$$PCE = \frac{Jsc \cdot Voc \cdot FF}{P_{in}} \quad (3)$$

Where V_{OC} is the Open Circuit Voltage, or the voltage in the terminals when the cell is operated at short-circuit conditions. J_{SC} stands for Short Circuit current density, or the current in the terminals when the voltage applied is equal to 0 V. FF is the Fill Factor, or the ratio of maximum power point against the product of V_{OC} and J_{SC}; and P_{in} is 100 $mWcm^{-2}$ when operating at AM 1.5G illumination. These measurements are usually performed under AM 1.5G, a standard solar

spectrum that allows to characterize solar cells all over the world and compare them.[80]

Solar cells can present hysteresis in their J-V curves. This effect is observed when there are distortions in the curve depending on the measurement direction: forward, negative to positive applied voltage, or reverse, positive to negative applied voltage.[81]

As an example, in Figure 12 both the EQE and J-V curve measuring can be observed for a wide-bandgap solar cell.

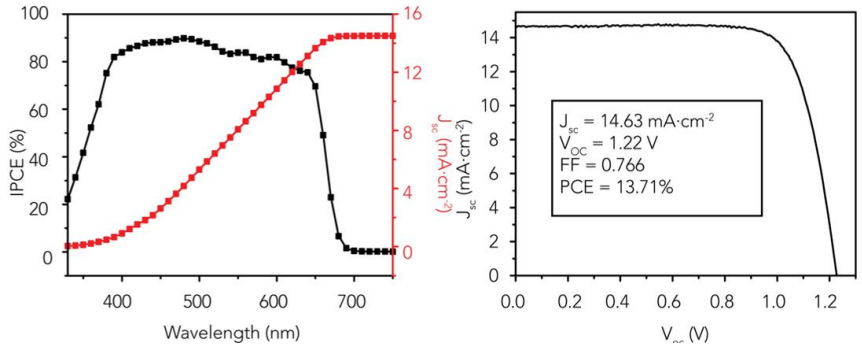

Figure 12. IPCE, where the integrated current obtained from IPCE is represented in red, and J-V curve measurement for a cesium lead europium iodide bromide $CsPb_{0.95}Eu_{0.05}I_2Br$ *solar cell.* [82]

1.6. Aim of the Thesis

The aim of this thesis is the development of narrow-bandgap and wide-bandgap perovskites through vacuum-based methods and their incorporation into devices employing organic charge transport layers.

As mentioned in section 1.3.1, one of the main issues of tin-lead alloyed perovskites preparation is the oxidation of Sn^{+2} to Sn^{+4} and the proper formation of the perovskite. In **chapter 3**, the preparation of the first narrow-bandgap sublimed perovskite working in efficient devices will be studied. The issue of formation and oxidation of the Sn^{+2} will be tackled through the introduction of a SnF_2 additive.

On the other hand, one of the main advantages of sublimation methods is the capability of controlling the composition in an efficient way. However, the use of small quantities of additives can be challenging. In **chapter 4**, the preparation of reproducible narrow-bandgap perovskites through vacuum deposition methods will be carried out by using more controllable cations and lower tin amounts. This chapter will be key for the progress of this kind of perovskites, as it aims to prepare perovskites showing the optimum bandgap of 1.34 eV.

Finally, as mentioned in section 1.3.2, one of the main issues of wide-bandgap perovskites is halide segregation. In **chapter 5**, a study on different vacuum-based methods to deposit $CsPbI_2Br$ is presented. As this kind of perovskites requires high temperature thermal post-treatments, with this study we will determine the proper routes to fabricate this perovskite without the need for further annealing.

Chapter 2
Experimental Methods

2. Experimental Methods

2.1. Solar Cell Fabrication

All the processes required to fabricate and characterize perovskite solar cells were carried out in a class 10000 clean room (Figure 13).

Figure 13. Class 10000 clean room situated in Instituto de Ciencia Molecular (ICMol) of the Universitat de València.

Preparation of the devices consisted of the following processes:

1. Substrate's preparation:

Indium tin oxide (ITO) coated glass substrates were cleaned in different steps starting by rubbing them with a Mucasol detergent solution, then washed with water, milliQ water and isopropanol. After each step, the substrates were sonicated for five minutes. Afterwards, the substrates were dried employing a nitrogen gun and finally they were exposed to UV-Ozone for 20 minutes.

2. Organic layers and metal cathode deposition:

Molybdenum oxide (MoO_3), 4,4',4"-tris [(3-methylphenyl) phenylamino] triphenylamine (m-MTDATA), N4,N4,N4",N4"-tetra ([1,1'-biphenyl]-4-yl)-[1,1':4',1"-terphenyl]-4,4"-diamine (TaTm), C_{60}, bathocuproine (BCP) and Ag

were deposited in three different evaporation chambers by heating the materials to their sublimation temperature. The chambers were evacuated until the pressure went down to ≈10^{-6} mbar. MoO_3 was deposited at a rate of 0.1 Å/s to a thickness of 5 nm, m-MTDATA was deposited at a rate of 0.5 Å/s to a thickness of 10 nm, TaTm was deposited at a rate of 0.5 Å/s to a thickness of 10 nm, C_{60} was deposited at a rate of 0.5 Å/s to a thickness of 25 nm, BCP was deposited at a rate of 0.1 Å/s to a thickness of 8 nm and Ag was deposited at a rate of 0.15 Å/s to a thickness of 100 nm employing a shadow mask with an aperture of 2.1 x 3.1 mm^2. Poly (triaryl amine) (PTAA) was deposited in solution. This deposition was done employing a spin-coater for 30 s at 1500 rpm. The bilayers of MoO_3-TATM, MoO_3-m-MTDATA and MoO_3-PTAA were annealed after preparation at 140, 100, and 100 ºC respectively, for 10 minutes. HTM structures are shown in Figure 14.

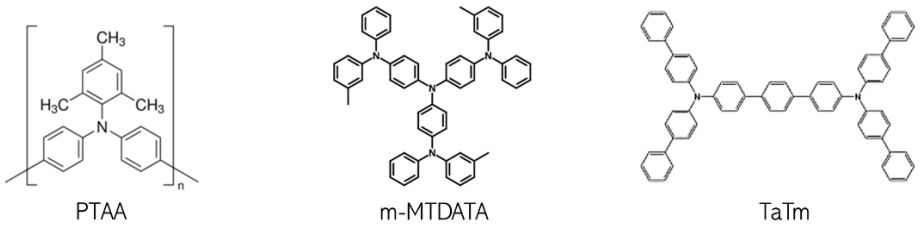

Figure 14. PTAA, m-MTDATA, and TaTm molecular structures.

3. Perovskite layers deposition:

- Formamidinium lead tin iodide ($FAPb_{0.5}Sn_{0.5}I_3$): four vapor deposition sources employing formamidinium iodide (FAI), PbI_2, tin iodide (SnI_2) and tin fluoride (SnF_2) as precursors.
- Methylammonium cesium lead tin iodide ($MA_{0.9}Cs_{0.1}Pb_{0.75}Sn_{0.25}I_3$): four sources vapor deposition employing methylammonium iodide (MAI), CsI, PbI_2 and SnI_2 as precursors.
- $CsPbI_2Br$: this perovskite was deposited using different methods to study how the deposition conditions affected its properties. As a summary, for the sublimation methods, the methods can be found in the scheme of Figure 15. For the solid-state synthesis stoichiometric amounts of CsBr and PbI_2 were mixed in a nitrogen-filled glovebox and ball-milled for 99 min at 30 Hz.

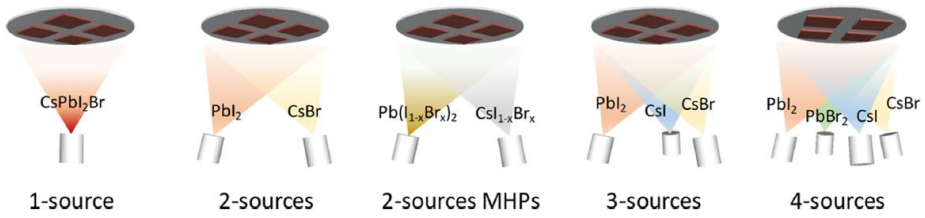

Figure 15. Scheme of the different vapor deposition techniques employed to synthesize $CsPbI_2Br$.

The photovoltaic devices employed in this thesis were based on three different main configurations (Figure 16).

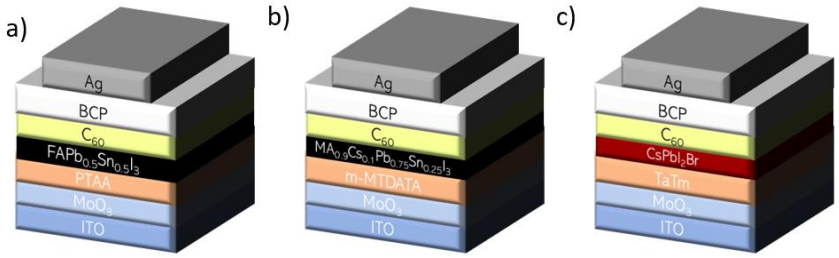

Figure 16. Solar cell configurations employed in a) Chapter 3, b) Chapter 4 and c) Chapter 5.

All three different configurations are p-i-n and employ different HTMs adjusted to the various valence bands of the employed perovskites.

In order to control the perovskites' stoichiometry, the sublimation rate is monitored in situ using QCMs. As commented in chapter 1, the sensors contain a QCM. The QCM consists of a quartz crystal between two metal electrodes. These microbalances are operated by applying an electrical field that causes a vibrational movement. When mass changes are produced because the material is deposited onto the QCM, the oscillation frequency is changed. Due to this change in the oscillation frequency, the mass deposited onto the QCM can be monitored. An initial calibration of each of them is performed to determine the amount of each material deposited in the QCM. The calibration was performed through evaporation of a known amount of material that can be determined by surface profilometry. Then, the calibration factor or tooling factor (TF) (Equation 4) is applied to the sensor.

$$TF_1 = TF_0 \cdot \frac{thickness_{measured}}{thickness_{QCM}} \quad (4)$$

Furthermore, some characteristics of each material, such as density and acoustic impedance, are introduced to improve the accuracy. The previously explained calibration was done for all the materials that were sublimed in this thesis.

2.2. Thin Film Characterization

As previously discussed, different perovskites were deposited during these studies. Several characterization techniques were employed to determine the quality of the films produced, which can be divided into structural and optical ones:

- Structural analysis: the thickness of the films was measured employing a contact profilometer (Ambios XP-1). The measurements were used to optimize the deposition conditions and for the specific thickness studies. A Hitachi S-4800 scanning electron microscope (SEM) operating at 20 kV and Veeco Instruments Inc. Atomic Force microscope (AFM) with a Si tip were employed to determine the surface morphology of the films. The scanning electron microscope was equipped with an X-Ray detector (Bruker) and the program QUANTAX 400 for the compositional Energy Dispersive X-Ray Analysis (EDAX). The crystalline structure of the films was determined by X-Ray Diffraction (XRD) employing an Empyrean PANalytical powder diffractometer in Bragg-Brentano geometry.

- Optical analysis: the absorbance of the films was measured employing a fiber optic Avantes Avaspec2048 spectrometer. Tauc plots were calculated using the formula $(\alpha h\upsilon)^2$ and plotting it vs the wavelength. Photoluminesce (PL) characterization was done employing a Hyperspectral Imager IMA VIS from Photon etc. coupled to a continuous wave laser of 532 nm.

2.3. Solar Cell Characterization

As for the solar cells, several characterization techniques were employed to determine their efficiency and performance parameters.

- Electrical characterization: EQE was calculated through the measurement of cell response under different wavelengths. The different wavelengths were obtained with a white halogen lamp and band-pass filters. J-V curves were obtained employing a solar simulator from Abet Technologies, model 10500, with a xenon lamp (AM 1.5G) as the light source and a Keithley 2400 source measure unit. The solar spectrum was adjusted employing a calibrated silicon reference cell (Minisun Simulator from ECN, Netherlands). All the samples were measured using a shadow mask of 2.2 x 1.2 mm^2 to be able to estimate the current density with precision.

- Sensitive EQE analysis (sEQE): cells were illuminated employing a Newport Apex 2-QTH Quartz-Tungsten-Halogen lamp through a Newport CS130-USB-3-MC monochromator, a chopper at 279 Hz and a focusing lens. The device current was measured as a function of energy using a lock-in amplifier (Stanford Research Systems SR830). The solar spectrum was corrected through calibration with a silicon reference cell.

- Electrochemical impedance spectroscopy (EIS): the measurements were obtained employing a Gamry Interface 1000 potentiostat to apply 20 mV perturbation with a frequency from 100 MHz to 100 mHz AC voltage, at different DC potentials under 1 sun illumination. The measurements were fitted with Z-View software to an equivalent circuit represented in Figure 17.

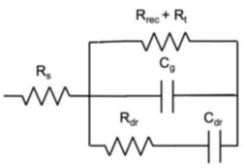

Figure 17. Equivalent circuit for the solar cells measured in Chapter 4.

Chapter 3

$FAPb_{0.5}Sn_{0.5}I_3$, A Narrow Bandgap Perovskite Synthesized through Evaporation Methods for Solar Cell Applications

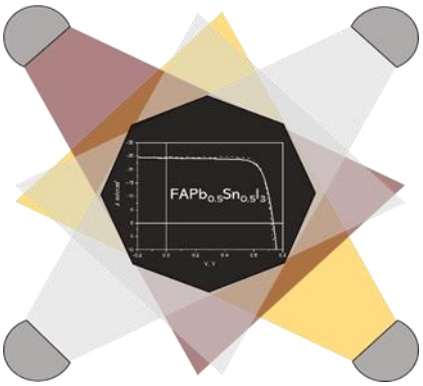

3. $FAPb_{0.5}Sn_{0.5}I_3$, A Narrow Bandgap Perovskite Synthesized through Evaporation Methods for Solar Cell Applications.

3.1. Introduction

PSCs have increased their efficiency in the last years from a 3.8% in 2009 to 25.5 % in 2020.[5,7,83,84] This evolution is quickly approaching the Shockley Queisser limit. Thus, absorbers with the optimum bandgap of 1.34 eV could help enhancing the power conversion efficiency reducing the losses.[31,85] Narrower E_g perovskites are also a key to develop perovskite-perovskite multijunction solar cells, which require a narrow-E_g absorber of 1.1-1.3 eV. As mentioned in section 1.3.1, the combination of tin and lead as perovskites' divalent cation results in a E_g narrowing, which can be accentuated by the bandgap bowing effect.[40,86–89] Furthermore, the introduction of FA, improves the thermal stability of the material.[29,90] Through successive optimization of the composition and configuration, solution-processed tin-lead perovskites have achieved PCEs up to 21.1%.[25] However, these solution-processed tin-lead perovskites require complicated synthetic routes, making them difficult to upscale. Therefore, new fabrication routes are required. In this chapter, we present the work carried out to achieve a tin-lead perovskite solar cell by sublimation methods, and discuss the main challenges involved.

3.2. Formamidinium tin-lead iodide perovskite as narrow-bandgap absorber in a solar cell

We present an innovative method to synthesize tin-lead perovskites working as absorbers in solar cells. This method consists in the multisource co-sublimation of different precursors to prepare $FAPb_{0.5}Sn_{0.5}I_3$. This study presents the optical, morphological, and structural characterization of the films and integrates them in diodes. The as-synthesized perovskite has a bandgap of 1.28 eV, close to the ideal one for single absorber solar cells and suitable for the preparation of tandem solar

cells with wider bandgap sub-cells.[39,91] Furthermore, the solar cells prepared with this absorber led to efficiencies of 13.98%, demonstrating vacuum-deposited tin-lead alloyed perovskite based solar cells for the first time.

3.3. The route to tin-lead perovskites synthesized through sublimation

The development of vacuum-deposited narrow-E_g tin-lead perovskites presented several challenges. This approach required a dedicated evaporator expressively for the preparation of this kind of material. The need to use a different evaporator for this material was based on the use of tin in the composition. Tin presents two oxidation states (Sn^{2+} and Sn^{4+}) being the Sn^{4+} more stable. Sn^{4+} can contaminate perovskites and be detrimental for their performance. Thus, a new evaporator was installed inside the glovebox to completely avoid the precursor exposure to oxygen or moisture. All the sensors present in the evaporator were carefully calibrated with several materials. Firstly, PbI_2 was employed to determine how the position of the sensor affected the reading. Then, each material employed was evaporated and successively recalibrated to be sure the reading was correct.

Puzzled by the low reproducibility of the resulting devices, several conditions were studied to determine their impact in the final device. Different HTMs were employed as substrates, such as TATM, m-MTDATA or PTAA. Also, a series of ETMs such as C_{60}, phenyl-C_{60}-butyric acid methyl ester (PCBM), and indene-C_{60}-acid hexyl ester (IPH) were investigated. Furthermore, a careful study on annealing temperatures was carried out. However, no clear correlation was found, which pointed towards other factor as the limiting ones. Other possible low reproducibility origins were investigated, such as the brand and purity of SnI_2 (with slightly more reproducible results obtained with SnI_2 supplied by Tokio Chemical Industries). It was clear that this work would not be easy at all due to the easy oxidation of Sn^{2+} to Sn^{4+}. However, although the results were often unconclusive due to the lack of reproducibility, some trends discussed in next pages allowed us to extract important information.

As a summary in Figure 18, the evolution of our perovskites is presented in two J-V curves, the first one for one of our first experiments and the next one for the best result achieved.

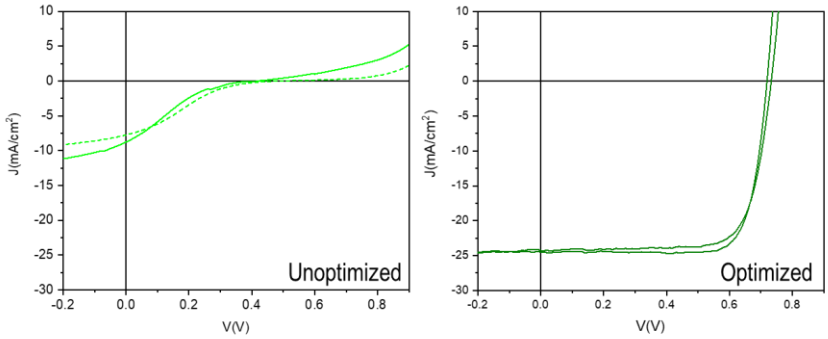

Figure 18. J-V Curves for tin-lead perovskites before and after optimization through several studies.

3.4. Experimental methods

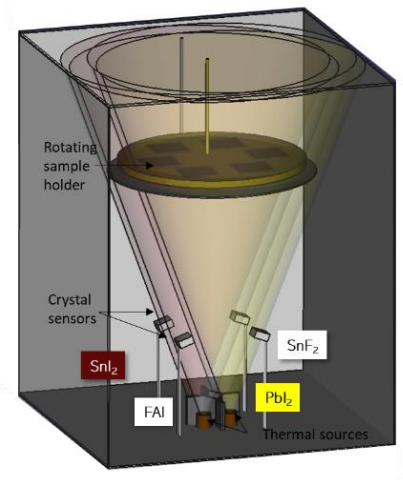

Figure 19. Scheme of the evaporator employed to synthesize $FAPb_{0.5}Sn_{0.5}I_3$ including the position of each precursor crucible inside the evaporator.

ITO-coated glasses were carefully cleaned employing the method described in chapter 2.1. Afterwards, 5 nm of MoO_3 was thermally evaporated at a pressure of $2x10^{-6}$ mbar. A layer of PTAA was spin-coated at 1500 rpm for 30 s and then thermally annealed at 100ºC for 10 min in nitrogen atmosphere. Then, the

perovskite was synthesized by simultaneous thermal vacuum deposition employing the precursors FAI, SnI_2, PbI_2 and SnF_2, as an additive. As explained in chapter 2.1, a careful calibration of the QCMs was done to determine the exact evaporated quantities of each material. A scheme of the evaporator can be observed in Figure 19. After subliming the perovskite, C_{60} and BCP were evaporated with thicknesses of 25 and 8 nm, respectively. The pressure during this evaporation was $3x10^{-6}$ mbar. Finally, the metal electrode consisting of Ag was thermally evaporated at a pressure of $2x10^{-6}$ mbar (thickness of 100 nm). Device characterization was performed employing the techniques and equipment described in chapter 2.2 and 2.3.

3.5. Results and discussion

Once certain degree of control was achieved, a careful study on the formation of the perovskite introducing SnF_2 as an additive was carried out. As previous reports based on solution processes showed, this additive improved film formation and reduced Sn^{4+} generation.[92–94] In this line, the co-sublimation of this additive leads to a better formation of the perovskite in our system, as observed in the absorbance spectrum (Figure 20a). XRD spectra in Figure 20b showed structural effects when different amounts of SnF_2 were introduced. Without the additive, the dominant peak is the one centered at 12.7º, normally attributed to PbI_2. However, when introducing small amounts of the additive, the peaks associated to the perovskite become prominent and the peak associated to PbI_2 is reduced, this implies a better formation of the perovskite.[20,95] On the other hand, when very high quantities of the additive are introduced, the peak at 12.7º is intensified and a new peak at 38.7º appears. This last peak is normally associated to SnI_2. Therefore, it seems that the introduction of an excess of SnF_2 leads to an excess of SnI_2 and PbI_2 in the final films.[23,96] These results led to the conclusion that 10% of the additive is the optimum amount of SnF_2.

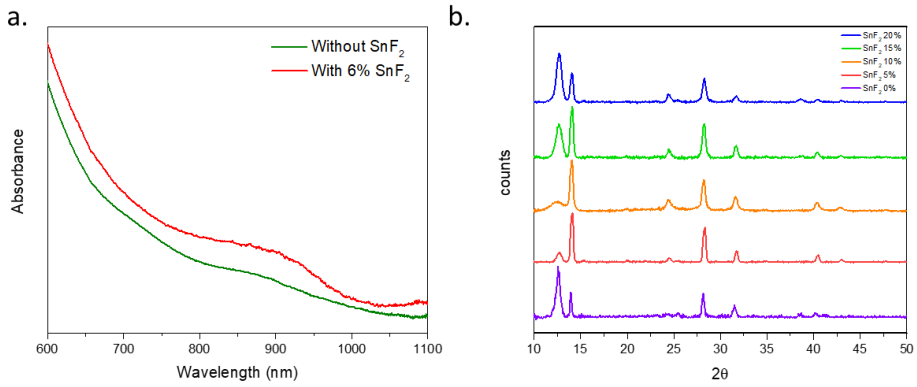

Figure 20. a) UV-Vis absorbance spectrum of the perovskite with and without the addition of a 6% of SnF_2 during sublimation. B) XRD pattern obtained for the perovskite with different amounts of SnF_2.

Furthermore, studies on the morphology of the films with different quantities of SnF_2 were also performed (Figure 21). As shown in the images, the different amounts of the additive on the film did not significantly affect their morphology.

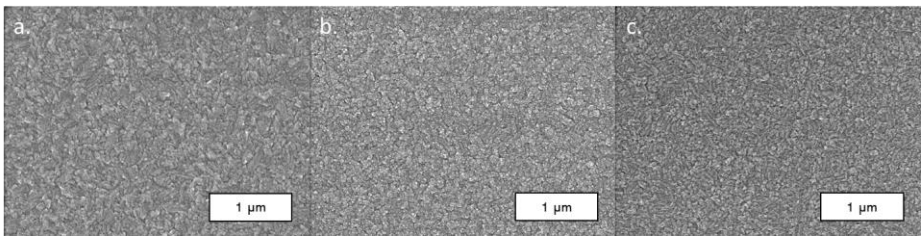

Figure 21. SEM images of the surface of $FAPb_{0.5}Sn_{0.5}I_3$ containing a a) 0%, b) 10% and c)20% of SnF_2.

The stability of these films under ambient conditions was also evaluated over time, by monitoring the UV-Visible absorbance and the conductivity under different air exposures. In Figure 22a, the UV-Visible spectrum of samples stored in ambient conditions can be observed. After one day of air exposure, the perovskite starts to degrade. Furthermore, the results in Figure 22b show how the conductivity of the perovskite remains similar for 12 days in nitrogen conditions but, after air exposure the conductivity increases one order of magnitude within 3 hours. This pronounced increase in the conductivity is associated to Sn^{4+} formation and can be interpretated as a clear sign of degradation.

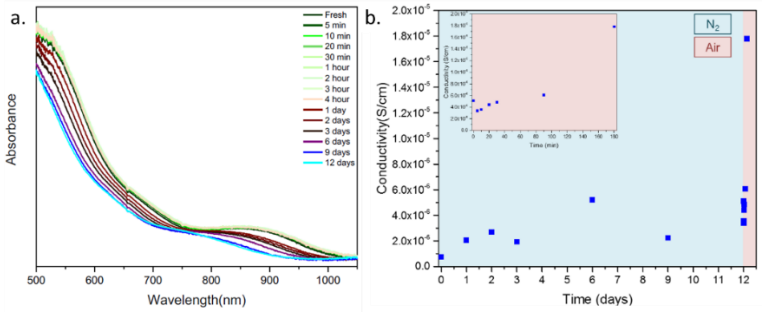

Figure 22. a) UV-Visible absorbance measurement up to 12 days in air. b) Conductivity of the samples up to 12 days in N_2 atmosphere and of the same sample for 3 hours in air (inset).

The bandgap and morphology of the films with 10% of SnF_2 were determined using detailed analysis of the absorption spectrum and SEM analysis (Figure 23).

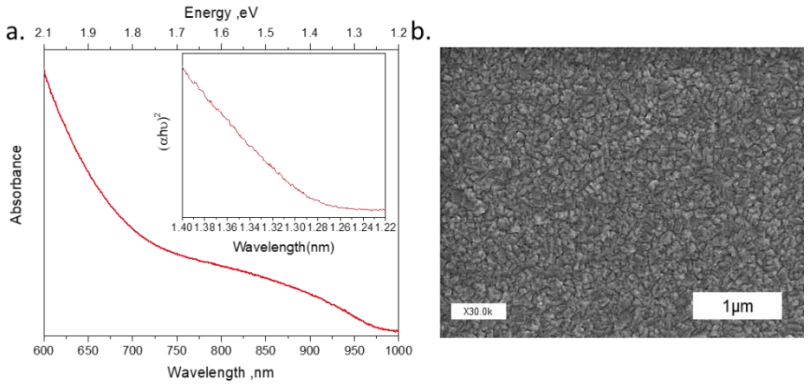

Figure 23. a. UV-Visible absorbance, Tauc plot calculations (inset) and b. SEM image of the surface on the $FAPb_{0.5}Sn_{0.5}I_3$ containing a 10% of SnF_2.

From the absorbance studies (Figure 23a) it is clear that the film absorbs up to 970 nm. Analysis of the calculated Tauc plot leads to a deduction, the bandgap to be 1.28 eV through a direct transition (Figure 23a inset).[97] Studies on the morphology of the films through SEM of the surface (Figure 23b). The image shows a very homogeneous surface with no signs of pinholes, ideal for solar cells. Although the grains have small sizes (60-100 nm) that are consistent with vacuum deposition, this small size has already shown in other studies to not be a limiting factor of the achievable PCE. [98]

Afterwards, to test the performance of these films for photovoltaic applications, they were integrated as the absorber in solar cells employing the configuration shown in Figure 24a, as discussed in chapter 2.1. First, we measure the J-V in the dark to determine the quality of the diode. From Figure 24b we see a small leakage current and good diode rectification can be seen. These characteristics suggest a suppression of Sn^{4+} formation during the sublimation in inert conditions. In Figure 24c, the IPCE spectrum can be observed. The spectrum reaches maximum values of 0.7. These relatively small values indicate that further optimization on the thickness and composition of the films should be done to achieve the maximum capability to generate hole and electron pairs from photons.

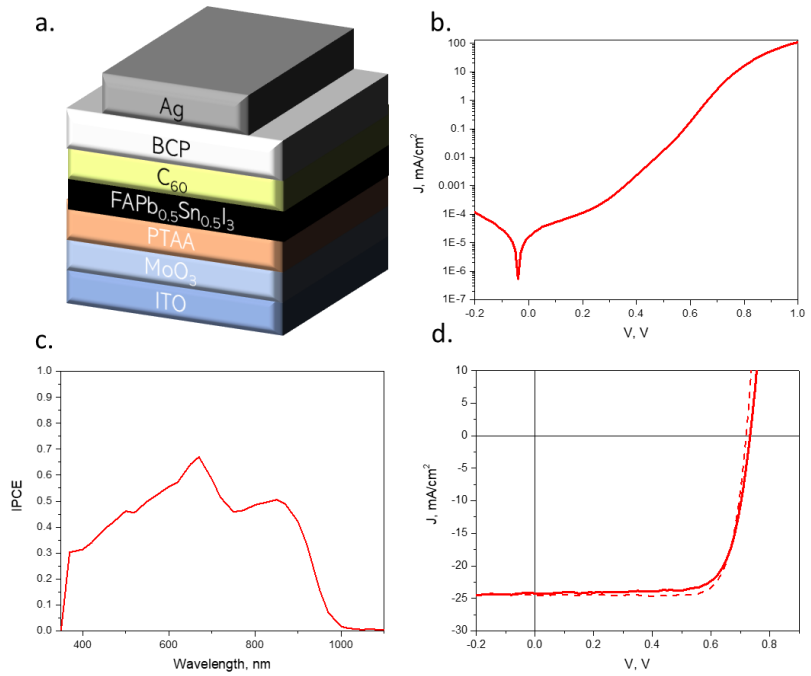

Figure 24. a) Device structure, b) J-V Curve in dark conditions, c) EQE and d) J-V Curve (dotted for reverse and solid for forward measurement) under illumination for the best performing device of $FAPb_{0.5}Sn_{0.5}I_3$ containing a 10% of SnF_2.

Finally, in Figure 24d the J-V curves under illumination are displayed. It can be seen how the solar cell presents no significant hysteresis, high FF values and a J_{SC} close to the expected one expected from the IPCE spectrum. However, loses on the V_{OC} compared to material E_g indicate recombination issues. The values obtained for these curves are presented in Table 1.

Table 1. Photovoltaic parameters under AM1.5G illumination measured for the solar cell presented in Figure 24.

Scan	J_{sc} (mA/cm^2)	V_{oc} (mV)	FF (%)	PCE (%)
Forward	24.3	730	73.3	13.42
Reverse	24.5	720	79.3	13.98

This vacuum-deposited Sn-Pb perovskite can display encouraging performances in solar cells, demonstrating the potential of vacuum deposition methods to fabricate tin-lead alloyed perovskites avoiding Sn^{4+} formation.

3.6. Conclusion

A novel method to synthesize $FAPb_{0.5}Sn_{0.5}I_3$ through vacuum deposition was developed. The co-evaporation of precursors including SnF_2 additive demonstrated to be an effective technique to suppress the formation of Sn^{4+} in the films. The process we developed resulted in pinhole-free films with homogeneous surface and a bandgap of 1.28 eV, demonstrating the high control of this technique to achieve the targeted narrow-E_g perovskite. Furthermore, the films were integrated into p-i-n solar cells performing with efficiencies close to 14%. These studies show the capability of vacuum deposition to synthesize tin-lead based perovskites with considerable efficiencies opening a new processing route to develop optimum-bandgap perovskites and narrow-E_g perovskites to be integrated in multijunction devices through a simple and well-known in industry technique. However, the results obtained in these studies were very difficult to reproduce, as the use of very small quantities of additive required high control during the sublimation. Therefore, alternative approaches to produce reproducible vacuum-deposited tin-lead perovskites should be carried out.

3.7. Contribution of the author

Igual-Muñoz, A. M.; Ávila, J.; Boix, P. P.; Bolink, H. J. "$FAPb_{0.5}Sn_{0.5}I_3$: A Narrow Bandgap Perovskite Synthesized through Evaporation Methods for Solar Cell Applications" Sol. RRL, 1900283, 1–5 (2019).

Chapter 4

Vacuum-Deposited Multication Tin–Lead Perovskite Solar Cells

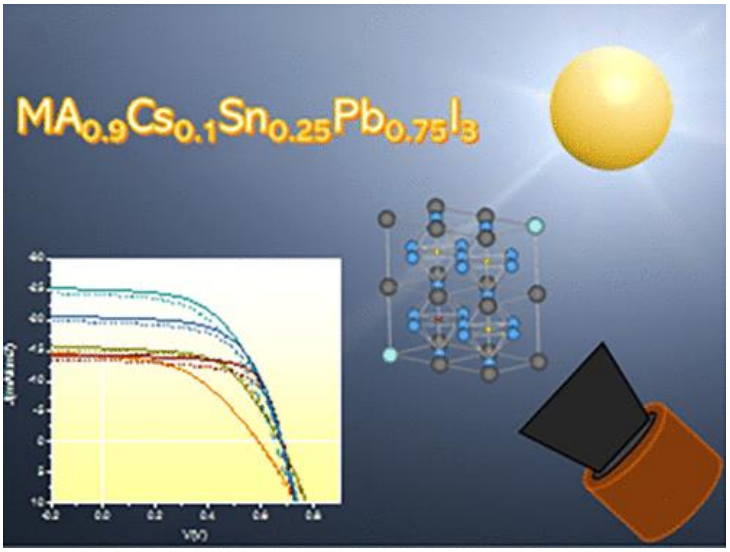

4. Vacuum-Deposited Multication Tin–Lead Perovskite Solar Cells

4.1. Introduction

High power conversion efficiency is a key factor determining the success of any photovoltaic technology. Considering the high soft costs, such as those related to the solar cells' installation, efficiency enhancements represent the most direct route to reduce the final energy price. As mentioned in section 1.3.1, two main routes can be considered to increase PSCs efficiency: developing more efficient absorbers through narrowing the E_g towards the "Optimum bandgap" of 1.34 eV, and manufacturing multijunction solar cells where a narrow-E_g absorber is required to exploit the potential of the full solar spectrum. [20,31,99] The synthesis of tin-lead alloyed perovskites results in narrower bandgap absorbers than their single metal counterparts. However, the use of tin needs to deal with the detrimental oxidation of Sn^{2+} to Sn^{4+}. This oxidation leads to p-type doping and compromises the stability and performance of devices,[92] yet alloyed perovskites are more stable than their purely tin-based counterparts.[40] Normally, the fabrication of tin-lead-based perovskites is done through solution-based processing methods that present several disadvantages against vacuum-based methods, such as the lack of control in the thickness of the absorber. Vacuum co-deposition of the precursors is a widely known technique in industry[100] that can be employed to prepare large-area devices. Also, it is intrinsically additive, a key point for the development of multijunction devices.[101] In Chapter 3, an efficient tin-lead-based perovskite developed through vacuum deposition methods was reported. However, the technique required the use of SnF_2 additive to suppress the formation of Sn^{4+} and the use of FA as the monovalent cation.[94] An accurate introduction of small quantities of SnF_2 is difficult to achieve through vacuum-based methods, and the use of FA cation hinders the phase control since it can result in detrimental yellow polymorphs. Therefore, these studies showed a lack of reproducibility, and the work served only as a proof of concept. One of the strategies that can be fruitful to overcome these problems is the incorporation of two monovalent cations. Combining MA and Cs has shown the capability to form Sn-based perovskites working as absorbers without the need for additional additives.[102] As an added

advantage, the introduction of Cs has been shown to enhance perovskites' thermal stability, photostability and efficiency.[103,104] In addition, MA has shown to be more stable and controllable than FA through sublimation methods, resulting in more reproducible perovskites. However, their combination on tin-lead alloyed perovskites synthesized via sublimation remained unexplored, thus this perovskite became an excellent candidate to prepare lower bandgap perovskites by vacuum deposition.

4.2. Studies on the thickness and solar cell performance of vacuum-deposited methylammonium cesium tin-lead iodide.

In this chapter, we explored the partial replacement of Pb by Sn in $MA_{0.9}Cs_{0.1}PbI_3$ to develop narrow-E_g perovskites through vacuum-based methods without the use of a SnF_2 additive. The study pursued the composition based on 75% of Pb and 25% of Sn employed in previous studies that displayed enhanced stability and higher efficiencies.[103] The obtained perovskite presented a narrower E_g than its Pb-based counterpart, close to the optimum single-junction bandgap of 1.34 eV. The development of the improved absorbers included a study on the film characteristics, which were adjusted by modifying deposition parameters such as the monovalent to divalent cation rate. Finally, a conscientious study on the thickness of the perovskite in sandwiched devices was done to obtain higher and reproducible efficiencies.

4.3. Achieving a reproducible tin-lead perovskite by sublimation

The efforts to prepare tin-lead perovskites by sublimation, detailed in Chapter 3, lead to the following conclusion: the capability to prepare tin-lead perovskites by sublimation methods is a real option. However, the low reproducibility of the perovskites represented a major issue. Part of these problems were attributed to the need to control the deposition of small amounts of SnF_2 in a steady and

accurate way along the whole perovskite formation. For this reason, we decided to start a new study searching for a new Pb-Sn perovskite that avoids the use of SnF_2. In this aspect, the main objective was to include the Cs and MA cation to circumvent the SnF_2 deposition. To do so, four evaporation sources had to be concurrently operated as MAI, CsI, SnI_2 and PbI_2 were the precursors. A scheme of the evaporator can be observed in Figure 25.

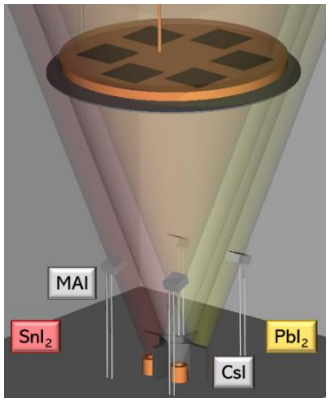

Figure 25. Scheme of the evaporator employed to prepare $MA_{0.9}Cs_{0.1}Pb_{0.75}Sn_{0.25}I_3$.

In our first studies, the temperature required to evaporate the same quantity of MAI in source four, the one that is presented for CsI in Figure 25, was higher. A perovskite with a whitish aspect was being obtained regardless of the hole transporter employed as a substrate. These observations indicated an excess of MAI in the films. Solar cells prepared with this perovskite were showing low IPCEs, V_{OC}s and J_{SC}s. For this reason, absorbance and XRD studies were performed, and they indicated a clear excess of MAI in the films. These results can be observed in Figure 26. From these results and further studies on the HTL employed with our optimized perovskite, we concluded the best HTL to employ for this perovskite was m-MTDATA, as the rest of HTLs tried were showing the same S-Shape in their J-V curves as PTAA in Figure 26. Furthermore, as MAI was the precursor that is most difficult to control in the evaporation process. We evaluated different MAI's originating from different suppliers. Our results clearly indicated the best MAI to employ was the one obtained from Lumtec.

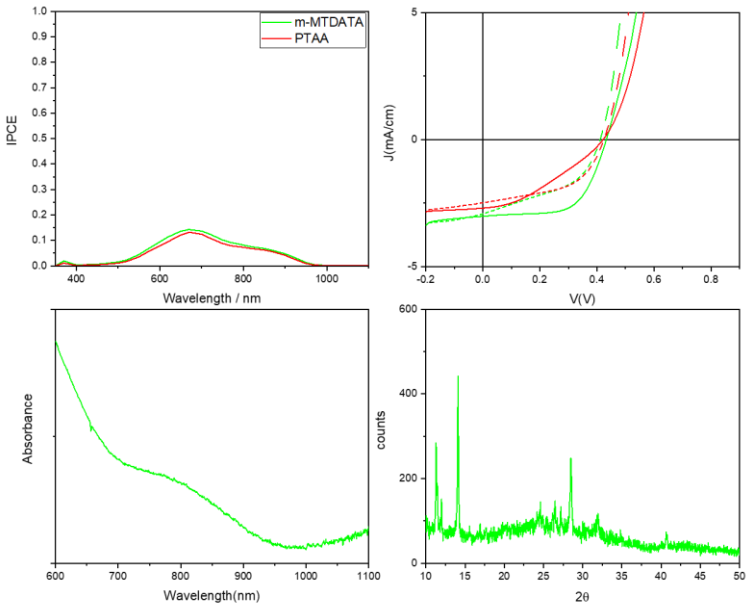

Figure 26. J-V curves, UV-Vis absorption spectrum and XRD diffractogram obtained for the first trial on synthesizing $MA_{0.9}Cs_{0.1}Pb_{0.75}Sn_{0.25}I_3$.

Although these first results may not seem encouraging, this perovskite presented higher reproducibility than the one in the previous chapter (based on FA and SnF_2 additive). For this reason, we were able to observe some trends and adjust different controllable variables during the synthesis to obtain the results presented in the next pages.

4.4. Experimental methods

ITO-coated glasses were cleaned employing the method described in chapter 2.1. Afterwards, 5 nm of MoO_3 were thermally evaporated at a pressure of $2x10^{-6}$ mbar. That layer was annealed at a temperature of 100ºC for 10 minutes in nitrogen atmosphere. 10 nm of m-MTDATA were sublimed at a pressure of $3x10^{-6}$ mbar to complete the hole selective layer. The perovskite was synthesized by simultaneous thermal vacuum deposition employing the precursors MAI, SnI_2, PbI_2 and CsI. Again, a careful calibration of the QCMs was done to determine the exact quantity of each material being evaporated. C_{60} and BCP were sequentially

evaporated onto the perovskite with thicknesses of 25 and 8 nm respectively, at a pressure of $3x10^{-6}$ mbar. Finally, 100 nm of Ag were thermally evaporated at a pressure of $2x10^{-6}$ mbar. Films and device characterization were performed employing the techniques and equipment described in chapter 2.2 and 2.3.

4.5. Results and discussion

The targeted composition in this study was $MA_{0.9}Cs_{0.1}Pb_{0.75}Sn_{0.25}I_3$. A study on the precursor's ratio was done. To maintain the monovalent ratio and the divalent ratio, MA:Cs and Sn:Pb ratios were kept constant while the MACs:SnPb ratio was changed. Perovskite films with the ratios 1.2:1 to 2.3:1 were synthesized and analyzed through XRD and absorbance.

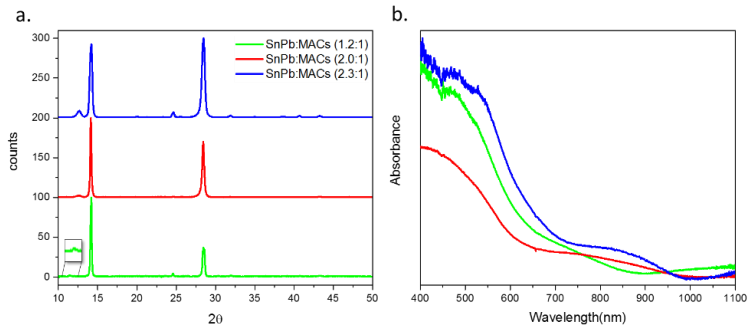

Figure 27. Studies on the (a) XRD and (b) absorbance for different precursor ratios of $MA_{0.9}Cs_{0.1}Pb_{0.75}Sn_{0.25}I_3$.

In the XRD diffractogram of the composition containing less divalent cation (1.2:1 in Figure 27a), a peak centered at 11.4º is observed. This peak is related to the formation of low-dimensional perovskites. Low-dimensional perovskites appear when there is an excess of monovalent cation, as MA, in the films. Thus, we concluded these films were containing a huge excess of MA. [105–107] Therefore, formulations introducing more divalent cations were introduced, labeled in Figure 27 as 2:1 and 2.3:1. Both showed a well-formed perovskite. However, the one with a formulation of 2.3:1 (SnPb:MaCs) showed a peak which is commonly attributed to PbI_2, indicating a small excess of divalent cation. In previous studies, it has been reported that a small excess of divalent cations

enhances the performance of these perovskites and avoids the need to employ additives to suppress Sn^{4+} formation.[23] On the other hand, absorbance studies (Figure 27b) show an absorption onset of 850 nm for the 1:1 perovskite (green line), implying the perovskite was not well-formed, as the expected onset for this perovskite was approximately 950 nm. However, for the 2:1 and 2.3:1 ratios, the perovskite shows the expected onset and higher absorption for the 2.3:1 ratio. To further investigate these ratios, solar cells with these unoptimized compositions were developed. The EQE measurements and J-V characteristics are shown in Figure 28 a and b, respectively. Furthermore, the representative values can be found in Table 2.

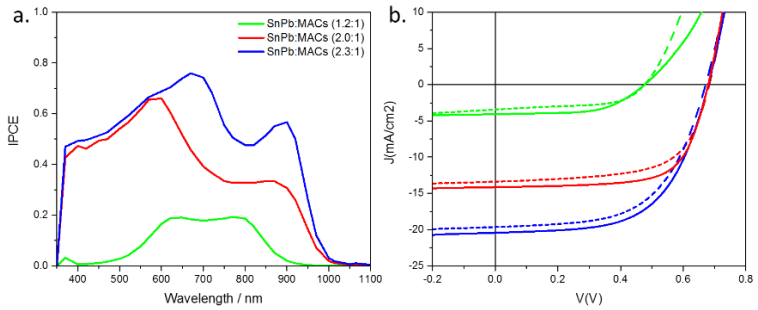

Figure 28. (a) EQEs and (b) J-V curves for the solar cells prepared with different ratios of MACs and SnPb.

Table 2. Values obtained for the efficiency parameters from the J-V curves for solar cells prepared with different ratios of MACs and SnPb.

Ratio (SnPb:MACs)	FF (%)	J_{sc} (mA/cm2)	V_{oc} (mV)	PCE (%)
1.2:1	57	3.7	477	1.0
2.0:1	66	13.7	681	6.1
2.3:1	59	21.1	673	8.4

From the EQE plots (Figure 28a) we concluded the 1:1 ratio did not form the expected perovskite because the IPCE was very low and only present in some of the expected wavelengths, this observation correlates well with the conclusions obtained before for XRD and absorbance measurements. On the other hand, for the ratios of 2:1 and 2.3:1, the IPCE was showing charge carrier generation in all the expected wavelengths for this perovskite. However, as in absorbance

measurements, the IPCE was more intense for the composition with a 2.3:1 (SnPb:MACs) ratio. For this reason, as observed in Figure 28b, the measured J_{SC} for this composition was higher. Therefore, the ratio of 2.3:1 was chosen to be the one employed in further optimizations, including a comprehensive study on the effect of thermal post-treatment (Figure 29 a and b) and stability of the films (Figure 29 c and d). Studies on thermal post-treatment confirmed that no beneficial result was obtained from thermal annealing on sublimed perovskites, which implies a stochiometric perovskite formation during the deposition (Figure 29a,b). The formation of Sn^{4+} is the main origin of losses in Sn-containing perovskites, and it is also a determining source of degradation. Thus, the stability of our films deposited without SnF_2 is a key aspect. We prepared solar cells and measured them before and after three days of storage in N_2 atmosphere, conditions comparable with optimal sealing. The results show a stable perovskite where the efficiency does not decrease although FF and J_{SC} are slightly affected(Figure 29c,d).

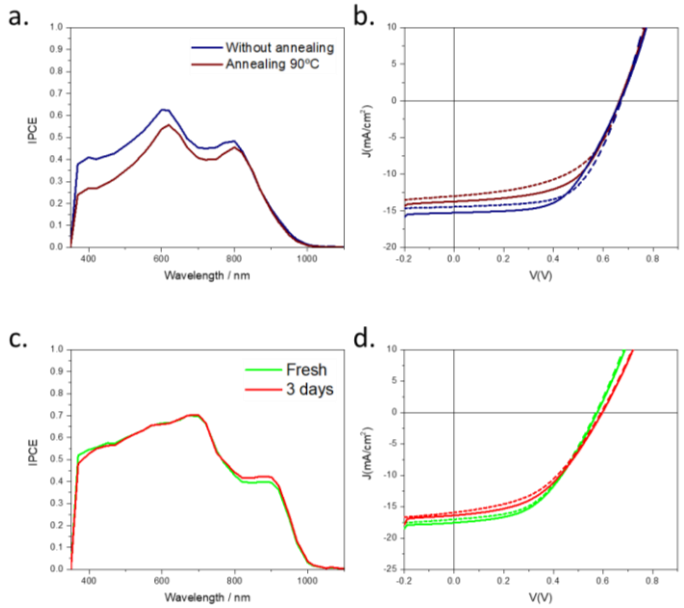

Figure 29. Thermal post-treatment studies (a) EQE and (b) J-V Curves. Stability studies (c) EQE and (d) J-V curves on devices prepared with the perovskite $MA_{0.9}Cs_{0.1}Pb_{0.75}Sn_{0.25}I_3$.

To identify the optimum thickness of the perovskite film for the solar cell efficiency, a study on the thickness of the perovskite was performed. The thickness

of this layer affects the final performance as it can absorb more light. However, there is more distance for the charge carriers to travel.

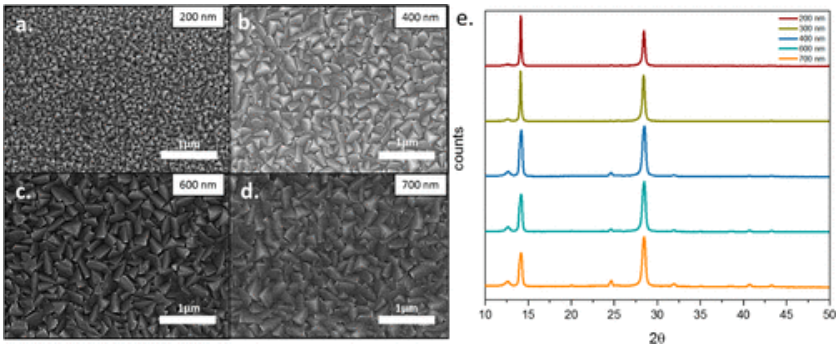

Figure 30. Surface morphology and crystallinity studies performed by (a-d) Scanning electron microscopy and (e) XRD of $MA_{0.9}Cs_{0.1}Pb_{0.75}Sn_{0.25}I_3$ with different thicknesses.

Top-view SEM images of the surface of the perovskite with different thicknesses are shown in Figure 30a-d. All the images suggest a high degree of crystallinity in the film. In addition, a homogeneous surface without pinholes was obtained. A slight increase in the grain size can be observed for thicker samples. This effect was attributed to a decrease in the MAI rate during longer sublimation times. The XRD patterns are shown in Figure 30e. Patterns displayed correspond to the expected ones for this perovskite, with the additional 12.7º peak attributed to an excess of divalent cations.[20] It can be observed how, when the thickness of the film is increased, the intensity of the (220) plane is also increased. However, this can be an artifact of the measurement, as in thicker perovskites in this angle, a bigger quantity of material is reached.

The E_g dependence on the film thickness can be explored by the absorbance measurements in Figure 31a. To further understand the changes in E_g, the composition of these films was studied by EDAX. A plot representing the composition and Eg variations with films' thickness is shown in Figure 31b. The obtained compositions with this methodology are very close to the targeted ones, with slight variations during different sublimations. The resulting E_g is also maintained in the range of 1.2 eV to 1.4 eV, confirming the significant degree of compositional control of the technique. It is also worth remarking that these values are very close to other studies previously reported for this perovskite.[103]

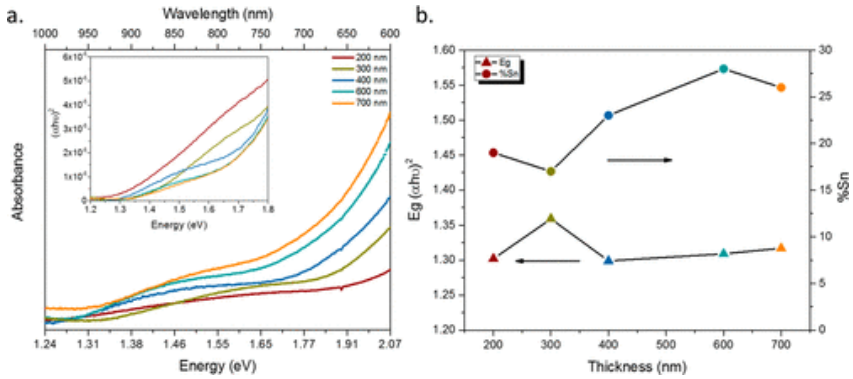

Figure 31. (a) Absorbance with Tauc plots in the inset and (b) Bandgap and composition vs thickness obtained for the films of $MA_{0.9}Cs_{0.1}Pb_{0.75}Sn_{0.25}I_3$.

As the morphological, structural, optical and compositional studies indicated the fabricated perovskites were of high quality, they were integrated into p-i-n devices. In this study, m-MTDATA was employed as the hole transporter because its highest occupied molecular orbital (HOMO) aligned well with this perovskite's energy levels, also the use of this hole transporter didn't show to provoke the formation of whitish films. [103,108] Representative J-V curves obtained for these devices are shown in Figure 32a along with the EQEs (Figure 32b) obtained for the same devices.

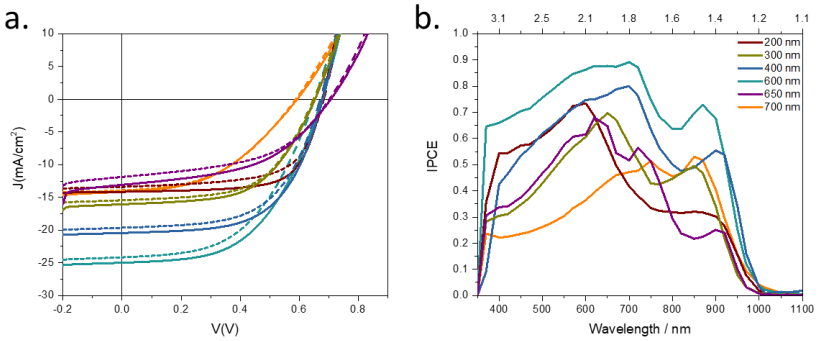

Figure 32. (a) J-V curves and (b) EQEs of representative devices with different thicknesses employing the perovskite $MA_{0.9}Cs_{0.1}Pb_{0.75}Sn_{0.25}I_3$.

For a better comprehension of the values obtained from the J-V curves Table 3 and Figure 33 are shown. Whereas Table 3 shows the values obtained for these curves and an average value, Figure 33 shows the statistics obtained for all the samples prepared with these configurations.

Table 3- Photovoltaic parameters under AM1.5G illumination measured for the representative solar cells of each thickness (Averaged values in Brackets).

Thickness (nm)	FF (%)	J_{sc} (mA/cm^2)	V_{oc} (mV)	PCE (%)
200	62 (63)	14.0 (14.9)	686 (671)	6.0 (6.2)
300	60 (57)	15.3 (14.6)	677 (673)	6.2 (5.6)
400	59 (59)	20.4 (19.4)	680 (674)	8.2 (7.7)
600	53 (51)	25.0 (23.6)	677 (660)	8.9 (7.9)
650	49 (48)	12.5 (11.8)	704 (699)	4.3 (3.9)
700	47 (46)	13.7 (13.4)	592 (595)	3.8 (3.6)

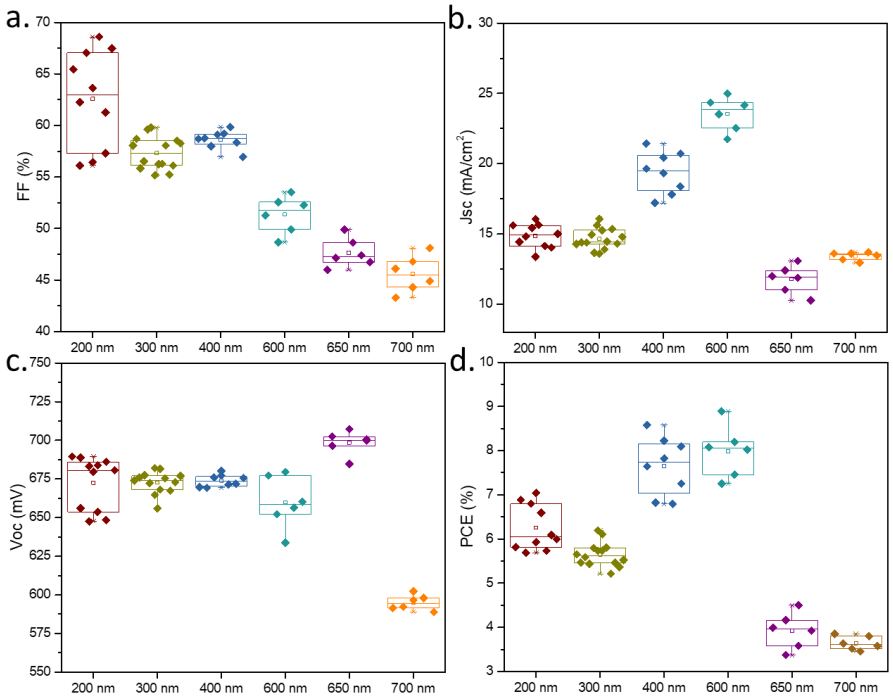

Figure 33. Photovoltaic parameters obtained from the J-V curves of devices with different perovskite thicknesses under AM1.5G illumination. (a) FF (b) J_{SC} (c) V_{OC} (d) PCE.

Devices with the best photovoltaic efficiency were the ones employing a 600 nm thick absorber, reaching PCEs as high as 8.9% with reproducible characteristics. Furthermore, J_{SC} is enhanced with increasing thickness, in good agreement with the absorbance results (Figure 31a) and EQEs (Figure 32b). When films are thinner, an EQE deficit is observed at longer wavelengths. This is

attributed to the lower absorption coefficient of this composition, requiring thicker films to absorb less energetic photons. When thicker films are employed, this deficit is not observed. [37,109] On the other hand, for films with thickness >600 nm, the EQE response is diminished in the whole spectrum, which indicates hindered charge extraction, due to higher distance to travel for the charge carriers. Further optimization on these films could lead to higher responses, as the theoretical current calculated for this bandgap should reach 35.8 mA/cm² and our best film presented 25 mA/cm². Figure 33a displays a FF decrease with increasing thickness. FF deficits are usually attributed to impaired charge transport or high carrier recombination. However, as a similar trend is not observed in V_{OC} (Figure 33c), it was attributed to charge transport deficits in our case.

In order to gain further insight on this FF reduction, we analyzed EIS response and the J-V curves in dark conditions.

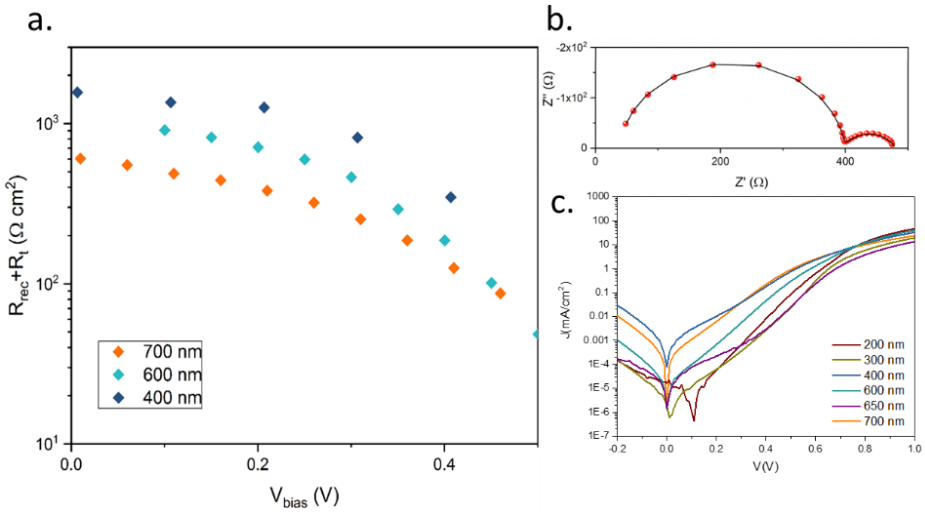

Figure 34. (a) Combination of recombination and transport resistances obtained through EIS measurements, (b) representative Nyquist plot of the sample with a thickness of 600 nm and (c) J-V curves in dark conditions obtained for the devices with different thicknesses.

The Nyquist plots (Figure 34b) display two regions at high and low frequency. These two regions have also been observed in previous reports for Pb-based perovskites,[110] and contain information about charge recombination and transport in the devices.[111] These spectrum were fitted employing the equivalent circuit shown in chapter 2.3.[112] In Figure 34a, the resistance accounting for recombination

and transport is plotted against de applied voltage. The trend of the resistances, which is aligned with the V_{oc} rather than with the FF, suggests that the parameter is determined by the recombination. Therefore, this increase in recombination rate (decrease in recombination resistance) with the thickness suggests a bulk recombination process.[79,102] Furthermore, in the J-V curves measured in dark conditions (Figure 34c), there is a resistance trend with thickness at higher injection potentials, which indicates larger series resistance in thicker films.[113] Finally, an investigation on the ideality factor was performed by analyzing the Voc values at different light intensities,[114] obtaining an ideality factor of 2.25, as shown in Figure 35. This ideality factor, ~2 is associated with trap-mediated recombination, in line with bulk-dominant recombination processes. Normally, smaller grain sizes observed for vacuum-deposited perovskites are not detrimental to devices' efficiency. However, in this case, as the perovskite also contains Sn^{2+} that can be oxidized to Sn^{4+}, probably the enhancement of this recombination should be attributed to the smaller grain sizes obtained.

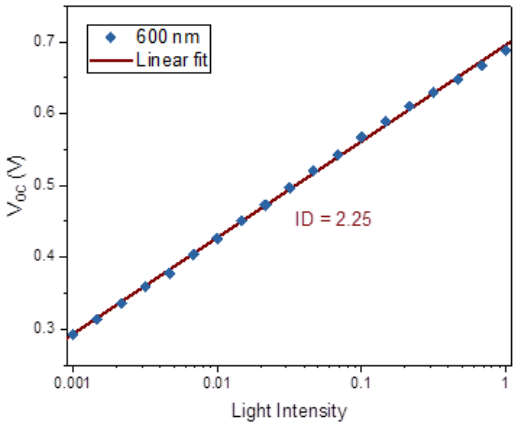

Figure 35. V_{OC} vs logarithm of the light intensity to determine the ideality factor of a sample with 600 nm's thickness.

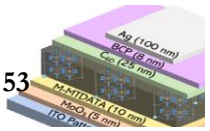

4.6. Conclusion

A vacuum deposition technique was employed to synthesize tin-lead perovskites with close-to-ideal bandgaps with reproducible results. Reproducibility was achieved by combining MA and Cs cations, and by avoiding the need for additives to suppress Sn^{2+} oxidation. A careful study on perovskites' thickness was done and both films and devices were characterized. Perovskites were integrated into sandwiched devices achieving reproducible efficiencies up to 8.9%. Limiting factors of efficiency were analyzed through EIS and dark current-voltage measurements, indicating the main recombination processes were dominated by trap-mediated recombination in the bulk.

4.7. Contribution of the author

Igual-Muñoz, A. M.; Castillo, A.; Dreessen, C.; Boix, P. P.; Bolink, H. J. "Vacuum-Deposited Multication Tin-Lead Perovskite Solar Cells." ACS Appl. Energy Mater., 3, 2755–2761 (2020).

Chapter 5

Room-Temperature Vacuum Deposition of $CsPbI_2Br$ Perovskite Films from Multiple Sources and Mixed Halide Precursors

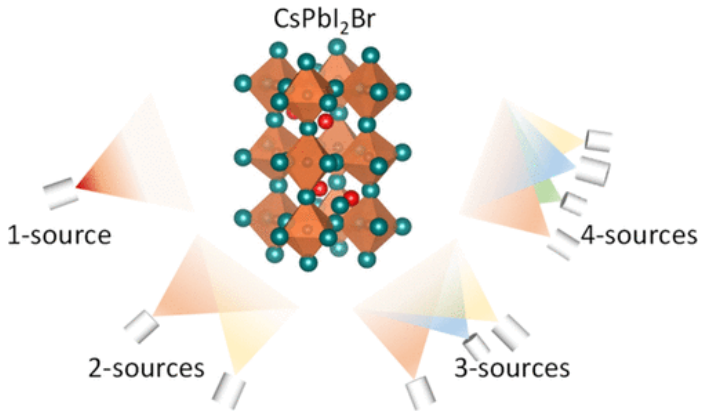

5. Room-Temperature Vacuum Deposition of $CsPbI_2Br$ Perovskite Films from Multiple Sources and Mixed Halide Precursors

5.1. Introduction

In the previous chapters, we demonstrated the fabrication of narrow-E_g tin-lead alloyed perovskites by sublimation and its use in solar cells. The next objective of our research was to develop a wide-E_g perovskite employing this method. Usually, perovskite solar cells that employ only organic MA and FA cations do not have high thermal stability [115,116] in contrast to those containing Cs [117–119] or even those using only Cs, that do reach high temperature stability.[43–45] $CsPbI_2Br$ presents a E_g of 1.9 eV, very suitable for tandem applications, and has reached single-junction efficiencies over 16% when synthesized through solution-process techniques.[53,56,120,121] However, the preparation of inorganic perovskites has several difficulties, as their stable phase at RT can only be achieved after annealing at high temperatures. For example, 300ºC is required for $CsPbI_3$ formation, as this composition is unstable due to its small Goldschmidt tolerance factor.[10,122–124] Introducing bromide in the composition can help to solve this issue, as it allows to stabilize the black phase.[46,48,49,125] The inorganic perovskite $CsPbI_2Br$ has also been synthesized by solution-process methods, and the process requires high-temperature annealing of 150-300ºC. Sublimation has been a successful approach to prepare other perovskites, such as those based on MA without thermal post-treatment.[74] Vacuum deposition has also been used for the preparation of $CsPbI_2Br$ perovskites, achieving record efficiencies of 13%,[57] these films still required high-temperature thermal post-treatment. This limited their applicability on temperature-sensitive substrates and on other perovskites in multijunction devices.[126] For this reason, further studies on the formation of this perovskite through sublimation are required.

5.2. Studies on the formation of $CsPbI_2Br$ through different vacuum-deposition methods and mixed-halide precursors and its integration in photovoltaic devices

In this chapter, we evaluate solvent-free synthesis methods for wide-E_g $CsPbI_2Br$ perovskite, including vacuum-based methods and the solid-state technique of mechanochemistry. We focus on strategies that avoid thermal post-treatments or employ low temperatures of less than 150ºC.

5.3. Experimental methods

Solid-state mechanochemical synthesis of the compounds was carried out employing a ball-mill (MM-40 shaking ball mill from Retsch). $CsPbI_2Br$ was synthesized by mixing CsBr and PbI_2 in a N_2 filled glovebox and introducing the materials in zirconia ball-mill jars with two zirconia beads. Jars were closed in N_2 atmosphere to avoid oxidation, and ball-milling was performed at 30 Hz for 99 min. The same procedure was employed for the mixed-halide precursors, although the precursors were CsBr/CsI for cesium mixed-halide precursors and $PbBr_2$/PbI_2 for lead mixed-halide precursors, in a ratio of 1:2 for both. Synthesis by melting was also investigated. The same precursors as in mechanochemical methods were weighted in a microbalance and introduced in a ceramic crucible. The crucible was heated in inert atmosphere and ambient pressure until 650ºC for $CsPbI_2Br$ and cesium mixed-halide precursors and 420ºC for lead mixed-halide precursors. Finally, for sublimation techniques, four different ways of synthesizing the perovskite were studied. A summary of these methods can be found in chapter 2.1 (Figure 15). In this case, the evaporator employed was a custom-made one represented in Figure 10 from chapter 1.4. The evaporator was evacuated up to 10^{-6} mbar. For the preparation of the perovskite with two sources and mixed-halide precursors, melted precursors were employed.

Sandwiched p-i-n solar cells were prepared with the sublimed perovskites. The solar cells were prepared as follows: ITO-coated glasses were cleaned employing the method described in chapter 2.1. Afterwards, 5 nm of MoO_3 were thermally evaporated at a pressure of $2x10^{-6}$ mbar. The layer of TATM, that functions as the hole extraction layer, was sublimed at a pressure of $3x10^{-6}$ mbar. Then, both layers

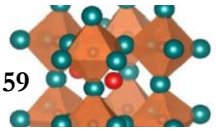

were annealed at a temperature of 140ºC for 10 minutes in a nitrogen atmosphere. Afterwards, the perovskite was synthesized as previously described. Calibration of all the materials was done by adjusting the real sublimed thickness in the QCMs. On top of the perovskite, C_{60} and BCP, that function as the electron extraction layer, were evaporated with thicknesses of 25 and 8 nm, respectively, at a pressure of $3x10^{-6}$ mbar. Finally, 100 nm of Ag were thermally evaporated at a pressure of $2x10^{-6}$ mbar.

Characterization of both films and solar cells was carried out employing the methods described in chapters 2.2 and 2.3.

5.4. Results and discussion

These studies started with the mechanochemical synthesis of $CsPbI_2Br$, and its deposition through flash evaporation, which has the potential to generate high-quality perovskite films without the need to use toxic solvents, as is the case for sublimation.[127,128] However, the $CsPbI_2Br$ synthesis was not successful, reproducing the same problems the technique presents for $CsPbI_3$ fabrication. In Figure 36a, the XRD diffractograms of the powders prepared by mixing CsBr and PbI_2 by ball-mill and melting are shown. A mixture of different phases was found in the XRD pattern of the ball-milled sample. Whereas the 3D structure of $CsPbI_2Br$ can be observed, a peak centered at 10º cannot be ascribed to the perovskite phase. This phase consists of PbX_6 partially disconnected octahedra, as shown in Figure 36b, which has been previously attributed to the as-called yellow phase of this perovskite. Indeed, at room temperature (RT) it is the most commonly found phase of $CsPbI_2Br$.[129] Nevertheless, the synthesized powder was not a mixture of CsPbBr3 and $CsPbI_3$, as the lattice constants were larger than for the bromide counterpart and smaller than the iodide counterpart, indicating the introduction of both halides into the structure. A similar effect is observed for the non-perovskite phase. Also, a melting process was employed to investigate the formation at high temperatures, but a pure perovskite phase was not obtained. However, a new phase corresponding to Cs_4PbX_6 was obtained, labelled as 4-1-6. There have been previous reports studying this phase and its conversion to the perovskite phase.[130–132]

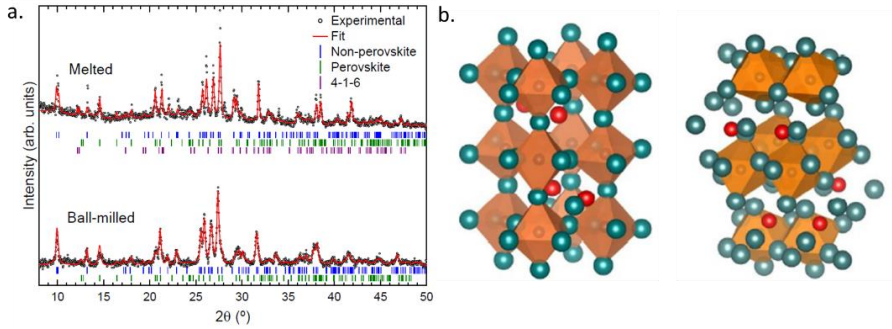

Figure 36. a) XRD characterization of ball-milled (bottom) and melted (top) CsBr:PbI_2 1:1 powders. b) Crystal structures of the distorted perovskite and non-perovskite phases. Where the colors represent red, blue and gray for Cs^+, halide and Pb^{+2} respectively.

On the other hand, to confirm the existence of the perovskite phase in the powders, UV-Vis Absorbance studies were carried out, as the color of the powders was the expected one (Figure 37). For the ball-milled and melted powders, the presence of $CsPbI_2Br$ in its perovskite phase is confirmed by the absorption onset at 1.85-1.90 eV.

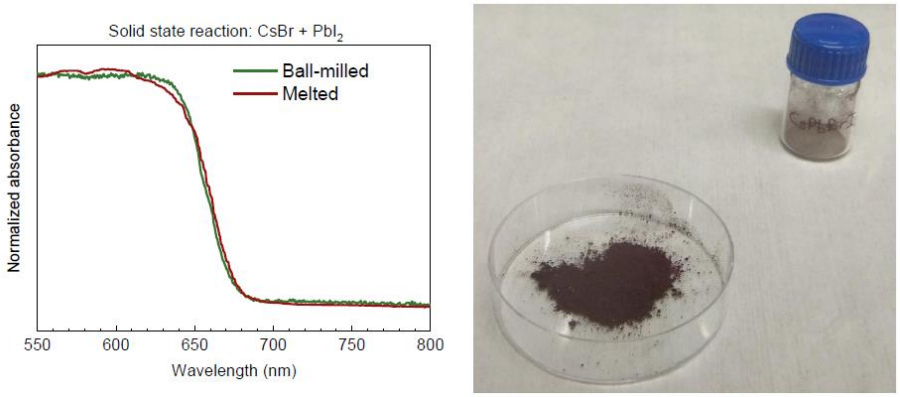

Figure 37. UV-Vis absorbance studies of melted and ball-milled perovskite and picture of the powders prepared by mechanochemical methods.

The next step of these studies was to evaluate the formation of $CsPbI_2Br$ through different methodologies of sublimation. Therefore, we started from the simplest to the most complicated. Initially, a *1-source* method was tested. This method consisted of *flash evaporation* of the melted powders shown before. After the evaporation chamber was evacuated, the crucible was heated to 750ºC at the

highest rate, corresponding to 5ºC/s. The rate was set at the highest possible to minimize changes in the composition as the different compounds present in the sample have different sublimation temperatures.[133] Films were analyzed by XRD, as shown in Figure 38a.

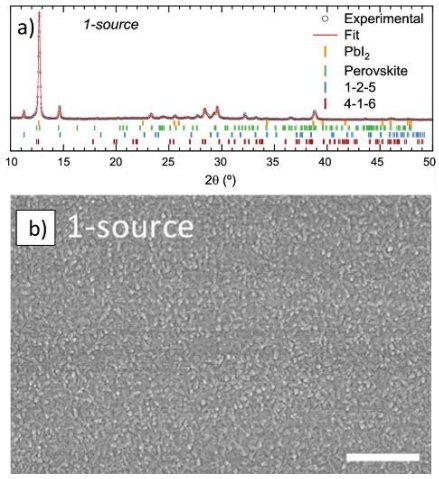

Figure 38. Characterization results of the flash evaporated sample (1 source) through (a) XRD and (b) SEM. Scale bar is 500 nm.

XRD pattern of the flash evaporated sample showed the coexistence of different phases, the most dominant was PbI_2, as observed in the peak centered at 12º. Other phases were characterized as perovskite, Cs_4PbX_6, and $CsPb_2X_5$. In summary, flash evaporation led to impure films. Flash evaporated films were also studied through SEM and UV-Vis absorbance. SEM of the sample (Figure 38b) showed homogeneous films with small grains of 50 nm. On the other hand, UV-Vis absorbance and Tauc Plot calculations showed a bandgap energy of 1.94 eV (Figure 39). This bandgap is slightly wider than the expected one due to the PbI_2 segregation caused by the high temperatures achieved during sublimation.

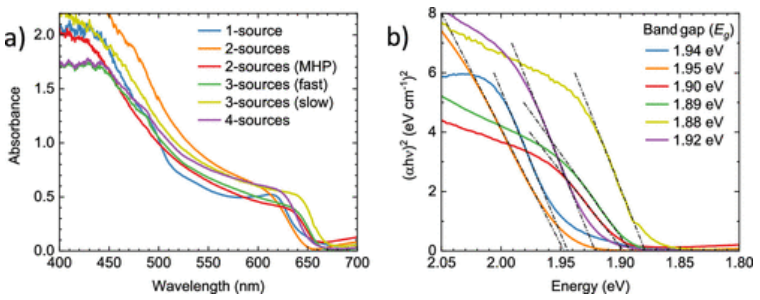

Figure 39. (a) UV-Vis absorbance spectra and (b) Tauc plot calculations for the as-prepared films.

Then, we proceeded with *2-sources* evaporation. Firstly, the *co-evaporation of CsBr and PbI_2* was studied. XRD of these films can be observed in Figure 40a. The pattern showed a film composed mainly of the perovskite phase without any preferential orientation, commonly observed for this kind of films.[129] Lack of orientation is also characteristic of vacuum-deposited films and can be related to the porosity observed in SEM studies (Figure 40b).[134,135]

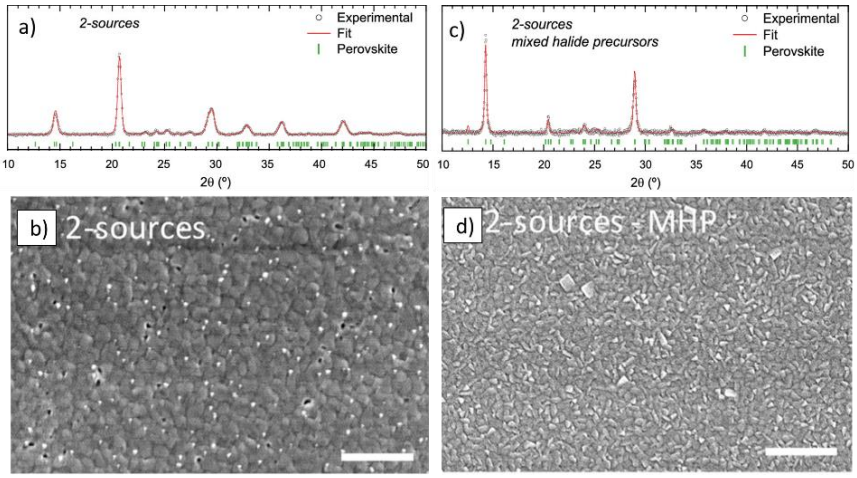

Figure 40. Characterization results of the sample prepared by co-evaporation of CsBr and PbI_2 (2 sources) through (a) XRD and (b) SEM, and of the sample prepared by co-evaporation of the mixed-halide precursors (2 sources MHP) through (c) XRD and (d) SEM. Scale bar is 500 nm in all images.

However, from these studies, we concluded that phase pure $CsPbBr_2I$ could be obtained by 2-sources co-evaporation, although the films had high porosity and some pin-holes. Vacuum-deposition requires the atomization of the precursors, which condense on a cold surface forming the final structure. This results in well-mixed compounds. Although XRD studies showed a well-mixed halide

composition, we proceeded to study another *2 sources* method employing *mixed halide precursors*, as the pre-alloying could lead to a more homogeneous insertion of the halides in the structure. XRD patterns of pre-alloyed mixed-halide precursors can be seen in Figure 41.

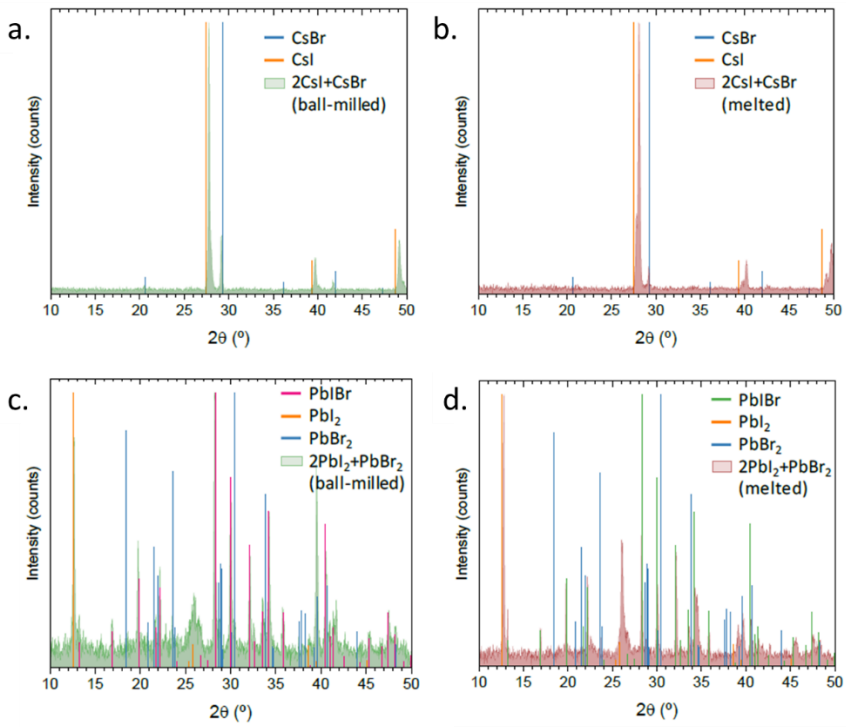

Figure 41. XRD patterns of mixed-halide precursors. Prepared by (a) ball mill of CsI:CsBr (2:1), (b) melting of CsI:CsBr (2:1), (c) ball mill of PbI_2:$PbBr_2$ (2:1) and (d) melting of PbI_2:$PbBr_2$ (2:1).

During the solid-state reaction of cesium, the incorporation of bromide into CsI was confirmed by the peak shifts. In Figure 41a,b the peaks for CsI were presented in orange, and for CsBr in blue. On the other hand, the measurement of our sample is represented in green where we can see how the peaks are always shifted between the pure CsI and CsBr, meaning a new compound is formed. On the other hand, an alloy of lead mixed-halide precursors is also obtained, although in its XRD diffractograms (Figure 41c,d) it is more difficult to observe the mixing because this pattern presents a higher amount of peaks. As the patterns obtained through melting presented more shifted peaks, indicating a better mixing between halides, this technique was the chosen one for the co-evaporation of mixed-halide precursors.

XRD pattern of the co-evaporated mixed-halide precursors' perovskite can be observed in Figure 40c. Here, a phase-pure perovskite with preferential orientation on the (110) and (002) planes was obtained. From the surface studies, the detailed morphology is obtained (Figure 40d), with well-defined grains of 50 nm. Furthermore, a E_g of 1.9 eV, as expected for well-mixed halides, is obtained (Figure 39b). Therefore, previous halide alloying is a good technique to enhance the quality of this perovskite.

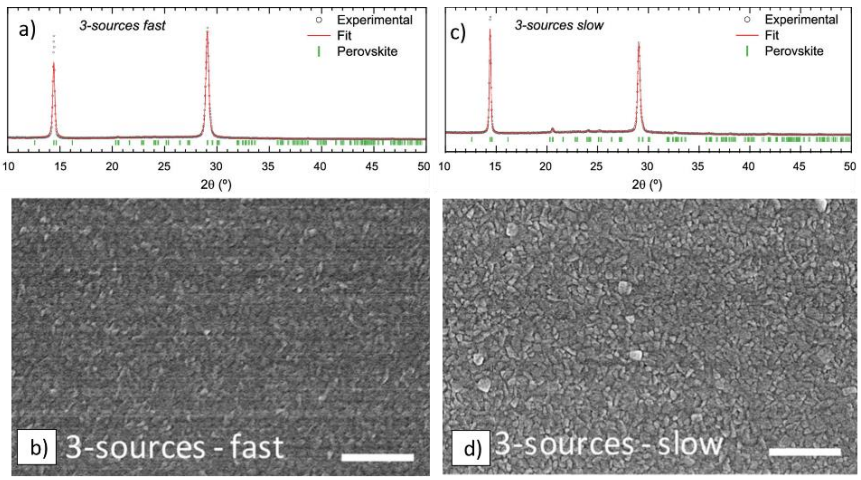

Figure 42. Characterization results of the sample prepared by co-evaporation of CsBr, CsI and PbI_2 at a fast rate (3 sources fast) through (a) XRD and (b) SEM, and of the sample prepared by co-evaporation of CsBr, CsI and PbI_2 at a slow rate (3 sources slow) through (c) XRD and (d) SEM. Scale bar is 500 nm in all images.

To obtain a more thorough comprehension on the introduction of more precursors during the synthesis, the deposition with *3 sources* was done by *co-evaporation of CsI, CsBr and PbI_2*. During vacuum deposition, the rate of precursors plays an important role, as a very fast deposition rate can originate an amorphous material. Therefore, different total rates of sublimation were studied. The first one, called "*fast*" for 2 Å/s, and the second one, called "*slow*" for 0.5 Å/s. XRD patterns of the two compounds are shown in Figure 42 a,c. Both, slow and fast, show a phase-pure perovskite with high crystallinity and preferential orientation on the (110) and (002) planes. However, the slowly deposited one shows narrower peaks indicating larger crystallites. This can be correlated to its improved morphology (Figure 42 b,d). Both show a similar bandgap of 1.88 and 1.89 eV for slow and

fast films, respectively. However, for the same thickness of 250nm, the slower one presents a more intense absorption (Figure 39a).

To understand better this 3 sources technique, we also tried halide mixing by co-evaporation of CsI, PbI_2, and $PbBr_2$ (employing two lead halides instead of cesium halides). This sublimation led to unstable films in air, with fast degradation of the sample (Figure 43). This fact can be observed in UV-Vis absorbance after air exposure (Figure 43a) and in the XRD pattern that was collected in air atmosphere (Figure 43c).

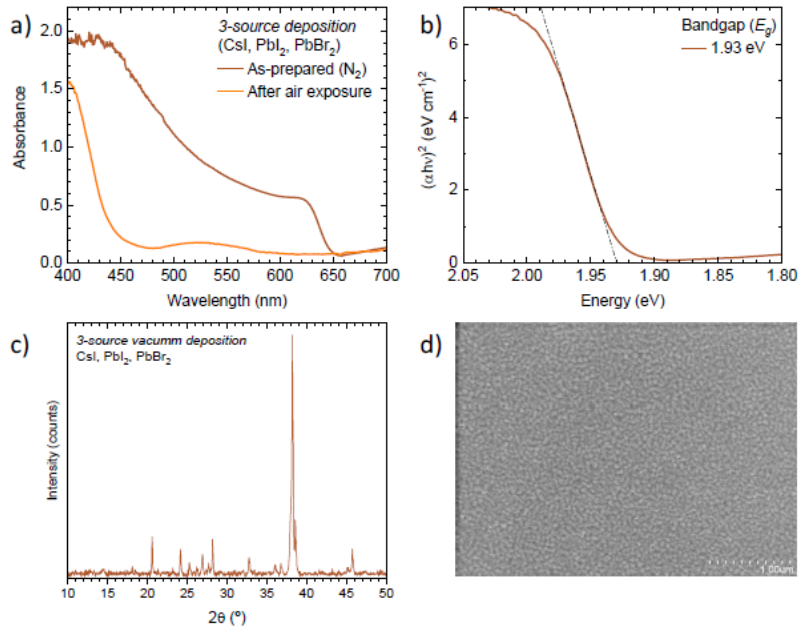

Figure 43. Measured (a) UV-Vis absorbance before and after air exposure, (b) Tauc plot calculations, (c) XRD pattern and (d) surface morphology through SEM of a sample prepared with CsI, PbI_2, and $PbBr_2$.

To conclude, the last experiment employing *4 sources* was performed to check if improved quality films were obtained when *subliming* all the possible starting precursors at the same time, which where *CsI, CsBr, PbI_2 and $PbBr_2$*. XRD patterns (Figure 44a) showed a phase-pure perovskite again. However, in this case, no preferential orientation was found. Surface morphology (Figure 44b) showed a homogeneous film with small grains of 50 nm and cuboids of 100 nm, similar to the structures observed for the 3 sources at a slow rate. This indicates that the

formation of these structures is favored when better halide alloying is achieved. Finally, its absorption onset (Figure 39b) showed the expected bandgap of 1.92 eV.

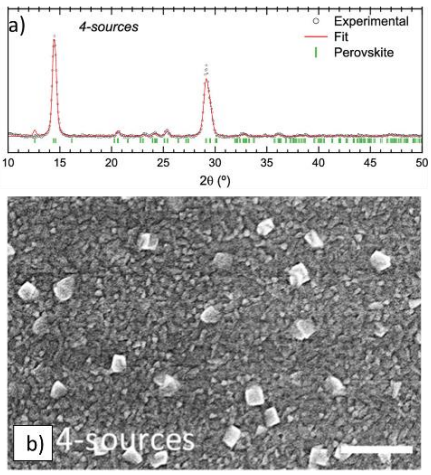

Figure 44. Characterization results of the sample prepared by co-evaporation of CsBr, CsI, PbI_2 and $PbBr_2$ (4 sources) through (a) XRD and (b) SEM. Scale bar is 500 nm.

As a summary, RT vacuum-deposited films showing phase-pure perovskites, homogeneous morphology and the expected E_g were successfully obtained for all the techniques (2 sources, 3 sources "fast" and "slow" and 4 sources) but for the flash evaporation (1 source). In view of the good quality of these films, they were integrated into sandwiched p-i-n devices to see how their performance in solar cells was. Their structure can be seen in Figure 45a.

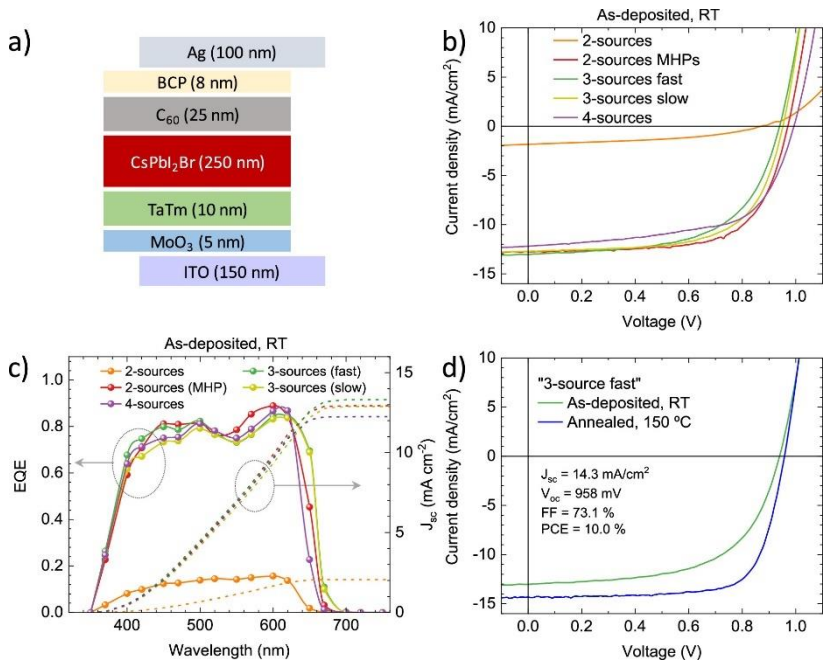

Figure 45. (a) Device structure of the PSCs and measurements done for the (b) J-V curves and (c) EQEs of the PSCs prepared with different vacuum-deposition methods. (d) Comparison between the as-deposited and annealed J-V curve of the perovskite prepared with 3 sources and a fast rate.

Furthermore, these devices were also annealed. The EQE and J-V curves of these devices can be seen in Figure 46.

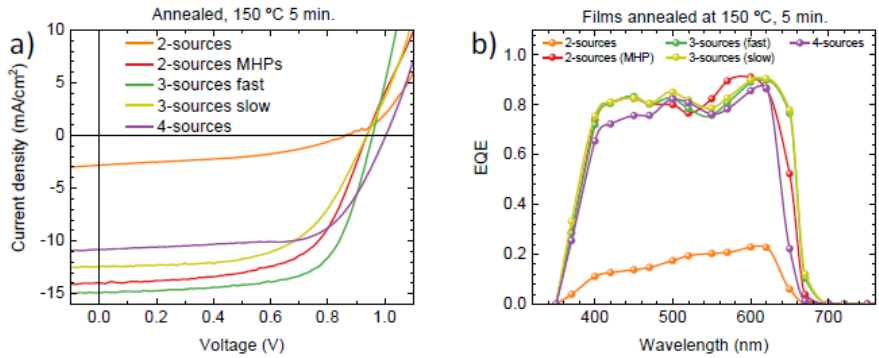

Figure 46. (a) J-V curves and (b) EQEs for the samples prepared by different vacuum-methods after a 5 min annealing at 150°C.

For a better understanding of the performance parameters of these devices, Figure 47 is introduced.

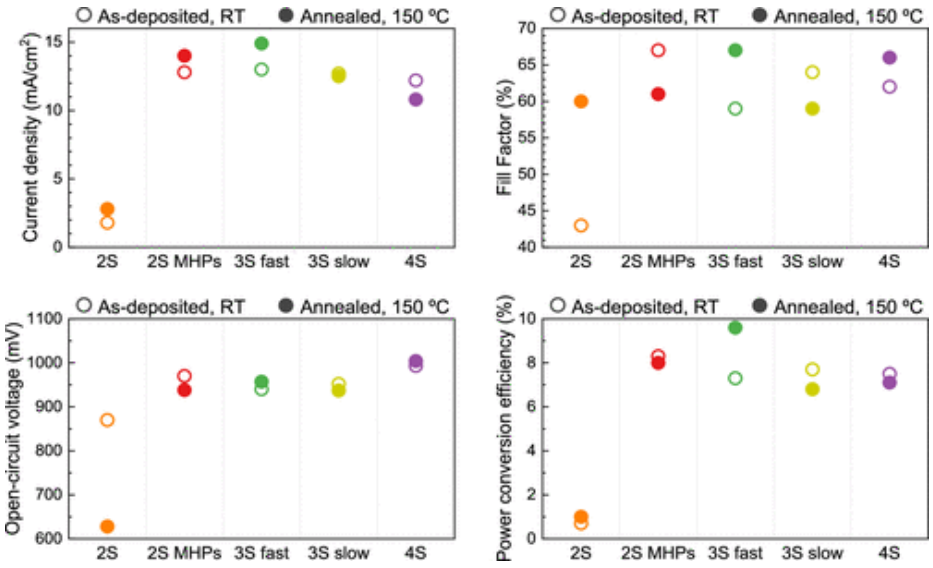

Figure 47. Performance parameters obtained for the samples prepared by different vacuum-deposition methods with and without thermal post-treatment. In the abscissa axis 2 sources (2S), 2 sources mixed-halide precursors (2S MHPs), 3 sources fast (3S fast), 3 sources slow (3S slow) and 4 sources (4S).

From the parameter studies, it can be noticed how the sample prepared with only 2 sources (2S) underperforms against the rest of them. 2 sources vacuum-deposition is the only one reported in the literature, and it only led to efficient devices after annealing at high temperatures of >260ºC. Improving halide alloying through mixed-halide precursors (2S MHPs) leads to better FFs of >65% and V_{OC}s of 970 mV (Figure 46b). Furthermore, its photocurrent is also enhanced because of its constant high spectral response (Figure 46c). For the solar cells prepared with 3 sources, the performance parameters were similar. However, a higher FF was obtained for the sample prepared with slow rates (3S slow), suggesting slower crystallization favors the charge transport due to the formation of larger crystallites. Their final efficiencies were 7.7 and 7.3% for slow and fast rates, respectively. However, it can be seen that when annealing the sample of 3 sources "fast" (3S fast) (Figure 46d), it improves its photovoltaic behavior, leading to the highest efficiencies of 10%. The efficiencies obtained for the 4 sources (4S) deposition were similar, although a higher V_{OC} was obtained. This increment suggests a reduction of the non-radiative recombination.

As a conclusion of the PSCs studies, improved alloying of the metal halides, either by the use of more sources or by pre-alloying, improves the formation of this perovskite at RT.

After this, the stability of the perovskite showing the best PCE, being 3 sources "fast", was evaluated under illumination (Figure 48a) and thermal stress in dark conditions (Figure 48b).

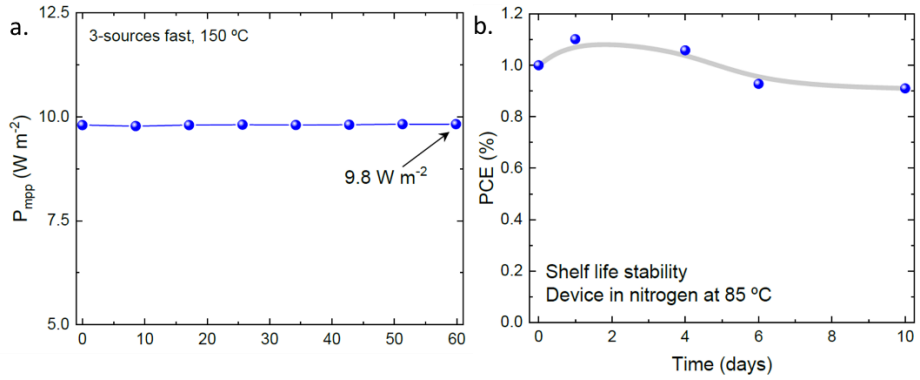

Figure 48. (a) Maximum power point under illumination and (b) PCE variations during thermal stress for the sample prepared with 3 sources and a fast rate.

The maximum power point (MPP) of this solar cell was found to be stable over an hour of measurement, and the efficiency under thermal stress retained 90% of its initial value over the 10 days.

Finally, although the performance of these PSCs was promising, it was clearly far from the maximum one expected theoretically (25% for an E_g of 1.9 eV). [31] To gain insight on the limitations of these PSCs, sensitive EQE (sEQE) measurements and photoluminesce (PL) response of the *3-sources* and a *fast* rate were studied (Figure 49). From the sEQE the E_g was estimated to be 1.870 eV, and the maximum values of the parameters of the PSCs prepared with this E_g can be extracted.[31,85] Furthermore, radiative V_{OC} and Urbach energy can be extracted.[136,137] Table 4 is presented for a comparison of the values obtained.

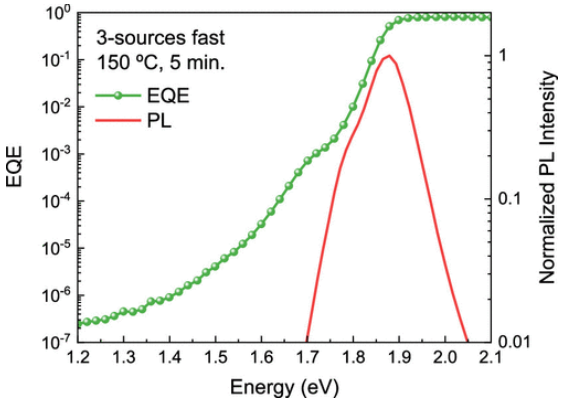

Figure 49. sEQE and PL measurements for the sample prepared with 3 sources and a fast rate after annealing.

Table 4. Solar cell parameters in the radiative limit and comparison with obtained for the sample prepared with 3 sources and a fast deposition rate. FF without resistive losses in brackets.

E_g/q (V)	1.870	**E_U (meV)**	17.96
V_{OC} rad (V)	1.563	**V_{OC}/ V_{OC} rad (%)**	61.3
J_{SC} max (mA/cm^2)	17.7	**J_{SC}/ J_{SC} max (%)**	80.8
FF max (%)	91.7 (86.9)	**FF/FF max (%)**	79.7 (84.1)
PCE max (%)	25.4	**PCE/PCE max (%)**	39.4

From the comparison of the obtained and the maximum values, one can extract that the main limitations are the V_{OC} and FF. The FF is rather high for the 3 sources fast deposition but for the rest of the samples it is lower. J_{SC} also suffers these resistive effects, nevertheless, in these studies, the thickness was not optimized, and we attribute its losses to this fact. High losses in V_{OC} are a widespread problem among wide-bandgap perovskites and they are normally attributed to photoinduced phase segregation or energy levels misalignment.[138] In Figure 49, an extra component can be observed at 1.7-1.78 eV. This component might be the responsible for the voltage loss. In the PL, this feature can be a sign of phase segregation. However, this feature is only present in some regions, as can be seen in Figure 50.

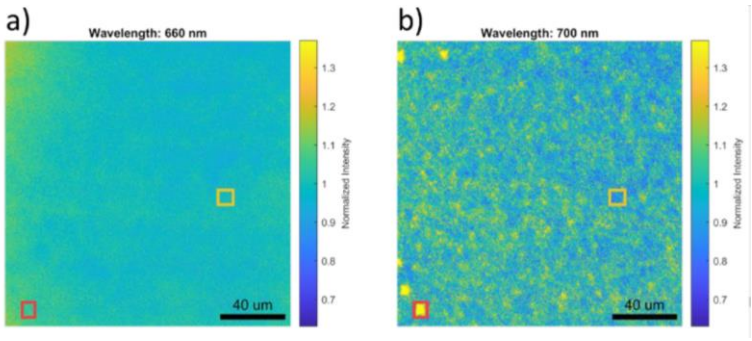

Figure 50. PL maps of the sample prepared with 3 sources in a fast deposition rate illuminated at (a) 660 nm, for the main emission, and (b) 700 nm, for the extra feature.

Finally, as the feature remains at a lower absorption than the one for pure $CsPbI_3$, and the sEQE was obtained at low illumination intensities, we can conclude the feature is originated from a misalignment of the energy levels between perovskite and transport layers.

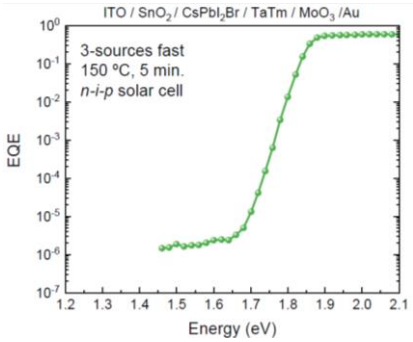

Figure 51. sEQE of the same perovskite employing SnO_2 as the ETL.

Another possible explanation for the feature was that it was generated by C_{60}. As this material can generate photocurrent at these energy levels.[139] To confirm this, devices employing SnO_2 as ETL were studied through sEQE, and the feature was not observed (Figure 51). Hence, a further investigation on the transport layers for this perovskite should be done in future studies.

5.5. Conclusion

Several methods to synthesize $CsPbI_2Br$ were employed to elucidate if it could be successfully formed at RT. Perovskite formation was obtained through several methods. Single source deposition led to a mixture of phases, while the rest of vacuum-based methods led to phase-pure perovskites. The higher quality of the films obtained through mixed-halide precursors evaporation indicated the importance of halide mixing during the synthesis. This effect could also be achieved by increasing the number of sources and diminishing the speed of evaporation. In the end, PCEs as high as 8.3% were obtained for the samples as-prepared, and they could be enhanced up to 10% with a low-temperature annealing process of 150ºC, which is compatible with the use of flexible substrates. The main limitation for the performance of these PSCs was found to be the electron transport layers, indicating further studies on them should be done.

5.6. Contribution of the author

Igual-Muñoz, A. M.; Navarro-Alapont, J.; Dreessen, C.; Palazon, F.; Sessolo, M.; Bolink, H. J. "Room-Temperature Vacuum Deposition of CsPbI 2 Br Perovskite Films from Multiple Sources and Mixed Halide Precursors." Chem. Mater., 32, 8641–8652 (2020).

Chapter 6
Conclusions

6. Conclusions

The aim of this thesis was the development of narrow and wide-bandgap perovskites through vacuum-based methods. The synthesis of three different materials with the targeted bandgaps of 1.28, 1.34 and 1.9 eV has been carefully studied.

In **chapter 3**, a novel method to deposit tin-lead perovskites was presented. The formation and stability of $FAPb_{0.5}Sn_{0.5}I_3$ were enhanced by suppressing the formation of Sn^{4+} with the co-evaporation of a SnF_2 additive. These films were integrated into solar cells achieving impressive efficiencies close to 14%. Furthermore, this study demonstrated the capability of vacuum-based methods to synthesize working tin-lead alloyed perovskites in PSCs. However, the efficiencies were not easy to reproduce due to difficulties in achieving the required control of the small quantities of additives needed. On the other hand, the uncontrollable partial oxidation of Sn^{2+} to Sn^{4+} affected the final efficiencies.

The issue of reproducibility of this method to synthesize narrow-bandgap tin-lead-based perovskites was addressed in **chapter 4**. In this work, cations more controllable during sublimation were employed. Furthermore, the introduction of higher quantities of lead in the structure led to more stable perovskites. $MA_{0.9}Cs_{0.1}Pb_{0.75}Sn_{0.25}I_3$ was synthesized without the need for additional SnF_2 additives. A careful study on the thickness of this perovskite was done to optimize the morphology, structure, and optical properties. In addition, the obtained films were integrated into p-i-n devices leading to reproducible efficiencies as high as 8.9%. The limiting factors of these devices were studied through EIS and J-V curves in dark conditions to elucidate which further studies should be done to enhance this perovskite's efficiency. In the end, the study led to the conclusion of a dominant bulk recombination process due to smaller grain size and Sn^{+2} oxidation.

Finally, once reproducible narrow-bandgap perovskites were achieved, the formation of wide-bandgap perovskites through sublimation methods was carried out in **chapter 5**. An inorganic perovskite ($CsPbI_2Br$) was chosen for this study due to its exceptional thermal stability and suitable bandgap for tandem

applications, 1.9 eV. $CsPbI_2Br$ was synthesized through several solid-state and vacuum-based methods to elucidate if its formation at room temperature or employing low-temperature annealing processes could be successful. This study highlights the importance of halide-mixing. Perovskites employing mixed-halide precursors prepared by melting, a higher number of co-evaporation sources, or a slow evaporation rate showed enhanced properties. Furthermore, all the layers, except for the flash-evaporated one, were integrated into solar cell devices. The study demonstrated the preparation of post-treatment-free working solar cells which achieved PCEs up to 8.3%. In addition, a low-temperature annealing process of 150ºC for 5 minutes was investigated, showing enhanced PCEs up to 10%. Limitations for the development of this perovskite as an absorber in a solar cell were investigated, with the transport layers being the main one, indicating further studies on the transport layers should also be done for this perovskite.

To conclude, during this thesis, we successfully synthesized two narrow-E_g and a wide-E_g perovskite integrating them into PSCs with organic transport layers. The results obtained were promising, as decent efficiencies were achieved for all the perovskites, remarking sublimation methods are a promising technique, not only for $MAPbI_3$ but for different kinds of perovskites. In addition, a fully-inorganic perovskite was deposited without the need of further annealing to work, opening a wide new range of applications, such as its integration in flexible devices.

Chapter 7
Resumen en castellano

7. Resumen en Castellano

Capítulo 1: Introducción y objetivo de la tesis.

1.1. El desafío de la energía

La demanda de energía global ha incrementado desde los 10.000 TWh en 1990 a más de 20.000 TWh en 2019. Este aumento en la producción de energía ha resultado en un incremento en la generación de gases de efecto invernadero provocando un aumento de la temperatura media de la tierra. De este modo, la necesidad de producir energía limpia es inminente.

Entre los distintos candidatos para producir energía limpia encontramos la energía solar. Gracias a la gran cantidad de energía en forma de irradiación solar que llega a la Tierra podríamos continuar con el desarrollo de nuestras actividades industriales y domésticas. Por este motivo, en 1883 ya comenzaron a desarrollarse dispositivos fotovoltaicos. Generalmente, se han empleado dispositivos con materiales del tipo GaAs, silicio, CdTe o CIGS. Sin embargo, una nueva generación de dispositivos ha comenzado a estudiarse en los últimos diez años.

1.2. Perovskitas de metal y haluro

Desde 2002, las células solares basadas en perovskitas han aumentado su eficiencia de conversión energética, pasando de un 2.2% hasta un 25.5% certificado. Estos dispositivos fotovoltaicos presentan muchas ventajas respecto a las tecnologías fotovoltaicas tradicionales, como la abundancia de sus componentes en la corteza terrestre, su bajo coste o la posibilidad de ajustar su banda prohibida químicamente. Las perovskitas deben su nombre a la estructura ABX_3, donde A representa a un catión monovalente, B a un metal divalente y X a un haluro. Uno de los parámetros que determinan su estabilidad es el Factor de tolerancia de Goldschmidt, que se estima entre 0.8 y 1 para compuestos estables y depende del tamaño de los átomos de la estructura. Éste también se puede controlar mediante la introducción de distintos componentes en la estructura. Las razones que explican el excelente funcionamiento de las perovskitas en dispositivos optoelectrónicos se basan en las propiedades semiconductoras de estos materiales, como la alta movilidad o las altas longitudes de difusión de sus

portadores de carga. Una de las características más interesantes que presentan es el anteriormente mencionado control de la banda prohibida, ya que permite obtener ajustar los materiales a aplicaciones concretas como la obtención de altas eficiencias mediante el desarrollo de dispositivos tándem, que emplean varios absorbedores para utilizar todo el espectro solar. Éste es uno de los principales objetivos planteados en la hoja de ruta desarrollada por EMIRI.

1.3. Control de la banda prohibida

Las perovskitas presentan la interesante característica de poder variar su banda prohibida mediante la variación de su composición. Por ejemplo, introduciendo formamidinio, la banda se estrecha, e introduciendo cesio, la banda se amplía. En este sentido, la presente tesis basa sus estudios en la síntesis de perovskitas de banda prohibida estrecha y de banda prohibida ancha con el objetivo de fabricar, en el futuro, tándems de alta eficiencia.

1.3.1. Perovskitas de banda prohibida estrecha

Las perovskitas comúnmente empleadas, como el $MAPbI_3$, presentan bandas prohibidas lejos del óptimo estimado por el límite de Schockley Queisser. Sin embargo, las basadas en aleaciones de estaño y plomo presentan un efecto poco convencional denominado arqueamiento de la banda prohibida. Este efecto permite sintetizar perovskitas con bandas prohibidas más estrechas, de hasta 1.1 eV. Gracias a este efecto ya se han preparado perovskitas con la banda prohibida óptima. Por otro lado, este efecto permite desarrollar perovskitas con bandas prohibidas adecuadas para su uso como absorbedores de banda prohibida estrecha en tándems.

1.3.1. Perovskitas de banda prohibida ancha

Estas perovskitas presentan bandas prohibidas de entre 1.7 y 1.9 eV. Así, se pueden usar como absorbedores de banda prohibida ancha en tándems. Normalmente, este efecto se consigue mediante la introducción de diferentes haluros. Sin embargo, las perovskitas que combinan diferentes haluros presentan un efecto negativo llamado segregación de haluros. Este efecto se da cuando, tras la iluminación, se produce una segregación de los haluros debido a las vacantes de haluro que están presentes en la estructura, dando lugar a dos fases con una banda prohibida ancha y la otra estrecha. Cuando estas regiones se forman, los

portadores se acumulan en las regiones de banda prohibida estrecha que actúan como centros de recombinación, dando lugar a pérdidas en el voltaje. Por otro lado, también se puede obtener un efecto similar al variarse los cationes monovalentes. Aunque los más empleados son el metilamonio y el formamidinio, la introducción de cationes inorgánicos como el cesio mejora la estabilidad de las perovskitas. Tanto es así, que las perovskitas puramente inorgánicas presentan una estabilidad superior. Sin embargo, las perovskitas inorgánicas presentan problemas para mantener su fase de perovskita, que pueden solucionarse mediante la introducción de bromo en su estructura. Por ese motivo, esta tesis basa su estudio en la perovskita $CsPbI_2Br$. Esta perovskita ha sido sintetizada mediante diversos métodos, obteniendo eficiencias de hasta un 16.79%. Sin embargo, los métodos que emplean técnicas de vacío no han sido optimizados, dando lugar a eficiencias más bajas.

1.4. Técnicas de deposición

Existen muchas técnicas para la deposición de perovskitas con características similares, entre ellas encontramos dos grandes variantes:

Métodos por disolución:

- Deposición en un solo paso.
- Deposición en dos pasos.
- Ingeniería de disolventes.

Métodos por sublimación:

- Evaporación instantánea.
- Evaporación secuencial.
- Evaporación mediante múltiples fuentes.

La evaporación mediante múltiples fuentes se basa en la sublimación conjunta de distintos precursores para formar la perovskita y requiere del uso de múltiples sensores para controlar con precisión la cantidad de cada precursor sublimada. Sin embargo, presenta gran cantidad de ventajas frente a otros tipos de deposición. Entre ellas encontramos:

- Alta pureza de los materiales sublimados.

- Compatibilidad con áreas grandes.
- Control preciso del espesor, la estequiometría y la morfología.
- Bajas temperaturas de uso sin necesidad de tratamientos térmicos posteriores.
- Técnica intrínsecamente aditiva. Permite depositar capas encima de otras sin afectar a las anteriores.
- No precisa de uso de disolventes tóxicos.
- Técnica consolidada y empleada en la industria.

Debido a todas las ventajas anteriormente señalas, los estudios de la presente tesis se basan en el uso de esta técnica.

1.5. Funcionamiento de las células solares

Las células solares se pueden preparar empleando distintas configuraciones, como son la llamada p-i-n o la n-i-p. En la p-i-n encontramos que la luz pasa primero por el electrodo transparente, atraviesa la capa transportadora de huecos, después al absorbedor y finaliza en el transportador de electrones y el metal. La disposición n-i-p es la inversa de la p-i-n.

Cuando las perovskitas se iluminan generan pares de electrones y huecos que se separan en electrones y huecos libres debido a su energía de unión relativamente baja. Éstos son los que se transportan en la estructura de la célula solar dando lugar a la energía eléctrica generada. Para determinar la eficiencia de las células solares se emplean principalmente dos métodos:

- Eficiencia cuántica externa: mide la cantidad de fotones que se convierten a corriente eléctrica dependiendo de la longitud de onda empleada.
- Curvas de voltaje y corriente bajo iluminación: esta medida permite obtener los parámetros que determinan la eficiencia de la célula solar. Se realiza bajo iluminación AM1.5G, un estándar empleado para que sea representativo de las condiciones de iluminación de la tierra.

La eficiencia de las celdas consiste en la multiplicación de la corriente de cortocircuito, el voltaje en circuito abierto y el factor de llenado y la división por la potencia introducida, que en AM1.5G es de 100 $mWcm^{-2}$. Por otro lado, las

células solares pueden presentar histéresis en sus curvas, ya que se miden en varias direcciones, directa y reversa.

1.6. Objetivo de la tesis

Como se comentó en la sección 1.3.1., dos de los principales problemas de las perovskitas de estaño y plomo es la oxidación del Sn^{+2} y la dificultad de formación de la perovskita en sí misma. En el **capítulo 3** se lleva a término la preparación de la primera perovskita de banda prohibida estrecha mediante sublimación dando lugar a dispositivos eficientes. Para conseguirlo, el aditivo SnF_2 se incluye en la perovskita para dificultar la oxidación de Sn^{+2}.

Aunque una de las ventajas del método de sublimación es el alto grado de control de la composición de las perovskitas, el uso de aditivos en pequeñas cantidades es difícil de controlar. En el **capítulo 4**, la preparación de perovskitas de banda estrecha con eficiencias reproducibles mediante sublimación será llevada a término mediante el desarrollo de un método de fabricación que evita el uso de aditivos. Por otro lado, este capítulo será determinante para las perovskitas de banda prohibida estrecha, ya que pretende preparar perovskitas con la banda prohibida de 1.34 eV, óptima para dispositivos fotovoltaicos de una sola capa recolectora. Además, las perovskitas se integrarán en dispositivos dando lugar a resultados reproducibles y, gracias a los mismos, se hará un estudio del efecto del espesor de la perovskita.

Finalmente, como se mencionó en la sección 1.3.2., uno de los problemas principales de las perovskitas de banda prohibida ancha es la segregación de haluros. En el **capítulo 5** se plantea un estudio de diferentes métodos de sublimación para depositar $CsPbI_2Br$ y estudiar su formación. Debido a que uno de los principales problemas de las perovskitas inorgánicas es su formación a temperatura ambiente, uno de los objetivos principales del capítulo será determinar las mejores rutas para la fabricación de esta perovskita sin necesidad de tratamiento térmico. De este modo, se integrarán las perovskitas en dispositivos sin tratamiento térmico y con un tratamiento térmico a temperatura moderada compatible con el uso de sustratos flexibles.

Capítulo 2: Métodos experimentales

2.1. Fabricación de células solares

Todos los procedimientos empleados se realizaron en una sala limpia de clase 10000 (Figura 13). La preparación de los sustratos consistió en el siguiente procedimiento:

- Limpieza de los sustratos:

Se comenzó con un frotado empleando un detergente, los sustratos se introdujeron en agua, agua milliQ e isopropanol. En cada paso se sonicaron durante 5 minutos. Finalmente, se introdujeron en una lámpara ultravioleta con ozono durante 20 minutos.

- Deposición de las capas orgánicas y el electrodo metálico.

Las capas orgánicas empleadas fueron MoO_3, m-MTDATA, TATM, C_{60} y BCP, sintetizadas mediante sublimación a una presión de $\approx 10^{-6}$ mbar. También se empleó PTAA sintetizado mediante "Spin coating" a una velocidad de 1500 rpm durante 30 s. Como electrodo metálico se empleó Ag sintetizada mediante sublimación a una presión de $\approx 10^{-6}$ mbar.

- Deposición de la capa de perovskita:

Se emplearon diversos procedimientos para las distintas perovskitas:

- $FAPb_{0.5}Sn_{0.5}I_3$: se realizó la sublimación coordinada en cuatro fuentes empleando como precursores FAI, PbI_2, SnI_2 y SnF_2.
- $MA_{0.9}Cs_{0.1}Pb_{0.75}Sn_{0.25}I_3$: se realizó la sublimación a cuatro fuentes empleando como precursores MAI, CsI, PbI_2 y SnI_2.
- $CsPbI_2Br$: esta perovskita se depositó mediante distintos métodos. Para la síntesis en estado sólido se introdujeron cantidades estequiométricas de CsBr y PbI_2 en un molino de bolas, que se utilizó durante 99 min a 30Hz. Para las técnicas de deposición por sublimación encontramos un resumen en la Figura 15.

Para depositar las perovskitas con la estequiometría deseada se realizó una calibración de cada precursor en su respectivo sensor mediante la medición del espesor realmente depositado en el QCM y el espesor medido por el mismo, y se aplicó un factor de calibración. Para la perovskita de $CsPbI_2Br$ también se calibró la cantidad de perovskita depositada en un quinto sensor al lado del soporte para los sustratos.

Los dispositivos fotovoltaicos emplearon distintos HTM, según su HOMO, siendo las configuraciones empleadas las representadas en la Figura 16.

2.2. Caracterización de las capas finas

Para determinar la calidad de las láminas se emplearon dos tipos de análisis:

- Análisis estructural: se realizó mediante medida del espesor con perfilómetro, de la morfología superficial mediante SEM y AFM, de la estructura cristalina mediante XRD y de la composición mediante XPS y EDAX.
- Análisis óptico: se midió la absorbancia de las capas, se calcularon los gráficos de Tauc mediante la fórmula $(\alpha h\upsilon)^2$, y la fotoluminescencia.

2.3. Caracterización de las células solares

Para determinar la calidad de las células solares se emplearon distintas técnicas de caracterización:

- Caracterización eléctrica: se obtuvieron los espectros EQE mediante iluminación a distintas longitudes de onda y medida de la respuesta de la célula. También se empleó un EQE pulsado de alta sensibilidad. Las curvas de corriente y voltaje en iluminación se obtuvieron empleando un simulador solar con iluminación AM1.5G y midiendo la respuesta de la célula. Las muestras fueron medidas empleando una máscara de 2.2 x 1.2 mm^2 para asegurar el área iluminada.
- Espectroscopía de impedancia: se realizaron las medidas de impedancia a distintas frecuencias y se ajustaron las curvas al circuito equivalente presentado en la Figura 17.

Capítulo 3: $FAPb_{0.5}Sn_{0.5}I_3$, una perovskita de banda prohibida estrecha sintetizada mediante métodos de evaporación para aplicaciones fotovoltaicas.

3.1. Introducción

En la actualidad, la evolución de las células solares de perovskita se ha aproximado mucho al límite de Schockley Queisser. Para aumentar aún más su eficiencia, se requiere de células solares con la banda prohibida óptima de 1.34 eV. Además, la necesidad de producir células solares con bandas prohibidas estrechas también es limitante para la producción de tándems, ya que éstos requieren de absorbedores con bandas prohibidas de entre 1.1 y 1.3 eV. La combinación de estaño y plomo en la perovskita resulta en un estrechamiento de la banda prohibida acentuado por el efecto de arqueamiento de la banda prohibida. Por otro lado, como se comentó previamente, también la introducción de formamidinio en la perovskita disminuye esta banda prohibida y aumenta su estabilidad térmica.

3.2. La perovskita de yoduro de formamidinio estaño y plomo como absorbedor en células solares de banda prohibida estrecha

En el presente estudio se desarrolla un método innovador para sintetizar perovskitas de estaño y plomo para su uso como absorbedores en células solares. El estudio presenta sus propiedades ópticas, morfológicas y estructurales, y las integra en dispositivos. La perovskita sintetizada presenta una banda prohibida de 1.28 eV cercana a la óptima y válida para su uso en tándems. Además, los dispositivos llegaron a eficiencias cercanas al 14%, demostrando la capacidad de la sublimación como método de síntesis de perovskitas de estaño y plomo.

3.3. Métodos experimentales

Los sustratos cubiertos con ITO se limpiaron siguiendo el método descrito en el capítulo 2. Posteriormente, se evaporaron las siguientes capas: 5 nm de MoO_3 y una capa de PTAA sintetizada mediante disolución, que se trataron térmicamente a 100ºC durante 10 min en atmósfera de nitrógeno. Sobre ellas, se evaporó la perovskita mediante sublimación simultánea de FAI, SnI_2, PbI_2 y SnF_2 como aditivo. Para la deposición de la perovskita se calibraron cuidadosamente las microbalanzas de cuarzo cristalinas. Finalmente, se evaporaron las siguientes

capas: 25 nm de C_{60}, 8 nm de BCP y 100 nm de plata. La caracterización siguió la metodología descrita en el capítulo 2.

3.4. Resultados y discusión

En primer lugar, se realizó un estudio de la formación de la perovskita analizando el efecto de la adición de SnF_2. Los estudios de absorbancia indicaron que la perovskita con SnF_2 daba lugar a un compuesto de mayor calidad (Figura 20a). Además, los espectros de difracción de rayos X (Figura 20b) mostraron que, sin aditivo, el pico predominante era el asociado al PbI_2. Sin embargo, al introducir pequeñas cantidades del aditivo, los picos predominantes observados fueron los de la perovskita. Finalmente, con cantidades muy altas de aditivo el pico asociado al PbI_2 vuelve a intensificarse y aparece uno nuevo normalmente asociado a SnI_2. Los resultados observados llevaron a la conclusión de que la cantidad óptima del aditivo era del 10%. Además, se realizaron estudios acerca de la morfología de las láminas (Figura 21) donde se observó que la adición de aditivo no tenía ninguna repercusión en la morfología.

Para comprobar la estabilidad de las láminas se realizaron estudios de absorbancia (Figura 22a) y de conductividad (Figura22b). Las absorbancias mostraron cómo, tras un día de exposición al aire la perovskita comienza a degradarse. Por otro lado, los estudios de conductividad mostraron cómo, en nitrógeno, la perovskita no parece degradarse tras 12 días y, sin embargo, en 3 horas de exposición al aire la conductividad aumenta un orden de magnitud. Esto indica que se está formando Sn^{+4} en la capa.

Escogida la cantidad óptima de aditivo de un 10%, se prepararon más láminas y se caracterizaron más concienzudamente para determinar su banda prohibida y morfología con precisión. En la Figura 23a se muestra el espectro de absorbancia y el cálculo del gráfico de Tauc para la determinación de la banda prohibida. En ellos puede observarse una banda prohibida de 1.28 eV. La morfología se determinó mediante microscopía electrónica de barrido (Figura 23b). Se observaron granos pequeños característicos de la metodología de sublimación de entre 60 y 100 nm.

Finalmente, para determinar la eficiencia como absorbedor de la perovskita ésta se integró en dispositivos de tipo "sándwich" empleando la

configuración mostrada en la Figura 24a. La medida de las curvas J-V en oscuridad (Figura 24b) muestra una corriente de fuga pequeña y una buena rectificación que dan lugar a pensar que se está suprimiendo la formación de Sn^{4+}. Los estudios de conversión de fotones a electrones incidente (IPCE) (Figura 24c) muestran valores relativamente bajos de 0.7, que indican que se debe optimizar el espesor de las láminas. Finalmente, en la Figura 24d se observa la curva J-V en iluminación. En la misma no se observa histéresis, pero si valores altos de FF y J_{SC}, muy cercanos a los esperados del IPCE. Para comprender mejor los valores obtenidos se muestra la Tabla 1. En la tabla podemos observar cómo el PCE obtenido es de 13.98%, demostrando que la perovskita actúa de manera eficiente como absorbedor. Éste estudio da lugar a la conclusión de que las técnicas de sublimación son aptas para la síntesis de perovskitas de estaño y plomo suprimiendo la formación de Sn^{4+}.

3.5. Conclusión

En el presente estudio se desarrolló un método para la síntesis de $FAPb_{0.5}Sn_{0.5}I_3$ mediante sublimación. La co-evaporación de los precursores empleando el aditivo SnF_2 demostró ser una técnica efectiva para la supresión del Sn^{4+}. Las láminas mostraron bandas prohibidas estrechas de 1.28 eV y una superficie uniforme sin poros. Además, las láminas se integraron en dispositivos dando lugar a eficiencias cercanas al 14%. En conclusión, este estudio demuestra la capacidad del método de sublimación para sintetizar perovskitas funcionales de estaño y plomo con eficiencias considerables. Así, abre una nueva ruta de procesado de este tipo de perovskitas tan interesantes debido a su capacidad de poseer la banda prohibida óptima y la necesaria para la preparación de tándems.

Capítulo 4: Células solares multicatión de estaño y plomo depositadas mediante vacío.

4.1. Introducción

Como se comentó en la sección 1.3.1, existen dos rutas principales para incrementar la eficiencia de las células solares de perovskita. El desarrollo de absorbedores con la banda prohibida óptima de 1.34 eV y la preparación de tándems. Sin embargo, la síntesis de perovskitas de banda prohibida estrecha mediante la aleación de estaño y plomo continúa presentando la dificultad de la formación de Sn^{4+}. Normalmente, estas perovskitas se sintetizan por disolución, aunque este método presenta desventajas como la falta de control en el espesor. Las técnicas de sublimación ya han demostrado ser eficientes en la preparación de estas perovskitas, como se observó en el capítulo 3. No obstante, la técnica requirió de la adición de SnF_2 en pequeñas cantidades, que es difícil de controlar y da lugar a una baja reproducibilidad. Por otro lado, se empleó formamidinio como catión, el cual también ha demostrado ser difícil de controlar mediante sublimación. Otros estudios han demostrado la capacidad del método de sintetizar estas perovskitas, pero también requirieron del uso de SnF_2 como aditivo. En este sentido, el uso de dos cationes monovalentes como son el metilamonio, altamente controlable mediante sublimación, y el cesio, que aumenta la estabilidad térmica y la fotoestabilidad, ha demostrado la capacidad de sintetizar estas perovskitas sin necesidad de usar aditivos.

4.2. Estudios en el espesor y el funcionamiento de la perovskita de yoduro de metilamonio cesio estaño y plomo depositada mediante vacío.

En este trabajo, se realiza la sustitución parcial del plomo por estaño en la perovskita $MA_{0.9}Cs_{0.1}PbI_3$ desarrollada mediante técnicas de vacío sin necesidad de emplear el aditivo SnF_2. La perovskita mostró bandas prohibidas más estrechas que la basada en plomo llegando a valores cercanos a 1.34 eV. Se estudiaron las características de las láminas cambiando los parámetros de evaporación y el espesor de las mismas para obtener eficiencias más altas y reproducibles.

4.3. Métodos experimentales

Los sustratos cubiertos con ITO se limpiaron siguiendo el método descrito en el capítulo 2. Sobre los mismos se evaporaron: 5 nm de MoO_3 y 10 nm

de m-MTDATA que se trataron térmicamente a 100ºC durante 10 min en atmósfera de nitrógeno. Sobre ellas, se evaporó la perovskita mediante sublimación simultánea de MAI, CsI, SnI_2 y PbI_2. Para la deposición de la perovskita se calibraron las microbalanzas de cuarzo cristalinas. Finalmente, se evaporaron: 25 nm de C_{60}, 8 nm de BCP y 100 nm de plata. La caracterización siguió la metodología descrita en el capítulo 2.

4.4. Resultados y discusión

La composición objetivo de este estudio fue $MA_{0.9}Cs_{0.1}Pb_{0.75}Sn_{0.25}I_3$. Para obtenerla se desarrollaron tres perovskitas variando el ratio de catión monovalente frente a catión divalente desde 1.2:1 a 2.3:1 (SnPb:MACs). Las láminas obtenidas se analizaron mediante rayos X y absorbancia. Los espectros de rayos X (Figura 27a) mostraron que para el menor de los ratios se formaban perovskitas de baja dimensionalidad, comúnmente asociadas al exceso de catión monovalente. Para el ratio 2:1 se observó una perovskita bien formada y al introducir más catión divalente se observó un exceso del mismo que ha reportado ser beneficioso para el funcionamiento de la perovskita en células solares. Por otro lado, en los espectros de absorbancia (Figura 27b) se observa que, con bajas cantidades de catión divalente, la perovskita no se forma bien y con las cantidades más altas tiene un mayor espectro de absorción. Para investigar mejor estos ratios se estudió su funcionamiento en células solares, observándose un IPCE mayor para la mayor cantidad de catión divalente (Figura 28a), así como una J_{SC} mayor en las curvas J-V (Figura 28b). Estos resultados se resumen en la Tabla 2. De este modo, el ratio escogido para los estudios posteriores fue el mayor, de 2.3:1. Para comprobar el efecto de tratamientos térmicos posteriores se prepararon dispositivos con y sin los mismos, en los cuales (Figura 29 a y b) se observa que los tratamientos térmicos no son necesarios. Además, se estudió la estabilidad de la perovskita integrada en dispositivos (Figura 29 c y d), que demostró ser satisfactoria tras tres días en atmósfera de nitrógeno.

Posteriormente, se realizaron estudios sobre el espesor de la perovskita. La calidad de las láminas se evaluó mediante estudios morfológicos, estructurales y ópticos para determinar el espesor óptimo. En las imágenes de microscopía electrónica de barrido (Figura 30a-d) se observan superficies homogéneas de alta cristalinidad sin poros. Además, se observa un aumento en el tamaño del grano para muestras de mayor espesor. Este efecto se atribuyó a la disminución de la

velocidad de evaporación del MAI a lo largo de la misma, dando lugar a un defecto de MAI en láminas de mayor espesor. Los difractogramas de XRD (Figura 30e) muestran el pico asociado a exceso de cationes divalentes buscado y además un incremento en la intensidad del plano (220) con el espesor, que puede asociarse a un artefacto de la medida ya que el haz incide más en láminas más gruesas. Para finalizar con los estudios de caracterización se realizaron medidas de absorbancia y composición mediante EDAX. En la Figura 31a observamos los espectros de absorción, que muestran un incremento en la misma con el espesor. El estudio de la banda prohibida en función de la composición (Figura 31b) pone de manifiesto el alto control del método, obteniéndose composiciones muy cercanas a la objetivo y con variaciones de la banda prohibida muy ligeras entre 1.2 y 1.4 eV.

Finalmente, puesto que las perovskitas demostraron poseer una alta calidad, se implementaron en dispositivos de tipo sándwich para estudiar su uso como recolectores de luz en células solares. Las curvas J-V e IPCE significativos se muestran en la Figura 32. Para entender mejor estos valores se preparó una estadística que se muestra en la Figura 33 y también una tabla (Tabla 3) que muestra los valores obtenidos de las medidas de la Figura 32 y los valores medios de eficiencia de los dispositivos. Tras un concienzudo estudio empleando diversos dispositivos, se determinó que el espesor óptimo para esta perovskita era de 600 nm, llegando a valores de PCE de 8.9%. En la estadística preparada se puede observar como la J_{SC} aumenta con el espesor, así como en el EQE se observa un déficit para espesores bajos, ya que esta perovskita presenta un menor coeficiente de absorción que las que emplean cantidades más altas de estaño. Se observa también que el FF disminuye con el espesor, lo que se explicaría debido a un transporte desapareado de portadores o a una recombinación alta. Sin embargo, esta tendencia no se observa en el V_{OC}, por ello se atribuyó a un déficit en el transporte. Para elucidar mejor la causa de estas pérdidas se realizaron medidas de espectroscopía de impedancia electroquímica y de las curvas en oscuridad. Los valores obtenidos para las resistencias mediante EIS (Figura 34a) indican una recombinación en el grosor de la perovskita, en contraposición a la superficie. Además, en las curvas en oscuridad (Figura 34b) también se observa una tendencia en las resistencias a altos potenciales de inyección. Para confirmar la suposición de que la recombinación se daba en el grueso de la perovskita se investigó el factor de idealidad de la misma, que se muestra en la Figura 35. El factor de 2.25 obtenido

confirma que la recombinación se ve mediada por trampas, en línea con la suposición de recombinación en el grueso de la perovskita.

4.5. Conclusión

La técnica de sublimación se empleó para preparar perovskitas de aleación de estaño y plomo dando lugar a bandas prohibidas estrechas cercanas a la ideal con resultados reproducibles. Esta reproducibilidad se consiguió mediante el uso de MA y Cs como cationes monovalentes, además de la disminución de la cantidad de estaño, evitando la necesidad de introducir aditivos poco controlables mediante el método. Las perovskitas se integraron en dispositivos dando lugar a eficiencias que llegaron al 8.9% gracias al estudio del espesor del absorbedor. Los factores limitantes para la eficiencia de la perovskita se estudiaron mediante EIS, medidas en oscuridad y factor de idealidad, dando lugar a la conclusión de que los procesos de recombinación eran dominados por el grueso de la perovskita.

Capítulo 5: Deposición mediante vacío de láminas de perovskita $CsPbI_2Br$ empleando múltiples fuentes y precursores mixtos de haluro, a temperatura ambiente.

5.1. Introducción

Normalmente, las células solares de perovskita emplean cationes como el MA y el FA que disminuyen su estabilidad térmica. Sin embargo, la introducción de Cs la aumenta, siendo las perovskitas que emplean solo Cs como catión más estables. En particular, la perovskita $CsPbI_2Br$ presenta una banda prohibida de 1.9 eV, compatible con su aplicación como absorbedor de banda prohibida ancha en tándems. De este modo, las células solares que emplean esta perovskita han sido ampliamente estudiadas llegando a eficiencias del 16%. Sin embargo, la preparación de perovskitas inorgánicas presenta grandes dificultades, como la estabilidad de su fase funcional a temperatura ambiente, que solo se consigue tras tratamientos térmicos a temperaturas muy altas. La introducción de bromo en la estructura estabiliza la fase funcional y ensancha la banda prohibida, pero como se ha comentado previamente, requiere de tratamientos térmicos de entre 150 y 300ºC. Como alternativa, la sublimación ha demostrado ser capaz de sintetizar perovskitas que no requieren tratamiento térmico posterior y ya ha sido estudiada para la preparación de $CsPbI_2Br$, aunque para alcanzar una perovskita funcional ésta requirió de tratamiento térmico. Los tratamientos térmicos suponen una gran desventaja, ya que, a tan alta temperatura, no permiten el uso de sustratos flexibles ni su combinación con otras capas sensibles a la temperatura.

5.2. Estudios sobre la formación de $CsPbI_2Br$ mediante distintas técnicas de sublimación y el uso de precursores de haluro mixtos y su integración en dispositivos fotovoltaicos

En el presente trabajo, se estudiaron distintos métodos de sublimación para la síntesis de $CsPbI_2Br$ sin necesidad de tratamiento térmico. También se emplearon tratamientos térmicos a baja temperatura (150ºC). El objetivo principal del mismo fue comparar las propiedades obtenidas mediante distintos métodos de preparación. Además, se estudió la síntesis en estado sólido, mostrando las dificultades para sintetizar la perovskita.

5.3. Métodos experimentales

Como primer paso, se estudió la síntesis mediante molino de bolas. La perovskita $CsPbI_2Br$ se sintetizó empleando CsBr y PbI_2 en una caja de guantes de nitrógeno. Los materiales se introdujeron en jarras de zirconio con bolas del mismo material dentro de la caja seca para evitar la oxidación y se realizó la molienda a 30 Hz durante 99 min. El mismo procedimiento se empleó para los precursores mixtos, mezclando CsI y CsBr, y PbI_2 y $PbBr_2$ en concentraciones de 1:2 (Br:I). La síntesis por fundición se realizó introduciendo los materiales en un crisol que se calentó a 650ºC para la perovskita y el precursor de cesio, y a 420ºC para el precursor de plomo. Finalmente, para las técnicas de sublimación se emplearon las 5 configuraciones resumidas en la Figura 15. Las células solares se prepararon limpiando los sustratos como se describe en el capítulo 2, evaporando una capa de MoO3 de 5 nm y una capa de TATM de 10 nm, que se calentaron a 140ºC durante 10 min en atmósfera de nitrógeno. Posteriormente, se depositó la perovskita, a la que, en caso de emplearlo, se le hizo el tratamiento térmico de 150ºC durante 5 minutos. En este caso, se calibraron tanto las microbalanzas de los precursores, como la de los sustratos, para obtener el espesor deseado. Encima de la perovskita se depositaron 25 nm de C_{60}, 8 nm de BCP y 100 nm de plata mediante sublimación. La caracterización se realizó siguiendo las técnicas descritas en los apartados 2.2 y 2.3.

5.4. Resultados y discusión

Los estudios comenzaron mediante la síntesis mecanoquímica de $CsPbI_2Br$. Como resultado de esta técnica, en la Figura 36a se observa una mezcla de distintas fases mediante XRD. A pesar de observarse la estructura tridimensional de perovskita también se observa un pico a 10º que indica la presencia de una fase adicional formada por octaedros de PbX_6 parcialmente desconectados como se muestra en la Figura 36b. Esta fase es la llamada fase amarilla de la perovskita, que es la más común a temperatura ambiente y no es activa fotovoltaicamente. Cabe destacar que no se encontró que el preparado fuera una mezcla de la perovskita de yodo y la de bromo, ya que las constantes del entramado eran mayores que para el caso de iodo. Para el caso de los compuestos fundidos, de nuevo no se obtuvo una fase pura de perovskita, si no la amarilla y una nueva correspondiente al compuesto con fórmula Cs_4PbX_6. Para confirmar la existencia de fase de perovskita en los preparados se realizaron estudios de

absorbancia (Figura 37), ya que el color indicaba que la perovskita se había formado. Así, se observó una caída a 1.85-1.90 eV que indicaba la presencia de esta.

El siguiente paso del estudio fue estudiar las técnicas de sublimación. Se comenzó por el más simple hasta llegar al más complicado. La síntesis mediante una fuente se realizó haciendo una evaporación instantánea del preparado de perovskita mediante los métodos anteriormente descritos. Las láminas se analizaron mediante XRD (Figura 38a). En el espectro se observa que coexisten distintas fases con predominancia de PbI_2, como conclusión esta técnica no fue fructuosa. También se estudió su morfología mediante SEM (Figura 38b), donde se observa homogeneidad. Sin embargo, en los estudios mediante absorbancia con cálculo del gráfico de Tauc (Figura 39), se observa una banda prohibida más ancha de la esperada, como consecuencia de la segregación del PbI_2. Así, se procedió a hacer el estudio mediante dos fuentes, co-evaporando CsBr y PbI_2. En el difractograma de XRD (Figura 40a), se observa una lámina compuesta por perovskita sin ninguna fase predominante. Esta falta de orientación se puede asociar a la morfología porosa observada mediante SEM (Figura 40b). Posteriormente, se realizó la síntesis mediante precursores de haluro mixtos, ya que la pre-aleación de los haluros podía dar lugar a una estructura más homogénea. Para tomar la decisión de qué haluros mixtos emplear se muestran los patrones de XRD obtenidos para los precursores en la Figura 41. Ya que los precursores fundidos presentaban mejores características, éstos fueron los precursores de haluro mixtos empleados para la sublimación. Los patrones de XRD se pueden observar en la Figura 40c. En ellos se observa una clara fase de perovskita con orientación preferencial en el plano (110) y (002). De los estudios de superficie (Figura 40d) se extrae que la perovskita posee una morfología con granos claramente definidos. Por otro lado, de los estudios de absorbancia (Figura 39a), se extrae una banda prohibida de 1.9eV que indica una buen mezclado de los haluros. Así, esta técnica demuestra ser muy fructuosa para la síntesis de $CsPbI_2Br$, aunque puede llevar a un gradiente composicional, ya que los materiales tienen distintas temperaturas de sublimación. De este modo, se procedió a estudiar la síntesis mediante 3 fuentes. Durante la sublimación, la velocidad de evaporación es un factor decisivo para la formación de la perovskita. Por este motivo, se estudió la formación mediante 3 fuentes a dos velocidades distintas, la llamada "rápida" a 2 Å/s y la llamada lenta, a 0.5Å/s. En los patrones de XRD (Figura 42 a,c) se

observan perovskitas bien formadas, aunque la deposición lenta da lugar a picos más estrechos que indican una mayor cristalinidad, lo que se correlaciona con la morfología (Figura 42 b,d). Ambas muestran bandas prohibidas similares de 1.88 y 1.89 eV, aunque la depositada lentamente muestra una absorción más intensa (Figura 39a). También se trató de sintetizar la perovskita implementando la mezcla de haluros mediante los compuestos plomados. Sin embargo, las láminas no eran estables en aire (Figura 43). Para concluir el estudio se realizó la sublimación mediante 4 fuentes. El difractograma de XRD mostró una perovskita pura, aunque sin orientación preferencial (Figura 44a). La morfología observada (Figura 44b), también fue homogénea, aunque presentaba algunos cuboides de 100 nm. Estos cuboides también se observaron en las muestras de precursores de haluro mixtos y 3 fuentes lenta, lo que parece indicar que estas estructuras se forman cuando se obtiene una mejor aleación de los haluros. Finalmente, la caída de su absorción indicó una banda prohibida de 1.92 eV (Figura 39b).

Como resumen, se obtuvieron láminas a temperatura ambiente formadas por perovskitas de alta calidad. Para comprobar su desempeño como recolectores fotovoltaicos, éstas se integraron en dispositivos empleando la estructura mostrada en la Figura 45a. Además, como se ha comentado previamente, también se estudiaron las mismas perovskitas empleando un tratamiento térmico sutil de 150ºC. El desempeño de los dispositivos obtenidos puede observarse en la Figura 46. Para una mayor comprensión de los parámetros de desempeño de los dispositivos estudiados se muestra la Figura 47, donde puede observarse claramente que la muestra sintetizada mediante dos fuentes sin precursores de haluro mixtos no funciona correctamente. Este tipo de deposición es la única que ha sido estudiada en la literatura existente y tan sólo da lugar a dispositivos eficientes tras tratamientos térmicos de más de 260ºC. La mejora de la aleación de haluros mediante el uso de precursores de haluro mixtos da lugar a un mejor desempeño de los dispositivos (Figura 45b) debido a una respuesta constante en todo el espectro (Figura 45c). Un funcionamiento similar se muestra en las células con el absorbedor de 3 fuentes, aunque el FF mejora con deposición lenta, dando lugar a eficiencias de 7.7%, en contraposición al 7.3% obtenido para la deposición rápida. Sin embargo, tras el tratamiento térmico se observa que el funcionamiento de la perovskita sintetizada rápidamente mejora, dando lugar a las eficiencias que superan el 10%. Finalmente, la perovskita sintetizada mediante 4 fuentes da lugar a eficiencias parecidas a las anteriormente descritas, aunque muestra un V_{OC} más

alto que sugiere una reducción de la recombinación no radiativa. Como conclusión de estos estudios, el uso de más fuentes o precursores de haluro mixtos da lugar a una mejor aleación de los haluros que lleva a perovskitas funcionales sin necesidad de tratamiento térmico.

Posteriormente, se estudió la estabilidad en iluminación (Figura 48a) y bajo estrés térmico (Figura 48b) de la perovskita con la mejor eficiencia, la denominada 3 fuentes rápida. Se observó un MPP estable durante una hora y una gran tolerancia al estrés térmico, manteniéndose la eficiencia en un 90% durante 10 días.

Finalmente, a pesar de obtenerse eficiencias prometedoras, éstas estaban lejos de las esperadas teóricamente, ya que para una banda prohibida de 1.9 eV se espera una eficiencia del 25%. Por tanto, se realizaron estudios de sEQE y fotoluminescencia empleando de nuevo la perovskita de 3 fuentes rápida (Figura 49). Del sEQE se estimó una banda prohibida de 1.870 eV y se extrajeron los parámetros máximos para esta banda prohibida, para realizar una comparativa. La Tabla 4 presenta los valores obtenidos para la comparación. De la comparativa de valores teóricos y obtenidos se extrae que los factores limitantes son el V_{OC} y el FF. En esta muestra, se observa un FF alto, aunque para el resto de la serie ésta sería la mayor limitación, indicando posibles barreras resistivas. La J_{SC} también sufre de estas barreras resistivas, aunque cabe indicar que no se estudió el espesor de la perovskita. Las altas pérdidas de V_{OC} son comunes en el caso de las perovskitas de banda prohibida ancha y se atribuyen a la segregación de fase fotoinducida o a la desalineación de los niveles de energía. En la Figura 49, se puede observar un pequeño componente extra a 1.7-1.78 eV, éste podría ser el responsable de la pérdida de voltaje. Para los estudios de PL, la existencia de este artefacto puede ser indicador de segregación de fase. Sin embargo, como vemos en la Figura 50, sólo está presente en algunas regiones de la superficie. Puesto que este artefacto presenta una caída de absorción más baja que la perovskita pura de iodo se pudo concluir que era debido a la mala alineación de los niveles de energía entre la perovskita y las capas de transporte.

Por otro lado, también se estudió la posibilidad de que el componente fuera generado por el C_{60}, ya que éste puede generar fotocorriente a esos niveles de energía. Para comprobarlo, se preparó una célula solar empleando SnO_2 como transportador de electrones y el componente no fue observado en la medida de

sEQE (Figura 51). De este modo, se concluye que se ha de realizar una investigación en las capas de transporte empleadas para esta perovskita en estudios futuros.

5.5. Conclusión

Se emplearon distintos métodos para sintetizar $CsPbI_2Br$ sin necesidad de tratamiento térmico. La sublimación mediante una fuente dio lugar a una mezcla de fases, mientras que el resto dieron lugar a perovskitas puras. La alta calidad de las perovskitas que empleaban precursores de haluro mixtos remarcó la importancia de una buena aleación de los haluros para la síntesis. Este efecto también se consiguió empleando un mayor número de fuentes o disminuyendo la velocidad de la sublimación. Finalmente, se obtuvieron eficiencias de 8.3% para las muestras sin tratamiento térmico, y de 10% para muestras con un tratamiento térmico de baja temperatura compatible con el uso de sustratos flexibles y otras perovskitas en tándems. La principal limitación en los dispositivos de este estudio son las capas de transporte, indicando que en el futuro deberían hacerse estudios concienzudos sobre este tema.

Capítulo 6: Conclusiones.

El objetivo de esta tesis era el desarrollo de perovskitas de banda prohibida estrecha y ancha mediante el método de la sublimación. La síntesis de tres materiales diferentes con las bandas prohibidas objetivo de 1.28, 1.34 y 1.9 eV ha sido cuidadosamente estudiada.

En el **capítulo 3**, un nuevo método para depositar perovskitas de aleación de estaño y plomo ha sido presentado. La formación y estabilidad de la perovskita $FAPb_{0.5}Sn_{0.5}I_3$ se mejoró mediante la supresión de la formación de Sn^{4+} gracias al uso del aditivo SnF_2. Las capas se integraron en células solares consiguiendo eficiencias cercanas a un 14%. Además, el estudio demostró la capacidad del método de la sublimación para sintetizar perovskitas de estaño y plomo funcionales en células solares. Sin embargo, las eficiencias no fueron fácilmente reproducibles debido a la dificultad de controlar la deposición de cantidades tan pequeñas de aditivo.

La cuestión de la reproducibilidad del método se abordó en el **capítulo 4**. En este trabajo se emplearon cationes más controlables durante la sublimación. Además, se introdujeron cantidades más altas de plomo en la estructura que dieron lugar a perovskitas más estables. $MA_{0.9}Cs_{0.1}Pb_{0.75}Sn_{0.25}I_3$ se sintetizó sin la necesidad de adicionar SnF_2. Un cuidadoso estudio acerca del espesor de la perovskita se llevó a cabo para optimizar las propiedades morfológicas, estructurales y ópticas. Por otro lado, las capas se integraron en dispositivos de tipo p-i-n dando lugar a eficiencias reproducibles de hasta un 8.9%. Los factores limitantes de los dispositivos se estudiaron mediante EIS y medidas en oscuridad para elucidar los estudios futuros a realizar para mejorar la eficiencia de estas perovskitas. Finalmente, el estudio concluyó que los procesos de recombinación se daban principalmente en el grueso de la perovskita debido a los granos más pequeños y la oxidación del Sn^{+2}.

Finalmente, una vez que se habían conseguido sintetizar perovskitas de banda prohibida estrecha mediante sublimación, en el **capítulo 5** se procedió a estudiar la formación de las perovskitas de banda prohibida ancha mediante el mismo método. Una perovskita inorgánica fue escogida para el estudio, debido a su banda prohibida compatible con la aplicación en tándems y a su excepcional estabilidad térmica. $CsPbI_2Br$ fue sintetizada mediante diversos métodos en estado

sólido y de sublimación para elucidar si su formación a temperatura ambiente y con tratamientos térmicos de baja temperatura podía ser llevada a término. Este estudio remarca la importancia del mezclado de haluros. Las perovskitas que emplearon precursores de haluro mixto preparados mediante fundición, un mayor número de fuentes o una velocidad baja de evaporación presentaron propiedades mejoradas. Además, todas las capas, excepto la preparada por sublimación instantánea debido a sus peores propiedades, fueron integradas en dispositivos fotovoltaicos. El estudio demostró, no solo la formación, si no la preparación de células solares tan eficientes como un 8.3% a temperatura ambiente. Además, se realizaron tratamientos térmicos moderados a 150ºC que mostraron eficiencias mejoradas hasta un 10%. Las limitaciones para la preparación de esta perovskita se investigaron y se concluyó que la principal fueron las capas de transporte, indicando que para futuros estudios este sería un punto por optimizar.

Bibliography

(1) Global Energy Consumption https://datos.enerdata.net/electricidad/datos-consumo-electricidad-hogar.html (accessed Dec 26, 2020).

(2) Agency, I. E. Solar Photovoltaic Energy, Technology Roadmap. 2014, p 107.

(3) International Technology Roadmap for Photovoltaics. 2018.

(4) Fritts, C. E. On a New Form of Selenium Cell, and Some Electrical Discoveries Made by Its Use. *Am. J. Sci.* **1883**, *s3-26* (156), 465–472. https://doi.org/10.2475/ajs.s3-26.156.465.

(5) Kojima, A.; Teshima, K.; Miyasaka, T.; Shirai, Y.; Miyasaka, T. Novel Photoelectrochemical Cell with Mesoscopic Electrodes Sensitized by Lead-Halide Compounds (2). In *210th ECS Meeting*; 2006. https://doi.org/10.1002/ibd.20004.

(6) Jeong, J.; Kim, M.; Seo, J.; Lu, H.; Ahlawat, P.; Mishra, A.; Yang, Y.; Hope, M. A.; Eickemeyer, F. T.; Kim, M.; et al. Pseudo-Halide Anion Engineering for α-FAPbI3 Perovskite Solar Cells. *Nature* **2021**, *592* (September 2020). https://doi.org/10.1038/s41586-021-03406-5.

(7) NREL Efficiency Chart https://www.nrel.gov/pv/cell-efficiency.html (accessed Dec 26, 2020).

(8) Gesetze, D.; Meinerung, V.-; Mensch, D.; Verdacht, G.-; Begriffe, B.; Haeci, E.; Betraehtungen, K.; Cephalopoden, D.; Mitteilung, V.; Auszug, N.; et al. Die Gesetze Der Krystallochemie. *Naturwissenschaften* **1926**.

(9) Saparov, B.; Mitzi, D. B. Organic − Inorganic Perovskites : Structural Versatility for Functional Materials Design. *Chem. Rev.* **2016**. https://doi.org/10.1021/acs.chemrev.5b00715.

(10) Li, Z.; Yang, M.; Park, J.; Wei, S.; Berry, J. J.; Zhu, K. Stabilizing Perovskite Structures by Tuning Tolerance Factor: Formation of Formamidinium and Cesium Lead Iodide Solid-State Alloys. *Chem. Mater.* **2016**, *2*. https://doi.org/10.1021/acs.chemmater.5b04107.

(11) Hutter, E. M.; Eperon, G. E.; Stranks, S. D.; Savenije, T. J. Charge Carriers in Planar and Meso-Structured Organic − Inorganic Perovskites: Mobilities, Lifetimes, and Concentrations of Trap States. *J. Phys. Chem. Lett.* **2015**. https://doi.org/10.1021/acs.jpclett.5b01361.

(12) Wehrenfennig, C.; Eperon, G. E.; Johnston, M. B.; Snaith, H. J.; Herz, L. M. High Charge Carrier Mobilities and Lifetimes in Organolead Trihalide Perovskites. *Adv. Mater.* **2014**, 1584–1589. https://doi.org/10.1002/adma.201305172.

(13) Ponseca, C. S.; Savenije, T. J.; Abdellah, M.; Zheng, K.; Yartsev, A.; Pascher, T.; Harlang, T.; Chabera, P.; Pullerits, T.; Stepanov, A.; et al. Organometal Halide Perovskite Solar Cell Materials Rationalized: Ultrafast Charge Generation, High and Microsecond-Long Balanced Mobilities, and Slow Recombination. *J. Am. Chem. Soc.* **2014**. https://doi.org/10.1021/ja412583t.

(14) Stranks, S. D.; Eperon, G. E.; Grancini, G.; Menelaou, C.; Alcocer, M. J. P.; Leijtens, T.; Herz, L. M.; Petrozza, A.; Snaith, H. J. Electron-Hole Diffusion Lengths Exceeding 1 Micrometer in an Organometal Trihalide Perovskite Absorber. *Science (80-.).* **2013**, *342* (October), 341–345.

(15) Xing, G.; Mathews, N.; Lim, S. S.; Lam, Y. M.; Mhaisalkar, S.; Sum, T. C. Long-Range Balanced Electron- and Hole-Transport Lengths in Organic-Inorganic CH 3 NH 3 PbI 3. *Science (80-.).* **2013**, *6960* (October), 498–500.

(16) Johnston, M. B.; Herz, L. M. Hybrid Perovskites for Photovoltaics: Charge-Carrier Recombination, Diffusion, and Radiative Efficiencies. *Acc. Chem. Res.* **2016**, *49* (1), 146–154. https://doi.org/10.1021/acs.accounts.5b00411.

(17) Park, N. Perovskite Solar Cells : An Emerging Photovoltaic Technology. *Mater. Today* **2015**, *18* (2), 65–72. https://doi.org/10.1016/j.mattod.2014.07.007.

(18) Jensen, N.; Hausner, R. M.; Bergmann, R. B.; Werner, J. H.; Rau, U. Optimization and Characterization of Amorphous/Crystalline Silicon Heterojunction Solar Cells. *Prog. Photovoltaics Res. Appl.* **2002**, *10* (1), 1–13. https://doi.org/10.1002/pip.398.

(19) Wood, D. L.; Tauc, J. Weak Absorption Tails in Amorphous Semiconductors. *Phys. Rev. B* **1972**, *5* (8).

(20) Eperon, G. E.; Leijtens, T.; Bush, K. A.; Prasanna, R.; Green, T.; Wang, J. T. W. J. C. J. J.; McMeekin, D. P.; Volonakis, G.; Milot, R. L.; May, R.; et al. Perovskite-Perovskite Tandem Photovoltaics with Optimized Band Gaps. *Science (80-.).* **2016**, *354* (6314), 861–865. https://doi.org/10.1126/science.aaf9717.

(21) Forgács, D.; Gil-Escrig, L.; Pérez-Del-Rey, D.; Momblona, C.; Werner, J.; Niesen, B.; Ballif, C.; Sessolo, M.; Bolink, H. J. Efficient Monolithic Perovskite/Perovskite Tandem Solar Cells. *Adv. Energy Mater.* **2017**, *7* (8), 1–6. https://doi.org/10.1002/aenm.201602121.

(22) Song, Z.; Chen, C.; Li, C.; Awni, R. A.; Zhao, D.; Yan, Y. Wide-Bandgap, Low-Bandgap, and Tandem Perovskite Solar Cells. *Semiconductor Science and Technology*. 2019, pp 1157–1160. https://doi.org/10.1088/1361-6641/ab27f7.

(23) McMeekin, D. P.; Mahesh, S.; Noel, N. K.; Klug, M. T.; Lim, J. C.; Warby, J. H.; Ball, J. M.; Herz, L. M.; Johnston, M. B.; Snaith, H. J. Solution-Processed All-Perovskite Multi-Junction Solar Cells. *Joule* **2019**, *3* (2), 387–401. https://doi.org/10.1016/j.joule.2019.01.007.

(24) Leijtens, T.; Bush, K. A.; Prasanna, R.; McGehee, M. D. Opportunities and Challenges for Tandem Solar Cells Using Metal Halide Perovskite Semiconductors. *Nat. Energy* **2018**, *3* (10), 828–838. https://doi.org/10.1038/s41560-018-0190-4.

(25) Lin, R.; Xiao, K.; Qin, Z.; Han, Q.; Zhang, C.; Wei, M.; Saidaminov, M. I.; Gao, Y.; Xu, J.; Xiao, M.; et al. Monolithic All-Perovskite Tandem Solar Cells with 24.8% Efficiency Exploiting Comproportionation to Suppress Sn(II) Oxidation in Precursor Ink. *Nat. Energy* **2019**, *4* (October). https://doi.org/10.1038/s41560-019-0466-3.

(26) Ierides, M.; Del Valle, R.; Fernandez, D.; Bax, L.; Jacques, P.; Stassin, F.; Meeus, M. Advanced Materials for Clean and Sustainable Energy and Mobility. *Emiri roadmap* **2019**.

(27) Jia, X.; Puthen-Veettil, B.; Xia, H.; Yang, T. C. J.; Lin, Z.; Zhang, T.; Wu, L.; Nomoto, K.; Conibeer, G.; Perez-Wurfl, I. All-Silicon Tandem Solar Cells: Practical Limits for Energy Conversion and Possible Routes for Improvement. *J. Appl. Phys.* **2016**, *119* (23). https://doi.org/10.1063/1.4954003.

(28) Leguy, A. M. A.; Azarhoosh, P.; Alonso, M. I.; Campoy-Quiles, M.; Weber, O. J.; Yao, J.; Bryant, D.; Weller, M. T.; Nelson, J.; Walsh, A.; et al. Experimental and Theoretical Optical Properties of Methylammonium Lead Halide Perovskites. *Nanoscale* **2016**, 6317–6327. https://doi.org/https://doi.org/10.1039/C5NR05435D.

(29) Liu, T.; Zhou, Y.; Li, Z.; Zhang, L.; Ju, M. G.; Luo, D.; Yang, Y.; Yang, M.; Kim, D. H.; Yang, W.; et al. Stable Formamidinium-Based Perovskite Solar Cells via In Situ Grain Encapsulation. *Adv. Energy Mater.* **2018**, *8* (22), 1800232. https://doi.org/10.1002/aenm.201800232.

(30) Eperon, G. E.; Stranks, S. D.; Menelaou, C.; Johnston, M. B.; Herz, L. M.; Snaith, H. J. Formamidinium Lead Trihalide: A Broadly Tunable Perovskite for Efficient Planar Heterojunction Solar Cells. *Energy Environ. Sci.* **2014**, *7* (3), 982–988. https://doi.org/10.1039/c3ee43822h.

(31) Rühle, S. Tabulated Values of the Shockley-Queisser Limit for Single Junction Solar Cells. *Sol. Energy* **2016**, *130*, 139–147. https://doi.org/10.1016/j.solener.2016.02.015.

(32) Im, J.; Stoumpos, C. C.; Jin, H.; Freeman, A. J.; Kanatzidis, M. G. Antagonism between Spin − Orbit Coupling and Steric E Ff Ects Causes Anomalous Band Gap Evolution in the Perovskite Photovoltaic Materials CH 3 NH 3 Sn 1 −. *J. Phys. Chem. Lett.* **2015**. https://doi.org/10.1021/acs.jpclett.5b01738.

(33) Kapil, G.; Ripolles, T. S.; Hamada, K.; Ogomi, Y.; Bessho, T.; Kinoshita, T.; Chantana, J.; Yoshino, K.; Shen, Q.; Toyoda, T.; et al. Highly Efficient 17.6% Tin-Lead Mixed Perovskite Solar Cells Realized through Spike Structure. *Nano Lett.* **2018**, *18* (6), 3600–3607. https://doi.org/10.1021/acs.nanolett.8b00701.

(34) Li, C.; Song, Z.; Zhao, D.; Xiao, C.; Subedi, B.; Shrestha, N.; Junda, M. M.; Wang, C.; Jiang, C. S.; Al-Jassim, M.; et al. Reducing Saturation-Current Density to Realize High-Efficiency Low-Bandgap Mixed Tin–Lead Halide Perovskite Solar Cells. *Adv. Energy Mater.* **2019**, *9* (3), 1–9. https://doi.org/10.1002/aenm.201803135.

(35) Zhao, B.; Abdi-Jalebi, M.; Tabachnyk, M.; Glass, H.; Kamboj, V. S.; Nie, W.; Pearson, A. J.; Puttisong, Y.; Gödel, K. C.; Beere, H. E.; et al. High Open-Circuit Voltages in Tin-Rich Low-Bandgap Perovskite-Based Planar Heterojunction Photovoltaics. *Adv. Mater.* **2017**, *29* (2), 1604744. https://doi.org/10.1002/adma.201604744.

(36) Hao, F.; Stoumpos, C. C.; Chang, R. P. H.; Kanatzidis, M. G. Anomalous Band Gap Behavior in Mixed Sn and Pb Perovskites Enables Broadening of Absorption Spectrum in Solar Cells. *J. Am. Chem. Soc.* **2014**, *136* (22), 8094–8099. https://doi.org/10.1021/ja5033259.

(37) Yang, Z.; Rajagopal, A.; Jen, A. K. Y. Ideal Bandgap Organic–Inorganic Hybrid Perovskite Solar Cells. *Adv. Mater.* **2017**, *29* (47), 1704418. https://doi.org/10.1002/adma.201704418.

(38) Wang, C.; Song, Z.; Li, C.; Zhao, D.; Yan, Y. Low-Bandgap Mixed Tin-Lead Perovskites and Their Applications in All-Perovskite Tandem Solar Cells. *Adv. Funct. Mater.* **2019**, *1808801*, 1–30. https://doi.org/10.1002/adfm.201808801.

(39) Zhao, D.; Yu, Y.; Wang, C.; Liao, W.; Shrestha, N.; Grice, C. R.; Cimaroli, A. J.; Guan, L.; Ellingson, R. J.; Zhu, K.; et al. Low-Bandgap Mixed Tin-Lead Iodide Perovskite Absorbers with Long Carrier Lifetimes for All-Perovskite Tandem Solar Cells. *Nat. Energy* **2017**, *2* (4), 17018. https://doi.org/10.1038/nenergy.2017.18.

(40) Ogomi, Y.; Morita, A.; Tsukamoto, S.; Saitho, T.; Fujikawa, N.; Shen, Q.; Toyoda, T.; Yoshino, K.; Pandey, S. S.; Hayase, S. CH3 NH3 Snx Pb(1-x) I3 Perovskite Solar Cells Covering up to 1060 Nm. *J. Phys. Chem. Lett.* **2014**, *5*, 1004–1011.

(41) Forgács, D.; Pérez-Del-Rey, D.; Ávila, J.; Momblona, C.; Gil-Escrig, L.; Dänekamp, B.; Sessolo, M.; Bolink, H. J. Efficient Wide Band Gap Double Cation-Double Halide Perovskite Solar Cells. *J. Mater. Chem. A* **2017**, *5* (7), 3203–3207. https://doi.org/10.1039/c6ta10727c.

(42) Kulkarni, S. A.; Baikie, T.; Boix, P. P.; Yantara, N.; Mathews, N.; Mhaisalkar, S. Band-Gap Tuning of Lead Halide Perovskites Using a Sequential Deposition Process. *J. Mater. Chem. A* **2014**, *2* (24), 9221–9225. https://doi.org/10.1039/c4ta00435c.

(43) Liang, J.; Zhao, P.; Wang, C.; Wang, Y.; Hu, Y.; Zhu, G.; Ma, L.; Liu, J.; Jin, Z. CsPb0.9Sn0.1IBr2 Based All-Inorganic Perovskite Solar Cells with Exceptional Efficiency and Stability. *J. Am. Chem. Soc.* **2017**, *139* (40), 14009–14012. https://doi.org/10.1021/jacs.7b07949.

(44) Wang, Y.; Zhang, T.; Kan, M.; Li, Y.; Wang, T.; Zhao, Y. Efficient α-CsPbI3 Photovoltaics with Surface Terminated Organic Cations. *Joule* **2018**, *2* (10), 2065–2075. https://doi.org/10.1016/j.joule.2018.06.013.

(45) Liu, C.; Li, W.; Li, H.; Wang, H.; Zhang, C.; Yang, Y.; Gao, X.; Xue, Q.; Yip, H. L.; Fan, J.; et al. Structurally Reconstructed CsPbI 2 Br Perovskite for Highly Stable and Square-Centimeter All-Inorganic Perovskite Solar Cells. *Adv. Energy Mater.* **2019**, *9* (7), 1803572. https://doi.org/10.1002/aenm.201803572.

(46) Beal, R. E.; Slotcavage, D. J.; Leijtens, T.; Bowring, A. R.; Belisle, R. A.; Nguyen, W. H.; Burkhard, G. F.; Hoke, E. T.; McGehee, M. D. Cesium Lead Halide Perovskites with Improved Stability for Tandem Solar Cells. *J. Phys. Chem. Lett.* **2016**, *7* (5), 746–751. https://doi.org/10.1021/acs.jpclett.6b00002.

(47) Rao, H.; Ye, S.; Gu, F.; Zhao, Z.; Liu, Z.; Bian, Z.; Huang, C. Morphology Controlling of All-Inorganic Perovskite at Low Temperature for Efficient Rigid and Flexible Solar Cells. *Adv. Energy Mater.* **2018**, *8* (23), 1–8. https://doi.org/10.1002/aenm.201800758.

(48) Sutton, R. J.; Eperon, G. E.; Miranda, L.; Parrott, E. S.; Kamino, B. A.; Patel, J. B.; Hörantner, M. T.; Johnston, M. B.; Haghighirad, A. A.; Moore, D. T.; et al. Bandgap-Tunable Cesium Lead Halide Perovskites with High Thermal Stability for Effi Cient Solar Cells. *Adv. Energy Mater.* **2016**, *6*, 1502458. https://doi.org/10.1002/aenm.201502458.

(49) Travis, W.; Glover, E. N. K.; Bronstein, H.; Scanlon, D. O.; Palgrave, R. G. On the Application of the Tolerance Factor to Inorganic and Hybrid Halide Perovskites: A Revised System. *Chem. Sci.* **2016**, *7* (7), 4548–4556. https://doi.org/10.1039/c5sc04845a.

(50) Bush, K. A.; Frohna, K.; Prasanna, R.; Beal, R. E.; Leijtens, T.; Swifter, S. A.; McGehee, M. D. Compositional Engineering for Efficient Wide Band Gap Perovskites with Improved Stability to Photoinduced Phase Segregation. *ACS Energy Lett.* **2018**, *3* (2), 428–435. https://doi.org/10.1021/acsenergylett.7b01255.

(51) Slotcavage, D. J.; Karunadasa, H. I.; McGehee, M. D. Light-Induced Phase Segregation in Halide-Perovskite Absorbers. *ACS Energy Lett.* **2016**, *1* (6), 1199–1205. https://doi.org/10.1021/acsenergylett.6b00495.

(52) Samu, G. F.; Janáky, C.; Kamat, P. V. A Victim of Halide Ion Segregation. How Light Soaking Affects Solar Cell Performance of Mixed Halide Lead Perovskites. *ACS Energy Lett.* **2017**, *2* (8), 1860–1861. https://doi.org/10.1021/acsenergylett.7b00589.

(53) Han, Y.; Zhao, H.; Duan, C.; Yang, S.; Yang, Z.; Liu, Z.; Liu, S. Controlled N-Doping in Air-Stable CsPbI2Br Perovskite Solar Cells with a Record Efficiency of 16.79%. *Adv. Funct. Mater.* **2020**, *1909972*, 1–8. https://doi.org/10.1002/adfm.201909972.

(54) Chen, C. Y.; Lin, H. Y.; Chiang, K. M.; Tsai, W. L.; Huang, Y. C.; Tsao, C. S.; Lin, H. W. All-Vacuum-Deposited Stoichiometrically Balanced Inorganic Cesium Lead Halide Perovskite Solar Cells with Stabilized Efficiency Exceeding 11%. *Adv. Mater.* **2017**, *29* (12), 1–7. https://doi.org/10.1002/adma.201605290.

(55) Yan, L.; Xue, Q.; Liu, M.; Zhu, Z.; Tian, J.; Li, Z.; Chen, Z.; Chen, Z.; Yan, H.; Yip, H. L.; et al. Interface Engineering for All-Inorganic CsPbI2Br Perovskite Solar Cells with Efficiency over 14%. *Adv. Mater.* **2018**, *30* (33), 1–7. https://doi.org/10.1002/adma.201802509.

(56) Zhang, Y.; Wu, C.; Wang, D.; Zhang, Z.; Qi, X.; Zhu, N.; Liu, G.; Li, X.; Hu, H.; Chen, Z.; et al. High Efficiency (16.37%) of Cesium Bromide—Passivated All-Inorganic CsPbI 2 Br Perovskite Solar Cells. *Sol. RRL* **2019**, *1900254*, 1900254. https://doi.org/10.1002/solr.201900254.

(57) Lin, H. Y.; Chen, C. Y.; Hsu, B. W.; Cheng, Y. L.; Tsai, W. L.; Huang, Y. C.; Tsao, C. S.; Lin, H. W. Efficient Cesium Lead Halide Perovskite Solar Cells through Alternative Thousand-Layer Rapid Deposition. *Adv. Funct. Mater.* **2019**, *29* (44), 1–7. https://doi.org/10.1002/adfm.201905163.

(58) Vaynzof, Y. The Future of Perovskite Photovoltaics — Thermal Evaporation or Solution Processing? *Adv. Energy Mater.* **2020**, *2003073*. https://doi.org/10.1002/aenm.202003073.

(59) Mcmeekin, D. P.; Wang, Z.; Rehman, W.; Pulvirenti, F.; Patel, J. B.; Noel, N. K.; Johnston, M. B.; Marder, S. R.; Herz, L. M.; Snaith, H. J. Crystallization Kinetics and Morphology Control of Formamidinium – Cesium Mixed-Cation Lead Mixed-Halide Perovskite via Tunability of the Colloidal Precursor Solution. *Adv. Mater.* **2017**. https://doi.org/10.1002/adma.201607039.

(60) Tang, Z.; Bessho, T.; Awai, F.; Kinoshita, T.; Maitani, M. M. Hysteresis-Free Perovskite Solar Cells Made of Potassium-Doped Organometal Halide Perovskite. *Sci. Rep.* **2017**, No. June, 1–7. https://doi.org/10.1038/s41598-017-12436-x.

(61) Xiang, W.; Wang, Z.; Kubicki, D. J.; Wang, X.; Tress, W.; Luo, J.; Zhang, J.; Hofstetter, A.; Zhang, L.; Emsley, L.; et al. Ba-Induced Phase Segregation and Band Gap Reduction in Mixed-Halide Inorganic Perovskite Solar Cells. *Nat. Commun.* **2019**, *10*, 4686. https://doi.org/10.1038/s41467-019-12678-5.

(62) Zhao, H.; Han, Y.; Xu, Z.; Duan, C.; Yang, S.; Yuan, S.; Yang, Z.; Liu, Z.; Liu, S. A Novel Anion Doping for Stable CsPbI2Br Perovskite Solar Cells with an Efficiency of 15.56% and an Open Circuit Voltage of 1.30 V. *Adv. Energy Mater.* **2019**, *9* (40), 1–11. https://doi.org/10.1002/aenm.201902279.

(63) Babaei, A.; Albero-Blanquer, L.; Igual-Muñoz, A. M.; Pérez-Del-Rey, D.; Sessolo, M.; Bolink, H. J.; Tadmouri, R. Hansen Theory Applied to the Identification of Nonhazardous Solvents for Hybrid Perovskite Thin-Films Processing. *Polyhedron* **2018**, *147*, 9–14. https://doi.org/10.1016/j.poly.2018.03.003.

(64) Liang, K.; Mitzi, D. B.; Prikas, M. T. Synthesis and Characterization of Organic - Inorganic Perovskite Thin Films Prepared Using a Versatile Two-Step Dipping Technique. *Chem. Mater.* **2013**, *4756* (8), 403–411. https://doi.org/10.1021/cm970568f.

(65) Xiao, L.; Xu, J.; Luan, J.; Zhang, B.; Yao, J.; Dai, S. Achieving Mixed Halide Perovskite via Halogen Exchange during Vapor-Assisted Solution Process for Ef Fi Cient and Stable Perovskite Solar Cells. *Org. Electron.* **2017**, *50*, 33–42. https://doi.org/10.1016/j.orgel.2017.07.020.

(66) Liu, C.; Fan, J.; Li, H.; Zhang, C.; Mai, Y. Highly Efficient Perovskite Solar Cells with Substantial Reduction of Lead Content. *Sci. Rep.* **2016**, *6*, 1–8. https://doi.org/10.1038/srep35705.

(67) Hu, Y.; Aygüler, M. F.; Petrus, M. L.; Bein, T.; Docampo, P. Impact of Rubidium and Cesium Cations on the Moisture Stability of Multiple-Cation Mixed-Halide Perovskites. *ACS Energy Lett.* **2017**, *2* (10), 2212–2218. https://doi.org/10.1021/acsenergylett.7b00731.

(68) Li, Y.; Duan, J.; Yuan, H.; Zhao, Y.; He, B.; Tang, Q. Lattice Modulation of Alkali Metal Cations Doped Cs 1− x R x PbBr 3 Halides for Inorganic Perovskite Solar Cells. *Sol. RRL* **2018**, *2* (10), 1800164. https://doi.org/10.1002/solr.201800164.

(69) Lee, S. J.; Shin, S. S.; Kim, Y. C.; Kim, D.; Ahn, T. K.; Noh, J. H.; Seo, J.; Seok, S. Il. Fabrication of Efficient Formamidinium Tin Iodide Perovskite Solar Cells through SnF 2 -Pyrazine Complex. *J. Am. Chem. Soc.* **2016**, *138* (12), 3974–3977. https://doi.org/10.1021/jacs.6b00142.

(70) Chen, W.; Chen, H.; Xu, G.; Xue, R.; Wang, S.; Li, Y.; Li, Y. Precise Control of Crystal Growth for Highly Efficient CsPbI 2 Br Perovskite Solar Cells. *Joule* **2019**, *3* (1), 191–204. https://doi.org/10.1016/j.joule.2018.10.011.

(71) Lee, W.; Lee, J.; Lee, H. D.; Kim, J.; Ahn, H.; Kim, Y.; Yoo, D.; Lee, J.; Lee, T. W.; Kang, K.; et al. Controllable Deposition of Organic Metal Halide Perovskite Films with Wafer - Scale Uniformity by Single Source Flash Evaporation. *Sci. Rep.* **2020**, 1–10. https://doi.org/10.1038/s41598-020-75764-5.

(72) Ajjouri, Y. El; Igual-muñoz, A. M.; Sessolo, M.; Palazon, F.; Bolink, H. J. Tunable Wide-Bandgap Monohalide Perovskites. *Adv. Opt. Mater.* **2020**, *2000423*, 1–5. https://doi.org/10.1002/adom.202000423.

(73) Longo, G.; Degen, M. J.; Sessolo, M.; Bolink, H. J. Perovskite Solar Cells Prepared by Flash Evaporation. *Chem. Commun.* **2015**, 7376–7378. https://doi.org/10.1039/c5cc01103e.

(74) Malinkiewicz, O.; Yella, A.; Lee, Y. H.; Mı, G.; Graetzel, M.; Nazeeruddin, M. K.; Bolink, H. J. Perovskite Solar Cells Employing Organic Charge-Transport Layers. *Nat. Photonics* **2014**, *8* (December 2013). https://doi.org/10.1038/nphoton.2013.341.

(75) Liu, M.; Johnston, M. B.; Snaith, H. J. Efficient Planar Heterojunction Perovskite Solar Cells by Vapour Deposition. *Nature* **2013**, *501* (7467), 395–398. https://doi.org/10.1038/nature12509.

(76) Pérez-Del-Rey, D.; Boix, P. P.; Sessolo, M.; Hadipour, A.; Bolink, H. J. Interfacial Modi Fi Cation for High-E Ffi Ciency Vapor-Phase-Deposited Perovskite Solar Cells Based on a Metal Oxide Bu Ff Er Layer. *J. Phys. Chem. Lett.* **2018**, 3–8. https://doi.org/10.1021/acs.jpclett.7b03361.

(77) Roß, M.; Gil-Escrig, L.; Al-Ashouri, A.; Tockhorn, P.; Jost, M.; Rech, B.; Albrecht, S. Co-Evaporated p - i - n Perovskite Solar Cells beyond 20% E Ffi Ciency: Impact of Substrate Temperature and Hole-Transport Layer ́. *ACS Appl. Mater. Interfaces* **2020**. https://doi.org/10.1021/acsami.0c10898.

(78) Ma, Q.; Huang, S.; Wen, X.; Green, M. A.; Ho-Baillie, A. W. Y. Hole Transport Layer Free Inorganic CsPbIBr2 Perovskite Solar Cell by Dual Source Thermal Evaporation. *Adv. Energy Mater.* **2016**, *6* (7), 2–6. https://doi.org/10.1002/aenm.201502202.

(79) Ball, J.; Buizza, L.; Sansom, H.; Farrar, M.; Klug, M.; Borchert, J.; Patel, J. B.; Herz, L. M.; Johnston, M. B.; Snaith, H. J. Dual-Source Co-Evaporation of Low-Bandgap FA1-XCsxSn1-YPbyI3 Perovskites for Photovoltaics. *ACS Energy Lett.* **2019**. https://doi.org/10.1021/acsenergylett.9b01855.

(80) Gueymard, C. A.; Myers, D.; Emery, K. Proposed Reference Irradiance Spectra for Solar Energy Systems Testing. *Sol. Energy* **2002**, *73* (6), 443–467.

(81) Snaith, H. J.; Abate, A.; Ball, J. M.; Eperon, G. E.; Leijtens, T.; Noel, N. K.; Stranks, S. D.; Wang, J. T.; Wojciechowski, K.; Zhang, W. Anomalous Hysteresis in Perovskite Solar Cells. *J. Phys. Chem. Lett.* **2014**, No. iii. https://doi.org/10.1021/jz500113x.

(82) Xiang, W.; Wang, Z.; Kubicki, D. J.; Tress, W.; Luo, J.; Prochowicz, D.; Akin, S.; Emsley, L.; Zhou, J.; Dietler, G.; et al. Europium-Doped CsPbI 2 Br for Stable and Highly Efficient Inorganic Perovskite Solar Cells. *Joule* **2019**, *3* (1), 205–214. https://doi.org/10.1016/j.joule.2018.10.008.

(83) Jeon, N. J.; Na, H.; Jung, E. H.; Yang, T. Y.; Lee, Y. G.; Kim, G.; Shin, H. W.; Il Seok, S.; Lee, J.; Seo, J. A Fluorene-Terminated Hole-Transporting Material for Highly Efficient and Stable Perovskite Solar Cells. *Nat. Energy* **2018**, *3* (8), 682–689. https://doi.org/10.1038/s41560-018-0200-6.

(84) Jiang, Q.; Zhao, Y.; Zhang, X.; Yang, X.; Chen, Y.; Chu, Z.; Ye, Q.; Li, X.; Yin, Z.; You, J. Surface Passivation of Perovskite Film for Efficient Solar Cells. *Nat. Photonics* **2019**, *13*, 460–466. https://doi.org/10.1038/s41566-019-0398-2.

(85) Shockley, W.; Queisser, H. J. Detailed Balance Limit of Efficiency of P-n Junction Solar Cells. *J. Appl. Phys.* **1961**, *32* (3), 510–519. https://doi.org/10.1063/1.1736034.

(86) Zhao, J.; Wei, L.; Jia, C.; Tang, H.; Su, X.; Ou, Y.; Liu, Z.; Wang, C.; Zhao, X.; Jin, H.; et al. Metallic Tin Substitution of Organic Lead Perovskite Films for Efficient Solar Cells. *J. Mater. Chem. A* **2018**, *6* (41), 20224–20232. https://doi.org/10.1039/c8ta05282d.

(87) Noel, N. K.; Stranks, S. D.; Abate, A.; Wehrenfennig, C.; Guarnera, S.; Haghighirad, A. A.; Sadhanala, A.; Eperon, G. E.; Pathak, S. K.; Johnston, M. B.; et al. Lead-Free Organic-Inorganic Tin Halide Perovskites for Photovoltaic Applications. *Energy Environ. Sci.* **2014**, *7* (9), 3061–3068. https://doi.org/10.1039/c4ee01076k.

(88) Liao, W.; Zhao, D.; Yu, Y.; Shrestha, N.; Ghimire, K.; Grice, C. R.; Wang, C.; Xiao, Y.; Cimaroli, A. J.; Ellingson, R. J.; et al. Fabrication of Efficient Low-Bandgap Perovskite Solar Cells by Combining Formamidinium Tin Iodide with Methylammonium Lead Iodide. *J. Am. Chem. Soc.* **2016**, *138* (38), 12360–12363. https://doi.org/10.1021/jacs.6b08337.

(89) Im, J.; Stoumpos, C. C.; Jin, H.; Freeman, A. J.; Kanatzidis, M. G. Antagonism between Spin-Orbit Coupling and Steric Effects Causes Anomalous Band Gap Evolution in the Perovskite Photovoltaic Materials CH<inf>3</Inf>NH<inf>3</Inf>Sn<inf>1-X</Inf>Pb<inf>x</Inf>I<inf>3</Inf>. *J. Phys. Chem. Lett.* **2015**, *6* (17), 3503–3509. https://doi.org/10.1021/acs.jpclett.5b01738.

(90) Koh, T. M.; Krishnamoorthy, T.; Yantara, N.; Shi, C.; Leong, W. L.; Boix, P. P.; Grimsdale, A. C.; Mhaisalkar, S. G.; Mathews, N. Formamidinium Tin-Based Perovskite with Low Eg for Photovoltaic Applications. *J. Mater. Chem. A* **2015**, *3* (29), 14996–15000. https://doi.org/10.1039/c5ta00190k.

(91) Zhao, D.; Chen, C.; Wang, C.; Junda, M. M.; Song, Z.; Grice, C. R.; Yu, Y.; Li, C.; Subedi, B.; Podraza, N. J.; et al. Efficient Two-Terminal All-Perovskite Tandem Solar Cells Enabled by High-Quality Low-Bandgap Absorber Layers. *Nat. Energy* **2018**, *3* (12), 1093–1100. https://doi.org/10.1038/s41560-018-0278-x.

(92) Gupta, S.; Cahen, D.; Hodes, G. How SnF2 Impacts the Material Properties of Lead-Free Tin Perovskites. *J. Phys. Chem. C* **2018**, *122* (25), 13926–13936. https://doi.org/10.1021/acs.jpcc.8b01045.

(93) Chung, I.; Lee, B.; He, J.; Chang, R. P. H.; Kanatzidis, M. G. All-Solid-State Dye-Sensitized Solar Cells with High Efficiency. *Nature* **2012**, *485* (7399), 486–489. https://doi.org/10.1038/nature11067.

(94) Kumar, M. H.; Dharani, S.; Leong, W. L.; Boix, P. P.; Prabhakar, R. R.; Baikie, T.; Shi, C.; Ding, H.; Ramesh, R.; Asta, M.; et al. Lead-Free Halide Perovskite Solar Cells with High Photocurrents Realized through Vacancy Modulation. *Adv. Mater.* **2014**, *26* (41), 7122–7127. https://doi.org/10.1002/adma.201401991.

(95) Wang, W.; Zhao, D.; Zhang, F.; Li, L.; Du, M.; Wang, C.; Yu, Y.; Huang, Q.; Zhang, M.; Li, L.; et al. Highly Sensitive Low-Bandgap Perovskite Photodetectors with Response from Ultraviolet to the Near-Infrared Region. *Adv. Funct. Mater.* **2017**, *27* (42), 1703953. https://doi.org/10.1002/adfm.201703953.

(96) Ramirez, D.; Schutt, K.; Wang, Z.; Pearson, A. J.; Ruggeri, E.; Snaith, H. J.; Stranks, S. D.; Jaramillo, F. Layered Mixed Tin-Lead Hybrid Perovskite Solar Cells with High Stability. *ACS Energy Lett.* **2018**, *3* (9), 2246–2251. https://doi.org/10.1021/acsenergylett.8b01411.

(97) Redinger, A.; Siebentritt, S.; Tauc, J.; Grigorovici, R.; Vancu, A. Optical Properties and Electronic Structure of Amorphous Germanium. *Phys. Status Solidi* **1966**, *15* (2), 627–637. https://doi.org/10.1002/pssb.19660150224.

(98) Momblona, C.; Gil-Escrig, L.; Bandiello, E.; Hutter, E. M.; Sessolo, M.; Lederer, K.; Blochwitz-Nimoth, J.; Bolink, H. J. Efficient Vacuum Deposited P-i-n and n-i-p Perovskite Solar Cells Employing Doped Charge Transport Layers. *Energy Environ. Sci.* **2016**, *9* (11), 3456–3463. https://doi.org/10.1039/c6ee02100j.

(99) Chen, B.; Zheng, X.; Bai, Y.; Padture, N. P.; Huang, J. Progress in Tandem Solar Cells Based on Hybrid Organic–Inorganic Perovskites. *Adv. Energy Mater.* **2017**, *7* (14), 1602400. https://doi.org/10.1002/aenm.201602400.

(100) Ávila, J.; Momblona, C.; Boix, P. P.; Sessolo, M.; Bolink, H. J. Vapor-Deposited Perovskites: The Route to High-Performance Solar Cell Production? *Joule* **2017**, *1* (3), 431–442. https://doi.org/10.1016/j.joule.2017.07.014.

(101) Ávila, J.; Momblona, C.; Boix, P.; Sessolo, M.; Anaya, M.; Lozano, G.; Vandewal, K.; Míguez, H.; Bolink, H. J. High Voltage Vacuum-Deposited $CH_3NH_3PbI_3$–$CH_3NH_3PbI_3$ Tandem Solar Cells. *Energy Environ. Sci.* **2018**, *11* (11), 3292–3297. https://doi.org/10.1039/C8EE01936C.

(102) Liu, X.; Yang, Z.; Chueh, C. C.; Rajagopal, A.; Williams, S. T.; Sun, Y.; Jen, A. K. Y. Improved Efficiency and Stability of Pb-Sn Binary Perovskite Solar Cells by Cs Substitution. *J. Mater. Chem. A* **2016**, *4* (46), 17939–17945. https://doi.org/10.1039/c6ta07712a.

(103) Zhu, Z.; Li, N.; Zhao, D.; Wang, L.; Jen, A. K. Y. Improved Efficiency and Stability of Pb/Sn Binary Perovskite Solar Cells Fabricated by Galvanic Displacement Reaction. *Adv. Energy Mater.* **2019**, *9* (7), 2–9. https://doi.org/10.1002/aenm.201802774.

(104) Niu, G.; Li, W.; Li, J.; Liang, X.; Wang, L. Enhancement of Thermal Stability for Perovskite Solar Cells through Cesium Doping. *RSC Adv.* **2017**, *7* (28), 17473–17479. https://doi.org/10.1039/c6ra28501e.

(105) Li, R.; Yi, C.; Ge, R.; Zou, W.; Cheng, L.; Wang, N.; Wang, J.; Huang, W. Room-Temperature Electroluminescence from Two-Dimensional Lead Halide Perovskites. *Appl. Phys. Lett.* **2016**, *109* (15). https://doi.org/10.1063/1.4964413.

(106) Dänekamp, B.; Droseros, N.; Palazon, F.; Sessolo, M.; Banerji, N.; Bolink, H. J. Efficient Photo- and Electroluminescence by Trap States Passivation in Vacuum-Deposited Hybrid Perovskite Thin Films. *ACS Appl. Mater. Interfaces* **2018**, *10* (42), 36187–36193. https://doi.org/10.1021/acsami.8b13100.

(107) Song, Z.; Watthage, S. C.; Phillips, A. B.; Tompkins, B. L.; Ellingson, R. J.; Heben, M. J. Impact of Processing Temperature and Composition on the Formation of Methylammonium Lead Iodide Perovskites. *Chem. Mater.* **2015**, *27* (13), 4612–4619. https://doi.org/10.1021/acs.chemmater.5b01017.

(108) Aonuma, M.; Oyamada, T.; Sasabe, H.; Miki, T.; Adachi, C. Material Design of Hole Transport Materials Capable of Thick-Film Formation in Organic Light Emitting Diodes. *Appl. Phys. Lett.* **2007**, *90* (18), 1–4. https://doi.org/10.1063/1.2733627.

(109) Wang, K.; Liu, C.; Du, P.; Chen, L.; Zhu, J.; Karim, A.; Gong, X. Efficiencies of Perovskite Hybrid Solar Cells Influenced by Film Thickness and Morphology of CH 3 NH 3 PbI 3-x Cl x Layer. *Org. Electron. physics, Mater. Appl.* **2015**, *21*, 19–26. https://doi.org/10.1016/j.orgel.2015.02.023.

(110) Contreras-Bernal, L.; Ramos-Terrón, S.; Riquelme, A.; Boix, P. P.; Idígoras, J.; Mora-Seró, I.; Anta, J. A. Impedance Analysis of Perovskite Solar Cells: A Case Study. *J. Mater. Chem. A* **2019**, *7* (19), 12191–12200. https://doi.org/10.1039/c9ta02808k.

(111) Zarazua, I.; Han, G.; Boix, P. P.; Mhaisalkar, S.; Fabregat-Santiago, F.; Mora-Seró, I.; Bisquert, J.; Garcia-Belmonte, G. Surface Recombination and Collection Efficiency in Perovskite Solar Cells from Impedance Analysis. *J. Phys. Chem. Lett.* **2016**, *7* (24), 5105–5113. https://doi.org/10.1021/acs.jpclett.6b02193.

(112) Yoo, S.-M.; Yoon, S. J.; Anta, J. A.; Lee, H. J.; Boix, P. P.; Mora-Seró, I. An Equivalent Circuit for Perovskite Solar Cell Bridging Sensitized to Thin Film Architectures. *Joule* **2019**, 1–15. https://doi.org/10.1016/j.joule.2019.07.014.

(113) Liu, D.; Gangishetty, M. K.; Kelly, T. L. Effect of $CH_3NH_3PbI_3$ Thickness on Device Efficiency in Planar Heterojunction Perovskite Solar Cells. *J. Mater. Chem. A* **2014**, *2* (46), 19873–19881. https://doi.org/10.1039/C4TA02637C.

(114) Tress, W.; Yavari, M.; Domanski, K.; Yadav, P.; Niesen, B.; Correa Baena, J. P.; Hagfeldt, A.; Graetzel, M. Interpretation and Evolution of Open-Circuit Voltage, Recombination, Ideality Factor and Subgap Defect States during Reversible Light-Soaking and Irreversible Degradation of Perovskite Solar Cells. *Energy Environ. Sci.* **2018**, *11* (1), 151–165. https://doi.org/10.1039/c7ee02415k.

(115) Yang, W. S.; Park, B. W.; Jung, E. H.; Jeon, N. J.; Kim, Y. C.; Lee, D. U.; Shin, S. S.; Seo, J.; Kim, E. K.; Noh, J. H.; et al. Iodide Management in Formamidinium-Lead-Halide-Based Perovskite Layers for Efficient Solar Cells. *Science (80-.).* **2017**, *356* (6345), 1376–1379. https://doi.org/10.1126/science.aan2301.

(116) Jeon, N. J.; Noh, J. H.; Yang, W. S.; Kim, Y. C.; Ryu, S.; Seo, J.; Seok, S. Il. Compositional Engineering of Perovskite Materials for High-Performance Solar Cells. *Nature* **2015**, *517* (7535), 476–480. https://doi.org/10.1038/nature14133.

(117) Saliba, M.; Matsui, T.; Seo, J. Y.; Domanski, K.; Correa-Baena, J. P.; Nazeeruddin, M. K.; Zakeeruddin, S. M.; Tress, W.; Abate, A.; Hagfeldt, A.; et al. Cesium-Containing Triple Cation Perovskite Solar Cells: Improved Stability, Reproducibility and High Efficiency. *Energy Environ. Sci.* **2016**, *9* (6), 1989–1997. https://doi.org/10.1039/c5ee03874j.

(118) Tan, H.; Jain, A.; Voznyy, O.; Lan, X.; De Arquer, F. P. G.; Fan, J. Z.; Quintero-Bermudez, R.; Yuan, M.; Zhang, B.; Zhao, Y.; et al. Efficient and Stable Solution-Processed Planar Perovskite Solar Cells via Contact Passivation. *Science (80-.).* **2017**, *355* (6326), 722–726. https://doi.org/10.1126/science.aai9081.

(119) Turren-Cruz, S. H.; Hagfeldt, A.; Saliba, M. Methylammonium-Free, High-Performance, and Stable Perovskite Solar Cells on a Planar Architecture. *Science (80-.).* **2018**, *362* (6413), 449–453. https://doi.org/10.1126/science.aat3583.

(120) Wang, Y.; Dar, M. I.; Ono, L. K.; Zhang, T.; Kan, M.; Li, Y.; Zhang, L.; Wang, X.; Yang, Y.; Gao, X.; et al. Thermodynamically Stabilized β-CsPbI 3 –Based Perovskite Solar Cells with Efficiencies >18% . *Science (80-.).* **2019**, *365* (6453), 591–595. https://doi.org/10.1126/science.aav8680.

(121) Zheng, Y.; Yang, X.; Su, R.; Wu, P.; Gong, Q.; Zhu, R. High-Performance CsPbIxBr3-x All-Inorganic Perovskite Solar Cells with Efficiency over 18% via Spontaneous Interfacial Manipulation. *Adv. Funct. Mater.* **2020**, *2000457*, 1–9. https://doi.org/10.1002/adfm.202000457.

(122) Eperon, G. E.; Paternò, G. M.; Sutton, R. J.; Zampetti, A.; Haghighirad, A. A.; Cacialli, F.; Snaith, H. J. Inorganic Caesium Lead Iodide Perovskite Solar Cells. *J. Mater. Chem. A* **2015**, *3* (39), 19688–19695. https://doi.org/10.1039/c5ta06398a.

(123) Dastidar, S.; Hawley, C. J.; Dillon, A. D.; Gutierrez-Perez, A. D.; Spanier, J. E.; Fafarman, A. T. Quantitative Phase-Change Thermodynamics and Metastability of Perovskite-Phase Cesium Lead Iodide. *J. Phys. Chem. Lett.* **2017**, *8* (6), 1278–1282. https://doi.org/10.1021/acs.jpclett.7b00134.

(124) Wang, P.; Zhang, X.; Zhou, Y.; Jiang, Q.; Ye, Q.; Chu, Z.; Li, X.; Yang, X.; Yin, Z.; You, J. Solvent-Controlled Growth of Inorganic Perovskite Films in Dry Environment for Efficient and Stable Solar Cells. *Nat. Commun.* **2018**, *9* (1), 1–7. https://doi.org/10.1038/s41467-018-04636-4.

(125) Tao, S.; Schmidt, I.; Brocks, G.; Jiang, J.; Tranca, I.; Meerholz, K.; Olthof, S. Absolute Energy Level Positions in Tin- and Lead-Based Halide Perovskites. *Nat. Commun.* **2019**, *10* (1), 1–10. https://doi.org/10.1038/s41467-019-10468-7.

(126) Yang, D.; Yang, R.; Priya, S.; Liu, S. (Frank). Recent Advances in Flexible Perovskite Solar Cells: Fabrication and Applications. *Angew. Chemie - Int. Ed.* **2019**, *58* (14), 4466–4483. https://doi.org/10.1002/anie.201809781.

(127) Palazon, F.; El Ajjouri, Y.; Bolink, H. J. Making by Grinding: Mechanochemistry Boosts the Development of Halide Perovskites and Other Multinary Metal Halides. *Adv. Energy Mater.* **2020**, *10* (13), 1–13. https://doi.org/10.1002/aenm.201902499.

(128) El Ajjouri, Y.; Palazon, F.; Sessolo, M.; Bolink, H. J. Single-Source Vacuum Deposition of Mechanosynthesized Inorganic Halide Perovskites. *Chem. Mater.* **2018**, *30* (21), 7423–7427. https://doi.org/10.1021/acs.chemmater.8b03352.

(129) Karmakar, A.; Dodd, M. S.; Zhang, X.; Oakley, M. S.; Klobukowski, M.; Michaelis, V. K. Mechanochemical Synthesis of 0D and 3D Cesium Lead Mixed Halide Perovskites. *Chem. Commun.* **2019**, *55* (35), 5079–5082. https://doi.org/10.1039/c8cc09622h.

(130) Liu, Z.; Bekenstein, Y.; Ye, X.; Nguyen, S. C.; Swabeck, J.; Zhang, D.; Lee, S. T.; Yang, P.; Ma, W.; Alivisatos, A. P. Ligand Mediated Transformation of Cesium Lead Bromide Perovskite Nanocrystals to Lead Depleted Cs4PbBr6 Nanocrystals. *J. Am. Chem. Soc.* **2017**, *139* (15), 5309–5312. https://doi.org/10.1021/jacs.7b01409.

(131) Palazon, F.; Urso, C.; De Trizio, L.; Akkerman, Q.; Marras, S.; Locardi, F.; Nelli, I.; Ferretti, M.; Prato, M.; Manna, L. Postsynthesis Transformation of Insulating Cs4PbBr6 Nanocrystals into Bright Perovskite CsPbBr3 through Physical and Chemical Extraction of CsBr. *ACS Energy Lett.* **2017**, *2* (10), 2445–2448. https://doi.org/10.1021/acsenergylett.7b00842.

(132) Palazon, F.; Almeida, G.; Akkerman, Q. A.; De Trizio, L.; Dang, Z.; Prato, M.; Manna, L. Changing the Dimensionality of Cesium Lead Bromide Nanocrystals by Reversible Postsynthesis Transformations with Amines. *Chem. Mater.* **2017**, *29* (10), 4167–4171. https://doi.org/10.1021/acs.chemmater.7b00895.

(133) Rumble, J.; Ed, R. *CRC Handbook of Chemistry and Physics*, 100 th.; Ltd., T. & F., Ed.; CRC Press: London, 2020.

(134) Burwig, T.; Fränzel, W.; Pistor, P. Crystal Phases and Thermal Stability of Co-Evaporated CsPbX3 (X = I, Br) Thin Films. *J. Phys. Chem. Lett.* **2018**, *9* (16), 4808–4813. https://doi.org/10.1021/acs.jpclett.8b02059.

(135) Pistor, P.; Burwig, T.; Brzuska, C.; Weber, B.; Fränzel, W. Thermal Stability and Miscibility of Co-Evaporated Methyl Ammonium Lead Halide (MAPbX3, X ¼ I, Br, Cl) Thin Films Analysed by in Situ X-Ray Diffraction. *J. Mater. Chem. A* **2018**, 11496–11506. https://doi.org/10.1039/c8ta02775g.

(136) Rau, U.; Blank, B.; Müller, T. C. M.; Kirchartz, T. Efficiency Potential of Photovoltaic Materials and Devices Unveiled by Detailed-Balance Analysis. *Phys. Rev. Appl.* **2017**, *7* (4), 1–9. https://doi.org/10.1103/PhysRevApplied.7.044016.

(137) Tvingstedt, K.; Malinkiewicz, O.; Baumann, A.; Deibel, C.; Snaith, H. J.; Dyakonov, V.; Bolink, H. J. Radiative Efficiency of Lead Iodide Based Perovskite Solar Cells. *Sci. Rep.* **2014**, *4*, 1–7. https://doi.org/10.1038/srep06071.

(138) Jaysankar, M.; Raul, B. A. L.; Bastos, J.; Burgess, C.; Weijtens, C.; Creatore, M.; Aernouts, T.; Kuang, Y.; Gehlhaar, R.; Hadipour, A.; et al. Minimizing Voltage Loss in Wide-Bandgap Perovskites for Tandem Solar Cells. *ACS Energy Lett.* **2019**, *4* (1), 259–264. https://doi.org/10.1021/acsenergylett.8b02179.

(139) Burkhard, G. F.; Hoke, E. T.; Beiley, Z. M.; Mcgehee, M. D. Free Carrier Generation in Fullerene Acceptors and Its Effect on Polymer Photovoltaics. *J. Phys. Chem. C* **2012**, *116*, 26674–26678. https://doi.org/10.1021/jp310821f.

Index of Figures

Index of Tables

Abbreviations

PV	Photovoltaic technology
GaAs	Gallium arsenide
CdTe	Cadmium telluride
CIGS	Copper indium gallium selenide / sulfide
E_g	Bandgap
MA	Methylammonium
FA	Formamidinium
$FAPbI_3$	Formamidinium lead iodide
V_{OC}	Open circuit voltage
EMIRI	Energy Materials Industrial Research Initiative
$MAPbI_3$	Methylammonium lead iodide
$CsPbI_3$	Cesium lead iodide
$FA_{1-x}Cs_xPbI_3$	Formamidinium cesium lead iodide
Narrow-E_g	Narrow bandgap
Wide-E_g	Wide bandgap
$MASnI_3$	Methylammonium tin iodide
$MAPb_xSn_{1-x}I_3$	Methylammonium lead tin iodide

$MAPbBr_3$	Methylammonium lead bromide
$CsPbI_xBr_{1-x}$	Cesium lead iodide bromide
$PbBr_2$	Lead bromide
CsI	Cesium iodide
CsBr	Cesium bromide
ETM	Electron transporting material
SnO_2	Tin oxide
ZnO	Zinc oxide
PCE	Power conversion efficiency
HTM	Hole transporting material
$Pb(Ac)_2$	Lead acetate
PSC	Perovskite solar cell
$CaCl_2$	Calcium chloride
PbI_2	Lead iodide
$FA_{1-x}Cs_xPb(I_{1-x}Br_x)_3$.	Formamidinium cesium lead iodide bromide
QCM	Quartz crystal microbalance
EQE	External Quantum Efficiency
IPCE	Incident photon-to-electron conversion efficiency
J-V curve	Current-voltage curve
J_{SC}	Short-circuit current density
FF	Fill factor

ITO	Indium tin oxide
MoO_3	Molibdenum oxide
m-MTDATA	4,4',4"-tris[(3-methylphenyl)phenylamino] triphenylamine
TaTm	N4,N4,N4",N4"-tetra([1,1'-biphenyl]-4-yl)-[1,1':4',1"-terphenyl]-4,4"-diamine
BCP	Bathocuproine
PTAA	Poly(triaryl amine)
$FAPb_{1-x}Sn_xI_3$	Formamidinium lead tin iodide
FAI	Formamidinium iodide
SnI_2	Tin iodide
SnF_2	Tin fluoride
$MA_{1-x}Cs_xPb_{1-x}SnI_3$	Methylammonium cesium lead tin iodide
MAI	Methylammonium iodide
TF	Tooling factor
SEM	Scanning electron microscope
AFM	Atomic force microscope
EDAX	Energy dispersive X-Rays analysis
XRD	X-Ray diffraction
PL	Photoluminescence
sEQE	Sensitive external quantum efficiency
EIS	Electrochemical impedance spectroscopy

PCBM	Phenyl-C_{60}-butyric acid methyl ester
IPH	Indene-C_{60}-acid hexyl ester
HOMO	Highest occupied molecular orbital
RT	Room temperature

List of Publications

Prior to Ph.D.

Culebras, M.; Igual-Muñoz, A. M.; Rodríguez-Fernández, C.; Gómez-Gómez, M. I.; Gómez, C.; Cantarero, A. "Manufacturing Te / PEDOT Films for Thermoelectric Applications." *ACS Appl. Mater. Interfaces* **2017**, *9*, 20826–20832.

Included in the doctoral thesis

Igual-Muñoz, A. M.; Ávila, J.; Boix, P. P.; Bolink, H. J. "$FAPb_{0.5}Sn_{0.5}I_3$: A Narrow Bandgap Perovskite Synthesized through Evaporation Methods for Solar Cell Applications." *Sol. RRL* **2019**, *1900283*, 1–5.

Igual-Muñoz, A. M.; Castillo, A.; Dreessen, C.; Boix, P. P.; Bolink, H. J. "Vacuum-Deposited Multication Tin-Lead Perovskite Solar Cells." *ACS Appl. Energy Mater.* **2020**, *3*, 2755–2761.

Igual-Muñoz, A. M.; Navarro-alapont, J.; Dreessen, C.; Palazon, F.; Sessolo, M.; Bolink, H. J. "Room-Temperature Vacuum Deposition of $CsPbI_2Br$ Perovskite Films from Multiple Sources and Mixed Halide Precursors." *Chem. Mater.* **2020**, *32*, 8641–8652.

Other publications

Babaei, A.; Albero-Blanquer, L.; Igual-Muñoz, A. M.; Pérez-Del-Rey, D.; Sessolo, M.; Bolink, H. J.; Tadmouri, R. "Hansen Theory Applied to the Identification of Nonhazardous Solvents for Hybrid Perovskite Thin-Films Processing." *Polyhedron* **2018**, *147*, 9–14.

La-Placa, M.-G.; Igual-Muñoz, A. M.; Romero, J.; Daniels, R. E.; Kozhevnikov, V. N.; Sessolo, M.; Bolink, H. J. "Red Light-Emitting Electrochemical Cells Employing Pyridazine-Bridged Cationic Diiridium Complexes." *ECS J. Solid State Sci. Technol.* **2019**, *8* (6), R84–R87.

Sicilia, V.; Arnal, L.; Chueca, A. J.; Fuertes, S.; Babaei, A.; Igual-Muñoz, A. M.; Sessolo, M.; Bolink, H. J. "Highly Photoluminescent Blue Ionic Platinum-Based Emitters." *Inorg. Chem.* **2019**, *59* (2), 1145–1152.

Ajjouri, Y.; Igual-Muñoz, A. M.; Sessolo, M.; Palazon, F.; Bolink, H. J. "Tunable Wide-Bandgap Monohalide Perovskites." *Adv. Opt. Mater.* **2020**, *2000423*, 1–5. *Y.E.A and A.M.I.M contributed equally to this work.

Pérez-del-Rey, D.; Dreessen, C.; Igual-Muñoz, A. M.; van den Hengel, L.; Gélvez-Rueda, M. C.; Savenije, T. J.; Grozema, F. C.; Zimmermann, C.; Bolink, H. J. "Perovskite Solar Cells: Stable under Space Conditions." *Sol. RRL* **2020**, *4*, 1–6.

Appendix A

$FAPb_{0.5}Sn_{0.5}I_3$, A Narrow Bandgap Perovskite Synthesized through Evaporation Methods for Solar Cell Applications.

Solar RRL
www.solar-rrl.com

$FAPb_{0.5}Sn_{0.5}I_3$: A Narrow Bandgap Perovskite Synthesized through Evaporation Methods for Solar Cell Applications

Ana M. Igual-Muñoz, Jorge Ávila, Pablo P. Boix, and Henk J. Bolink**

The tunability of the optoelectrical properties upon compositional modification is a key characteristic of metal halide perovskites. In particular, bandgaps narrower than those in conventional lead-based perovskites are essential to achieve the theoretical efficiency limit of single-absorber solar cells, as well as develop multijunction tandem devices. Herein, the solvent-free vacuum deposition of a narrow bandgap perovskite based on tin–lead metal and formamidinium cation is reported. Pinhole-free films with 1.28 eV bandgap are obtained by thermal codeposition of precursors. The optoelectrical quality of these films is demonstrated by their use in solar cells with a power conversion efficiency of 13.98%.

Halide perovskite-based optoelectronics have become a topic of intense research during the last decade. The excellent properties of this family of materials, such as high optical absorption coefficients and long charge diffusion lengths,[1] are particularly interesting for photovoltaic applications and have attracted the attention of the research community. As a result, their photovoltaic conversion efficiency has increased from 3.8% in 2009 to 24.2% in 2019.[2–5] The unprecedented evolution of perovskite solar cells' photovoltaic efficiency is currently approaching the theoretical Shockley–Queisser limit, and further efficiency enhancements require a careful analysis of the losses. In that context, achieving perovskite light harvesters with a bandgap close to the optimal one (≈1.34 eV) would constitute a promising approach to reduce the losses of single-absorber devices.[6–8]

On the other hand, multijunction solar cells are an alternative strategy to exceed the Shockley–Queisser limit. Multijunction solar cells use two or more absorbers to maximize the harvesting of the solar spectrum yet minimize thermalization losses. These kinds of devices can deliver a superior power per area compared with standard single-junction devices, but the use of absorbers with complementary bandgaps is needed to maximize the maximum efficiency. Therefore, perovskites with a narrower bandgap than the widely extended $CH_3NH_3PbI_3$ (1.55–1.6 eV) and derivatives are needed to use the full potential of multijunction solar cells.[9,10]

A. M. Igual-Muñoz, J. Ávila, Dr. P. P. Boix, Prof. H. J. Bolink
Instituto de Ciencia Molecular
Universidad de Valencia
C/J. Beltran 2, Paterna, 46980 Valencia, Spain
E-mail: Pablo.P.Boix@uv.es; henk.bolink@uv.es

The ORCID identification number(s) for the author(s) of this article can be found under https://doi.org/10.1002/solr.201900283.

DOI: 10.1002/solr.201900283

One of the advantages of halide perovskite semiconductors is the compositional tunability of their optoelectrical properties.[11] Complete or partial substitution of lead (Pb) by tin (Sn) in these kinds of perovskites leads to a reduction of the bandgap.[12,13] While replacing Pb with Sn is demonstrated to decrease the bandgap down to 1.1 eV,[14–16] the industrial-scale synthesis and further commercialization of these perovskites have obstacles, due to the easy oxidation of Sn^{2+} and further doping of the perovskites by Sn^{4+}.[17] In recent studies, it has been reported how perovskites based on tin–lead mixtures can enhance the stability of this species, while it allows to tune the bandgap to suitable values for their use as a narrow-bandgap absorber in perovskite–perovskite multijunction solar cells.[18] Moreover, the introduction of the formamidinium ($CH_5N_2^+$, FA^+) cation into perovskite composition can further reduce the absorption bandgap[19] while improving the thermal stability of the material.[20] Successive optimization of these tin–lead alloyed perovskites has resulted in power conversion efficiencies up to 19.03%.[21,22]

In this work, we study the partial replacement of Pb^{+2} by Sn^{+2} in a $FAPbI_3$ perovskite fabricated by simultaneous thermal vacuum deposition of the precursors. This fabrication technique is solvent free and intrinsically additive,[23] which results in a reduction of the toxicity in the production chain and has the potential to be directly applied to the fabrication of complex multilayer stacks required in the multijunction solar cell design.[24] We developed a method to fabricate vacuum-deposited $FAPb_{0.5}Sn_{0.5}I_3$ and present the optical, morphological, and structural characterization of the resulting films. The targeted composition, 50% Sn 50% Pb, leads to a bandgap of 1.28 eV, similar to what has been previously reported for perovskites prepared using the same starting materials and ratios by solution methods of 1.23 eV.[18] These bandgaps are suitable for use in a tandem solar cell with a corresponding wider bandgap sub-cell.[25,26] The films were implemented in solar cells reaching a maximum efficiency close to 14%, demonstrating the potential of these films and preparation method.

$FAPb_{0.5}Sn_{0.5}I_3$ films were fabricated by simultaneous thermal vacuum deposition of FAI, SnI_2, and PbI_2 precursors in a N_2-filled glovebox. A fourth thermal source was used to codeposit SnF_2 as an additive. The fate of each evaporation source was monitored by an individual microbalance crystal sensor during the sublimation. A scheme of the evaporation chamber is shown in **Figure 1**.

An independent calibration of each sensor source was carried out prior to the synthesis of the perovskite to establish the proper

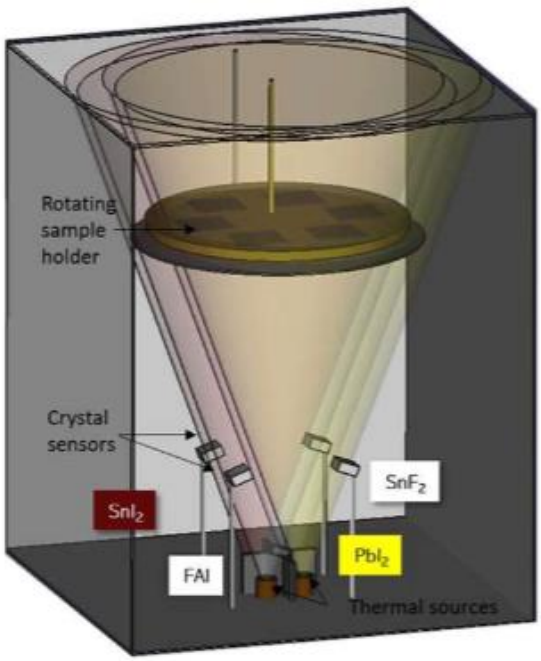

Figure 1. Scheme of the evaporator during the perovskite evaporation including the position for the materials and the relevant components of the evaporator.

deposition conditions of the precursors. This calibration was done by depositing a thick (50–100 nm) film of each precursor on a glass substrate while simultaneously monitoring the microbalance crystal sensor reading and verifying the indicated thickness by offline thickness measurement using a mechanical profilometer. To avoid the cross-reading of the crystal sensors, the sources are sequentially operated, starting from the material that introduces more cross-reading in the other sensors, which is FAI. Afterward, the temperatures of PbI_2 and SnI_2 were increased to obtain the desired rates. Finally, as the rate required for the SnF_2 source is significantly lower, it was the last source to be heated. The final rates were obtained by the sum of the rate desired plus the cross-reading on each sensor.

The thickness of all the different perovskite films was carefully maintained between 350 and 420 nm, showing an accurate thickness control achieved by sublimation methods. The addition of SnF_2 leads to improved film formation, as observed in the absorbance data (**Figure 2**a). This point is supported by the crystallinity of the perovskite films, which was studied using X-ray diffraction (XRD) in a grazing incident X-ray diffraction (GIXRD) setup. The sample prepared without the SnF_2 additive displays an XRD pattern where the peaks corresponding to the perovskite are significantly less intense, while the peak at 12.7°, classically ascribed to PbI_2, is the dominant one (Figure 2b). Furthermore, a small peak attributed to SnI_4 may be observed centered at 25.2°. Therefore, the improved film formation upon SnF_2 addition appears as an effect additional to the reduction of the detrimental Sn^{+4} generation, as it was previously reported for Sn–Pb perovskites prepared using a solvent-based procedure.[17,27,28] Interestingly, despite the reduction of the peak at 12.7°, when small amounts of SnF_2 are added, higher rates of SnF_2 gradually make this diffraction peak more prominent and generate an additional peak at 38.7°, observed for the 20% SnF_2 sample. These signals (12.7° and 38.7°) can be associated with PbI_2 and SnI_2, which suggest that SnF_2 addition induces an excess of these materials in the resulting perovskite film. A similar effect has been reported to have a beneficial impact in the resulting perovskites.[29,30] The rest of the peaks are consistent with a perovskite containing 50% of Sn and 50% of Pb, as expected from the rates of deposition.[18,31] Considering a trade-off between perovskite formation and metal salts' excess, we decided to use the rate of 10% for subsequent studies. A preliminary evaluation of the stability of these films was carried out by monitoring the evolution of the UV–vis absorbance of air-exposed films (Figure S1, Supporting Information). While there is no significant decay of perovskite absorption during the initial hours, the degradation is clear after 1 day, which suggests a decomposition of the film. The ambient effect is also evident

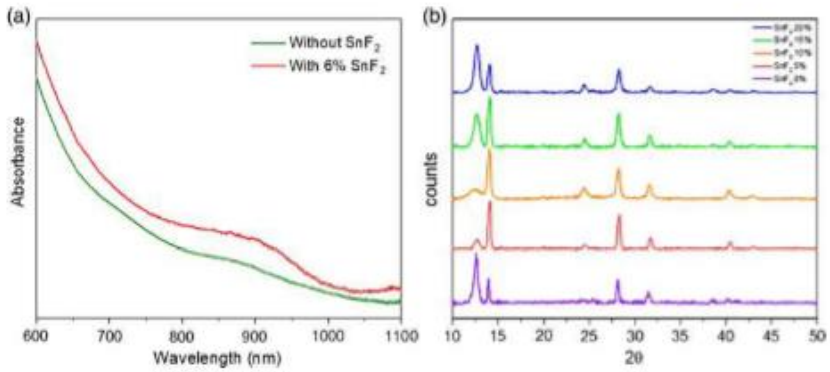

Figure 2. a) UV–vis absorbance of $FAPb_{0.5}Sn_{0.5}I_3$ with 6% SnF_2 and without SnF_2. b) XRD pattern obtained for a $FAPb_{0.5}Sn_{0.5}I_3$ film on PTAA, with different amounts of SnF_2 (percentage related to SnI_2).

when the film conductivity is measured (Figure S2, Supporting Information). Under N_2 atmosphere, the perovskite conductivity remains almost unaffected during the explored timeframe. In contrast, the air exposure results in a conductivity enhancement of almost one order of magnitude in few minutes, which is attributed to the Sn^{+4} formation.

Once deposited onto ambient temperature substrates, the perovskite films were used without further annealing treatment. The absorbance of this perovskite extends up to 970 nm (shown in **Figure 3**a) according to the Tauc plot corresponding to a direct allowed transition in the bandgap of 1.28 eV (Figure 3a).[32] This value is in line with that obtained from solution-processed perovskites with similar Sn–Pb precursor ratios.[18] The surface of this perovskite thin film can be observed in Figure 3b from a scanning electron microscopy (SEM) image. This image shows a homogeneous distribution of the grains, sized between 60 and 100 nm. It is worth mentioning that vacuum deposition of perovskites usually results in a smaller grain size than the one obtained by the solution process. However, this is not necessarily limiting the achievable power conversion efficiency of the solar cells employing them.[33] More importantly, the SEM top view also displays a smooth pinhole-free surface, crucial to avoid leakage paths in the full device, an encouraging sign of the suitability of vapor-deposition methods for these kinds of perovskites. SEM images of samples containing three different quantities of SnF_2 are shown in Figure S3, Supporting Information, where no significant morphological differences are observed.

To assess the quality of the films, some were employed to fabricate photovoltaic devices with a p-i-n configuration (hole selective material deposited on the incident light side of the device), as detailed in the Experimental Section. The layers that constitute the full stack were ITO/MoO_3/poly[bis(4-phenyl) (2,4,6-trimethylphenyl) amine] (PTAA)/$FAPb_{0.5}Sn_{0.5}I_3$/fullerene (C_{60})/2,9-dimethyl-4,7-diphenyl-1,10-phenanthroline (BCP)/Ag, as shown in **Figure 4**a. The dark current–voltage characteristics of the devices (Figure 4b) show a reduced leakage current and a good diode rectification, suggesting that the formation of Sn^{+4} is effectively suppressed during fabrication.

Figure 4c shows the incident photon to current efficiency (IPCE) of the $FAPb_{0.5}Sn_{0.5}I_3$ solar cell. These devices were synthesized with a thickness of 340 nm, implying that further optimization of the films, including their thickness, could increase current generation in the IR region of the spectra. Figure 4d shows the current–voltage (J–V) characteristics under AM1.5G-simulated illumination for the best performing device. Power conversion efficiency achieves a value of 13.98% in the reverse scan (from V_{OC} to short circuit, J_{SC}), with a V_{OC} of 0.72 V, fill factor (FF) of 79.3%, and J_{SC} of 24.5 mA cm^{-2}, close to the one obtained from the IPCE integration. V_{OC} of 0.73 V, FF of 73.3%, and J_{SC} of 24.3 mA cm^{-2} are obtained at forward scans (from J_{SC} to V_{OC}), which results in an almost negligible hysteresis.

These results demonstrate the potential of vacuum deposition for the fabrication of tin–lead perovskite solar cells.

We have developed a method to fabricate $FAPb_{0.5}Sn_{0.5}I_3$ from vacuum-deposition methods. The coevaporation of the precursors, along with the deposition of the SnF_2 additive, results in pinhole-free homogeneous perovskite films with 60–100 nm grains and a ≈1.28 eV bandgap without additional annealing. These films, when integrated in a sandwich-type diode structure, show low dark conductivity indicative of the effective suppression of the oxidation of the Sn^{2+} precursor to Sn^{4+}. When illuminated by simulated sun light, these diodes have a power conversion efficiency >13%, further demonstrating the high quality of the perovskite films. This work opens a new processing route to fabricate narrow-bandgap perovskites by vacuum deposition, with the potential to achieve the efficiency limit of single-absorber solar cells or integrate them in multijunction perovskite tandems upon further optimization.

Experimental Section

Molybdenum oxide (MoO_3) and bathocuproine (BCP) were obtained from Lumtec, poly(triaryl amine) (PTAA), and C_{60} was obtained from Sigma-Aldrich; patterned ITO-containing glass substrates were obtained from Naranjo substrates. The perovskite precursors used in this study were obtained from Tokio Chemical Industries; PbI_2 >98% purity,

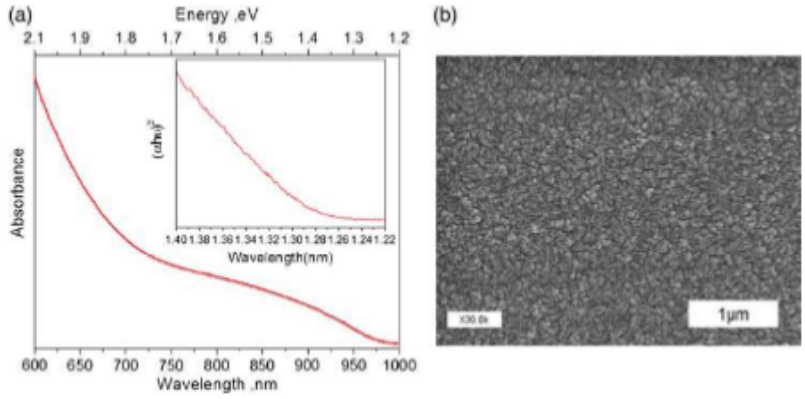

Figure 3. a) UV–vis absorbance for a $FAPb_{0.5}Sn_{0.5}I_3$ film with 10% SnF_2 as an additive. Tauc plot calculation from the absorbance in the inset. b) SEM image for the surface of a $FAPb_{0.5}Sn_{0.5}I_3$ film.

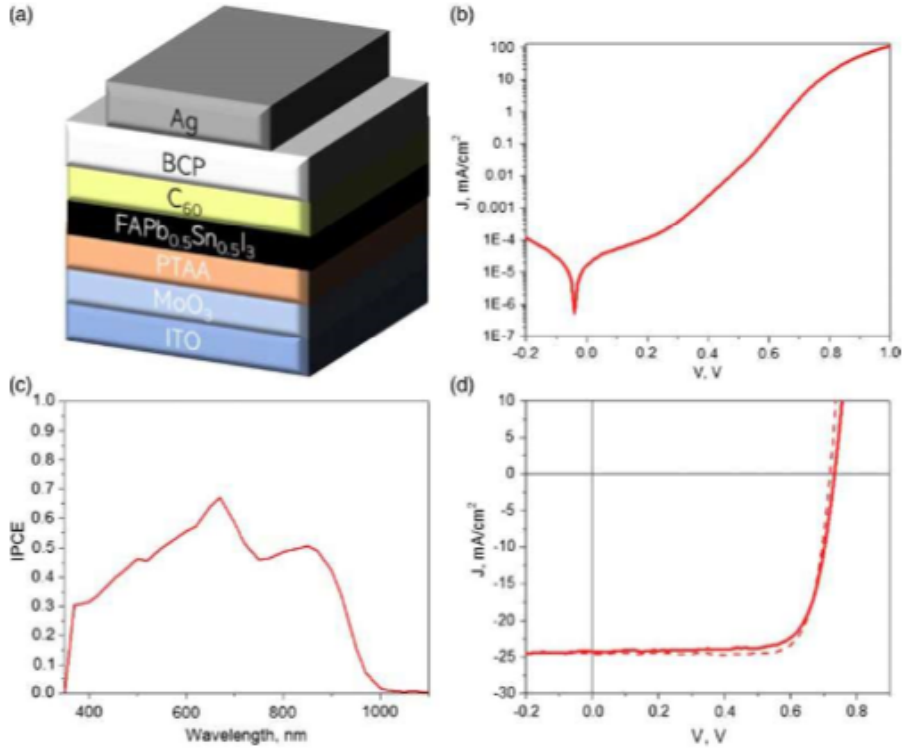

Figure 4. a) Device structure. b) *J–V* characteristics measured in dark conditions for the best-performing device. c) External quantum efficiency of a $FAPb_{0.5}Sn_{0.5}I_3$ solar cell. d) *J–V* characteristics under illumination for the best-performing device (from positive to negative potential) and solid lines represent forward measurements (from negative to positive potential).

Sigma-Aldrich; SnF_2 >99% purity, Cymit (Alfa Aesar); SnI_2 >99.999% purity, ultradry and Lumtec; FAI >99.5%.

To facilitate hole extraction, 5 nm of MoO_3 was thermally evaporated at a base pressure of 2×10^{-6} mbar on indium tin oxide (ITO)-containing substrates. After this, on top of these films, a layer of PTAA was spin coated at 1500 rpm for 30 s and then thermally annealed at 100 °C for 10 min in a nitrogen atmosphere. These ITO/MoO_3/PTAA-covered substrates were used for the deposition of $FASn_{0.5}Pb_{0.5}I_3$ films following the procedure described later. On top of the perovskite, thin layers of C_{60} and BCP (25 and 8 nm, respectively) were thermally evaporated using a dedicated vacuum chamber with a base pressure of 3×10^{-6} mbar. Finally, the films were transferred to a dedicated vacuum chamber used solely for metal deposition, where 100 nm of *Ag* as the top electrode was deposited by thermal evaporation at a pressure of 2×10^{-6} mbar. The resulting diodes were then characterized by current voltage sweeps (using a Keithley Model 2400) in the dark and illuminated IPCE, and measurements were done by measuring the cell response at different wavelengths obtained with a white halogen lamp combined with band-pass filters. The solar spectrum was corrected by calibration with a silicon reference cell, previously calibrated (MiniSun simulator by ECN, the Netherlands). The current density voltage (*J–V*) characteristics were obtained using a solar simulator by Abet Technologies, model 10500, with an AM1.5G xenon lamp as the light source. Keithley 2400 source measure unit and under white light illumination. A shadow mask with an aperture of 0.01 cm^2 was used to prevent illumination of the nonactive area.

Perovskite Film Preparation Procedure: $FAPb_{0.5}Sn_{0.5}I_3$ films were fabricated by simultaneous thermal vacuum deposition of the precursors FAI, SnI_2, PbI_2, and SnF_2 on ITO/MoO_3/PTAA-covered substrates at ambient temperature. The evaporation was done in a chamber at a pressure of 3×10^{-6} mbar. Four crucibles were filled with different precursors and evaporated at the following temperatures, which were identified after a study of sublimation rates and final perovskite compositions as discussed in the main section of this manuscript: 170 °C for FAI, 180 °C for SnI_2, 210 °C for PbI_2, and 145 °C for SnF_2. The thickness of the films was estimated as the double of the thickness measured by the FAI crystal sensor. Structural properties were studied using XRD. GIXRD patterns were collected at room temperature on an Empyrean PANanalytical powder diffractometer using the Cu Kα1 radiation. Optical properties were studied using UV–vis spectroscopy. A fiber optics–based Avantes Avaspec2048 Spectrometer was used. Morphological properties were studied using an SEM Hitachi S-4800 microscope at an accelerating voltage of 20 kV. The samples were metallized prior to observation with an Au–Pd coating.

Supporting Information

Supporting Information is available from the Wiley Online Library or from the author.

Acknowledgements

The research that led to these results received funding from the European Union Programme for Research and Innovation Horizon 2020 (2014-2020) under the project INFORM (grant 675867), the Spanish Ministry of

Economy and Competitiveness (MINECO) via the Unidad de Excelencia María de Maeztu MDM-2015-0538, MAT2017-88821-R, MAT2017-88905-P, and PCIN-2015-255, and the Generalitat Valenciana (Prometeo/2016/135). H.J.B. acknowledges the support of ERA NET PCIN-2017-014. P.P.B. thanks the MINECO for his post-doctoral RyC contracts. P.P.B. acknowledges the financial support from the Conselleria d'Educació, Investigació, Cultura i Esport Valenciana (SEJI2017/2017/012).

Conflict of Interest

The authors declare no conflict of interest.

Keywords

lead, perovskites, photovoltaics, tin, vacuum deposition

Received: June 17, 2019
Revised: July 18, 2019
Published online:

[1] N. J. Jeon, J. H. Noh, W. S. Yang, Y. C. Kim, S. Ryu, J. Seo, S. Il Seok, *Nature* **2015**, *517*, 476.
[2] A. Kojima, K. Teshima, T. Miyasaka, Y. Shirai, in 210th ECS Meet, Cancun, Mexico **2006**.
[3] N. J. Jeon, H. Na, E. H. Jung, T. Y. Yang, Y. G. Lee, G. Kim, H. W. Shin, S. Il Seok, J. Lee, J. Seo, *Nat. Energy* **2018**, *3*, 682.
[4] Q. Jiang, Y. Zhao, X. Zhang, X. Yang, Y. Chen, Z. Chu, Q. Ye, X. Li, Z. Yin, J. You, *Nat. Photonics* **2019**, *13*, 460.
[5] NREL, https://www.nrel.gov/pv/cell-efficiency.html (accessed: June 2019).
[6] S. Rühle, *Sol. Energy* **2016**, *130*, 139.
[7] W. Shockley, H. J. Queisser, *J. Appl. Phys.* **1961**, *32*, 510.
[8] Z. Yang, A. Rajagopal, A. K. Y. Jen, *Adv. Mater.* **2017**, *29*, 1704418.
[9] M. Anaya, G. Lozano, M. E. Calvo, H. Míguez, *Joule* **2017**, *1*, 769.
[10] B. Chen, X. Zheng, Y. Bai, N. P. Padture, J. Huang, *Adv. Energy Mater.* **2017**, *7*, 1602400.
[11] W. Li, Z. Wang, F. Deschler, S. Gao, R. H. Friend, A. K. Cheetham, *Nat. Rev. Mater.* **2017**, *2*, 16099.
[12] J. Zhao, L. Wei, C. Jia, H. Tang, X. Su, Y. Ou, Z. Liu, C. Wang, X. Zhao, H. Jin, P. Wang, G. Yu, G. Zhang, J. Liu, *J. Mater. Chem. A* **2018**, *6*, 20224.
[13] Y. Ogomi, A. Morita, S. Tsukamoto, T. Saitho, N. Fujikawa, Q. Shen, T. Toyoda, K. Yoshino, S. S. Pandey, S. Hayase, *J. Phys. Chem. Lett.* **2014**, *5*, 1004.
[14] W. Liao, D. Zhao, Y. Yu, N. Shrestha, K. Ghimire, C. R. Grice, C. Wang, Y. Xiao, A. J. Cimaroli, R. J. Ellingson, N. J. Podraza, K. Zhu, R. G. Xiong, Y. Yan, *J. Am. Chem. Soc.* **2016**, *138*, 12360.
[15] N. K. Noel, S. D. Stranks, A. Abate, C. Wehrenfennig, S. Guarnera, A. A. Haghighirad, A. Sadhanala, G. E. Eperon, S. K. Pathak, M. B. Johnston, A. Petrozza, L. M. Herz, H. J. Snaith, *Energy Environ. Sci.* **2014**, *7*, 3061.
[16] J. Im, C. C. Stoumpos, H. Jin, A. J. Freeman, M. G. Kanatzidis, *J. Phys. Chem. Lett.* **2015**, *6*, 3503.
[17] S. Gupta, D. Cahen, G. Hodes, *J. Phys. Chem. C* **2018**, *122*, 13926.
[18] G. E. Eperon, T. Leijtens, K. A. Bush, R. Prasanna, T. Green, J. T. W. Wang, D. P. McMeekin, G. Volonakis, R. L. Milot, R. May, A. Palmstrom, D. J. Slotcavage, R. A. Belisle, J. B. Patel, E. S. Parrott, R. J. Sutton, W. Ma, F. Moghadam, B. Conings, A. Babayigit, H. G. Boyen, S. Bent, F. Giustino, L. M. Herz, M. B. Johnston, M. D. McGehee, H. J. Snaith, *Science*, **2016**, *354*, 861.
[19] T. M. Koh, T. Krishnamoorthy, N. Yantara, C. Shi, W. L. Leong, P. P. Boix, A. C. Grimsdale, S. G. Mhaisalkar, N. Mathews, *J. Mater. Chem. A* **2015**, *3*, 14996.
[20] T. Liu, Y. Zhou, Z. Li, L. Zhang, M. G. Ju, D. Luo, Y. Yang, M. Yang, D. H. Kim, W. Yang, N. P. Padture, M. C. Beard, X. C. Zeng, K. Zhu, Q. Gong, R. Zhu, *Adv. Energy Mater.* **2018**, *8*, 1800232.
[21] G. Kapil, T. S. Ripolles, K. Hamada, Y. Ogomi, T. Bessho, T. Kinoshita, J. Chantana, K. Yoshino, Q. Shen, T. Toyoda, T. Minemoto, T. N. Murakami, H. Segawa, S. Hayase, *Nano Lett.* **2018**, *18*, 3600.
[22] C. Li, Z. Song, D. Zhao, C. Xiao, B. Subedi, N. Shrestha, M. M. Junda, C. Wang, C. S. Jiang, M. Al-Jassim, R. J. Ellingson, N. J. Podraza, K. Zhu, Y. Yan, *Adv. Energy Mater.* **2019**, *9*, 1803135.
[23] J. Ávila, C. Momblona, P. P. Boix, M. Sessolo, H. J. Bolink, *Joule* **2017**, *1*, 431.
[24] J. Ávila, C. Momblona, P. Boix, M. Sessolo, M. Anaya, G. Lozano, K. Vandewal, H. Míguez, H. J. Bolink, *Energy Environ. Sci.* **2018**, *11*, 3292.
[25] D. Zhao, C. Chen, C. Wang, M. M. Junda, Z. Song, C. R. Grice, Y. Yu, C. Li, B. Subedi, N. J. Podraza, X. Zhao, G. Fang, R. G. Xiong, K. Zhu, Y. Yan, *Nat. Energy* **2018**, *3*, 1093.
[26] D. Zhao, Y. Yu, C. Wang, W. Liao, N. Shrestha, C. R. Grice, A. J. Cimaroli, L. Guan, R. J. Ellingson, K. Zhu, X. Zhao, R. G. Xiong, Y. Yan, *Nat. Energy* **2017**, *2*, 17018.
[27] I. Chung, B. Lee, J. He, R. P. H. Chang, M. G. Kanatzidis, *Nature* **2012**, *485*, 486.
[28] M. H. Kumar, S. Dharani, W. L. Leong, P. P. Boix, R. R. Prabhakar, T. Baikie, C. Shi, H. Ding, R. Ramesh, M. Asta, M. Graetzel, S. G. Mhaisalkar, N. Mathews, *Adv. Mater.* **2014**, *26*, 7122.
[29] D. P. McMeekin, S. Mahesh, N. K. Noel, M. T. Klug, J. C. Lim, J. H. Warby, J. M. Ball, L. M. Herz, M. B. Johnston, H. J. Snaith, *Joule* **2019**, *3*, 387.
[30] D. Ramirez, K. Schutt, Z. Wang, A. J. Pearson, E. Ruggeri, H. J. Snaith, S. D. Stranks, F. Jaramillo, *ACS Energy Lett.* **2018**, *3*, 2246.
[31] W. Wang, D. Zhao, F. Zhang, L. Li, M. Du, C. Wang, Y. Yu, Q. Huang, M. Zhang, L. Li, J. Miao, Z. Lou, G. Shen, Y. Fang, Y. Yan, *Adv. Funct. Mater.* **2017**, *27*, 1703953.
[32] J. Tauc, R. Grigorovici, A. Vancu, *Phys. Status Solidi.* **1966**, *15*, 627.
[33] C. Momblona, L. Gil-Escrig, E. Bandiello, E. M. Hutter, M. Sessolo, K. Lederer, J. Blochwitz-Nimoth, H. J. Bolink, *Energy Environ. Sci.* **2016**, *9*, 3456.

SUPPORTING INFORMATION

$FAPb_{0.5}Sn_{0.5}I_3$, A narrow Bandgap Perovskite Synthesized through Evaporation Methods for Solar Cell Applications

Ana M. Igual-Muñoz, Jorge Ávila, Pablo P. Boix*, and Henk J. Bolink*.

Instituto de Ciencia Molecular, Universidad de Valencia, C/J. Beltran 2, 46980 Paterna, Spain.

*E-mail: Pablo.P.Boix@uv.es; henk.bolink@uv.es

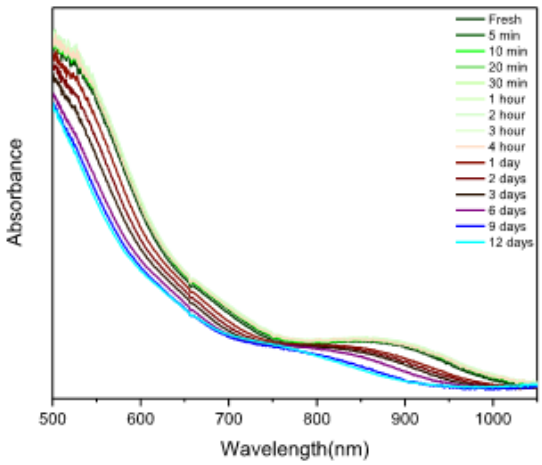

Figure S1. UV-Vis absorbance of a sample of $FAPb_{0.5}Sn_{0.5}I_3$ with 10% SnF_2 measured before and after the days indicated in air.

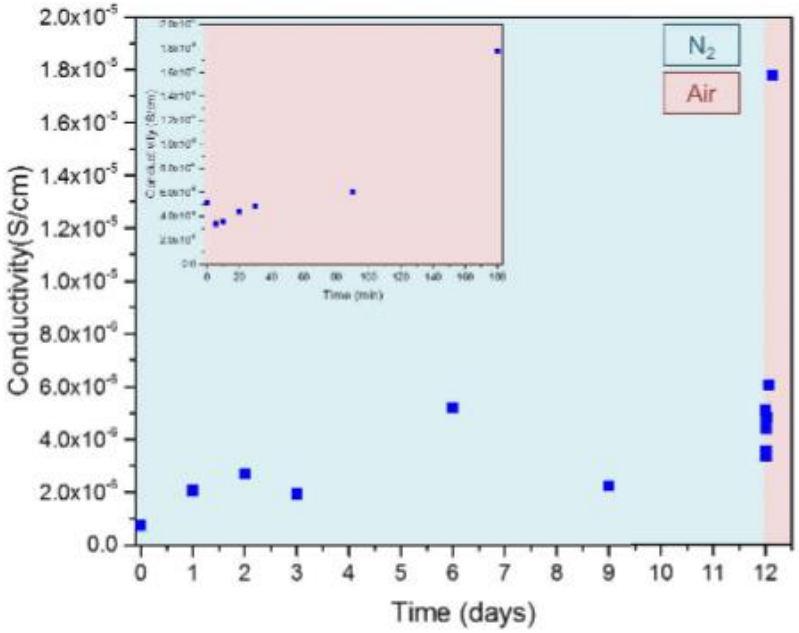

Figure S2. Conductivity of a sample of $FAPb_{0.5}Sn_{0.5}I_3$ with 10% SnF_2 measured after the days indicated in N_2 atmosphere and from twelve days in air (inset).

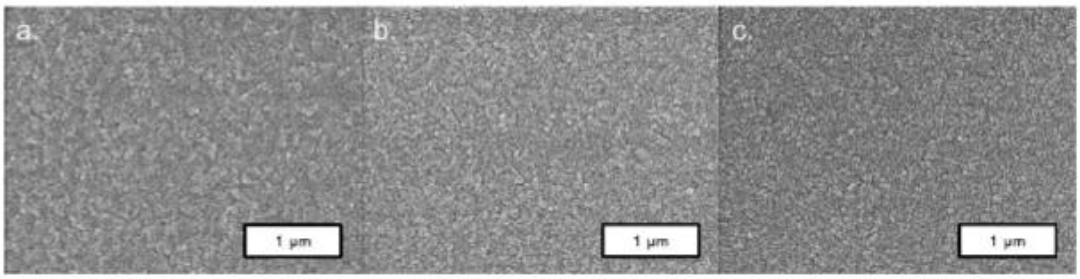

Figure S3. SEM images of the surface of $FAPb_{0.5}Sn_{0.5}I_3$ with (a) 0% (b)10% (c)20% SnF_2.

Appendix B

Vacuum-Deposited Multication Tin–Lead Perovskite Solar Cells

ACS APPLIED ENERGY MATERIALS

www.acsaem.org Article

Vacuum-Deposited Multication Tin−Lead Perovskite Solar Cells

Ana M. Igual-Muñoz, Aroa Castillo, Chris Dreessen, Pablo P. Boix,* and Henk J. Bolink*

Cite This: ACS Appl. Energy Mater. 2020, 3, 2755−2761 Read Online

ACCESS | Metrics & More | Article Recommendations | Supporting Information

ABSTRACT: The use of a combination of tin and lead is the most promising approach to fabricate narrow bandgap metal halide perovskites. This work presents the development of reproducible tin and lead perovskites by vacuum codeposition of the precursors, a solvent-free technique which can be easily implemented to form complex stacks. Crystallographic and optical characterization reveal the optimal film composition based on cesium and methylammonium monovalent cations. Device optimization makes use of the intrinsically additive nature of vacuum deposition, resulting in solar cells with 8.89% photovoltaic efficiency. The study of the devices by impedance spectroscopy identifies bulk recombination as one of the performance limiting factors.

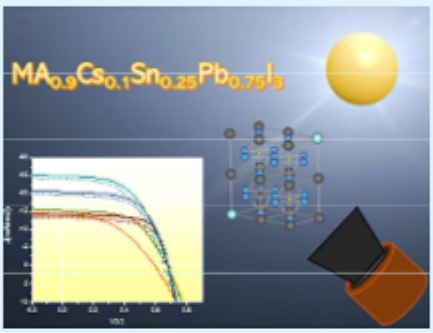

KEYWORDS: *perovskite, low bandgap, tin−lead, solar cell, vacuum deposition*

INTRODUCTION

The efficiency of metal halide perovskite solar cells has increased from 2.2% in 2006 up to 25.2% in 2019.[1−3] The best results to date are based on perovskites employing lead (Pb) and a combination of multiple monovalent cations and halides, with a bandgap between 1.5 and 1.6 eV.[4] A number of approaches can be adopted to further increase the perovskite solar cells' power conversion efficiency, most of which require adjusting the absorber's bandgap, for example, targeting single junction cells with efficiency close to the Shockley−Queisser limit (ideal bandgap of ∼1.34 eV)[5] or exploiting the full potential of multijunction solar cells with current-matching absorbers.[6]

The substitution of Pb by tin (Sn) in this family of materials leads to an absorption bandgap narrowing, with values down to 1.1 eV.[7,8] Nevertheless, the use and manufacturing of pure tin based perovskites is not trivial due to the easy oxidation of Sn^{2+} to Sn^{4+} which leads to p-type doping and compromises the device stability and performance.[9] Partial Pb substitution is an alternative route which increases the flexibility of the approach, widening the number of possible compositions. Indeed, perovskites combining both metals can form narrower bandgap materials as the values are not linear with the metals ratio,[10] particularly useful for the fabrication of perovskite−perovskite tandems.[11] More interestingly, mixed tin and lead compositions present enhanced stability compared to pure Sn based ones, as the introduction of Pb into the perovskite retards the oxidation from Sn^{2+} to Sn^{4+},[12] analogously to the introduction of germanium in the structures which forms a native-oxide layer on the perovskite.[13] Recent studies have achieved efficiencies as high as 20.5% with devices employing tin−lead based perovskites.[14−16] The fabrication of these devices employs a solution-based process with important restrictions on the thickness control and solvent compatibility, which limit their direct application to multijunction devices. Among all the alternative methods for the perovskite synthesis, physical vapor codeposition of the precursors presents several advantages that make it particularly interesting for the industrialization of the field.[17] This technique is intrinsically additive and solvent-free which allows for an accurate control on the film thickness and multistack formation versatility—key points for the fabrication of multijunction tandem devices.[18] Vacuum deposition is also compatible with large area film formation, enabling the control over the morphology and thickness of the film. In addition to these advantages, the technique has led to high-efficiency photovoltaic devices with different Pb based perovskite compositions.[19,20] We recently reported efficient vacuum-deposited formamidinium (FA) tin−lead based perovskite solar cells.[21] However, these studies rely on the use of SnF_2 to reduce the formation of Sn^{4+} as a degradation byproduct[9,22] and on the formamidinium as the sole monovalent cation in the final perovskite. Small quantities of reactants, such as those required for the SnF_2 in Sn−Pb perovskites, are less easy to control by coevaporation, and the crystallization of pure formamidinium is associated with phase control difficulties. The combination of these factors results in low reproducibility

Received: December 11, 2019
Accepted: February 5, 2020
Published: February 5, 2020

https://dx.doi.org/10.1021/acsaem.9b02413
ACS Appl. Energy Mater. 2020, 3, 2755−2761

and compromises the material stability, and the work serves primarily as a proof of concept of the capability to synthesize these perovskites by coevaporation. The fabrication of tin−lead based perovskites combining cesium (Cs) and formamidinium as monovalent cations through dual source evaporation has also been reported.[23] That work presynthesized some of the precursors as an alloy and still required the use of SnF_2. Following that path, the incorporation of two monovalent cations is a promising approach to palliate the above-mentioned drawbacks, as methylammonium (MA) and Cs based tin−lead perovskites have shown the capability to operate without SnF_2 additives.[24] In particular, introducing Cs can enhance the perovskite thermal stability, photostability, and efficiency,[25,26] yet their use in Sn−Pb perovskites fabricated by precursor coevaporation remains unexplored. In addition, MA is more stable and controllable than FA through evaporation methods. As a result, these vacuum-deposited perovskites are significantly more reproducible than those employing FA.[21]

In this work, we study the partial replacement of Pb^{2+} by Sn^{2+} in a $MA_{0.9}Cs_{0.1}PbI_3$ perovskite fabricated by simultaneous thermal vacuum deposition of the precursors, avoiding the use of SnF_2. The targeted composition was 25% Sn 75% Pb, following previous reports which showed that this composition leads to enhanced stability and higher efficiencies.[25] The obtained perovskite presents a lower energy absorption onset than its Pb based counterpart, with a bandgap close to the optimal one for single junction solar cells (1.34 eV)[5] and suitable for future use as low-bandgap absorber in a tandem device. The film characteristics, such as morphology and crystallinity, are modified by adjusting the evaporation parameters. Evaluating different thicknesses of Sn−Pb perovskites in a multilayer solar cell results in devices with efficiency close to 9%.

EXPERIMENTAL SECTION

Synthesis of $MA_{0.9}Cs_{0.1}Sn_{0.25}Pb_{0.75}I_3$. The precursors used in this study were tin(II) iodide (SnI_2, >97%), lead(II) iodide (PbI_2, >98%), and cesium iodide (CsI, >99%) from Tokyo Chemical Industries (TCI) and methylammonium iodide (MAI, >99.5%) from Lumtec. The $MA_{0.9}Cs_{0.1}Sn_{0.25}Pb_{0.75}I_3$ films were fabricated by simultaneous thermal vacuum deposition of the precursors MAI, SnI_2, PbI_2, and CsI without further thermal treatment on the substrate. To establish the proper deposition of the precursors, calibration of their thickness was done prior to the synthesis of the perovskite. This calibration factor was obtained by depositing an amount of each precursor on a glass substrate and measurement of its thickness with a mechanical profilometer. Furthermore, it should be indicated that the rates of evaporation depend on the reading capability of the quartz crystal microbalances (Fil-Tech). This factor can slightly change during long evaporations due to material deposition on the microcrystal. The evaporation was done in a vacuum chamber at a pressure of 3×10^{-6} mbar. Four crucibles were filled with the different precursors and evaporated at the temperatures of 90 °C for MAI, 176 °C for SnI_2, 287 °C for PbI_2, and 386 °C for CsI. The thickness of the films was controlled by the sum of the rates of SnI_2 and PbI_2 being 0.2 and 0.59 Å s^{-1} each. Employing these rates, it takes between 1 and 3 h to synthesize the perovskites, depending on the final film thicknesses. A scheme of the evaporator may be found in Figure S1 to identify each precursor with the source that was employed for them.

Device Preparation. Molybdenum oxide (MoO_3) and bathocuproine (BCP) were obtained from Lumtec; 4,4′,4″-tris[(3-methylphenyl)phenylamino]triphenylamine (m-MTDATA) and C_{60} were obtained from Sigma-Aldrich. Inside a metal chamber at a pressure of 2×10^{-6} mbar, 5 nm of MoO_3 was thermally evaporated on indium tin oxide (ITO) patterned substrates and annealed at 100 °C for 10 min. After this, 10 nm of m-MTDATA was thermally evaporated at a pressure of 3×10^{-6} mbar. Then, the $MA_{0.9}Cs_{0.1}Sn_{0.25}Pb_{0.75}I_3$ films were fabricated following a similar procedure as described above. On top of the perovskite 25 nm of C_{60} and 8 nm films of BCP were evaporated at a pressure of 3×10^{-6} mbar. Finally, 100 nm of Ag was deposited at a pressure of 2×10^{-6} mbar, resulting in completely sublimed devices. The samples were kept in an inert atmosphere in between the deposition of the different materials.

Current−Voltage Characteristics. Solar cells were characterized by current−voltage sweeps recorded with a Keithley Model 2400. The solar spectrum (AM1.5G) used for the illuminated curves was corrected with a calibrated silicon reference cell (Minisun simulator by ECN, Netherlands). IPCE measurements were done by applying different wavelengths employing band-pass filters on a white halogen lamp and measuring the response of the cell. A shadow mask with an aperture of 0.0264 cm^2 was employed to avoid illumination of nonactive area.

Impedance Spectroscopy. A Gamry Interface 1000 potentiostat was used to apply a frequency variable (from 100 MHz to 0.1 Hz) AC voltages (20 mV amplitude) at different DC potentials (from open circuit to short circuit conditions) under 1 sun illumination. Z-View software was used to fit the results to an equivalent circuit.

Structural Analysis. The crystalline structure of the perovskites was studied by grazing incident X-ray diffraction (GIXRD). The patterns were collected on an Empyrean PANalytical powder diffractometer using Cu $K\alpha_1$ radiation. A scanning electron microscope (SEM) Hitachi S-4800 operating at 20 kV accelerating voltage was used to obtain SEM images. Samples were platinum-metallized prior to their observation. The microscope incorporated an X-ray detector (Bruker) and the program QUANTAX 400 for energy dispersive X-ray analysis (EDAX).

Optical Analysis. UV−vis absorption spectra were collected by using a fiber-optic Avantes Avaspec2048 spectrometer. Tauc plots were calculated employing the formula $(\alpha h\upsilon)^2$.

RESULTS AND DISCUSSION

The monovalent to divalent metal cation ratio determines the ultimate optoelectronic properties of the resulting perovskite film. We targeted the composition $MA_{0.9}Cs_{0.1}Sn_{0.25}Pb_{0.75}I_3$. To achieve this, films of different conditions were explored and evaluated off-line. This was done by modifying the precursor deposition rates. The PbI_2:SnI_2 and CsI:MAI ratios were maintained unaltered, and the parameter explored was the SnPb to MACs ratio (defined as the sum of the SnI_2 and PbI_2 deposition rates and the sum of MAI and CsI deposition rates, respectively).

To find the optimal deposition conditions, perovskite films with precursor ratios varying from 1.2:1 to 2.3:1 (SnPb:MACs) were analyzed by XRD (Figure S2a) to understand possible crystallographic differences and by UV−vis absorbance (Figure S2b) to understand their optical properties. These films when integrated into a device were also used in preliminary solar cells to evaluate their photovoltaic performance (Figure S3). In the XRD patterns in Figure S2 a peak at 11.4° related to low-dimensional perovskites can be observed. This suggests a lack of divalent cationic component in the 1.2:1 ratio because this feature appears when there is an excess of MA in the films.[27−29] The XRD pattern for the 2.03:1 ratio is the expected one, with all the peaks observed related to the formation of the targeted perovskite. The small excess of divalent cations has been reported to increase the device performance and circumvent the need of SnF_2.[30] For this purpose, a final ratio of 2.3:1 was investigated, which results in a peak related to excess of SnI_2/PbI_2 centered at 12.7°.

https://dx.doi.org/10.1021/acsaem.9b02413
ACS Appl. Energy Mater. 2020, 3, 2755−2761

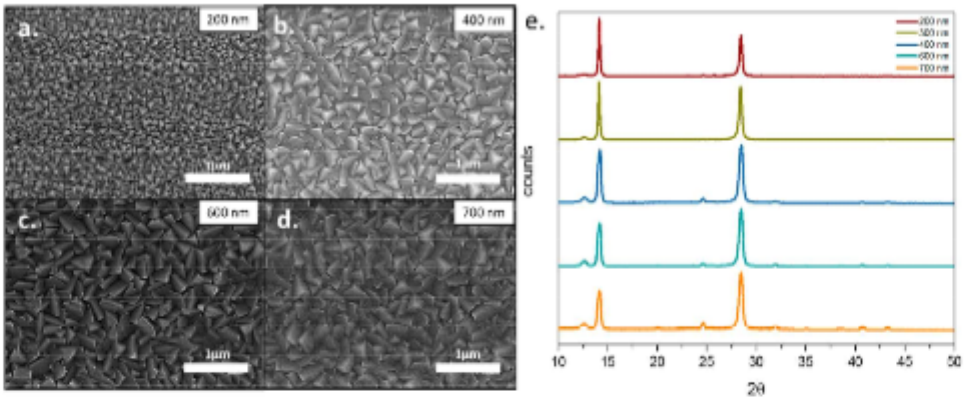

Figure 1. (a–d) Top-view SEM images of $MA_{0.9}Cs_{0.1}Sn_{0.25}Pb_{0.75}I_3$ films with different thicknesses. (e) XRD diagrams of $MA_{0.9}Cs_{0.1}Sn_{0.25}Pb_{0.75}I_3$ films with different thicknesses.

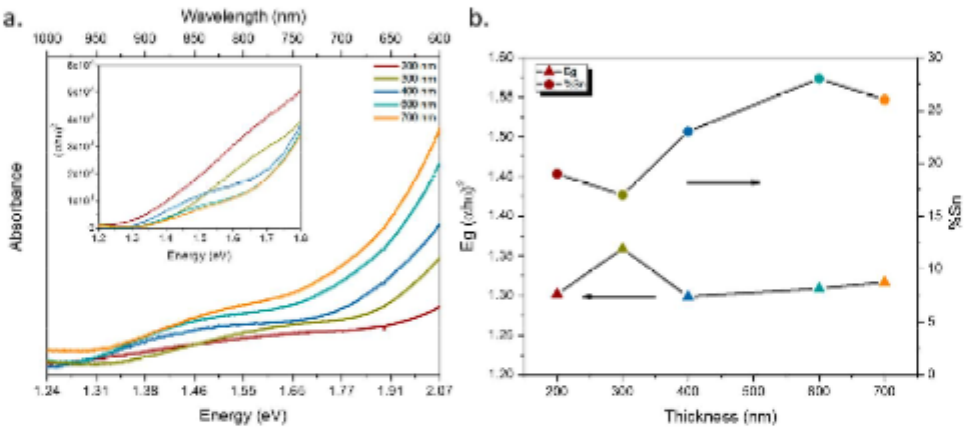

Figure 2. (a) UV–vis absorbance for $MA_{0.9}Cs_{0.1}Sn_{0.25}Pb_{0.75}I_3$ films with different thicknesses. Inset: Tauc plot of the absorbance data. (b) Bandgap obtained from the Tauc plot and %Sn relative to Pb–Sn obtained from EDAX studies.

The absorbance analysis (Figure S2b) of samples based on the 1.2:1 ratio shows the decay of absorption around 850 nm, corresponding to a not fully formed perovskite bandgap. In contrast, the ratios 2:1 and 2.3:1 result in the expected absorbance onset at 950 nm, with higher absorption in the whole spectrum for the 2.3:1 sample. Unoptimized solar cell performance for all the compositions is displayed in Figure S3 and Table S1. Based on the unoptimized solar cells performance and in concordance with previous studies indicating that the perovskite with a small excess of divalent cations has benefits,[30] the perovskite based on the 2.3:1 ratio was chosen for the detailed study described in this article. A preliminary evaluation of thermal post-treatment effects, shown in Figure S4a,b, indicates that the annealing in N_2 atmosphere does not result in a photovoltaic improvement, which confirms previous results on coevaporated solar cells. Finally, we estimated the shelf-stability of these cells. These cells were measured as prepared and after 3 days of storage in a glovebox, showing no significant changes in performance but a slight decrease in current and fill factor. This results are shown in Figure S5a,b.

The thickness and quality of the films (morphology, crystallinity, and optoelectrical properties) are key parameters for incorporating a film as the absorber in a photovoltaic device. Figure 1a–d shows the top-view SEM images for perovskite films with different thicknesses. In general, the vacuum-based deposition process results in a pinhole-free film with well-defined crystals, which suggests that high quality crystalline perovskite films can be obtained. On the other hand, a slight increase of the grain size may be observed for thicker films. This was attributed to the slight decrease in MAI rate during the deposition, which is more pronounced for thicker samples as the procedure is longer. The previously discussed XRD pattern is reproduced for all the samples, corresponding to the typical pattern for Sn–Pb perovskites[11,25] and an additional peak at 12.7° related to tin–lead excess (see Figure 1e), which was shown to be beneficial for the solar cells' performance in previous studies.[30] The XRD results display a trend related to the film thickness, with thicker films increasing the intensity in the plane (220). This, however, could be considered an artifact of the measurement, as the incident beam at low angles only reaches the surface whereas at higher angles it reaches the whole sample. As a result, thicker samples present more intense peaks at higher angles.

To determine the bandgap of the films in detail, UV–vis absorbance results of the films were analyzed (Figure 2a) with a Tauc plot, plotted as $(\alpha h\nu)^2$ vs energy (eV) (inset of Figure 2a). As expected, an increase in the absorbance is concomitant to the increase in the film thickness while the bandgap is maintained.

https://dx.doi.org/10.1021/acsaem.9b02413
ACS Appl. Energy Mater. 2020, 3, 2755–2761

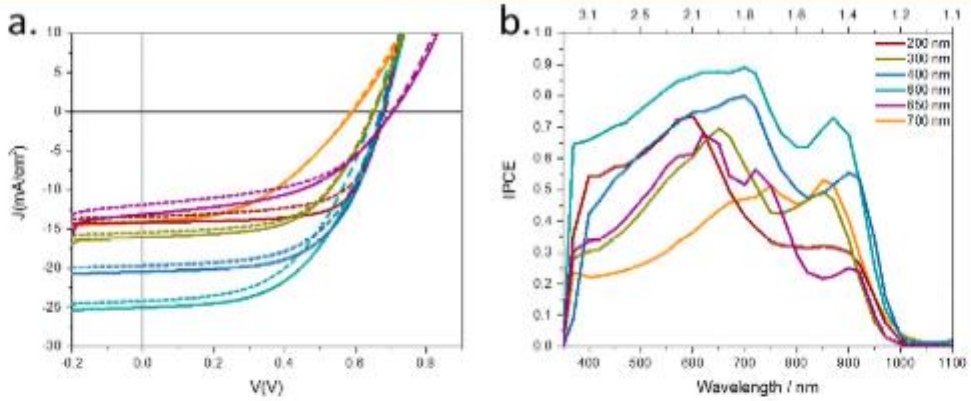

Figure 3. (a) $J-V$ measurements of solar cells with different $MA_{0.9}Cs_{0.1}Sn_{0.25}Pb_{0.75}I_3$ thicknesses under AM1.5G illumination. Dashed lines represent backward measurements, and solid lines represent forward measurements (from negative to positive potential). (b) EQE of the representative devices.

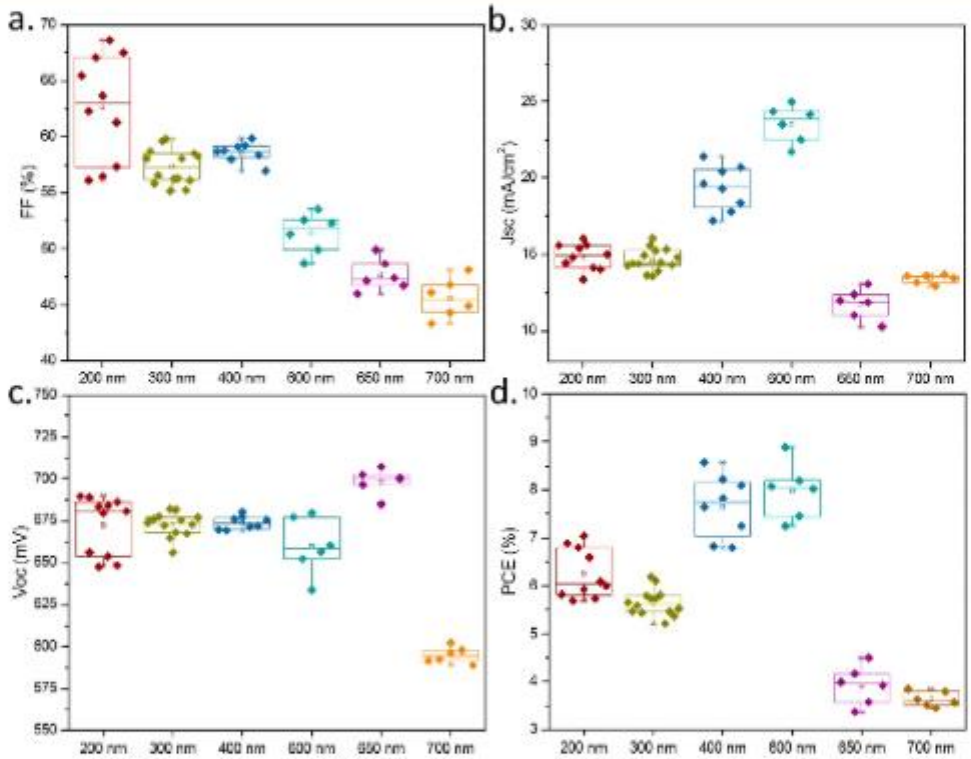

Figure 4. Photovoltaic parameters of the devices with different perovskite thicknesses measured under AM1.5G illumination: (a) FF, (b) J_{sc}, (c) V_{oc}, and (d) PCE.

These values can be compared to the expected composition estimated via EDAX. Figure 2b shows the results obtained by both approaches. It is worth to remark that our process results in films with compositions that are very close to the targeted ones, with insignificant batch-to-batch variations. The bandgap obtained for the different film thickness remains within the expected range, 1.2 and 1.4 eV, which confirms the compositional control achieved with the technique. These values are also close to previous reports on $MA_{0.9}Cs_{0.1}Sn_{0.25}Pb_{0.75}I_3$.[25]

The morphological, structural, and optical characterizations of the perovskite films indicate their suitability as absorbers in solar cells. The perovskite solar cells were prepared by using a p−i−n configuration MoO_3/m-MTDATA/$MA_{0.9}Cs_{0.1}Sn_{0.25}$-$Pb_{0.75}I_3$/$C_{60}$/BCP/Ag. m-MTDATA was used as its highest occupied molecular orbital (HOMO) aligns well with the expected perovskite energy levels, blocking electrons and allowing holes to pass.[25,32]

The current−voltage characteristics of representative devices under AM1.5G illumination are plotted in Figure 3a, with their main averaged photovoltaic parameters represented in Figure 4

https://dx.doi.org/10.1021/acsaem.9b02413
ACS Appl. Energy Mater. 2020, 3, 2755−2761

and Table 1. The current voltage curve reaches a power conversion efficiency value of 8.9% in forward measurement

Table 1. Photovoltaic Parameters under AM1.5G Illumination Measured for the Representative Solar Cells of Each Thickness (Averaged Values in Parentheses)

thickness (nm)	FF (%)	J_{sc} (mA/cm^2)	V_{oc} (mV)	PCE (%)
200	62 (63)	14.0 (14.9)	686 (671)	6.0 (6.2)
300	60 (57)	15.3 (14.6)	677 (673)	6.2 (5.6)
400	59 (59)	20.4 (19.4)	680 (674)	8.2 (7.7)
600	53 (51)	25.0 (23.6)	677 (660)	8.9 (7.9)
650	49 (48)	12.5 (11.8)	704 (699)	4.3 (3.9)
700	47 (46)	13.7 (13.4)	592 (595)	3.8 (3.6)

for devices based on an ~600 nm thick absorber. To understand the suitability of this thickness, it is important to analyze the main photovoltaic parameters of the devices. The short circuit current of the devices (J_{sc}) is enhanced as the perovskite thickness is increased from 200 to 600 nm (Figure 3a), directly related to the absorbance shown in Figure 2a. The external quantum efficiency (EQE) results (Figure 3b) confirm this point. Devices based on thinner films show an EQE deficit at longer wavelengths, which is improved by increasing the film thickness up to 600 nm, in accordance with previous studies.[33] This can be explained by the lower absorption coefficient of Sn:Pb (0.25:0.75) vs Sn:Pb (0.5:0.5), which requires thicker films to absorb the less energetic photons, but this ratio presents the bandgap we are searching for.[34] However, further increase of the perovskites thickness (650 and 700 nm) results in a reduction of the whole EQE response. Indeed, the trend with the film thickness in the shorter wavelengths is less clear, which can be due to problems related to the charge collection efficiency or to the parasitic absorption of unconverted metal halides compounds as suggested by the XRD analysis. As a result, the best performing devices were prepared with a perovskite film thickness of 600 nm, implying that by increasing the thickness some of the losses in the IR region could be avoided. The maximum theoretical J_{sc} for a bandgap of 1.3 eV is 35.8 mA/cm^2,[5] which indicates that further optimization could lead to higher currents.

In addition to the J_{sc} increase, the decrease of fill factor (FF) is also correlated to the film thickness, as displayed in Figures 3a and 4a. FF reductions are usually originated by an impaired charge transport or by higher charge carrier recombination. The open circuit potential (V_{oc}) values do not show significant differences between 200 and 400 nm thick devices (Figure 4c), which indicates similar recombination for the three groups and hints toward charge transport deficits as the origin of the FF reduction. This is in line with the resistances obtained for dark current voltage at high injection potential (>0.9 V) plotted in Figure S6, which suggest that thicker films have larger series resistance.[35] The combination of all these parameters results in an optimal PCE for devices based on perovskite absorbers with thickness between 400 and 600 nm, as displayed in Figure 4d.

V_{oc} decreases when perovskite films thicker than 400 nm are used. To understand this decrease, we measure impedance spectroscopy of 400, 600, and 700 nm samples under 0.5 sun illumination. Generally, the impedance spectrum consisted of two features: a high frequency and a lower frequency one (see Figure S7a), similar to previous reports on Pb-based perovskite solar cells.[36] Both arcs include information about the recombination,[37] which can be fitted with the equivalent circuit in Figure S7 as discussed elsewhere.[38] In detail, the parameters of the circuit include an ohmic series resistance (R_s) which accounts for the TCO and cables transport with negligible capacitance, a low-frequency capacitance (C_{lf}) whose origin is currently under discussion,[39−42] a device geometrical capacitance (C_g), and a resistance which includes the recombination resistance effects (R_{rec}) and a third of the transport resistance (displayed as R_{tr}), combined as (R_{rec} + R_{tr}). The R_{rec}+ R_{tr} values, represented in Figure 5, clearly

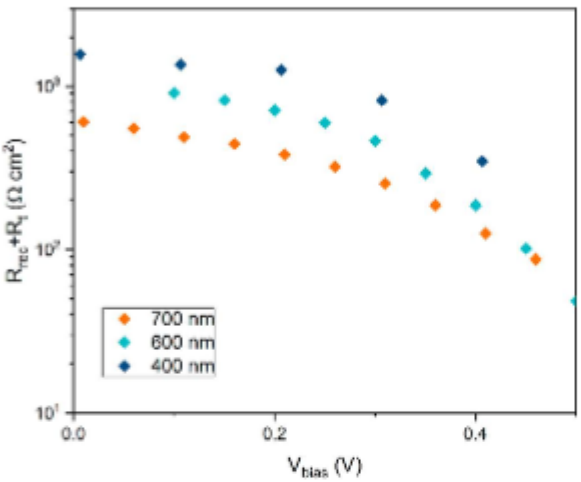

Figure 5. Combination of recombination and transport resistances extracted from the impedance spectra of devices with different perovskite thicknesses measured under 0.5 sun illumination.

follow the trend of the V_{oc}, suggesting the they are dominated by the recombination processes. More interestingly, the volumetric normalization of this resistance reduces notably the differences among the samples (Figure S7b). Altogether, the results suggest a bulk-dominant recombination process, in line with the V_{oc} and FF evolution.[23−25]

This trend is in good agreement with the V_{oc} evolution with the light intensity for the 600 nm absorber device, represented in Figure S8. These measurements result in an ideality factor of ~2, which indicates trap-mediated recombination as the main loss process associated with these devices, in line with a bulk-dominated recombination. Vacuum-deposited Sn−Pb perovskites reported here present significantly smaller grain domains than their solution-processed counterparts.[34] Although the smaller grain size does not seem to have a significantly detrimental effect in vacuum-deposited lead perovskites, its combination with the Sn^{2+} oxidation could explain this bulk-recombination enhancement. Altogether, these results imply the need to reduce the bulk recombination in the films to be able to absorb longer wavelengths yet circumventing the losses associated with thicker absorbers.

■ CONCLUSIONS

We present a vacuum-deposition route to fabricate tin−lead perovskites for photovoltaic applications with reproducible results. Power conversion efficiencies of 8.9% were achieved with an optimization of the material composition and film thickness. The characterization of relevant material properties allowed to assess the suitability of this kind of perovskite for

https://dx.doi.org/10.1021/acsaem.9b02413
ACS Appl. Energy Mater. 2020, 3, 2755−2761

photovoltaic applications, correlating to the film operation in working devices. The limiting factors of the photovoltaic performance are analyzed by impedance spectroscopy, which indicates significant bulk recombination in devices with thicker perovskite absorbers.

■ ASSOCIATED CONTENT

Supporting Information

The Supporting Information is available free of charge at https://pubs.acs.org/doi/10.1021/acsaem.9b02413.

Schematic representation of evaporation chamber, XRD measurements, optical absorbance, photovoltaic characterization, current−voltage characteristics in dark conditions, impedance spectroscopy data, ideality factor estimation (PDF)

■ AUTHOR INFORMATION

Corresponding Authors

Pablo P. Boix − *Institut de Ciència dels Materials, Universitat de Valencia, 46980 Paterna, Spain;* orcid.org/0000-0001-9518-7549; Email: Pablo.P.Boix@uv.es

Henk J. Bolink − *Instituto de Ciencia Molecular, Universidad de Valencia, 46980 Paterna, Spain;* orcid.org/0000-0001-9784-6253; Email: henk.bolink@uv.es

Authors

Ana M. Igual-Muñoz − *Instituto de Ciencia Molecular, Universidad de Valencia, 46980 Paterna, Spain*

Aroa Castillo − *Instituto de Ciencia Molecular, Universidad de Valencia, 46980 Paterna, Spain*

Chris Dreessen − *Instituto de Ciencia Molecular, Universidad de Valencia, 46980 Paterna, Spain*

Complete contact information is available at: https://pubs.acs.org/10.1021/acsaem.9b02413

Notes

The authors declare no competing financial interest.

■ ACKNOWLEDGMENTS

The research leading to these results has received funding from the European Union's Horizon 2020 research and innovation programme under grant agreement no. 763977 of the PerTPV project. Additionally, this work was also in part funded by the Spanish Ministry of Economy and Competitiveness (MINECO) via the Unidad de Excelencia Maria de Maeztu MDM-2015-0538, MAT2017-88821-R, MAT2017-88905-P, and PCIN-2015-255 and the Generalitat Valenciana (Prometeo/2016/135). H.J.B. acknowledges the support of ERA NET PCIN-2017-014. P.P.B. thanks the MINECO for his postdoctoral RyC contracts. P.P.B. acknowledges the financial support from the Conselleria d'Educació, Investigació, Cultura i Esport Valenciana (SEJI2017/2017/012).

■ REFERENCES

(1) Kojima, A.; Teshima, K.; Miyasaka, T.; Shirai, Y.; Miyasaka, T. Novel Photoelectrochemical Cell with Mesoscopic Electrodes Sensitized by Lead-Halide Compounds (2). In *210th ECS Meeting*, 2006.

(2) Jiang, Q.; Zhao, Y.; Zhang, X.; Yang, X.; Chen, Y.; Chu, Z.; Ye, Q.; Li, X.; Yin, Z.; You, J. Surface Passivation of Perovskite Film for Efficient Solar Cells. *Nat. Photonics* **2019**, *13*, 460−466.

(3) NREL https://www.nrel.gov/pv/cell-efficiency.html, 2019.

(4) Jeon, N. J.; Na, H.; Jung, E. H.; Yang, T. Y.; Lee, Y. G.; Kim, G.; Shin, H. W.; Il Seok, S.; Lee, J.; Seo, J. A Fluorene-Terminated Hole-Transporting Material for Highly Efficient and Stable Perovskite Solar Cells. *Nat. Energy* **2018**, *3* (8), 682−689.

(5) Rühle, S. Tabulated Values of the Shockley-Queisser Limit for Single Junction Solar Cells. *Sol. Energy* **2016**, *130*, 139−147.

(6) Chen, B.; Zheng, X.; Bai, Y.; Padture, N. P.; Huang, J. Progress in Tandem Solar Cells Based on Hybrid Organic-Inorganic Perovskites. *Adv. Energy Mater.* **2017**, *7* (14), 1602400.

(7) Noel, N. K.; Stranks, S. D.; Abate, A.; Wehrenfennig, C.; Guarnera, S.; Haghighirad, A. A.; Sadhanala, A.; Eperon, G. E.; Pathak, S. K.; Johnston, M. B.; Petrozza, A.; Herz, L. M.; Snaith, H. J. Lead-Free Organic-Inorganic Tin Halide Perovskites for Photovoltaic Applications. *Energy Environ. Sci.* **2014**, *7* (9), 3061−3068.

(8) Im, J.; Stoumpos, C. C.; Jin, H.; Freeman, A. J.; Kanatzidis, M. G. Antagonism between Spin-Orbit Coupling and Steric Effects Causes Anomalous Band Gap Evolution in the Perovskite Photovoltaic Materials CH3NH3Sn1-XPbxI3. *J. Phys. Chem. Lett.* **2015**, *6* (17), 3503−3509.

(9) Gupta, S.; Cahen, D.; Hodes, G. How SnF2 Impacts the Material Properties of Lead-Free Tin Perovskites. *J. Phys. Chem. C* **2018**, *122* (25), 13926−13936.

(10) Hao, F.; Stoumpos, C. C.; Chang, R. P. H.; Kanatzidis, M. G. Anomalous Band Gap Behavior in Mixed Sn and Pb Perovskites Enables Broadening of Absorption Spectrum in Solar Cells. *J. Am. Chem. Soc.* **2014**, *136* (22), 8094−8099.

(11) Eperon, G. E.; Leijtens, T.; Bush, K. A.; Prasanna, R.; Green, T.; Wang, J. T. W.; McMeekin, D. P.; Volonakis, G.; Milot, R. L.; May, R.; Palmstrom, A.; Slotcavage, D. J.; Belisle, R. A.; Patel, J. B.; Parrott, E. S.; Sutton, R. J.; Ma, W.; Moghadam, F.; Conings, B.; Babayigit, A.; Boyen, H. G.; Bent, S.; Giustino, F.; Herz, L. M.; Johnston, M. B.; McGehee, M. D.; Snaith, H. J. Perovskite-Perovskite Tandem Photovoltaics with Optimized Band Gaps. *Science (Washington, DC, U. S.)* **2016**, *354* (6314), 861−865.

(12) Ogomi, Y.; Morita, A.; Tsukamoto, S.; Saitho, T.; Fujikawa, N.; Shen, Q.; Toyoda, T.; Yoshino, K.; Pandey, S. S.; Ma, T.; Hayase, S. CH3 NH3 Snx Pb(1-x) I3 Perovskite Solar Cells Covering up to 1060 Nm. *J. Phys. Chem. Lett.* **2014**, *5*, 1004−1011.

(13) Chen, M.; Ju, M. G.; Garces, H. F.; Carl, A. D.; Ono, L. K.; Hawash, Z.; Zhang, Y.; Shen, T.; Qi, Y.; Grimm, R. L.; Pacifici, D.; Zeng, X. C.; Zhou, Y.; Padture, N. P. Highly Stable and Efficient All-Inorganic Lead-Free Perovskite Solar Cells with Native-Oxide Passivation. *Nat. Commun.* **2019**, *10* (1), 1−8.

(14) Kapil, G.; Ripolles, T. S.; Hamada, K.; Ogomi, Y.; Bessho, T.; Kinoshita, T.; Chantana, J.; Yoshino, K.; Shen, Q.; Toyoda, T.; Minemoto, T.; Murakami, T. N.; Segawa, H.; Hayase, S. Highly Efficient 17.6% Tin-Lead Mixed Perovskite Solar Cells Realized through Spike Structure. *Nano Lett.* **2018**, *18* (6), 3600−3607.

(15) Li, C.; Song, Z.; Zhao, D.; Xiao, C.; Subedi, B.; Shrestha, N.; Junda, M. M.; Wang, C.; Jiang, C. S.; Al-Jassim, M.; Ellingson, R. J.; Podraza, N. J.; Zhu, K.; Yan, Y. Reducing Saturation-Current Density to Realize High-Efficiency Low-Bandgap Mixed Tin-Lead Halide Perovskite Solar Cells. *Adv. Energy Mater.* **2019**, *9* (3), 1803135.

(16) Tong, J.; Song, Z.; Kim, D. H.; Chen, X.; Chen, C.; Palmstrom, A. F.; Ndione, P. F.; Reese, M. O.; Dunfield, S. P.; Reid, O. G.; Liu, J.; Zhang, F.; Harvey, S. P.; Li, Z.; Christensen, S. T.; Teeter, G.; Zhao, D.; Al-Jassim, M. M.; van Hest, M. F. A. M.; Beard, M. C.; Shaheen, S. E.; Berry, J. J.; Yan, Y.; Zhu, K. Carrier Lifetimes of > 1 Ms in Sn-Pb Perovskites Enable Efficient All-Perovskite Tandem Solar Cells. *Science (Washington, DC, U. S.)* **2019**, *364* (6439), 475−479.

(17) Ávila, J.; Momblona, C.; Boix, P. P.; Sessolo, M.; Bolink, H. J. Vapor-Deposited Perovskites: The Route to High-Performance Solar Cell Production? *Joule* **2017**, *1* (3), 431−442.

(18) Ávila, J.; Momblona, C.; Boix, P.; Sessolo, M.; Anaya, M.; Lozano, G.; Vandewal, K.; Miguez, H.; Bolink, H. J. High Voltage Vacuum-Deposited $CH_3NH_3PbI_3$-$CH_3NH_3PbI_3$ Tandem Solar Cells. *Energy Environ. Sci.* **2018**, *11* (11), 3292−3297.

(19) Momblona, C.; Gil-Escrig, L.; Bandiello, E.; Hutter, E. M.; Sessolo, M.; Lederer, K.; Blochwitz-Nimoth, J.; Bolink, H. J. Efficient

Vacuum Deposited P-i-n and n-i-p Perovskite Solar Cells Employing Doped Charge Transport Layers. *Energy Environ. Sci.* **2016**, *9* (11), 3456−3463.
(20) Gil-Escrig, L.; Momblona, C.; La-Placa, M. G.; Boix, P. P.; Sessolo, M.; Bolink, H. J. Vacuum Deposited Triple-Cation Mixed-Halide Perovskite Solar Cells. *Adv. Energy Mater.* **2018**, *8* (14), 1703506.
(21) Igual-Muñoz, A. M.; Ávila, J.; Boix, P. P.; Bolink, H. J. FAPb 0.5 Sn 0.5 I 3: A Narrow Bandgap Perovskite Synthesized through Evaporation Methods for Solar Cell Applications. *Sol. RRL* **2020**, *4* (2), 1900283.
(22) Kumar, M. H.; Dharani, S.; Leong, W. L.; Boix, P. P.; Prabhakar, R. R.; Baikie, T.; Shi, C.; Ding, H.; Ramesh, R.; Asta, M.; Graetzel, M.; Mhaisalkar, S. G.; Mathews, N. Lead-Free Halide Perovskite Solar Cells with High Photocurrents Realized through Vacancy Modulation. *Adv. Mater.* **2014**, *26* (41), 7122−7127.
(23) Ball, J.; Buizza, L.; Sansom, H.; Farrar, M.; Klug, M.; Borchert, J.; Patel, J. B.; Herz, L. M.; Johnston, M. B.; Snaith, H. J. Dual-Source Co-Evaporation of Low-Bandgap FA1-XCsxSn1-YPbyI3 Perovskites for Photovoltaics. *ACS Energy Lett.* **2019**, *4*, 2748−2756.
(24) Liu, X.; Yang, Z.; Chueh, C. C.; Rajagopal, A.; Williams, S. T.; Sun, Y.; Jen, A. K. Y. Improved Efficiency and Stability of Pb-Sn Binary Perovskite Solar Cells by Cs Substitution. *J. Mater. Chem. A* **2016**, *4* (46), 17939−17945.
(25) Zhu, Z.; Li, N.; Zhao, D.; Wang, L.; Jen, A. K. Y. Improved Efficiency and Stability of Pb/Sn Binary Perovskite Solar Cells Fabricated by Galvanic Displacement Reaction. *Adv. Energy Mater.* **2019**, *9* (7), 1802774.
(26) Niu, G.; Li, W.; Li, J.; Liang, X.; Wang, L. Enhancement of Thermal Stability for Perovskite Solar Cells through Cesium Doping. *RSC Adv.* **2017**, *7* (28), 17473−17479.
(27) Li, R.; Yi, C.; Ge, R.; Zou, W.; Cheng, L.; Wang, N.; Wang, J.; Huang, W. Room-Temperature Electroluminescence from Two-Dimensional Lead Halide Perovskites. *Appl. Phys. Lett.* **2016**, *109* (15), 151101.
(28) Dänekamp, B.; Droseros, N.; Palazon, F.; Sessolo, M.; Banerji, N.; Bolink, H. J. Efficient Photo- and Electroluminescence by Trap States Passivation in Vacuum-Deposited Hybrid Perovskite Thin Films. *ACS Appl. Mater. Interfaces* **2018**, *10* (42), 36187−36193.
(29) Song, Z.; Watthage, S. C.; Phillips, A. B.; Tompkins, B. L.; Ellingson, R. J.; Heben, M. J. Impact of Processing Temperature and Composition on the Formation of Methylammonium Lead Iodide Perovskites. *Chem. Mater.* **2015**, *27* (13), 4612−4619.
(30) McMeekin, D. P.; Mahesh, S.; Noel, N. K.; Klug, M. T.; Lim, J. C.; Warby, J. H.; Ball, J. M.; Herz, L. M.; Johnston, M. B.; Snaith, H. J. Solution-Processed All-Perovskite Multi-Junction Solar Cells. *Joule* **2019**, *3* (2), 387−401.
(31) Palazon, F.; Pérez-del-Rey, D.; Dänekamp, B.; Dreessen, C.; Sessolo, M.; Boix, P. P.; Bolink, H. J. Room-Temperature Cubic Phase Crystallization and High Stability of Vacuum-Deposited Methylammonium Lead Triiodide Thin Films for High-Efficiency Solar Cells. *Adv. Mater.* **2019**, *31* (39), 1902692.
(32) Aonuma, M.; Oyamada, T.; Sasabe, H.; Miki, T.; Adachi, C. Material Design of Hole Transport Materials Capable of Thick-Film Formation in Organic Light Emitting Diodes. *Appl. Phys. Lett.* **2007**, *90* (18), 183503.
(33) Wang, K.; Liu, C.; Du, P.; Chen, L.; Zhu, J.; Karim, A.; Gong, X. Efficiencies of Perovskite Hybrid Solar Cells Influenced by Film Thickness and Morphology of CH 3 NH 3 PbI 3-x Cl x Layer. *Org. Electron.* **2015**, *21*, 19−26.
(34) Yang, Z.; Rajagopal, A.; Jen, A. K. Y. Ideal Bandgap Organic-Inorganic Hybrid Perovskite Solar Cells. *Adv. Mater.* **2017**, *29* (47), 1704418.
(35) Liu, D.; Gangishetty, M. K.; Kelly, T. L. Effect of $CH_3NH_3PbI_3$ Thickness on Device Efficiency in Planar Heterojunction Perovskite Solar Cells. *J. Mater. Chem. A* **2014**, *2* (46), 19873−19881.
(36) Contreras-Bernal, L.; Ramos-Terrón, S.; Riquelme, A.; Boix, P. P.; Idígoras, J.; Mora-Seró, I.; Anta, J. A. Impedance Analysis of Perovskite Solar Cells: A Case Study. *J. Mater. Chem. A* **2019**, *7* (19), 12191−12200.
(37) Zarazua, I.; Han, G.; Boix, P. P.; Mhaisalkar, S.; Fabregat-Santiago, F.; Mora-Seró, I.; Bisquert, J.; Garcia-Belmonte, G. Surface Recombination and Collection Efficiency in Perovskite Solar Cells from Impedance Analysis. *J. Phys. Chem. Lett.* **2016**, *7* (24), 5105−5113.
(38) Yoo, S.-M.; Yoon, S. J.; Anta, J. A.; Lee, H. J.; Boix, P. P.; Mora-Seró, I. An Equivalent Circuit for Perovskite Solar Cell Bridging Sensitized to Thin Film Architectures. *Joule* **2019**, *3* (10), 2535.
(39) Zarazua, I.; Bisquert, J.; Garcia-Belmonte, G. Light-Induced Space-Charge Accumulation Zone as Photovoltaic Mechanism in Perovskite Solar Cells. *J. Phys. Chem. Lett.* **2016**, *7* (3), 525−528.
(40) Contreras, L.; Idígoras, J.; Todinova, A.; Salado, M.; Kazim, S.; Ahmad, S.; Anta, J. A. Specific Cation Interactions as the Cause of Slow Dynamics and Hysteresis in Dye and Perovskite Solar Cells: A Small-Perturbation Study. *Phys. Chem. Chem. Phys.* **2016**, *18* (45), 31033−31042.
(41) Ebadi, F.; Taghavinia, N.; Mohammadpour, R.; Hagfeldt, A.; Tress, W. Origin of Apparent Light-Enhanced and Negative Capacitance in Perovskite Solar Cells. *Nat. Commun.* **2019**, *10* (1), 1574.
(42) Moia, D.; Gelmetti, I.; Calado, P.; Fisher, W.; Stringer, M.; Game, O.; Hu, Y.; Docampo, P.; Lidzey, D.; Palomares; Nelson, J.; Barnes, P. R.F. Ionic-to-Electronic Current Amplification in Hybrid Perovskite Solar Cells: Ionically Gated Transistor-Interface Circuit Model Explains Hysteresis and Impedance of Mixed Conducting Devices. *Energy Environ. Sci.* **2019**, *12* (4), 1296−1308.
(43) Pockett, A.; Eperon, G. E.; Peltola, T.; Snaith, H. J.; Walker, A.; Peter, L. M.; Cameron, P. J. Characterization of Planar Lead Halide Perovskite Solar Cells by Impedance Spectroscopy, Open-Circuit Photovoltage Decay, and Intensity-Modulated Photovoltage/Photocurrent Spectroscopy. *J. Phys. Chem. C* **2015**, *119* (7), 3456−3465.
(44) Jacobs, D. A.; Shen, H.; Pfeffer, F.; Peng, J.; White, T. P.; Beck, F. J.; Catchpole, K. R. The Two Faces of Capacitance: New Interpretations for Electrical Impedance Measurements of Perovskite Solar Cells and Their Relation to Hysteresis. *J. Appl. Phys.* **2018**, *124* (22), 225702.
(45) Pitarch-Tena, D.; Ngo, T. T.; Vallés-Pelarda, M.; Pauporté, T.; Mora-Seró, I. Impedance Spectroscopy Measurements in Perovskite Solar Cells: Device Stability and Noise Reduction. *ACS Energy Lett.* **2018**, *3* (4), 1044−1048.

https://dx.doi.org/10.1021/acsaem.9b02413
ACS Appl. Energy Mater. 2020, 3, 2755−2761

SUPPORTING INFORMATION

Vacuum-Deposited Multication Tin-Lead Perovskite Solar Cells

Ana M. Igual-Muñoz[1], Aroa Castillo[1], Chris Dreessen[1], Pablo P. Boix*[2], and Henk J. Bolink*[1].

[1] Instituto de Ciencia Molecular, Universidad de Valencia, C/J. Beltran 2, 46980 Paterna, Spain.

[2] Institut de Ciència dels Materials, Universitat de València, C/ J. Beltran 2, 46980 Paterna, Spain.

*E-mail: Pablo.P.Boix@uv.es; henk.bolink@uv.es

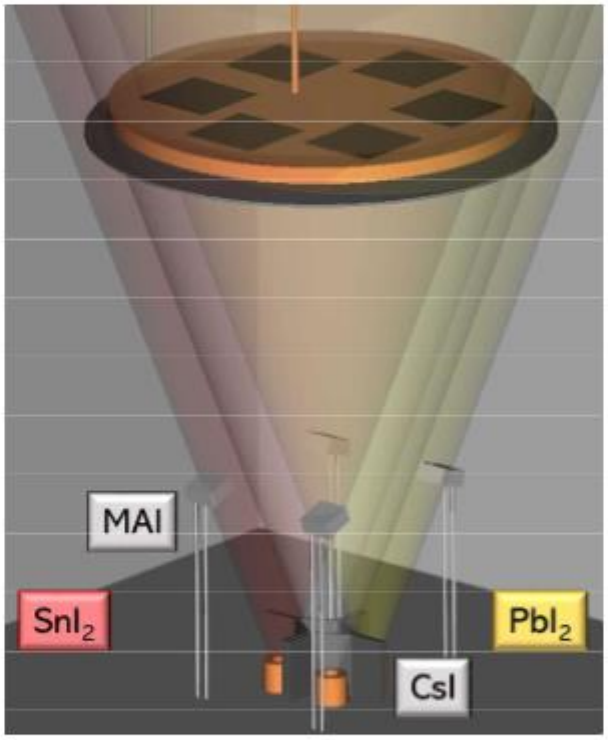

Figure S1. Scheme of the evaporator machine.

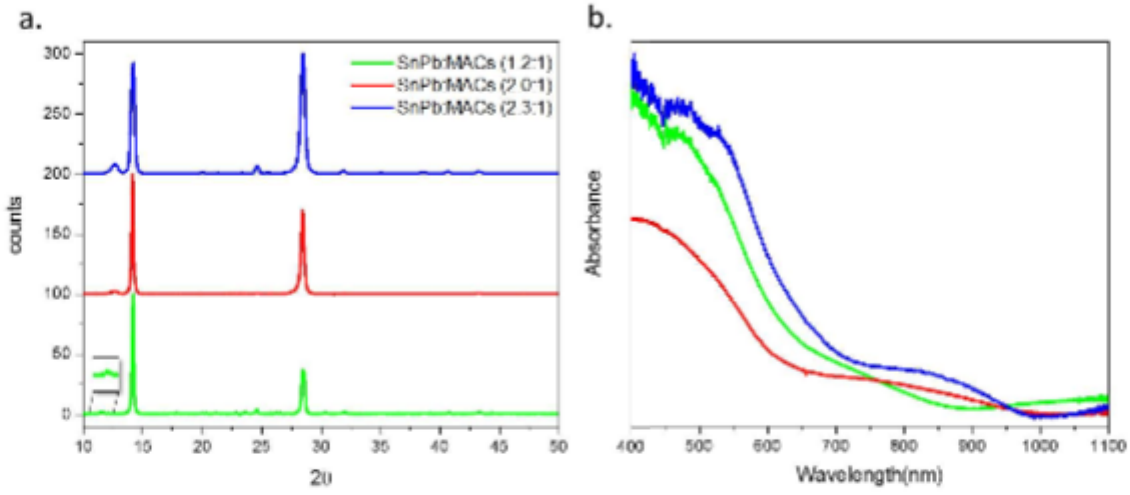

Fig. S2. a) XRD diagrams and b) absorbance of $MA_{0.9}Cs_{0.1}Sn_{0.25}Pb_{0.75}I_3$ films with different SnPb:MACs ratios.

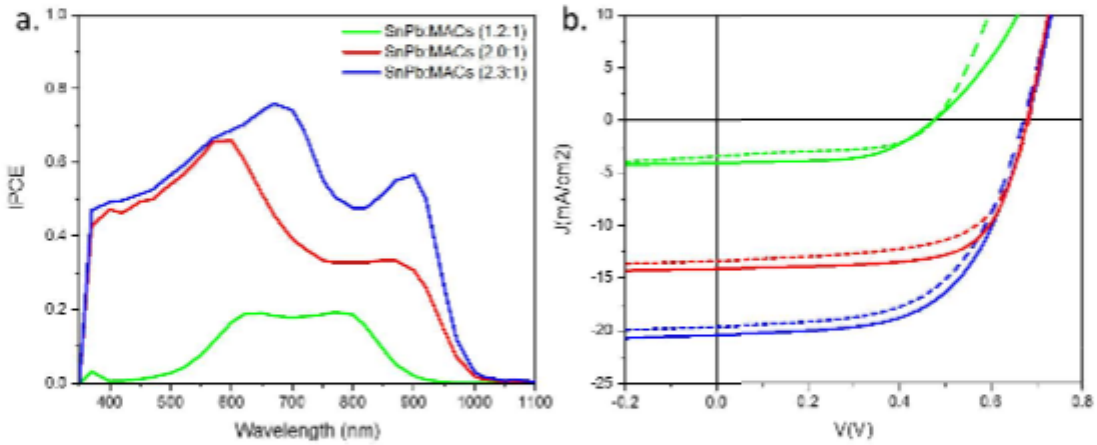

Fig. S3. (a) External quantum efficiency (EQE) and (b) JV measurement under light conditions for the solar cells made with different SnPb to MACs ratios. Dashed lines represent backward measurements and solid lines represent forward measurements (from negative to positive potential).

Table S1. Photovoltaic parameters under AM1.5G illumination measured for the solar cells represented in Fig. S2.

Ratio (SnPb:MACs)	FF (%)	J_{sc} (mA/cm^2)	V_{oc} (mV)	PCE (%)
1.2:1	57	3.7	477	1.0
2.0:1	66	13.7	681	6.1

2.3:1	59	21.1	673	8.4

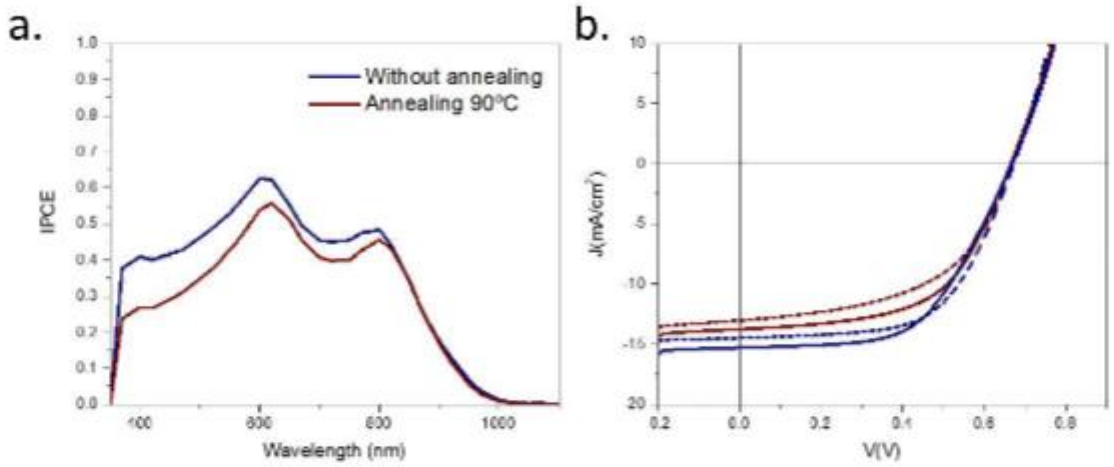

Fig. S4. J-V characteristics measured in light conditions for cells prepared with and without thermal post-treatment of 90ºC for 5 minutes.

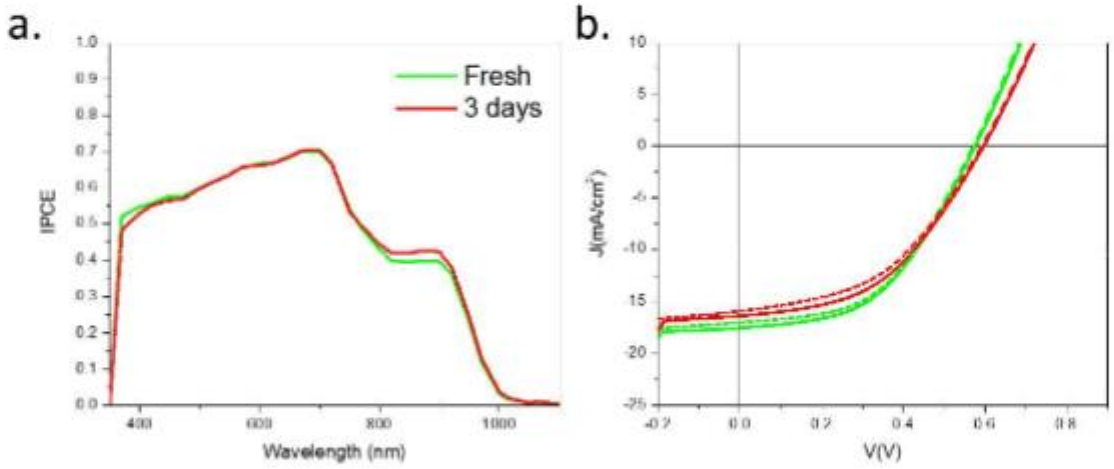

Fig. S5. J-V characteristics measured in light conditions for cells as prepared and after three days of storage in a glovebox containing N_2.

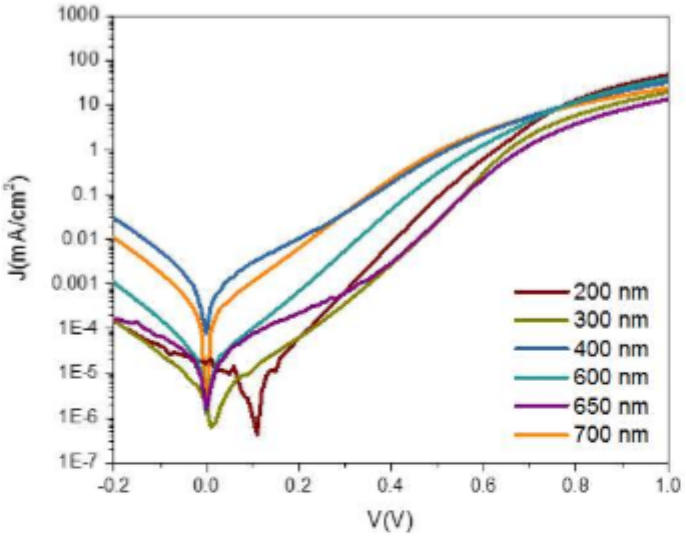

Fig. S6. J-V characteristics measured in dark conditions for the representative devices with different thicknesses.

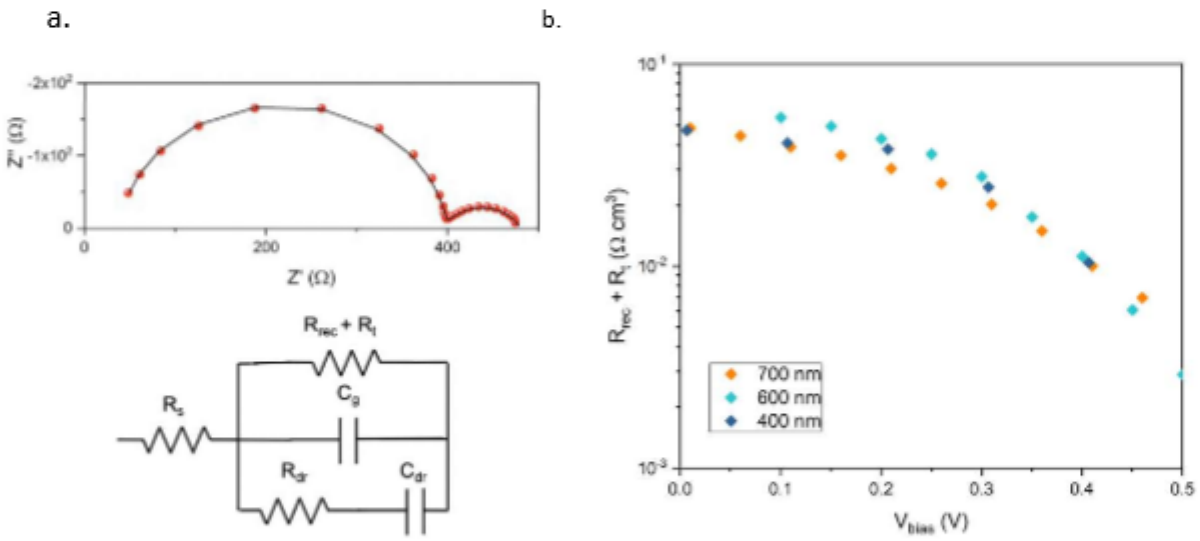

Fig. S7. (a) Representative Nyquist plot obtained for the 600 nm sample under 0.5 sun illumination. The dots correspond to the experimental data and the solid line is the fitting using the equivalent circuit in (b). (c) Volumetric normalization of R_{rec} + R_t.

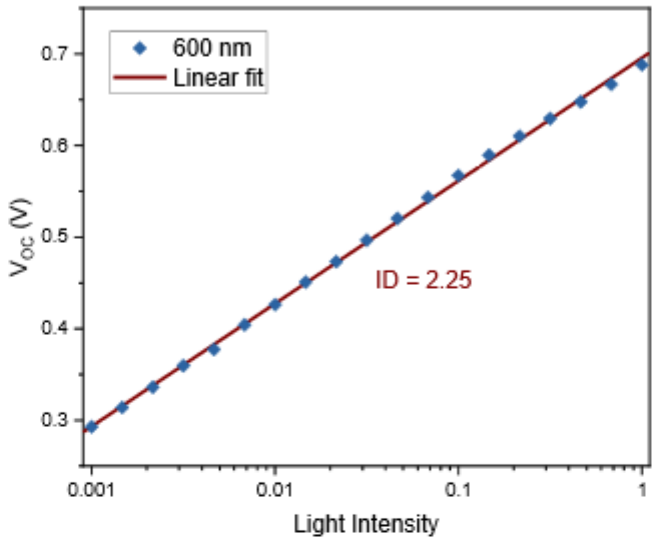

Figure S8. Voc vs the logarithm of light intensity for the determination of the ideality factor. Note that a light intensity of 1 corresponds to more than one sun illumination.

Appendix C

Room-Temperature Vacuum Deposition of $CsPbI_2Br$ Perovskite Films from Multiple Sources and Mixed Halide Precursors

CHEMISTRY OF MATERIALS

pubs.acs.org/cm

Article

Room-Temperature Vacuum Deposition of $CsPbI_2Br$ Perovskite Films from Multiple Sources and Mixed Halide Precursors

Ana M. Igual-Muñoz, Javier Navarro-Alapont, Chris Dreessen, Francisco Palazon, Michele Sessolo,* and Henk J. Bolink

Cite This: *Chem. Mater.* 2020, 32, 8641−8652

Read Online

ACCESS | Metrics & More | Article Recommendations | Supporting Information

ABSTRACT: Fully inorganic cesium lead halide perovskites, such as $CsPbI_2Br$, show enhanced thermal stability compared to hybrid ones and are being widely investigated as wide bandgap absorbers for tandem applications. Despite their simple stoichiometry, the preparation of highly crystalline and stable cesium lead halide thin films is not trivial. In general, high-efficiency solar cells based on solution-processed $CsPbI_2Br$ thin films are prepared by high-temperature annealing or the use of chemical additives. In this work, we use solvent-free synthesis to investigate the formation of $CsPbI_2Br$ in bulk or in thin films via mechanochemical synthesis and multiple-source vacuum deposition, respectively. We demonstrate the importance of fostering halide alloying in the vacuum processing of inorganic lead halide perovskites, which can be attained either by using mixed halide precursors or by increasing the number of precursors (and hence deposition sources). These strategies lead to highly oriented perovskite films even at room temperature, with improved optoelectronic properties. We obtained promising power conversion efficiencies of 8.3% for solar cells employing as-deposited perovskites (without any annealing) and 10.0% for devices based on $CsPbI_2Br$ annealed at low temperatures (150 °C). This study allowed us to highlight the most promising processes and strategies to further optimize the material deposition as well as the solar cell architecture.

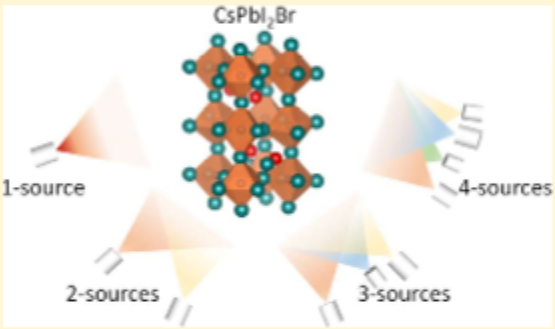

■ INTRODUCTION

Organic−inorganic (hybrid) perovskites have become one of the most promising semiconductors for application in photovoltaics (PV), since the first perovskite solar cells were reported in 2009.[1] Nowadays, the power conversion efficiencies (PCEs) of perovskite solar cells have improved up to 25% for single junction and to 28% for tandem devices with silicon.[2] Those solar cells are based on perovskite absorbers using a combination of, at least, methylammonium and formamidinium cations.[3,4] These cations might undermine the thermal stability of the material, which can be partially recovered by their substitution with cesium (Cs^+).[5−7] In general, fully inorganic, cesium lead halide perovskites show enhanced thermal stability compared to hybrid ones.[8−10] They are especially interesting for tandem applications because of their wide bandgaps of about 1.7 eV for $CsPbI_3$ and 1.9 eV for the archetypical mixed halide $CsPbI_2Br$.[11,12] In view of these characteristics, inorganic lead halide perovskites are being widely investigated.[13−17] As a result, perovskite solar cells employing inorganic perovskite absorbers have currently achieved PCEs exceeding 18% for pure iodide and over 16% for mixed halide compounds.[18−21]

Despite their simple stoichiometry, the preparation of highly crystalline and stable cesium lead halide thin films is not trivial. The stable phase at room temperature (RT) for $CsPbI_3$ is an insulating, orthorhombic phase ("yellow" phase), and the perovskite ("black") phase can only be obtained upon annealing at high temperatures (>300 °C).[22−24] The inclusion of bromide, as in $CsPbI_2Br$, favors the stabilization of the perovskite phase at lower temperatures, although it implies a widening of the bandgap as a consequence of the substitution of iodide with a more electronegative halide.[11,25−28] In general, high-efficiency (>15%) solar cells based on solution-processed $CsPbI_2Br$ thin films are prepared with thermal treatments at temperatures ranging from 150 to 300 °C. Additionally, in most cases, other synergistic approaches are used to foster the perovskite crystallization from solution, such as the addition of group 1 and group 2 ions,[29−33] divalent transition metals,[34−39]

Received: July 22, 2020
Revised: September 14, 2020
Published: September 15, 2020

https://dx.doi.org/10.1021/acs.chemmater.0c03038
Chem. Mater. 2020, 32, 8641−8652

Scheme 1. Schematics of the Type of Thermal Vacuum Deposition Methods Investigated in the Preparation of $CsPbI_2Br$ Thin Films[a]

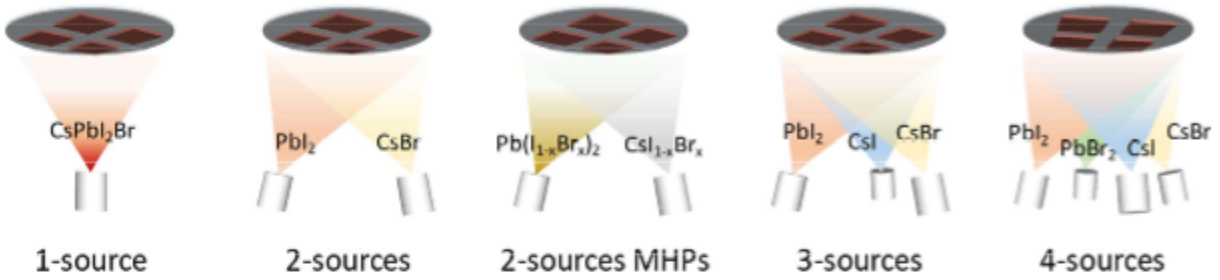

[a]For the deposition from 1-source or 2-source MHPs (x = 1/3), the compounds to be sublimed were prepared by melting. 3-Source vacuum deposition was performed at 0.5 Å/s (3-source slow) and 2.0 Å/s (3-source fast).

Rare earth elements,[40−42] organic cations/anions,[43−48] or the use of interfacial materials promoting the perovskite formation and passivation, notably metal oxides (in particular, ZnO and its derivatives),[49−54] and novel organic hole-transport layers (HTLs).[55−58]

An alternative solvent-free technique to deposit perovskite thin films is thermal vacuum deposition.[59,60] Vacuum deposition methods are intrinsically additive (suitable for tandem devices)[61−63] and can be used to deposit highly crystalline perovskite films at RT.[64] Importantly, vacuum deposition allows the preparation of perovskite films with controllable thickness (not limited by the solubility of the precursors)[65−67] and composition,[68−71] although the latter might be limited by the number of available deposition sources, as well as by the available stable single-phase compounds in the compositional phase space. The formation of perovskite films by thermal vacuum deposition differs substantially from solution processing because of the absence of solvents, intermediate species, and distinctive crystallization kinetics as a function of stoichiometry and temperature.[72−74] Vacuum-deposited, cesium lead halide perovskite films and solar cells have also been investigated. In particular, $CsPbI_3$ as well as $CsPbI_2Br$ films have been prepared by dual-source vacuum deposition and applied to solar cells.[75−79] Stabilization of the perovskite $CsPbI_3$ phase has been achieved by working with Cs-rich compositions and by simultaneous heating of the substrate holder during deposition.[80] Alternatively, the sequential deposition of multiple very thin films of CsX and PbX_2 (X = I, Br) has also been proven to be a reliable method to obtain stable and crystalline films,[81] with $CsPbI_2Br$ solar cells exhibiting a record efficiency of 13%.[82] In all these cases, however, the as-deposited films were annealed at temperatures ranging from 260 to 320 °C, which might limit their compatibility with temperature-sensitive substrates, such as textiles or plastic foils,[83] and with narrow-bandgap perovskite absorbers when targeting tandem solar cells.

In this work, we study the properties of $CsPbI_2Br$ films prepared by thermal vacuum deposition. We focus on films deposited at RT and with mild annealing at 150 °C, which would be compatible with the aforementioned applications. We compare the properties of perovskite films deposited by single-, dual-, triple-, and quadruple sources using CsI, CsBr, PbI_2, and $PbBr_2$ as precursors (Scheme 1). We also use another solvent-free method to prepare perovskite powders, mechanochemical synthesis,[84] to demonstrate the challenges in achieving alloyed halide compounds. Finally, we prepared fully vacuum-deposited solar cells, obtaining promising PCEs of 8% for $CsPbI_2Br$ films prepared at RT and 10% for those annealed at 150 °C.

RESULTS AND DISCUSSION

In order to evaluate the stability and the ease of formation of $CsPbI_2Br$, we initially tested mechanochemical synthesis, ball-milling the CsBr and PbI_2 precursors. We have previously shown the mechanochemical synthesis of cesium lead trihalide perovskite $CsPbX_3$ (X = I, Br, and Cl) powders, as well as their single-source vacuum deposition into highly crystalline thin films.[85] In those experiments, we showed that $CsPbI_3$ was not obtained in its perovskite phase by ball-milling of the precursors. This observation suggests that it might also be challenging to obtain the mixed halide $CsPbI_2Br$ by mechanochemical synthesis at RT. Indeed, when ball-milling an equimolar amount of CsBr and PbI_2 at RT, we obtained a mixture of different phases, as evidenced by X-ray diffraction (XRD, Figure S1). The diffractogram of the ball-milled sample can be fitted considering the coexistence of two phases, a perovskite and a non-perovskite one. The presence of the two phases is apparent considering the low-angle diffractions (2θ = 10−15°), where the first peak around 2θ = 10° cannot be ascribed to the perovskite phase, which is characterized by the reflections around 2θ = 14°. While both phases correspond to the same space group (62; orthorhombic crystal system), one maintains the overall 3D perovskite structure with a slight distortion of the PbX_6 octahedra, while the "non-perovskite" phase consists of partially disconnected PbX_6 octahedra (Figure S2).[86] As the distorted perovskite phase is the most commonly reported one for $CsPbBr_3$ at RT and the non-perovskite (sometimes called "yellow phase") is the most commonly found for $CsPbI_3$, it could be thought that our ball-milled sample consists of a mixture of pure-bromide and pure-iodide phases (i.e., $CsPbBr_3$ + $CsPbI_3$). Nevertheless, the lattice parameters obtained for both phases formed by mechanochemical synthesis are clearly different than those expected for pure-halide compounds (see Table S1). In particular, the perovskite phase shows lattice constants larger than the reference $CsPbBr_3$, pointing to the incorporation of the larger I^- anion. Similarly, the non-perovskite phase shows lattice parameters slightly smaller than the reference $CsPbI_3$, suggesting the incorporation of the smaller Br^- anion. These observations imply that alloying of halides occurs in both the non-perovskite and perovskite phases. Previous reports on the mechanochemical synthesis of mixed iodide/bromide CsPb-

https://dx.doi.org/10.1021/acs.chemmater.0c03038
Chem. Mater. 2020, 32, 8641−8652

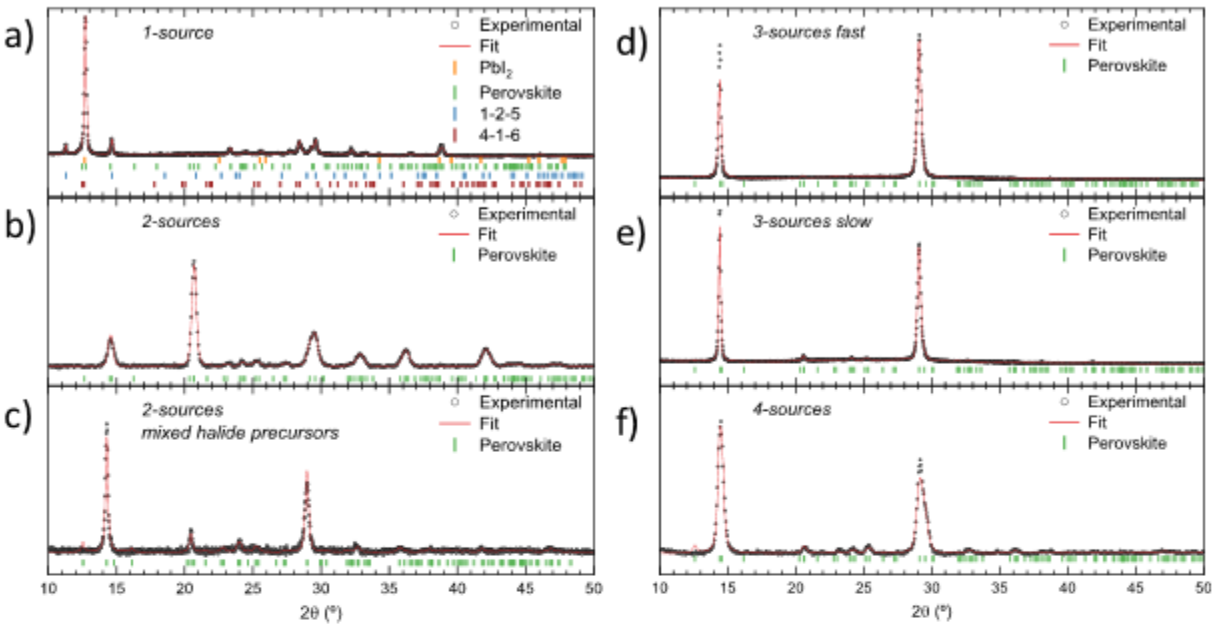

Figure 1. XRD pattern obtained from $CsPbI_2Br$ thin films deposited with several different vacuum deposition techniques (as indicated in each graph). Open circles are raw data, red lines are whole-pattern Le Bail fits, and vertical lines represent calculated Bragg's reflections for different phases. Slight differences in the measurement conditions prevent relating the peak width to microstructural properties (e.g., grain size) of the samples.

$(I_{1-x}Br_x)_3$ perovskites also mentioned that these compounds cannot be obtained at RT but only after annealing at elevated temperatures (>250 °C).[87] In our case, we were not able to obtain phase-pure $CsPbI_2Br$ even after melting of the two precursors at 650 °C in a nitrogen atmosphere (Figure S1). A possible origin of the different reaction routes is that all our experiments are carried out in an inert atmosphere (nitrogen-filled glovebox), while the previously reported mechanochemical synthesis was done in air. The XRD patterns of the melted sample closely resemble those of the ball-milled compound, with the addition of a new phase corresponding to Cs_4PbX_6 (labeled "4-1-6" for simplicity). The occurrence of this phase is mostly visible by the new (although relatively weak) peaks at 2θ = 12.0−12.5°. Several previous reports have observed the appearance of this phase and its possible conversion into or from $CsPbX_3$ under different conditions.[88−90] In both samples obtained by mechanochemical synthesis and melting, the presence of the perovskite phase can also be identified by its optical absorption (Figure S3), which corresponds to the band-to-band transition of $CsPbI_2Br$ at approximately 1.85−1.90 eV.

In order to prepare thin films, we initially tested the single-source (referred to as "1-source") vacuum deposition of the as-prepared ball-milled and melted compounds obtained by the solid-state reaction of CsBr and PbI_2 in stoichiometric proportions. The materials were loaded into a ceramic crucible and rapidly heated in vacuum (5 °C/s, base pressure: 10^{-6} mbar) up to the maximum temperature compatible with our setup, 750 °C. The fast-heating ramp and the high-target temperature were chosen to minimize the decomposition of the material into its precursors, which have different volatilities (Melting points at ambient pressure for PbI_2 and CsBr are 410 and 636 °C, respectively).[91] The resulting films were initially analyzed by XRD (Figure 1a), showing the coexistence of several phases with a predominance of PbI_2, whose main peak appears at 2θ = 12.8°. Other phases present in the films include the desired $CsPbX_3$ perovskite phase as well as the Cs-rich Cs_4PbX_6 (labeled "4-1-6") and Pb-rich $CsPb_2X_5$ (labeled "1-2-5"). Overall, it is evident that single-source deposition leads to a very inhomogeneous composition of this type of compound. The as-deposited films were also analyzed by scanning electron microscopy (SEM, Figure 2a), showing a rather homogeneous morphology, with very fine grains and no relevant features. The bandgap energy (E_g) estimated from the Tauc plot of the corresponding optical absorbance (Figure 3) is 1.94 eV, which is slightly higher compared to the powders as a consequence of PbI_2 segregation (the perovskite phase is hence bromide-rich). Subsequently, we performed the dual-source vacuum deposition (referred to as "2-sources") of $CsPbI_2Br$, consisting of the simultaneous sublimation of CsBr and PbI_2 upon calibration of their respective deposition rates. The XRD pattern of an as-deposited film (Figure 1b) is mainly composed of a pure perovskite phase, without any preferential orientation, which is characteristic of powders with similar compositions.[87,92] The lack of orientation, otherwise observed for cesium lead halides and other vacuum-deposited perovskite films,[93,94] might be related to the porosity observed by SEM (Figure 2b), suggesting a limited connectivity and hence uncorrelated growth of the grains. It is interesting to point out that phase-pure $CsPbI_2Br$ can be readily obtained through vacuum deposition, while it cannot be formed by mechanochemical synthesis even after thermal treatment at 650 °C. The likely main difference is that in vacuum deposition, where atomization/fragmentation of the precursors takes place, the atoms/clusters condense on a cold substrate, essentially freezing the structure and resulting in well-mixed compounds. When heating at high temperatures, the cooling process is slow, resulting in phase segregation, as dictated by thermodynamics. The reaction kinetics are very different as well because by

https://dx.doi.org/10.1021/acs.chemmater.0c03038
Chem. Mater. 2020, 32, 8641−8652

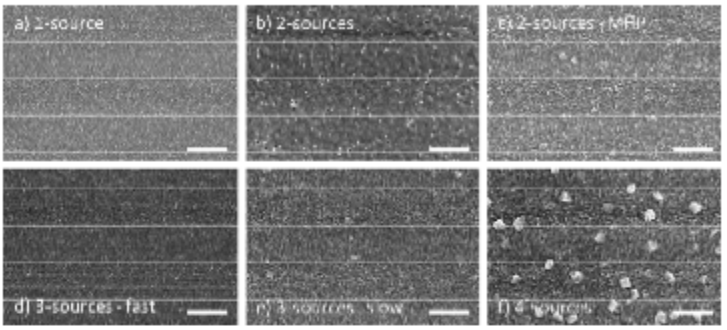

Figure 2. SEM images of the surface of $CsPbI_2Br$ thin films deposited by several different vacuum deposition techniques (as indicated in each graph). Scale bar is 500 nm in all images.

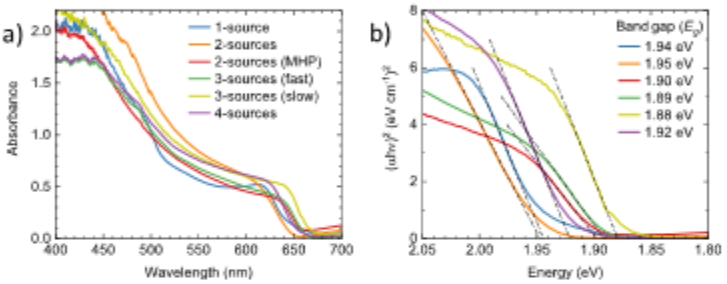

Figure 3. (a) Absorbance and (b) the corresponding Tauc plots (with the estimated bandgap energy) spectra for $CsPbI_2Br$ thin films deposited on glass with several different vacuum deposition techniques. The thickness for all films is 250 nm.

vacuum sublimation, the atomic fragments deposit with a high kinetic energy, whereas the heating after mechanochemical synthesis is done without friction.

Although the unit cell volume for the 2-source $CsPbI_2Br$ (907 Å^3) confirms halide mixing in the as-deposited films (it is larger than that of pure $CsPbBr_3$, 797 Å^3), we decided to investigate the dual-source deposition starting from mixed halide precursors (MHPs). Prealloying of halides in the precursors might help the formation of a perovskite with a more homogeneous structure. For this, we carried out the solid-state reactions by mixing $PbBr_2$ with PbI_2 and CsBr with CsI in 1:2 molar ratios in both cases. The ratio was chosen in view of the desired $CsPbI_2Br$ perovskite stoichiometry, where the Br/I ratio is also 1:2. The XRD patterns of the as-prepared compounds, both ball-milled or melted, are shown in Figures S5 and S6. We observed that after reaction, the reflections belonging to CsI and CsBr are shifted to higher and lower angles, respectively, indicating the incorporation of bromide into CsI and vice versa (Figure S5). On the other hand, an alloyed $Pb(I_{1-x}Br_x)_2$ phase is indeed obtained when reacting PbI_2 and $PbBr_2$, although not quantitatively, as suggested by the presence of XRD peaks of the precursors (Figure S6). These observations confirm that halide alloying is not favored even for these simple binary precursors. Based on the XRD characterization, we chose melting as the technique to prepare the MHPs to be used in dual-source vacuum deposition ("2-source MHP"). The experiment consisted of melting $PbBr_2$ with PbI_2 and CsBr with CsI, in 1:2 molar ratios, in a separated heated crucible in a vacuum chamber (not evacuated under a nitrogen atmosphere). After melting and cooling to RT, the chamber was evacuated to 10^{-6} mbar and the MHPs were codeposited using the calibration factors previously calculated for the 2-source deposition while maintaining the substrates at RT. Remarkably, the films obtained from MHPs consist of phase-pure $CsPbI_2Br$, with preferred orientation along the (110) and (002) directions (Figure 1c), that is, perpendicular to the substrate surface. The as-deposited films also show a more compact morphology (compared to those prepared by 2-source deposition of the single-halide precursors), with small but well-defined grains homogeneously organized on the sample surface (Figure 2c). The low unit cell volume (891 Å^3) and phase purity suggest homogeneous halide mixing, resulting in a bandgap energy of 1.90 eV (Figure 3). Hence, it seems that fostering halide alloying can indeed enhance the quality of mixed halide perovskite deposited by vacuum methods.

One of the possible drawbacks of depositing MHPs is the formation of films with a compositional gradient, as the high-vapor pressure constituent vaporizes more rapidly than the low-vapor pressure material.[95] This might happen as CsI and PbI_2 have larger vapor pressures as compared to their bromide analogues.[96] An alternative way to enhance halide alloying and homogeneity in perovskite vacuum deposition is the use of more than two deposition sources.[97] Hence, we investigated a 3-source deposition process, consisting of the simultaneous sublimation of CsI, CsBr, and PbI_2 from separate thermal sources. In vacuum deposition of compounds, such as metal halides, the material might vaporize with a range of species, from atoms to clusters of molecules to dissociated or partially dissociated molecules. These small fragments then condense and react with each other on the substrate surface forming a solid film. In the process, the deposition rate plays a crucial role, as an excessively fast evaporation would result in an increased content of amorphous material. We therefore tested the 3-source vacuum deposition of $CsPbI_2Br$ at different deposition rates (measured at the substrate): 2.0 Å/s ("3-source fast") and 0.5 Å/s ("3-source slow"), with the substrates

https://dx.doi.org/10.1021/acs.chemmater.0c03038
Chem. Mater. 2020, 32, 8641−8652

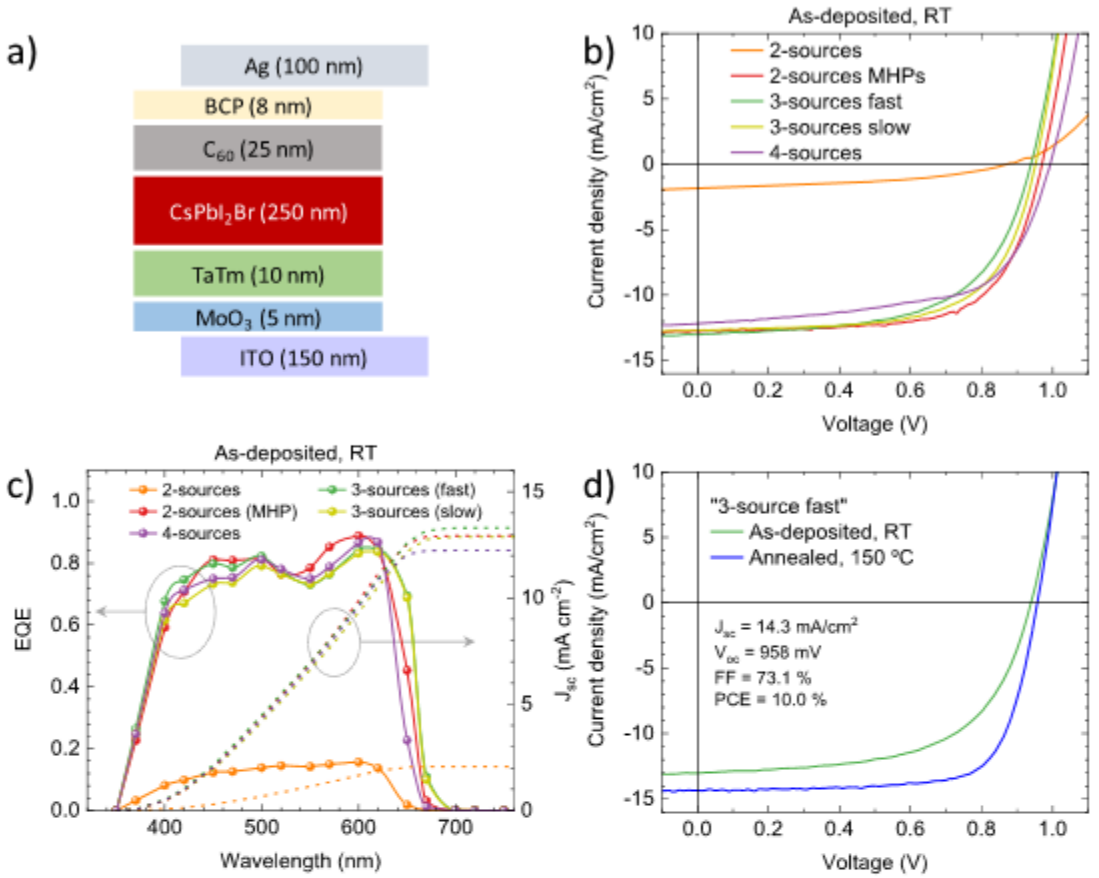

Figure 4. (a) Solar cell layout, (b) $J-V$ curves under illumination, and (c) EQE spectra for a series of solar cells employing $CsPbI_2Br$ deposited at RT with different vacuum techniques. The corresponding short circuit current density, obtained by integration of each EQE spectra over the reference AM1.5 solar irradiance spectrum, is reported on the right axis. (d) $J-V$ curves of solar cells with $CsPbI_2Br$ prepared by 3-source vacuum deposition at the rate of 2.0 Å/s (fast), either at RT (green) or by annealing at 150 °C for 5 min (blue).

kept at RT. The diffractograms of both compounds (Figure 1d,e) show a phase-pure perovskite with high crystallinity and no signs of precursors or derivatives. Both samples have a strong preferential orientation along the (110) and (002) directions, with the perovskite film deposited at a slow rate showing narrower diffraction peaks, which might suggest the presence of larger crystallites. Although not apparent, this fact might be correlated with the improved morphology of $CsPbI_2Br$ deposited at 0.5 Å/s (Figure 2e), when compared with the film deposited at 2.0 Å/s (Figure 2c). These films exhibit very similar bandgap energies of 1.88 eV (slow) and 1.89 eV (fast), with the "3-source slow" layers showing a more intense optical absorption (for the same thickness of 250 nm) over the whole spectral region (Figure 3).

A complementary 3-source deposition scheme, which can also lead to the formation of $CsPbI_2Br$ films, consists of the simultaneous sublimation of CsI, PbI_2, and $PbBr_2$. The as-prepared films obtained through this process showed the expected absorption profile and bandgap (1.93 eV, Figure S7a,b), confirming the formation of the perovskite phase at RT, using mixed lead halide precursors. However, in this case, the resulting films were found to be particularly unstable in an ambient atmosphere to a point that we were not able to collect a single XRD scan before complete discoloration and degradation of the sample (Figure S7c). Considering that phase-pure and stable films were obtained using CsI, CsBr, and PbI_2 as precursors (as discussed above), it appears more important to foster halide mixing of the cesium halide precursor, likely in view of the larger lattice energies of the ionic compounds CsI and CsBr, compared to PbI_2 and $PbBr_2$. As a final test, we performed the deposition of $CsPbI_2Br$ employing four sources (cosublimation of CsI, CsBr, PbI_2, and $PbBr_2$) to investigate whether the use of both iodide and bromide precursors for Cs and Pb during the sublimation process provides advantages in the formation of the perovskite film. The XRD pattern (Figure 1f) of as-deposited "4-source" films can again be fitted with a single and pure perovskite phase. However, the presence of several diffraction signals in the range $20° \leq 2\theta \leq 26°$ (and of others at $2\theta > 30°$) indicates that this material has a lower preferential orientation compared to the 2- and 3-source-deposited ones. The surface morphology of films deposited by 4-source vacuum deposition shows a homogeneous coverage with very fine grains (diameter < 50 nm), and the formation of cuboids with edges of approximately 100 nm (the low dimensions of these structure prohibit their structural/compositional analysis). Similar structures, although much scarcer and smaller, have been observed for the "2-source MHP" and the "3-source slow"

https://dx.doi.org/10.1021/acs.chemmater.0c03038
Chem. Mater. 2020, 32, 8641−8652

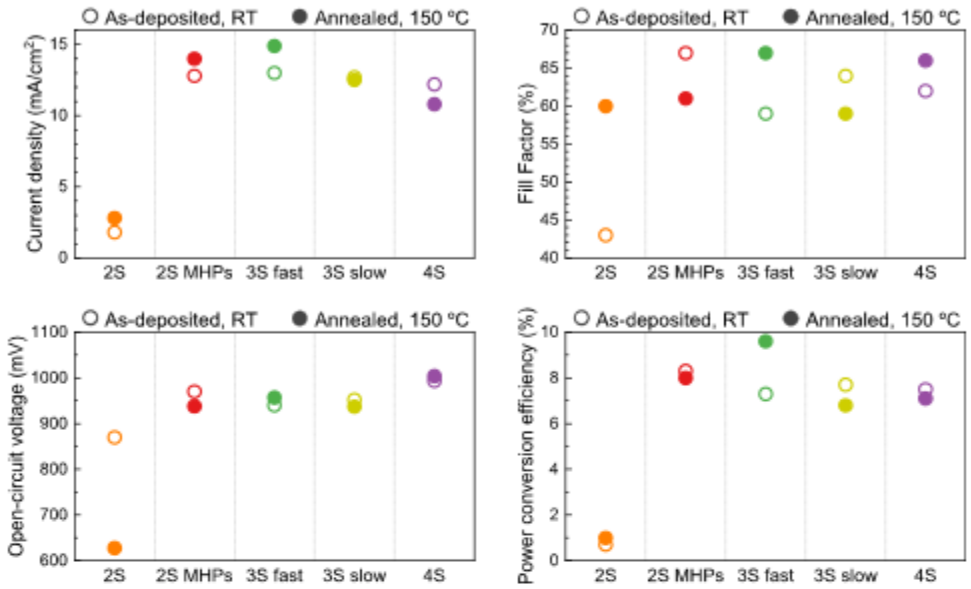

Figure 5. PV parameters extracted from $J-V$ scans in reverse bias (from open to short circuit) for solar cells with $CsPbI_2Br$ films either as-deposited (empty symbols) or annealed at 150 °C for 5 min (full symbols).

(Figure 2c,e, respectively), which might suggest that their crystallization is favored either by enhanced halide alloying or slower growth. The absorption onset of the "4-source" $CsPbI_2Br$ is essentially unaltered, showing the excepted E_g = 1.92 eV.

To shortly summarize, we demonstrated the successful RT deposition of $CsPbI_2Br$ films with high crystallinity, preferential orientation, homogeneous morphology, and the expected bandgap of approximately 1.9 eV. This was possible when subliming MHPs or by increasing the number of deposition sources (hence of precursors). In view of the favorable properties of the $CsPbI_2Br$ films presented above, we used them as the light-absorbing layer in fully vacuum-deposited perovskite solar cells. We fabricated p−i−n solar cells with the structure reported in Figure 4a. Briefly, indium tin oxide (ITO) transparent electrodes were coated with MoO_3 (5 nm) to enhance hole transfer between ITO and the HTL, a 10 nm thick film of *N*4,*N*4,*N*4″,*N*4″-tetra([1,1′-biphenyl]-4-yl)-[1,1′:4′,1″-terphenyl]-4,4″-diamine (TaTm, 10 nm). Afterward, a 250 nm thick $CsPbI_2Br$ film was deposited on top with the different sublimation methods described before. We did not evaluate in devices the perovskite films deposited by single-source vacuum deposition ("1-source"), in view of their unfavorable morphological and structural properties. The perovskite films were capped with an electron-transport layer (ETL, C_{60}, 25 nm), and a thin (8 nm) film of bathocuproine (BCP) was used to ensure Ohmic contact in between the ETL and a silver electrode (100 nm thick). The use of such thin selective transport layers in a planar diode configuration is justified by the very homogeneous morphology and very low roughness of the $CsPbI_2Br$ films (Figure S8), which is, in general, a benchmark of vacuum-deposited perovskite films when compared to their solution-processed analogues.

The current density versus voltage characteristics ($J-V$) under simulated solar illumination for the entire series of solar cells are reported in Figure 4b. $J-V$ curves are reported in a reverse voltage scan (from open to short circuit; curves in both scan directions are reported in Figure S10). We noted some extent of hysteresis in the devices, which denotes the presence of both charge accumulation and ionic motion in the device. The characteristic PV parameters extracted from the $J-V$ curves are presented in Figure 5. One can immediately notice how the device with the perovskite deposited from 2-source underperforms as compared to the others. This type of vacuum deposition (cosublimation of CsBr and PbI_2) is the only one reported in the literature and is known to lead to efficient devices only after annealing at high temperatures >260 °C.[79] The corresponding external quantum efficiency (EQE) spectrum shows a very limited photocurrent generation over the whole spectral range. These observations correlate with the poor structural (Figure 1b) and morphological (Figure 2b) features of the material. Improving halide alloying (using MHPs) leads to a strong improvement of the solar cell performance, with good rectification (fill factor, FF > 65%) and open-circuit voltage (V_{oc} = 970 mV). The short-circuit current density (J_{sc}) was found to be as high as 12.8 mA/cm^2, a consequence of the rather constant and high spectral response over the whole visible spectrum (Figure 4c). The resulting PCE was found to be 8.3%, which is remarkable for solar cells based on inorganic lead halide perovskites deposited at RT. From the solar cells prepared with the "3-source" perovskites, we observed similar performance parameters. The J_{sc} was found to be approximately 13 mA/cm^2, which is slightly higher compared to the "2-source MHP"-based devices because of the enhanced response in the red, a consequence of the narrower bandgap (Figure 3b). Interestingly, the FF was found to be higher (65 vs 60%) for solar cells with $CsPbI_2Br$ prepared with the slowest deposition rate (0.5 Å/s, "3-source slow"), suggesting that a slow crystallization might favor charge transport within the film because of the formation of larger crystallites and more oriented materials. However, the observed photovoltage was rather similar for the two devices (940 and 950 mV for the fast and slow depositions,

https://dx.doi.org/10.1021/acs.chemmater.0c03038
Chem. Mater. 2020, 32, 8641−8652

respectively), resulting in similar PCEs of 7.7 and 7.3% for cells using $CsPbI_2Br$ deposited at 0.5 and 2.0 Å/s, respectively. We note that lead halide perovskite thin films have been reported with different orientations, yet without a clear understanding of the factors governing it or of the implications for their optoelectronic properties.[74] Similar efficiency was observed for solar cells using the "4-source"-deposited perovskite, with a lower photocurrent (11 mA/cm^2) but with the largest V_{oc} of 1 V, indicating a reduction of the nonradiative recombination rate. Overall, we can conclude that improved alloying of the different metal halides, either by the synthesis of mixed precursors or through the use of additional deposition sources, can indeed help the formation of high-quality cesium lead halide perovskites at RT. Importantly, we observed that halide alloying results in preferentially oriented films, which leads to the best performance when used in solar cells. Indeed, the only sample (aside from 1-source, which we excluded from this discussion) which is not oriented, the simple 2-source $CsPbI_2Br$, is the one that gives by far the worst PV performance.

We also explored the effect of short annealing at low temperatures (150 °C for 5 min) on the optoelectronic properties of $CsPbI_2Br$ films. We choose this temperature as it would be compatible with most flexible plastic substrates as well as with tandem architectures.[83] The $J-V$ curves under illumination and the corresponding spectral response for the entire series of solar cells with annealed $CsPbI_2Br$ layers are reported in Figure S11 (scans in both directions are reported in Figure S12). The characteristic PV parameters extracted from the $J-V$ curves are presented in Figure 5 together with the RT data.

With this moderate annealing, the J_{sc} was found to be unvaried or slightly increased, and in the latter case, it is due to enhanced response of the devices in the blue region of the spectrum (Figure S11b). On the other hand, the FF decreased by about 5% absolute for the perovskites prepared by 2-sources with MHPs and by 3-sources at a slow rate, while it improved for the other samples. Interestingly, the photovoltage was unvaried upon annealing for all samples except for the simple 2-source-deposited one, confirming that a good perovskite semiconductor is formed already at RT. The overall efficiency was found to be similar for the devices based on $CsPbI_2Br$ with and without annealing, with the exception of those obtained by fast deposition (2 Å/s) from 3-sources. The solar cells based on this material and annealed at 150 °C showed the highest efficiency among the series, with the best pixel having a PCE of 10.0%. Despite the hysteresis observed between $J-V$ scans in forward and reverse biases, the power output measured at the maximum power point was found to be rather stable, with an efficiency of 9.8% over an hour of measurement (Figure S12f). In view of the superior thermal stability of inorganic perovskite (compared to the hybrid counterparts), we evaluated the stability of unencapsulated solar cells in an inert atmosphere and at continuous thermal stress at 85 °C. The best solar cell configuration (3-source fast, annealed at 150 °C) was found to retain 90% of the initial power efficiency after 10 days at 85 °C in the dark (Figure S13).

In spite of the promising performance of the low-temperature-deposited $CsPbI_2Br$ solar cells, their efficiency is far from the maximum theoretical one (approximately 25% for a bandgap of 1.9 eV).[98] To shed light on the limitations of the devices, we investigated the EQE in the bandgap region and the photoluminescence (PL) response (Figure 6) of the best working device based on annealed "3-source fast" perovskites (the corresponding $J-V$ characteristics are shown in Figure 4d). From the sensitive EQE measurement, one can extract the bandgap E_g, the radiative limit of the open-circuit voltage $V_{oc,rad}$, and the Urbach energy E_U, assuming that the EQE scales linearly with absorption (see Table 1).[99,100] The

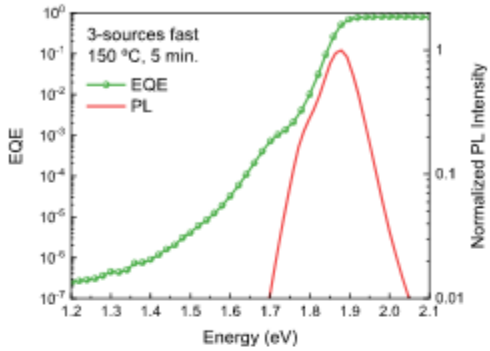

Figure 6. Sensitive EQE spectrum and PL measurements of the solar cell based on the $CsPbI_2Br$ film prepared by 3-source fast vacuum deposition with annealing.

Table 1. Solar Cell Parameters for the Device with "3-Source-Fast" $CsPbI_2Br$ Annealed at 150 °C in the Radiative Limit and Comparison with the Measured Values[a]

E_g/q (V)	1.870	E_U (meV)	17.96
V_{oc},rad (V)	1.563	$V_{oc}/V_{oc,rad}$ (%)	61.3
J_{sc}max (mA/cm^2)	17.7	$J_{sc}/J_{sc,max}$ (%)	80.8
FF_{max} (%)	91.7 (86.9)	FF/FF_{max} (%)	79.7 (84.1)
PCE_{max} (%)	25.4	PCE/PCE_{max} (%)	39.4

[a] E_g, $V_{oc,rad}$, and E_U are extracted from the EQE measurement in Figure 6. The FF in brackets shows the FF limit without resistive losses obtained by taking into account the measured V_{oc}.

Shockley−Queisser limit of the short-circuit current density ($J_{sc,max}$), the maximum fill factor (FF_{max}), and the power conversion efficiency (PCE_{max}) can also be estimated for a specific E_g.[101,102]

From the comparison of these maximum (theoretical) values with the measured ones, it is clear that the main limitations of the device are the V_{oc} and, to a lesser extent, the FF. The FF scales with the V_{oc} so that with the measured V_{oc} and the ideality factor of 1 (Figure S14a), the ratio FF/FF_{max} lies at 84.1%.[103] However, this is only true for the best solar cell prepared in this series, where otherwise the FF was low on average (Figure 5). This indicates that there are significant resistive losses in the device, which might originate from shunts, from energy barriers resulting from the misalignment between the transport layers and perovskite energy levels, or from the low conductivity of the perovskite itself. The J_{sc} could also suffer from these effects but in our case is rather high and mainly limited by reflection losses and a non-unitary absorption due to the not-optimized layer thickness. The trend of intensity-dependent current density for the same device might suggest hindered charge extraction (increased recombination) at high light intensities, as the power factor α becomes <1 (Figure S14b). The high losses in V_{oc} are common to wide bandgap perovskites and are usually attributed to photoinduced phase segregation or energy level misalignment.[104] In both the EQE and PL spectra in Figure 6, an extra

https://dx.doi.org/10.1021/acs.chemmater.0c03038
Chem. Mater. 2020, 32, 8641−8652

component can be observed at low energies (at 1.7 and 1.78 eV, respectively), which might account for a voltage loss.

The PL feature might be a sign of weak phase segregation; however, this is limited to a few regions where the low-energy component can be appreciated, as shown in the PL maps in Figure S15. On the other hand, the EQE secondary absorption lies at an energy even lower than that of pure $CsPbI_3$ (1.72 eV) and was obtained at low illumination intensities (≈0.001 sun) where phase segregation is usually not occurring. Therefore, the EQE feature is likely an effect originating from the misalignment of energy levels between the perovskite and the transport layers, or from the C_{60} itself, which can lead to a photocurrent at very similar energies.[105] This hypothesis is supported by the fact that n−i−p devices using SnO_2 as the ETL (without C_{60}) do not show this feature in the EQE spectrum (Figure S16). Therefore, it might be necessary to find alternative electron-transport layers for these and other wide bandgap perovskite solar cells. Finally, the Urbach energy, extracted by fitting the EQE tail between 1.78 and 1.85 eV, is of only 18 meV, which is lower than the thermal energy at RT and is crucial for high-performance devices.[106]

■ CONCLUSIONS

We demonstrate the RT formation of $CsPbI_2Br$ using dry vacuum sublimation processes. The perovskite formation is achieved through a number of different methods with increasing levels of complexity. We performed the single-source deposition of previously prepared perovskite powders, which led to a mixture of phases and unreacted compounds. We then compared the 2-source sublimation using either CsBr and PbI_2 or presynthesized MHPs. The superior quality of the latter process highlights the importance of fostering halide alloying in the vacuum processing of inorganic lead halide perovskites. A similar effect can be attained by increasing the number of precursors (and hence deposition sources) to a 3- or 4-source process. We observed that these methods led to strongly oriented perovskite films at RT, and this orientation was found to be beneficial for the PV behavior of the semiconductors. We also explored the effect of the sublimation rate and found that slow sublimation of the precursors leads to $CsPbI_2Br$ films with better structural and optical properties. Importantly, all these processes were performed while maintaining the substrate at RT. Overall, we obtained promising PCEs of 8.3% for solar cells employing as-deposited perovskites (without any annealing) and 10.0% for devices based on $CsPbI_2Br$ annealed at a low temperature (150 °C). Through optoelectronic analysis, we found the open-circuit voltage to be the main limitation of these devices, most likely due to the use of non-optimal electron-transport layers.

■ EXPERIMENTAL SECTION

Materials. Cesium bromide (CsBr, >99%), lead(II) bromide ($PbBr_2$ [perovskite precursor]), and cesium iodide (CsI, >99%) were purchased from Tokyo Chemical Industries (TCI); molybdenum oxide (MoO_3), BCP, and lead(II) iodide (PbI_2, 99.999%) were from Lumtec; *N4,N4,N4″,N4″*-tetra([1,1′-biphenyl]-4-yl)-[1,1′:4′,1″-terphenyl]-4,4″-diamine (TaTm) was from Novaled GmbH; and C_{60} was obtained from Sigma-Aldrich.

Solid-State Synthesis of Perovskite and MHPs. (1) *$CsPbI_2Br$ by ball-milling*: Stoichiometric amounts of CsBr and PbI_2 powders (1:1) were mixed in a nitrogen-filled glovebox. Then, approximately 4 g of mixed precursor powders was introduced into 10 mL zirconia ball mill jars with two zirconia beads of 10 mm in diameter. The jars were closed under nitrogen so that the powders were not exposed to air. Then, ball milling was performed with an MM-400 shaking ball mill from Retsch at a frequency of 30 Hz for 99 min. (2) *MHPs by ball-milling*: CsBr/CsI and $PbBr_2/PbI_2$ powders (1:2) were weighed in a microbalance. Then, approximately 4 g of the mixed precursor powders was introduced into 10 mL zirconia ball mill jars with two zirconia beads (diameter 10 mm). The jars were closed under nitrogen so that the powders were not exposed to air. Then, ball milling was performed with an MM-400 shaking ball mill from Retsch at a frequency of 30 Hz for 99 min. (3) *$CsPbI_2Br$ by melting*: CsBr and PbI_2 were weighed in a microbalance with stoichiometric quantities. The powders were introduced into a thermally controlled crucible and heated in a nitrogen atmosphere until complete melting (650 °C for 2 min). (4) *MHPs by melting*: Stoichiometric amounts of CsBr and CsI were weighed in a microbalance to obtain $CsI_{1-x}Br_x$ (x = 1/3). Afterward, the powders were introduced in a thermally controlled crucible and heated in a nitrogen atmosphere until complete melting (650 °C for 2 min). Stoichiometric quantities of $PbBr_2$ and PbI_2 were weighed in a microbalance to obtain $Pb(I_{1-x}Br_x)_2$ (x = 1/3). Afterward, the powders were introduced in a thermally controlled crucible and heated in a nitrogen atmosphere until complete melting (420 °C for 2 min).

$CsPbI_2Br$ Thin-Film Deposition. All vacuum deposition runs were carried out in a custom-made chamber integrated into a nitrogen-filled glovebox. The chamber is equipped with four evaporation sources (CreaPhys) fitted with ceramic crucibles and independent temperature controllers and shutters. A dedicated QCM sensor is installed above each source plus one close to the substrate for the overall deposition rate measurement. The base pressure at the beginning of the deposition was 10^{-6} mbar. All the sources were individually calibrated for its respective material. If not otherwise specified, the thickness of the films used in this study was 250 nm. 1-Source vacuum deposition: after melting the precursors in a crucible as detailed above, the chamber was evacuated and the material was sublimed at 750 °C for 1 min, obtaining a film with a thickness of approximately 700 nm. Multisource vacuum deposition: all materials were codeposited after calibration of their deposition rates, using 2-, 3-, or 4-sources simultaneously, with a total deposition rate of 2 Å/s (if not otherwise stated).

Device Preparation. ITO-coated glass substrates were subsequently cleaned with soap, water, and isopropanol in an ultrasonic bath, followed by UV−ozone treatment. They were transferred to a nitrogen-filled glovebox with integrated vacuum chambers for the deposition of solar cell components. Organic semiconductors, perovskites, MoO_3, and Au, were deposited in three different chambers and evacuated to a pressure of 10^{-6} mbar. MoO_3 was deposited at a rate of 0.1 Å/s to a thickness of 5 nm and coated with TaTm (10 nm, deposited at 0.5 Å/s). The bilayer was annealed at 140 °C for 10 min. The $CsPbBrI_2$ perovskite films were fabricated following the procedures described above and coated with C_{60} (25 nm) and BCP (8 nm). Finally, a Ag electrode (100 nm) was deposited through a shadow mask to define the device layout (active area 2.1 × 3.1 mm^2).

Electrical Characterization. EQE was estimated by measuring the cell response at different wavelengths obtained with a white halogen lamp combined with band-pass filters. The solar spectrum was corrected by calibration with a silicon reference cell, previously calibrated (MiniSun simulator from ECN, the Netherlands). The current density−voltage (J−V) characteristics were obtained using a solar simulator from Abet Technologies, model 10500, with an AM1.5G xenon lamp as the light source and a Keithley 2400 source measure unit. A shadow mask with an aperture of 2.2 × 1.2 mm^2 was used to precisely estimate the current density.

Structural Analysis. The crystalline structure of the powder and film samples was studied by XRD. The patterns were collected in Bragg−Brentano geometry on an Empyrean PANalytical powder diffractometer with a copper anode operated at 45 kV and 40 mA. Further analysis including Le Bail fits was performed with Fullprof software. A Hitachi S-4800 scanning electron microscope operating at 20 kV accelerating voltage was used to obtain SEM images. Samples were platinum-metallized prior to their observation. Atomic force

https://dx.doi.org/10.1021/acs.chemmater.0c03038
Chem. Mater. 2020, 32, 8641−8652

microscopy (AFM) measurements were collected using a multimode atomic force microscope (Veeco Instruments, Inc.). The images were obtained with a Si tip (with a frequency and K of ca. 320 kHz and 42 $N \cdot m^{-1}$, respectively) using the tapping mode in air at RT. Images were recorded at 0.5−1 Hz scan rate.

Optical Analysis. UV−vis absorption spectra were collected using a fiber-optic Avantes Avaspec2048 spectrometer. The PL characteristics were studied using a Hyperspectral Imager IMA VIS from Photon etc. coupled to a continuous-wave laser of 532 nm. The power density at the sample was set to AM1.5G 1 sun equivalence (41 mW/cm^2). For the analysis, the exposure time was set to 0.5 s and the area of the field of view measured was 333 × 333 μm. The spectrum was obtained by averaging the spectra of each pixel.

Sensitive EQE Analysis. For sensitive EQE measurements, the cell was illuminated by a Quartz−Tungsten−Halogen lamp (Newport Apex 2-QTH) through a monochromator (Newport CS130-USB-3-MC), a chopper at 279 Hz, and a focusing lens. The device current was measured as a function of energy from 2.1 to 1.2 eV in 0.02 eV steps using a lock-in amplifier (Stanford Research Systems SR830). The system was calibrated and the solar spectrum mismatch was corrected using a calibrated silicon reference cell.

■ ASSOCIATED CONTENT

Supporting Information

The Supporting Information is available free of charge at https://pubs.acs.org/doi/10.1021/acs.chemmater.0c03038.

XRD analysis of powders and lattice parameters for all compounds; optical absorption spectra, XRD of all precursors; thin-film characterization by AFM, SEM, and XPS; PV characterization of annealed devices; intensity-dependent V_{oc} and J_{sc}; and hyperspectral imaging and sensitive EQE of best samples (PDF)

■ AUTHOR INFORMATION

Corresponding Author

Michele Sessolo − *Instituto de Ciencia Molecular, Universidad de Valencia, 46980 Paterna, Spain;* orcid.org/0000-0002-9189-3005; Email: michele.sessolo@uv.es

Authors

Ana M. Igual-Muñoz − *Instituto de Ciencia Molecular, Universidad de Valencia, 46980 Paterna, Spain*

Javier Navarro-Alapont − *Instituto de Ciencia Molecular, Universidad de Valencia, 46980 Paterna, Spain*

Chris Dreessen − *Instituto de Ciencia Molecular, Universidad de Valencia, 46980 Paterna, Spain;* orcid.org/0000-0001-7444-6900

Francisco Palazon − *Instituto de Ciencia Molecular, Universidad de Valencia, 46980 Paterna, Spain;* orcid.org/0000-0002-1503-5965

Henk J. Bolink − *Instituto de Ciencia Molecular, Universidad de Valencia, 46980 Paterna, Spain;* orcid.org/0000-0001-9784-6253

Complete contact information is available at: https://pubs.acs.org/10.1021/acs.chemmater.0c03038

Notes

The authors declare no competing financial interest.

■ ACKNOWLEDGMENTS

The research leading to these results received funding from the European Research Council (ERC) under the European Union's Horizon 2020 research and innovation programme (Grant agreement no. 834431), the Spanish Ministry of Science, Innovation and Universities (MAT2017-88821-R, RTI2018-095362-A-I00, PCI2019-111829-2, and EQC2018-004888-P), the Comunitat Valenciana, IDIFEDER/2018/061, and the support of a fellowship from "la Caixa" Foundation (ID 100010434). The fellowship code is LCF/BQ/DI19/11730020. M.S. and F.P. acknowledge the Spanish Ministry for their RyC and JdC contracts, respectively.

■ REFERENCES

(1) Kojima, A.; Teshima, K.; Shirai, Y.; Miyasaka, T. Organometal Halide Perovskites as Visible-Light Sensitizers for Photovoltaic Cells. *J. Am. Chem. Soc.* **2009**, *131*, 6050−6051.

(2) Green, M. A.; Dunlop, E. D.; Hohl-Ebinger, J.; Yoshita, M.; Kopidakis, N.; Ho-Baillie, A. W. Y. Solar Cell Efficiency Tables (Version 55). *Prog. Photovoltaics Res. Appl.* **2020**, *28*, 3−15.

(3) Yang, W. S.; Park, B.-W.; Jung, E. H.; Jeon, N. J.; Kim, Y. C.; Lee, D. U.; Shin, S. S.; Seo, J.; Kim, E. K.; Noh, J. H.; et al. Iodide Management in Formamidinium-Lead-Halide−Based Perovskite Layers for Efficient Solar Cells. *Science* **2017**, *356*, 1376−1379.

(4) Jeon, N. J.; Noh, J. H.; Yang, W. S.; Kim, Y. C.; Ryu, S.; Seo, J.; Seok, S. I. Il. Compositional Engineering of Perovskite Materials for High-Performance Solar Cells. *Nature* **2015**, *517*, 476−480.

(5) Saliba, M.; Matsui, T.; Seo, J.-Y.; Domanski, K.; Correa-Baena, J.-P.; Nazeeruddin, M. K.; Zakeeruddin, S. M.; Tress, W.; Abate, A.; Hagfeldt, A.; et al. Cesium-Containing Triple Cation Perovskite Solar Cells: Improved Stability, Reproducibility and High Efficiency. *Energy Environ. Sci.* **2016**, *9*, 1989−1997.

(6) Tan, H.; Jain, A.; Voznyy, O.; Lan, X.; García de Arquer, F. P.; Fan, J. Z.; Quintero-Bermudez, R.; Yuan, M.; Zhang, B.; Zhao, Y.; et al. Efficient and Stable Solution-Processed Planar Perovskite Solar Cells via Contact Passivation. *Science* **2017**, *355*, 722−726.

(7) Turren-Cruz, S.-H.; Hagfeldt, A.; Saliba, M. Methylammonium-Free, High-Performance, and Stable Perovskite Solar Cells on a Planar Architecture. *Science* **2018**, *362*, 449−453.

(8) Liang, J.; Zhao, P.; Wang, C.; Wang, Y.; Hu, Y.; Zhu, G.; Ma, L.; Liu, J.; Jin, Z. $CsPb_{0.9}Sn_{0.1}IBr_2$ Based All-Inorganic Perovskite Solar Cells with Exceptional Efficiency and Stability. *J. Am. Chem. Soc.* **2017**, *139*, 14009−14012.

(9) Wang, Y.; Zhang, T.; Kan, M.; Li, Y.; Wang, T.; Zhao, Y. Efficient α-$CsPbI_3$ Photovoltaics with Surface Terminated Organic Cations. *Joule* **2018**, *2*, 2065−2075.

(10) Liu, C.; Li, W.; Li, H.; Wang, H.; Zhang, C.; Yang, Y.; Gao, X.; Xue, Q.; Yip, H.-L.; Fan, J.; et al. Structurally Reconstructed $CsPbI_2Br$ Perovskite for Highly Stable and Square-Centimeter All-Inorganic Perovskite Solar Cells. *Adv. Energy Mater.* **2019**, *9*, 1803572.

(11) Beal, R. E.; Slotcavage, D. J.; Leijtens, T.; Bowring, A. R.; Belisle, R. A.; Nguyen, W. H.; Burkhard, G. F.; Hoke, E. T.; McGehee, M. D. Cesium Lead Halide Perovskites with Improved Stability for Tandem Solar Cells. *J. Phys. Chem. Lett.* **2016**, *7*, 746−751.

(12) Zeng, Q.; Zhang, X.; Liu, C.; Feng, T.; Chen, Z.; Zhang, W.; Zheng, W.; Zhang, H.; Yang, B. Inorganic $CsPbI_3Br$ Perovskite Solar Cells: The Progress and Perspective. *Sol. RRL* **2019**, *3*, 1800239.

(13) Faheem, M. B.; Khan, B.; Feng, C.; Farooq, M. U.; Raziq, F.; Xiao, Y.; Li, Y. All-Inorganic Perovskite Solar Cells: Energetics, Key Challenges, and Strategies toward Commercialization. *ACS Energy Lett.* **2019**, *5*, 290−320.

(14) Li, X.; Wu, J.; Wang, S.; Qi, Y. Progress of All-Inorganic Cesium Lead-Free Perovskite Solar Cells. *Chem. Lett.* **2019**, *48*, 989−1005.

(15) Ho-Baillie, A.; Zhang, M.; Lau, C. F. J.; Ma, F.-J.; Huang, S. Untapped Potentials of Inorganic Metal Halide Perovskite Solar Cells. *Joule* **2019**, *3*, 938−955.

(16) Xiang, W.; Tress, W. Review on Recent Progress of All-Inorganic Metal Halide Perovskites and Solar Cells. *Adv. Mater.* **2019**, *31*, 1902851.

(17) Tai, Q.; Tang, K.-C.; Yan, F. Recent Progress of Inorganic Perovskite Solar Cells. *Energy Environ. Sci.* **2019**, *12*, 2375−2405.

(18) Wang, Y.; Dar, M. I.; Ono, L. K.; Zhang, T.; Kan, M.; Li, Y.; Zhang, L.; Wang, X.; Yang, Y.; Gao, X.; et al. Thermodynamically Stabilized β-$CsPbI_3$ −Based Perovskite Solar Cells with Efficiencies >18%. *Science* **2019**, *365*, 591−595.
(19) Zheng, Y.; Yang, X.; Su, R.; Wu, P.; Gong, Q.; Zhu, R. High-Performance $CsPbI_xBr_{3-x}$ All-Inorganic Perovskite Solar Cells with Efficiency over 18% via Spontaneous Interfacial Manipulation. *Adv. Funct. Mater.* **2020**, 2000457.
(20) Han, Y.; Zhao, H.; Duan, C.; Yang, S.; Yang, Z.; Liu, Z.; Liu, S. Controlled N-Doping in Air-Stable $CsPbI_2Br$ Perovskite Solar Cells with a Record Efficiency of 16.79%. *Adv. Funct. Mater.* **2020**, *30*, 1909972.
(21) Zhang, Y.; Wu, C.; Wang, D.; Zhang, Z.; Qi, X.; Zhu, N.; Liu, G.; Li, X.; Hu, H.; Chen, Z.; et al. High Efficiency (16.37%) of Cesium Bromide—Passivated All-Inorganic $CsPbI_2Br$ Perovskite Solar Cells. *Sol. RRL* **2019**, *3*, 1900254.
(22) Eperon, G. E.; Paternò, G. M.; Sutton, R. J.; Zampetti, A.; Haghighirad, A. A.; Cacialli, F.; Snaith, H. J. Inorganic Caesium Lead Iodide Perovskite Solar Cells. *J. Mater. Chem. A* **2015**, *3*, 19688−19695.
(23) Dastidar, S.; Hawley, C. J.; Dillon, A. D.; Gutierrez-Perez, A. D.; Spanier, J. E.; Fafarman, A. T. Quantitative Phase-Change Thermodynamics and Metastability of Perovskite-Phase Cesium Lead Iodide. *J. Phys. Chem. Lett.* **2017**, *8*, 1278−1282.
(24) Wang, P.; Zhang, X.; Zhou, Y.; Jiang, Q.; Ye, Q.; Chu, Z.; Li, X.; Yang, X.; Yin, Z.; You, J. Solvent-Controlled Growth of Inorganic Perovskite Films in Dry Environment for Efficient and Stable Solar Cells. *Nat. Commun.* **2018**, *9*, 1−7.
(25) Sutton, R. J.; Eperon, G. E.; Miranda, L.; Parrott, E. S.; Kamino, B. A.; Patel, J. B.; Hörantner, M. T.; Johnston, M. B.; Haghighirad, A. A.; Moore, D. T.; et al. Bandgap-Tunable Cesium Lead Halide Perovskites with High Thermal Stability for Efficient Solar Cells. *Adv. Energy Mater.* **2016**, *6*, 1502458.
(26) Tao, S.; Schmidt, I.; Brocks, G.; Jiang, J.; Tranca, I.; Meerholz, K.; Olthof, S. Absolute Energy Level Positions in Tin- and Lead-Based Halide Perovskites. *Nat. Commun.* **2019**, *10*, 2560.
(27) Sutton, R. J.; Eperon, G. E.; Miranda, L.; Parrott, E. S.; Kamino, B. A.; Patel, J. B.; Hörantner, M. T.; Johnston, M. B.; Haghighirad, A. A.; Moore, D. T.; et al. Bandgap-Tunable Cesium Lead Halide Perovskites with High Thermal Stability for Efficient Solar Cells. *Adv. Energy Mater.* **2016**, *6*, 1502458.
(28) Travis, W.; Glover, E. N. K.; Bronstein, H.; Scanlon, D. O.; Palgrave, R. G. On the Application of the Tolerance Factor to Inorganic and Hybrid Halide Perovskites: A Revised. *Chem. Sci.* **2016**, *7*, 4548−4556.
(29) Palgrave, J. K.; Chai, S. U.; Cha, W.; Choi, Y. J.; Kim, W.; Jung, M. S.; Kwon, J.; Kim, D.; Park, J. H. Potassium Incorporation for Enhanced Performance and Stability of Fully Inorganic Cesium Lead Halide Perovskite Solar Cells. *Nano Lett.* **2017**, *17*, 2028−2033.
(30) Han, Y.; Zhao, H.; Duan, C.; Yang, S.; Yang, Z.; Liu, Z.; Liu, S. Controlled N-Doping in Air-Stable $CsPbI_2Br$ Perovskite Solar Cells with a Record Efficiency of 16.79%. *Adv. Funct. Mater.* **2020**, *30*, 1909972.
(31) Lau, C. F. J.; Zhang, M.; Deng, X.; Zheng, J.; Bing, J.; Ma, Q.; Kim, J.; Hu, L.; Green, M. A.; Huang, S.; et al. Strontium-Doped Low-Temperature-Processed $CsPbI_2Br$ Perovskite Solar Cells. *ACS Energy Lett.* **2017**, *2*, 2319−2325.
(32) Xiang, W.; Wang, Z.; Kubicki, D. J.; Wang, X.; Tress, W.; Luo, J.; Zhang, J.; Hofstetter, A.; Zhang, L.; Emsley, L.; et al. Ba-Induced Phase Segregation and Band Gap Reduction in Mixed-Halide Inorganic Perovskite Solar Cells. *Nat. Commun.* **2019**, *10*, 4686.
(33) Mali, S. S.; Patil, J. V.; Hong, C. K. Hot-Air-Assisted Fully Air-Processed Barium Incorporated $CsPbI_2Br$ Perovskite Thin Films for Highly Efficient and Stable All-Inorganic Perovskite Solar Cells. *Nano Lett.* **2019**, *19*, 6213−6220.
(34) Wang, K.-L.; Wang, R.; Wang, Z.-K.; Li, M.; Zhang, Y.; Ma, H.; Liao, L.-S.; Yang, Y. Tailored Phase Transformation of $CsPbI_2Br$ Films by Copper(II) Bromide for High-Performance All-Inorganic Perovskite Solar Cells. *Nano Lett.* **2019**, *19*, 5176−5184.
(35) Sun, H.; Zhang, J.; Gan, X.; Yu, L.; Yuan, H.; Shang, M.; Lu, C.; Hou, D.; Hu, Z.; Zhu, Y.; et al. Pb-Reduced $CsPb_{0.9}Zn_{0.1}I_2$ Br Thin Films for Efficient Perovskite Solar Cells. *Adv. Energy Mater.* **2019**, *9*, 1900896.
(36) Chen, L.; Wan, L.; Li, X.; Zhang, W.; Fu, S.; Wang, Y.; Li, S.; Wang, H.-Q.; Song, W.; Fang, J. Inverted All-Inorganic $CsPbI_2Br$ Perovskite Solar Cells with Promoted Efficiency and Stability by Nickel Incorporation. *Chem. Mater.* **2019**, *31*, 9032−9039.
(37) Mali, S. S.; Patil, J. V.; Hong, C. K. Simultaneous Improved Performance and Thermal Stability of Planar Metal Ion Incorporated $CsPbI_2Br$ All-Inorganic Perovskite Solar Cells Based on MgZnO Nanocrystalline Electron Transporting Layer. *Adv. Energy Mater.* **2020**, *10*, 1902708.
(38) Bai, D.; Zhang, J.; Jin, Z.; Bian, H.; Wang, K.; Wang, H.; Liang, L.; Wang, Q.; Liu, S. F. Interstitial Mn^{2+} -Driven High-Aspect-Ratio Grain Growth for Low-Trap-Density Microcrystalline Films for Record Efficiency $CsPbI_2Br$ Solar Cells. *ACS Energy Lett.* **2018**, *3*, 970−978.
(39) Ye, L.; Wang, H.; Wei, Y.; Guo, P.; Yang, X.; Ye, Q.; Wang, H. Acetate-Based Crystallization Kinetics Modulation of $CsPbI_2Br$ for Improved Photovoltaic Performance. *ACS Appl. Energy Mater.* **2020**, *3*, 658−665.
(40) Xiang, W.; Wang, Z.; Kubicki, D. J.; Tress, W.; Luo, J.; Prochowicz, D.; Akin, S.; Emsley, L.; Zhou, J.; Dietler, G.; et al. Europium-Doped $CsPbI_2Br$ for Stable and Highly Efficient Inorganic Perovskite Solar Cells. *Joule* **2019**, *3*, 205−214.
(41) Shi, J.; Li, F.; Yuan, J.; Ling, X.; Zhou, S.; Qian, Y.; Ma, W. Efficient and Stable $CsPbI_3$ Perovskite Quantum Dots Enabled by in Situ Ytterbium Doping for Photovoltaic Applications. *J. Mater. Chem. A* **2019**, *7*, 20936−20944.
(42) Yang, S.; Zhao, H.; Han, Y.; Duan, C.; Liu, Z.; Liu, S. Europium and Acetate Co-doping Strategy for Developing Stable and Efficient CsPbI 2 Br Perovskite Solar Cells. *Small* **2019**, *15*, 1904387.
(43) Xu, W.; He, F.; Zhang, M.; Nie, P.; Zhang, S.; Zhao, C.; Luo, R.; Li, J.; Zhang, X.; Zhao, S.; et al. Minimizing Voltage Loss in Efficient All-Inorganic $CsPbI_2Br$ Perovskite Solar Cells through Energy Level Alignment. *ACS Energy Lett.* **2019**, *4*, 2491−2499.
(44) Chen, W.; Chen, H.; Xu, G.; Xue, R.; Wang, S.; Li, Y.; Li, Y. Precise Control of Crystal Growth for Highly Efficient $CsPbI_2Br$ Perovskite Solar Cells. *Joule* **2019**, *3*, 191−204.
(45) Shao, Z.; Wang, Z.; Li, Z.; Fan, Y.; Meng, H.; Liu, R.; Wang, Y.; Hagfeldt, A.; Cui, G.; Pang, S. A Scalable Methylamine Gas Healing Strategy for High-Efficiency Inorganic Perovskite Solar Cells. *Angew. Chem., Int. Ed.* **2019**, *58*, 5587−5591.
(46) Zhao, H.; Han, Y.; Xu, Z.; Duan, C.; Yang, S.; Yuan, S.; Yang, Z.; Liu, Z.; Liu, S. A Novel Anion Doping for Stable $CsPbI_2Br$ Perovskite Solar Cells with an Efficiency of 15.56% and an Open Circuit Voltage of 1.30 V. *Adv. Energy Mater.* **2019**, *9*, 1902279.
(47) Ma, J.; Qin, M.; Li, Y.; Zhang, T.; Xu, J.; Fang, G.; Lu, X. Guanidinium Doping Enabled Low-Temperature Fabrication of High-Efficiency All-Inorganic $CsPbI_2Br$ Perovskite Solar Cells. *J. Mater. Chem. A* **2019**, *7*, 27640−27647.
(48) Jiang, H.; Feng, J.; Zhao, H.; Li, G.; Yin, G.; Han, Y.; Yan, F.; Liu, Z.; Liu, S. F. Low Temperature Fabrication for High Performance Flexible $CsPbI_2Br$ Perovskite Solar Cells. *Adv. Sci.* **2018**, *5*, 1801117.
(49) Yang, X.; Yang, H.; Hu, X.; Li, W.; Fang, Z.; Zhang, K.; Huang, R.; Li, J.; Yang, Z.; Song, Y. Low-Temperature Interfacial Engineering for Flexible $CsPbI_2Br$ Perovskite Solar Cells with High Performance beyond 15%. *J. Mater. Chem. A* **2020**, *8*, 5308−5314.
(50) Liu, C.; Yang, Y.; Zhang, C.; Wu, S.; Wei, L.; Guo, F.; Arumugam, G. M.; Hu, J.; Liu, X.; Lin, J.; et al. Tailoring C 60 for Efficient Inorganic $CsPbI_2Br$ Perovskite Solar Cells and Modules. *Adv. Mater.* **2020**, *32*, 1907361.
(51) Yan, L.; Xue, Q.; Liu, M.; Zhu, Z.; Tian, J.; Li, Z.; Chen, Z.; Chen, Z.; Yan, H.; Yip, H.-L.; et al. Interface Engineering for All-Inorganic $CsPbI_2Br$ Perovskite Solar Cells with Efficiency over 14%. *Adv. Mater.* **2018**, *30*, 1802509.

https://dx.doi.org/10.1021/acs.chemmater.0c03038
Chem. Mater. 2020, 32, 8641−8652

(52) Liu, C.; Li, W.; Zhang, C.; Ma, Y.; Fan, J.; Mai, Y. All-Inorganic $CsPbI_2Br$ Perovskite Solar Cells with High Efficiency Exceeding 13%. *J. Am. Chem. Soc.* **2018**, *140*, 3825−3828.
(53) Ma, J.; Su, J.; Lin, Z.; Zhou, L.; He, J.; Zhang, J.; Liu, S.; Chang, J.; Hao, Y. Improve the Oxide/Perovskite Heterojunction Contact for Low Temperature High Efficiency and Stable All-Inorganic CsPbI2Br Perovskite Solar Cells. *Nano Energy* **2020**, *67*, 104241.
(54) Shen, E. C.; Chen, J. D.; Tian, Y.; Luo, Y. X.; Shen, Y.; Sun, Q.; Jin, T. Y.; Shi, G. Z.; Li, Y. Q.; Tang, J. X. Interfacial Energy Level Tuning for Efficient and Thermostable CsPbI 2 Br Perovskite Solar Cells. *Adv. Sci.* **2020**, *7*, 1901952.
(55) Jiang, K.; Wang, J.; Wu, F.; Xue, Q.; Yao, Q.; Zhang, J.; Chen, Y.; Zhang, G.; Zhu, Z.; Yan, H.; et al. Dopant-Free Organic Hole-Transporting Material for Efficient and Stable Inverted All-Inorganic and Hybrid Perovskite Solar Cells. *Adv. Mater.* **2020**, *32*, 1908011.
(56) Xiao, Q.; Tian, J.; Xue, Q.; Wang, J.; Xiong, B.; Han, M.; Li, Z.; Zhu, Z.; Yip, H. L.; Li, Z. a. Dopant-Free Squaraine-Based Polymeric Hole-Transporting Materials with Comprehensive Passivation Effects for Efficient All-Inorganic Perovskite Solar Cells. *Angew. Chem., Int. Ed.* **2019**, *58*, 17724−17730.
(57) Zhao, H.; Yang, S.; Han, Y.; Yuan, S.; Jiang, H.; Duan, C.; Liu, Z.; Liu, S. A High Mobility Conjugated Polymer Enables Air and Thermally Stable $CsPbI_2Br$ Perovskite Solar Cells with an Efficiency Exceeding 15%. *Adv. Mater. Technol.* **2019**, *4*, 1900311.
(58) Tian, J.; Xue, Q.; Tang, X.; Chen, Y.; Li, N.; Hu, Z.; Shi, T.; Wang, X.; Huang, F.; Brabec, C. J.; et al. Dual Interfacial Design for Efficient $CsPbI_2Br$ Perovskite Solar Cells with Improved Photostability. *Adv. Mater.* **2019**, *31*, 1901152.
(59) Liu, M.; Johnston, M. B.; Snaith, H. J. Efficient Planar Heterojunction Perovskite Solar Cells by Vapour Deposition. *Nature* **2013**, *501*, 395−398.
(60) Ávila, J.; Momblona, C.; Boix, P. P.; Sessolo, M.; Bolink, H. J. Vapor-Deposited Perovskites: The Route to High-Performance Solar Cell Production? *Joule* **2017**, *1*, 431−442.
(61) Forgács, D.; Gil-Escrig, L.; Pérez-Del-Rey, D.; Momblona, C.; Werner, J.; Niesen, B.; Ballif, C.; Sessolo, M.; Bolink, H. J. Efficient Monolithic Perovskite/Perovskite Tandem Solar Cells. *Adv. Energy Mater.* **2017**, *7*, 1602121.
(62) Ávila, J.; Momblona, C.; Boix, P.; Sessolo, M.; Anaya, M.; Lozano, G.; Vandewal, K.; Míguez, H.; Bolink, H. J. High Voltage Vacuum-Deposited $CH_3NH_3PbI_3$−$CH_3NH_3PbI_3$ Tandem Solar Cells. *Energy Environ. Sci.* **2018**, *11*, 3292−3297.
(63) Sahli, F.; Werner, J.; Kamino, BA; Bräuninger, M.; Monnard, R.; Paviet-Salomon, B.; Barraud, L.; Ding, L.; Diaz Leon, JJ; Sacchetto, D.; et al. Fully Textured Monolithic Perovskite/Silicon Tandem Solar Cells with 25.2% Power Conversion Efficiency. *Nat. Mater.* **2018**, *17*, 820−826.
(64) Malinkiewicz, O.; Yella, A.; Lee, Y. H.; Espallargas, G. M.; Graetzel, M.; Nazeeruddin, M. K.; Bolink, H. J. Perovskite Solar Cells Employing Organic Charge-Transport Layers. *Nat. Photonics* **2014**, *8*, 128−132.
(65) Lin, Q.; Armin, A.; Nagiri, R. C. R.; Burn, P. L.; Meredith, P. Electro-Optics of Perovskite Solar Cells. *Nat. Photonics* **2015**, *9*, 106−112.
(66) Chirvony, V. S.; Sekerbayev, K. S.; Pérez-del-Rey, D.; Martínez-Pastor, J. P.; Palazon, F.; Boix, P. P.; Taurbayev, T. I.; Sessolo, M.; Bolink, H. J. Short Photoluminescence Lifetimes in Vacuum-Deposited $CH_3NH_3PbI_3$ Perovskite Thin Films as a Result of Fast Diffusion of Photogenerated Charge Carriers. *J. Phys. Chem. Lett.* **2019**, *10*, 5167−5172.
(67) Patel, J. B.; Wright, A. D.; Lohmann, K. B.; Peng, K.; Xia, C. Q.; Ball, J. M.; Noel, N. K.; Crothers, T. W.; Wong-Leung, J.; Snaith, H. J.; et al. Light Absorption and Recycling in Hybrid Metal Halide Perovskite Photovoltaic Devices. *Adv. Energy Mater.* **2020**, *10*, 1903653.
(68) Longo, G.; Momblona, C.; La-Placa, M.-G.; Gil-Escrig, L.; Sessolo, M.; Bolink, H. J. Fully Vacuum-Processed Wide Band Gap Mixed-Halide Perovskite Solar Cells. *ACS Energy Lett.* **2018**, *3*, 214−219.
(69) Gil-Escrig, L.; Momblona, C.; La-Placa, M.-G.; Boix, P. P.; Sessolo, M.; Bolink, H. J. Vacuum Deposited Triple-Cation Mixed-Halide Perovskite Solar Cells. *Adv. Energy Mater.* **2018**, *8*, 1703506.
(70) Babaei, A.; Soltanpoor, W.; Tesa-Serrate, M. A.; Yerci, S.; Sessolo, M.; Bolink, H. J. Preparation and Characterization of Mixed Halide $MAPbI_{3-x}Cl_x$ Perovskite Thin Films by Three-Source Vacuum Deposition. *Energy Technol.* **2020**, *8*, 1900784.
(71) Igual-Muñoz, A. M.; Castillo, A.; Dreessen, C.; Boix, P. P.; Bolink, H. J. Vacuum-Deposited Multication Tin−Lead Perovskite Solar Cells. *ACS Appl. Energy Mater.* **2020**, *3*, 2755−2761.
(72) Burwig, T.; Fränzel, W.; Pistor, P. Crystal Phases and Thermal Stability of Co-Evaporated $CsPbX_3$ (X = I, Br) Thin Films. *J. Phys. Chem. Lett.* **2018**, *9*, 4808−4813.
(73) Palazon, F.; Pérez-del-Rey, D.; Dänekamp, B.; Dreessen, C.; Sessolo, M.; Boix, P. P.; Bolink, H. J. Room-Temperature Cubic Phase Crystallization and High Stability of Vacuum-Deposited Methylammonium Lead Triiodide Thin Films for High-Efficiency Solar Cells. *Adv. Mater.* **2019**, *31*, 1902692.
(74) Lohmann, K. B.; Patel, J. B.; Rothmann, M. U.; Xia, C. Q.; Oliver, R. D. J.; Herz, L. M.; Snaith, H. J.; Johnston, M. B. Control over Crystal Size in Vapor Deposited Metal-Halide Perovskite Films. *ACS Energy Lett.* **2020**, *5*, 710−717.
(75) Shahiduzzaman, M.; Yonezawa, K.; Yamamoto, K.; Ripolles, T. S.; Karakawa, M.; Kuwabara, T.; Takahashi, K.; Hayase, S.; Taima, T. Improved Reproducibility and Intercalation Control of Efficient Planar Inorganic Perovskite Solar Cells by Simple Alternate Vacuum Deposition of PbI_2 and CsI. *ACS Omega* **2017**, *2*, 4464−4469.
(76) Kottokkaran, R.; Gaonkar, H. A.; Bagheri, B.; Dalal, V. L. Efficient P-i-n Inorganic $CsPbI_3$ Perovskite Solar Cell Deposited Using Layer-by-Layer Vacuum Deposition. *J. Vac. Sci. Technol., A* **2018**, *36*, 041201.
(77) Frolova, L. A.; Anokhin, D. V.; Piryazev, A. A.; Luchkin, S. Y.; Dremova, N. N.; Stevenson, K. J.; Troshin, P. A. Highly Efficient All-Inorganic Planar Heterojunction Perovskite Solar Cells Produced by Thermal Coevaporation of CsI and PbI_2. *J. Phys. Chem. Lett.* **2017**, *8*, 67−72.
(78) Park, C.-G.; Choi, W.-G.; Na, S.; Moon, T. All-Inorganic Perovskite $CsPbI_2Br$ Through Co-Evaporation for Planar Heterojunction Solar Cells. *Electron. Mater. Lett.* **2019**, *15*, 56−60.
(79) Chen, C.-Y.; Lin, H.-Y.; Chiang, K.-M.; Tsai, W.-L.; Huang, Y.-C.; Tsao, C.-S.; Lin, H.-W. All-Vacuum-Deposited Stoichiometrically Balanced Inorganic Cesium Lead Halide Perovskite Solar Cells with Stabilized Efficiency Exceeding 11%. *Adv. Mater.* **2017**, *29*, 1605290.
(80) Becker, P.; Márquez, J. A.; Just, J.; Al-Ashouri, A.; Hages, C.; Hempel, H.; Jošt, M.; Albrecht, S.; Frahm, R.; Unold, T. Low Temperature Synthesis of Stable γ-$CsPbI_3$ Perovskite Layers for Solar Cells Obtained by High Throughput Experimentation. *Adv. Energy Mater.* **2019**, *9*, 1900555.
(81) Hutter, E. M.; Sutton, R. J.; Chandrashekar, S.; Abdi-Jalebi, M.; Stranks, S. D.; Snaith, H. J.; Savenije, T. J. Vapour-Deposited Cesium Lead Iodide Perovskites: Microsecond Charge Carrier Lifetimes and Enhanced Photovoltaic Performance. *ACS Energy Lett.* **2017**, *2*, 1901−1908.
(82) Lin, H. Y.; Chen, C. Y.; Hsu, B. W.; Cheng, Y. L.; Tsai, W. L.; Huang, Y. C.; Tsao, C. S.; Lin, H. W. Efficient Cesium Lead Halide Perovskite Solar Cells through Alternative Thousand-Layer Rapid Deposition. *Adv. Funct. Mater.* **2019**, *29*, 1905163.
(83) Yang, D.; Yang, R.; Priya, S.; Liu, S. Recent Advances in Flexible Perovskite Solar Cells: Fabrication and Applications. *Angew. Chem., Int. Ed.* **2019**, *58*, 4466−4483.
(84) Palazon, F.; El Ajjouri, Y.; Bolink, H. J. Making by Grinding: Mechanochemistry Boosts the Development of Halide Perovskites and Other Multinary Metal Halides. *Adv. Energy Mater.* **2020**, *10*, 1902499.
(85) El Ajjouri, Y.; Palazon, F.; Sessolo, M.; Bolink, H. J. Single-Source Vacuum Deposition of Mechanosynthesized Inorganic Halide Perovskites. *Chem. Mater.* **2018**, *30*, 7423−7427.
(86) Akkerman, Q. A.; Manna, L. What Defines a Halide Perovskite? *ACS Energy Lett.* **2020**, *5*, 604−610.

https://dx.doi.org/10.1021/acs.chemmater.0c03038
Chem. Mater. 2020, 32, 8641−8652

(87) Karmakar, A.; Dodd, M. S.; Zhang, X.; Oakley, M. S.; Klobukowski, M.; Michaelis, V. K. Mechanochemical Synthesis of 0D and 3D Cesium Lead Mixed Halide Perovskites. *Chem. Commun.* **2019**, *55*, 5079−5082.
(88) Liu, Z.; Bekenstein, Y.; Ye, X.; Nguyen, S. C.; Swabeck, J.; Zhang, D.; Lee, S.-T.; Yang, P.; Ma, W.; Alivisatos, A. P. Ligand Mediated Transformation of Cesium Lead Bromide Perovskite Nanocrystals to Lead Depleted Cs_4PbBr_6 Nanocrystals. *J. Am. Chem. Soc.* **2017**, *139*, 5309−5312.
(89) Palazon, F.; Urso, C.; De Trizio, L.; Akkerman, Q.; Marras, S.; Locardi, F.; Nelli, I.; Ferretti, M.; Prato, M.; Manna, L. Postsynthesis Transformation of Insulating Cs_4PbBr_6 Nanocrystals into Bright Perovskite $CsPbBr_3$ through Physical and Chemical Extraction of CsBr. *ACS Energy Lett.* **2017**, *2*, 2445−2448.
(90) Palazon, F.; Almeida, G.; Akkerman, Q. A.; De Trizio, L.; Dang, Z.; Prato, M.; Manna, L. Changing the Dimensionality of Cesium Lead Bromide Nanocrystals by Reversible Postsynthesis Transformations with Amines. *Chem. Mater.* **2017**, *29*, 4167−4171.
(91) *CRC Handbook of Chemistry and Physics*, 100th ed.; Rumble, J. R., Ed.; Taylor & Francis Ltd; CRC Press: London, 2020.
(92) Palazon, F.; El Ajjouri, Y.; Sebastia-Luna, P.; Lauciello, S.; Manna, L.; Bolink, H. J. Mechanochemical Synthesis of Inorganic Halide Perovskites: Evolution of Phase-Purity, Morphology, and Photoluminescence. *J. Mater. Chem. C* **2019**, *7*, 11406−11410.
(93) Burwig, T.; Fränzel, W.; Pistor, P. Crystal Phases and Thermal Stability of Co-Evaporated $CsPbX_3$ (X = I, Br) Thin Films. *J. Phys. Chem. Lett.* **2018**, *9*, 4808−4813.
(94) Pistor, P.; Burwig, T.; Brzuska, C.; Weber, B.; Fränzel, W. Thermal Stability and Miscibility of Co-Evaporated Methyl Ammonium Lead Halide ($MAPbX_3$, X = I, Br, Cl) Thin Films Analysed by in Situ X-Ray Diffraction. *J. Mater. Chem. A* **2018**, *6*, 11496−11506.
(95) Mattox, D. M. Vacuum Evaporation and Vacuum Deposition. *Handbook of Physical Vapor Deposition (PVD) Processing*, 2nd ed.; Elsevier: Boston, 2010; pp 195−235.
(96) Vapor Pressure Graphs for Inorganic Compounds and Elements. In *Inorganic Compounds and Elements*; Yaws, C. L., Ed.; Gulf Professional Publishing, 1995; Vol. *4*, pp 1−343.
(97) Gil-Escrig, L.; Momblona, C.; La-Placa, M.-G.; Boix, P. P.; Sessolo, M.; Bolink, H. J. Vacuum Deposited Triple-Cation Mixed-Halide Perovskite Solar Cells. *Adv. Energy Mater.* **2018**, *8*, 1703506.
(98) Rühle, S. Tabulated Values of the Shockley−Queisser Limit for Single Junction Solar Cells. *Sol. Energy* **2016**, *130*, 139−147.
(99) Tvingstedt, K.; Malinkiewicz, O.; Baumann, A.; Deibel, C.; Snaith, H. J.; Dyakonov, V.; Bolink, H. J. Radiative Efficiency of Lead Iodide Based Perovskite Solar Cells. *Sci. Rep.* **2014**, *4*, 6071.
(100) Rau, U.; Blank, B.; Müller, T. C. M.; Kirchartz, T. Efficiency Potential of Photovoltaic Materials and Devices Unveiled by Detailed-Balance Analysis. *Phys. Rev. Appl.* **2017**, *7*, 044016.
(101) Shockley, W.; Queisser, H. J. Detailed Balance Limit of Efficiency of P-n Junction Solar Cells. *J. Appl. Phys.* **1961**, *32*, 510−519.
(102) Rühle, S. Tabulated Values of the Shockley-Queisser Limit for Single Junction Solar Cells. *Sol. Energy* **2016**, *130*, 139−147.
(103) Green, M. A. Solar Cell Fill Factors: General Graph and Empirical Expressions. *Solid State Electron.* **1981**, *24*, 788−789.
(104) Jaysankar, M.; Raul, B. A. L.; Bastos, J.; Burgess, C.; Weijtens, C.; Creatore, M.; Aernouts, T.; Kuang, Y.; Gehlhaar, R.; Hadipour, A.; et al. Minimizing Voltage Loss in Wide-Bandgap Perovskites for Tandem Solar Cells. *ACS Energy Lett.* **2019**, *4*, 259−264.
(105) Burkhard, G. F.; Hoke, E. T.; Beiley, Z. M.; Mcgehee, M. D. Free Carrier Generation in Fullerene Acceptors and Its Effect on Polymer Photovoltaics. *J. Phys. Chem. C* **2012**, *116*, 26674−26678.
(106) Chantana, J.; Kawano, Y.; Nishimura, T.; Mavlonov, A.; Minemoto, T. Impact of Urbach Energy on Open-Circuit Voltage Deficit of Thin-Film Solar Cells. *Sol. Energy Mater. Sol. Cells* **2020**, *210*, 110502.

https://dx.doi.org/10.1021/acs.chemmater.0c03038
Chem. Mater. 2020, 32, 8641−8652

Supporting Information

Room temperature vacuum-deposition of $CsPbI_2Br$ perovskite films from multiple-sources and mixed halide precursors.

Ana M. Igual-Muñoz, Javier Navarro-Alapont, Chris Dreessen, Francisco Palazon, Michele Sessolo*, Henk J. Bolink

Instituto de Ciencia Molecular, Universidad de Valencia, C/ J. Beltran 2, 46980 Paterna, Spain.

*E-mail: michele.sessolo@uv.es

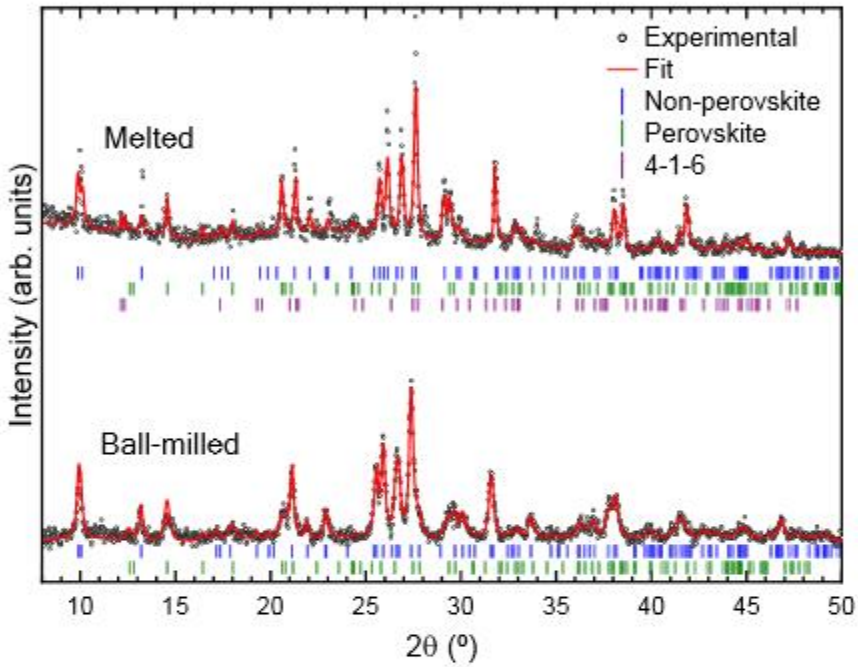

Figure S1. XRD characterization of ball-milled (bottom) and melted (top) $CsBr:PbI_2$ 1:1 powders. Open circles represent raw data, red lines are whole-pattern Le Bail fit and vertical lines indicate the calculated Bragg's reflections for different phases. More details about the different phases in the discussion.

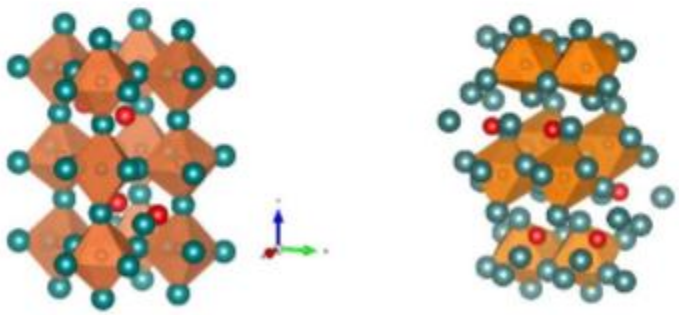

Figure S2. Crystal structures of the distorted perovskite and non-perovskite phases. Cs^{+} ions are depicted in red, halide anions in teal, Pb^{2+} cations in grey and PbX_6 octahedra in orange.

Table S1. Lattice parameters for perovskite and non-perovskite phases of ball-milled and melted samples together with reference values for $CsPbBr_3$ and $CsPbI_3$ retrieved from the Inorganic Crystal Structure Database (references 97851 and 161480 respectively).

Ball-milled	*a (Å)*	*b (Å)*	*c (Å)*	*α*	*β*	*γ*	*Vol (Å³)*
Perovskite	8.392	8.624	12.168	90	90	90	880
($CsPbBr_3$)	(8.207)	(8.255)	(11.759)	(90)	(90)	(90)	(797)
Non-Perovskite	10.341	4.770	17.621	90	90	90	869
($CsPbI_3$)	(10.458)	(4.802)	(17.776)	(90)	(90)	(90)	(893)
Melted	*a (Å)*	*b (Å)*	*c (Å)*	*α*	*β*	*γ*	*Vol (Å³)*
Perovskite	8.435	8.629	12.151	90	90	90	880
($CsPbBr_3$)	(8.207)	(8.255)	(11.759)	(90)	(90)	(90)	(797)
Non-Perovskite	10.424	4.730	17.486	90	90	90	869
($CsPbI_3$)	(10.458)	(4.802)	(17.776)	(90)	(90)	(90)	(893)

Table S2. Lattice parameters calculated for thin-films deposited by different methods referred to the values for $CsPbBr_3$ retrieved from the Inorganic Crystal Structure Database (reference 97851).

	a (Å)	*b (Å)*	*c (Å)*	*α*	*β*	*γ*	*Vol (Å³)*
$CsPbBr_3$ (ICSD-97851)	8.207	8.255	11.759	90	90	90	797
2-sources	8.587	8.737	12.086	90	90	90	907
2-sources (MHP)	8.614	8.732	11.848	90	90	90	891
3-sources (slow)	8.627	8.746	12.136	90	90	90	916
3-sources (fast)	8.627	8.724	12.076	90	90	90	909
4-sources	8.573	8.725	12.068	90	90	90	903

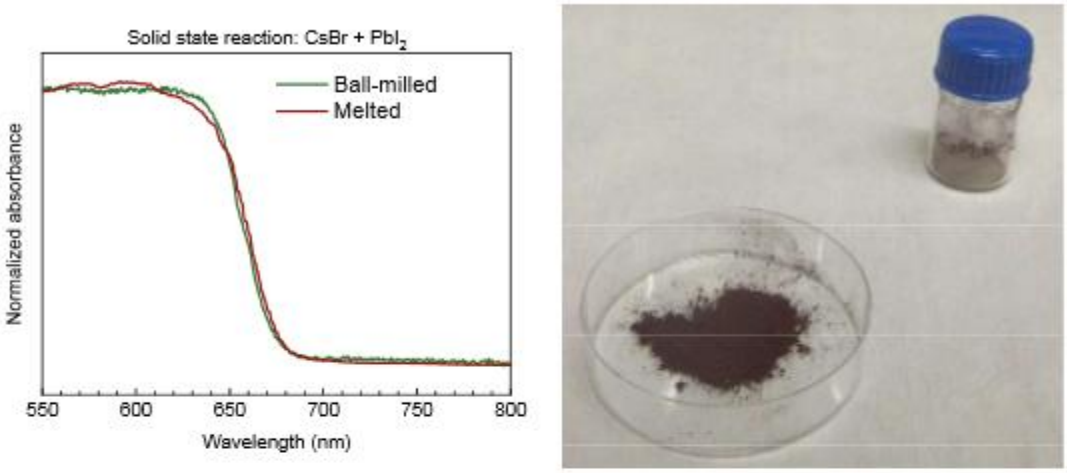

Figure S3. UV-Vis optical absorption for powders obtained by mechanochemical and melting techniques. A photograph of as-prepared perovskite from mechanochemical synthesis is shown as reference.

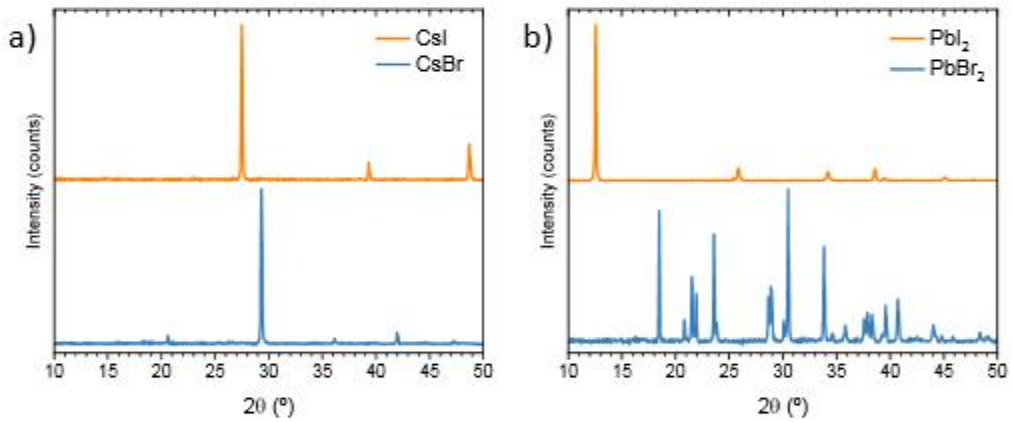

Figure S4. XRD patterns obtained for powders of the pure halide precursors used in this work: a) CsI, CsBr, and b) PbI_2, $PbBr_2$.

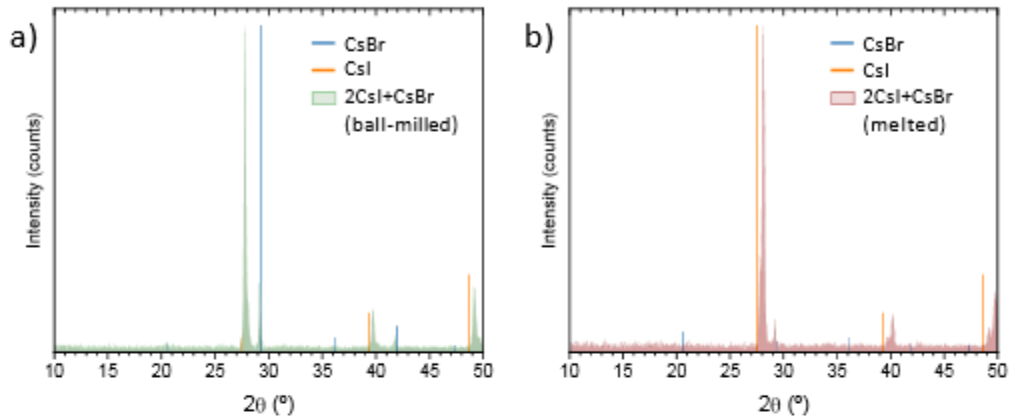

Figure S5. XRD patterns of the products obtained by solid state reactions of 2CsI + CsBr, either by a) ball-milling or by b) melting. The reference diffraction patterns for CsI and CsBr are extracted from the XRD presented in Figure S4a.

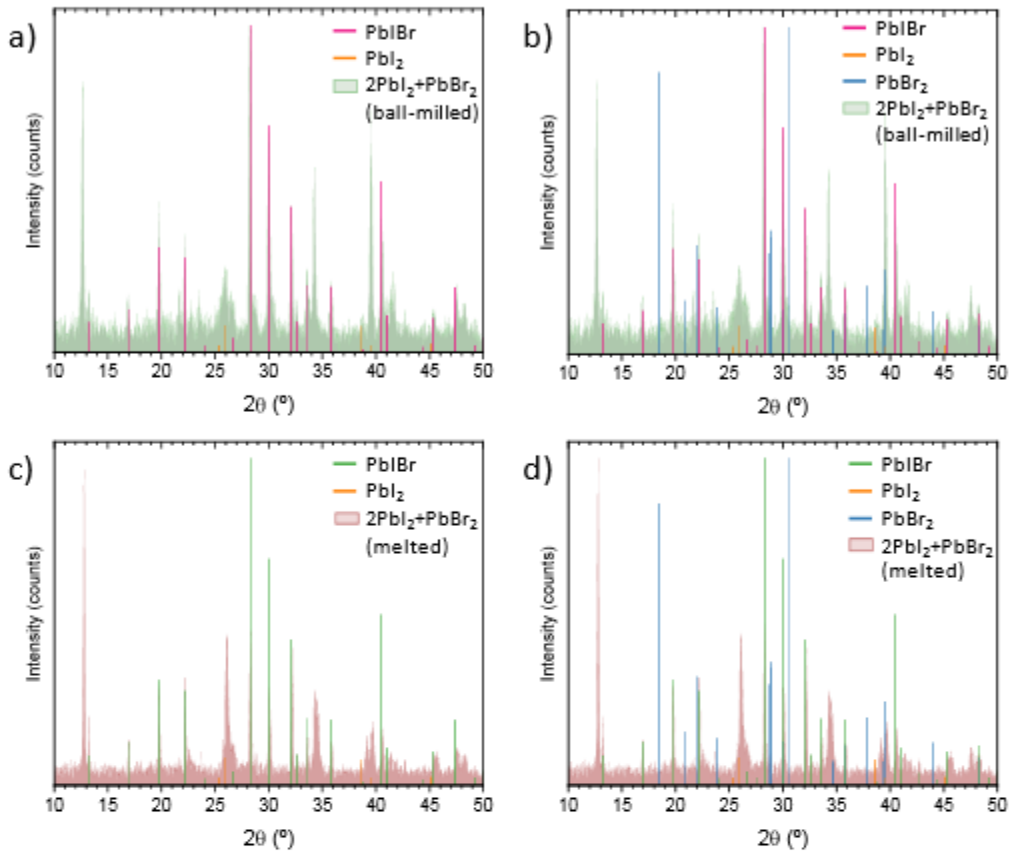

Figure S6. XRD patterns of the products obtained by solid state reactions of $2PbI_2 + PbBr_2$, either by a,b) ball-milling or by c,d) melting. The reference diffraction patterns for PbI_2 and $PbBr_2$ are extracted from the XRD presented in Figure S4b. The reference for the mixed halide PbIBr is taken from the Inorganic Crystal Structure Database (ICSD, Collection Code 22138). In a,c) our reference pattern for $PbBr_2$ was omitted to enhance clarity.

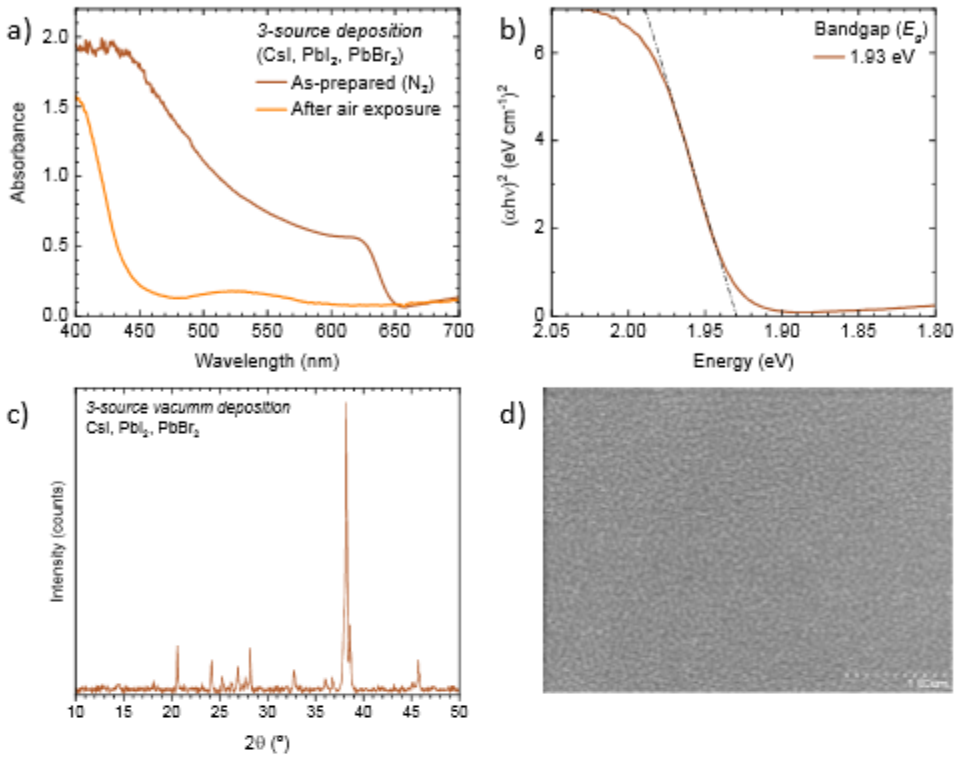

Figure S7. Characterization of $CsPbI_2Br$ films obtained by simultaneous sublimation of CsI, PbI_2 and $PbBr_2$. a) Optical absorption spectra of as-deposited films (brown) and immediately after air exposure (orange). b) Tauc plot for as-deposited films recorded in nitrogen atmosphere, and c) XRD pattern of the film, showing complete degradation of the material upon air-exposure. d) SEM image of an as-deposited film obtained with the same process.

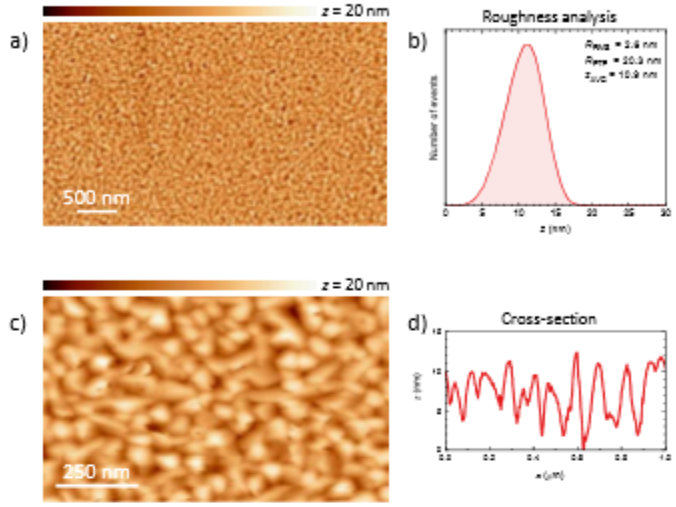

Figure S8. Atomic force microscopy of $CsPbI_2Br$ films prepared by 3-sources fast vacuum deposition at RT. a) Large area topography showing a homogeneous and pinhole-free surface with b) corresponding roughness analysis. c) Higher resolution scan of the sample surface, with d) cross-section trace showing a maximum z variation of approximately 10 nm within the grains.

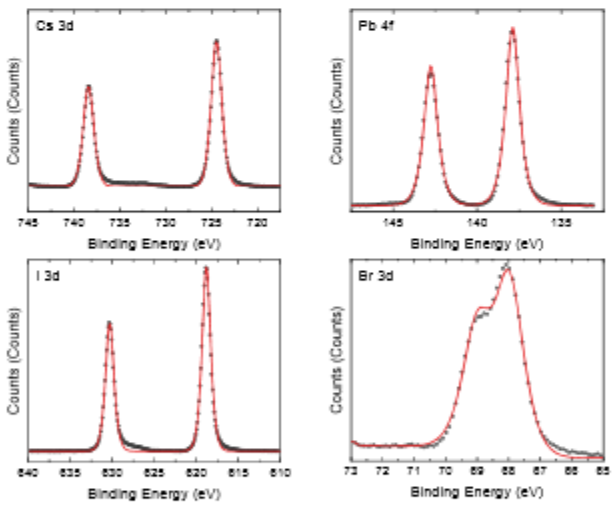

Figure S9. High-resolution XPS spectra of all the main elements as detected from a $CsPbI_2Br$ film obtained by 3-sources vacuum deposition: Cs 3d, Pb 4f, I 3d, and Br 3d regions. The calculated I/Br ratio is 1.8, close to the expected value of 2 for this particular perovskite stoichiometry. We also found an excess of Cs on the perovskite surface (Cs/Pb = 1.7 instead of 1), which is most likely a surface accumulation, as there is no indication of the presence of phase-segregated cesium halides from bulk XRD measurements.

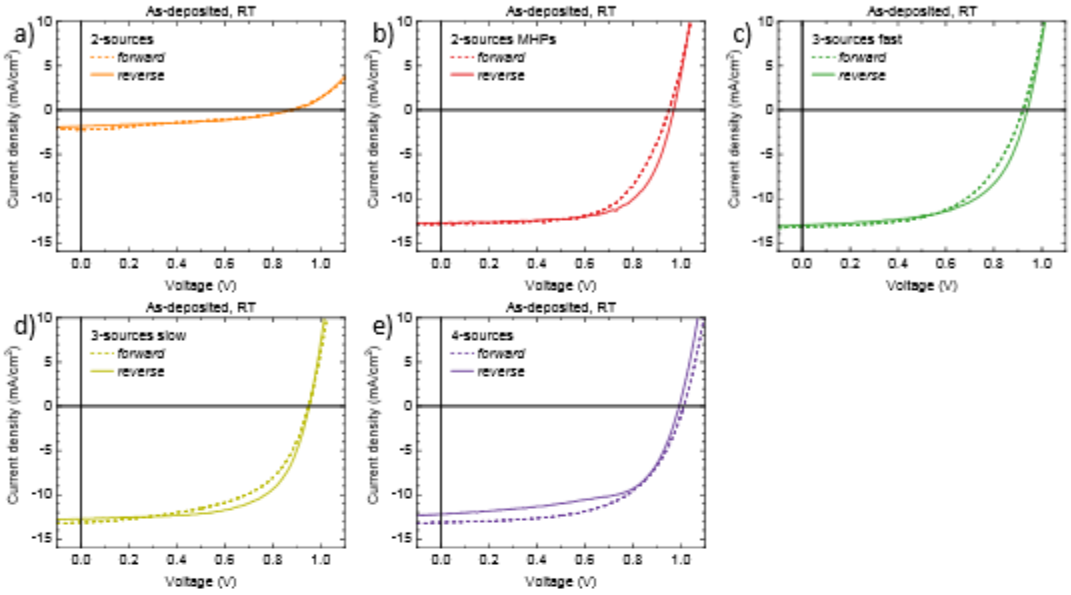

Figure S10. J-V curves in forward (from short to open circuit) and reverse (from open to short circuit) bias for a series of solar cells employing CsPbI2Br deposited at room temperature with the different vacuum techniques.

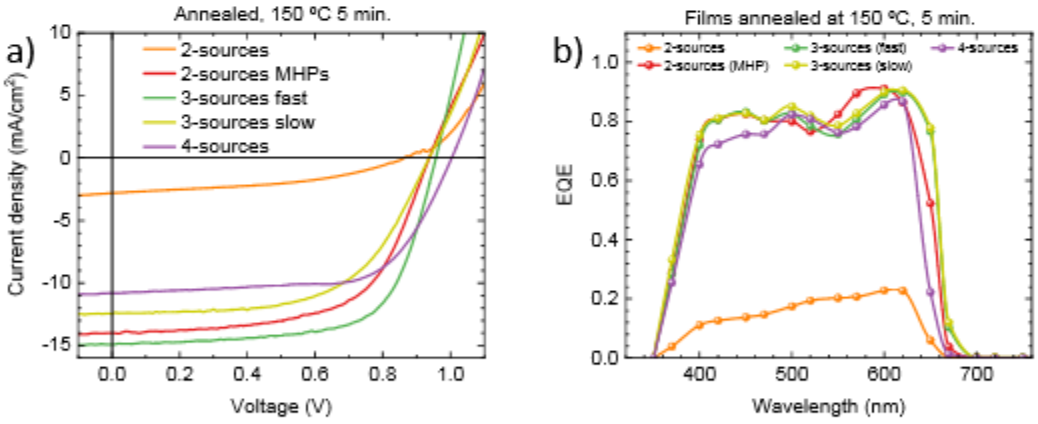

Figure S11. a) J-V curves under illumination in reverse scan and b) corresponding spectral response for the entire series of solar cells with annealed $CsPbI_2Br$ thin films.

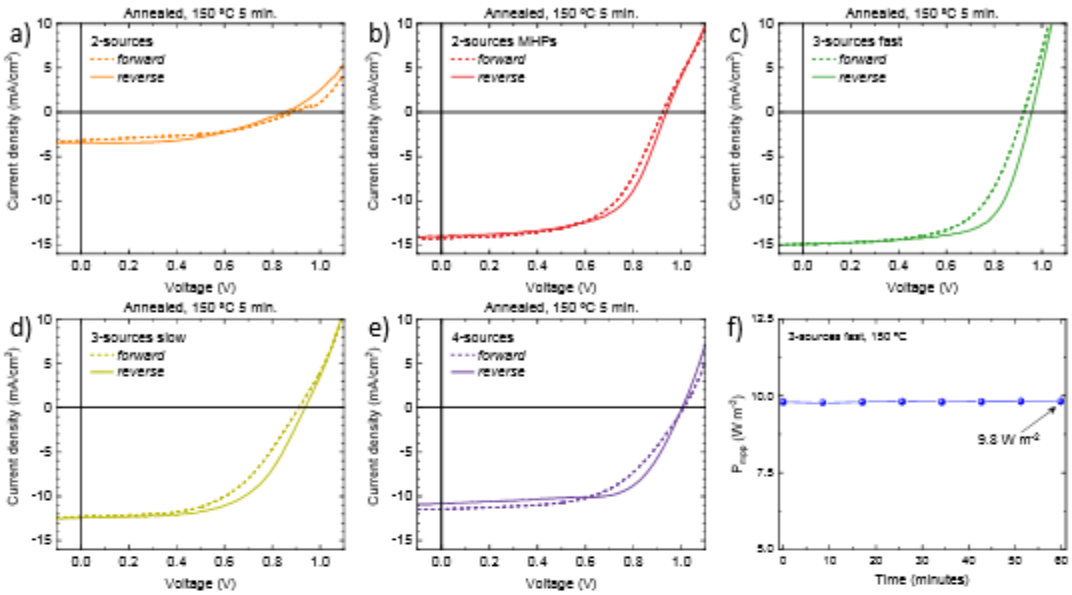

Figure S12. (a-e) J-V curves in forward (from short to open circuit) and reverse (from open to short circuit) bias for a series of solar cells employing CsPbI2Br with annealing at 150 °C for 5 minutes and prepared with the different vacuum techniques. (f) Steady power output under maximum power point tracking for a solar cells with CsPbI2Br prepared by 3-sources vacuum deposition at the rate of 2.0 Å/s (fast) with annealing at 150 °C for 5 minutes (blue).

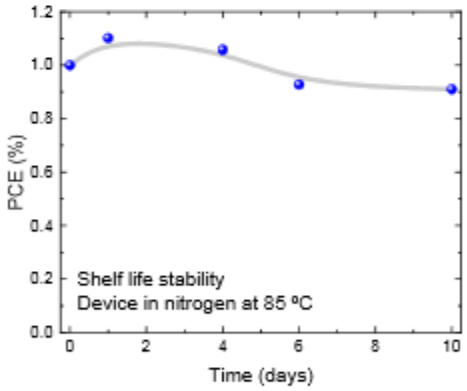

Figure S13. Shelf-life thermal stability measurement obtained by collecting J-V curves at different times for an encapsulated device, stored in nitrogen and in the dark on a hot plate at 85 °C. The device is based on a $CsPbI_2Br$ film obtained by 3-sources fast deposition and annealed at 150 °C.

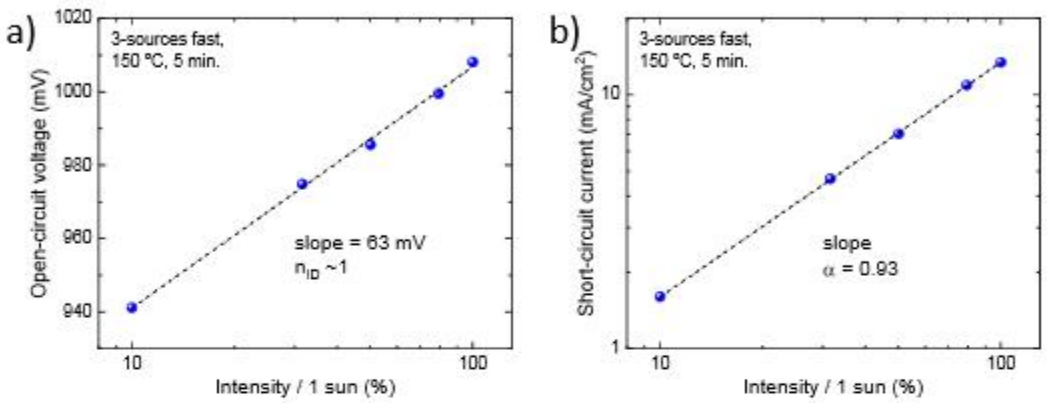

Figure S14. Intensity dependent (a) open-circuit voltage and (b) short-circuit current for a solar cell with a $CsPbI_2Br$ film deposited by 3-sources vacuum deposition at 2.0 Å/s, annealed at 150 °C for 5 minutes. The ideality factor (n_{ID}) is estimated with the slope of the semi-log plot (a), while the short-circuit current in (b) has been fitted with a power law $J \propto I^{\alpha}$, where I is the incident light intensity.

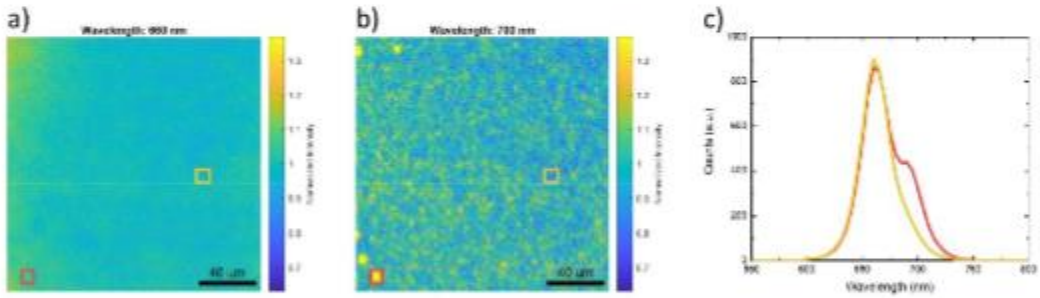

Figure S15. PL maps of a p-i-n solar cells based on $CsPbI_2Br$ (3 sources "fast" with annealing) a) at the wavelength of the main emission (660 nm) and b) at a wavelength of the low energy component (700 nm), which highlight the homogeneity of the $CsPbI_2Br$ film and the inhomogeneous spatial distribution of the low energy emission. Both maps are normalized to their individual mean value. c) Not-normalized spectra at two positions of the map (indicated by the colored boxes) showing the intensity of the low energy feature in few locations and the absence in others.

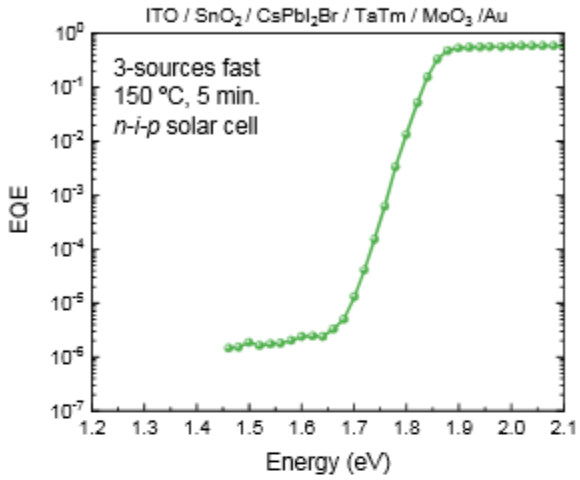

Figure S16. Sensitive EQE spectrum of a n-i-p device with 3 sources "fast" annealed with SnO_2 as ETL and TaTm as HTL, not showing the feature at 1.7 eV as in Fig 4.